PhD thesis

Switchable molecular magnets: from synthesis and polymer matrix integration to stimuli-responsive composite materials

Aleksandra Pacanowska

Supervisor:

dr hab. inż. Magdalena Fitta, prof. IFJ

The Henryk Niewodniczański Institute of Nuclear Physics
Polish Academy of Sciences

Department of Molecular Magnetism

Kraków, 2025

Acknowledgments

First and foremost, I would like to express my deepest gratitude to my supervisor, ***dr hab. Magdalena Fitta****, for granting me the opportunity to carry out my research within such a supportive and inspiring academic community. Over the past five years, her vision, encouragement, and willingness to share her expertise have been invaluable in the expansion of my ideas and the consolidation of my scientific knowledge. Her insightful feedback and constant guidance have steered this work to its fruition.*

I am profoundly indebted to my auxiliary supervisor, the late ***dr hab. Małgorzata Jasiurkowska-Delaporte****, in whose memory I dedicate this dissertation. For nearly four years, her inspiration, thought-provoking discussions, and unwavering support opened the doors to the fascinating world of electrospinning and laid the foundation for my scientific growth.*

I wish to express my gratitude to the ***members of the Department of Molecular Magnetism*** *and* ***my colleagues from Division of Condensed Matter Physics*** *at the Institute of Nuclear Physics, Polish Academy of Sciences for their assistance in realizing my research objectives and for fostering a pleasant and collaborative working environment.*

My thanks also go to the colleagues at the Faculty of Chemistry, Jagiellonian University, under the leadership of ***dr hab. Beata Nowicka****, for their support in achieving our common research goals, as well as to the group of* ***dr hab. Wojciech Tabiś*** *at AGH University for introducing me to X-ray absorption spectroscopy and for their support throughout this journey.*

I would also like to thank ***dr Alicia Forment-Aliaga*** *for her encouragement and fruitful discussions, as well as the group of prof. Eugenio Coronado for their warm welcome during my research stay at the Institute of Molecular Science, University of Valencia in Spain.*

I am grateful to ***my peers*** *at the Kraków School of Interdisciplinary PhD Studies for creating an engaging atmosphere and for allowing me to serve as President of the PhD Student Council, an experience that enriched my doctoral training.*

Finally, I extend my heartfelt thanks to ***my family and friends*** *for their constant support, belief in me, and interest in my work. Their encouragement has been the bedrock upon which this dissertation was built.*

Streszczenie

Przełączalne magnetyki molekularne stanowią atrakcyjną klasę związków koordynacyjnych, których stan spinowy może być przełączany pod wpływem zewnętrznych czynników fizycznych, takich jak temperatura, ciśnienie czy naświetlanie. Dzięki precyzyjnemu doborowi bloków budulcowych w trakcie syntezy oraz otrzymanym właściwościom przełączalnym, badane układy wykazują znaczący potencjał w projektowaniu zaawansowanych czujników, inteligentnych tekstyliów oraz materiałów do zapisu danych. Wprowadzenie przełączalnych układów do matryc polimerowych nie tylko zwiększa ich wytrzymałość mechaniczną i przetwarzalność, ale także umożliwia materiałom kompozytowym wykazywanie wielofunkcyjnej wydajności.

W poniższej rozprawie doktorskiej została przedstawiona metodyka i charakterystyka serii materiałów kompozytowych na bazie polimerów zawierających trzy prototypowe układy koordynacyjne: mikro- i nanocząstki analogów błękitu pruskiego (PBA), które wykazują uporządkowanie magnetyczne dalekiego zasięgu; nanocząstki żelaza(II) z możliwością przełączania stanów spinowych (przejście typu spin-crossover, SCO), które charakteryzują się zmianą ze stanu nisko- do wysokospinowego pod wpływem temperatury; oraz dwu-metaliczny łańcuch oparty na jonach niklu i żelaza, wykazujący odwracalny efekt przeniesienia ładunku między metalami pod wpływem temperatury lub przyłożonego ciśnienia zewnętrznego. Każdy z badanych systemów cechuje się unikalnym mechanizmem przełączania, co stwarza wszechstronną platformę badawczą do analizy wpływu magnetycznej domieszki na ostateczne właściwości kompozytów.

Wprowadzenie przełączalnych układów molekularnych jako dodatek do matryc polimerowych zostało zrealizowane poprzez wykorzystanie techniki elektroprzędzenia i metodę nakropienia na powierzchnię (drop-casting). Elektroprzędzenie to proces, dzięki któremu możliwe jest wytworzenie stałych, elastycznych mat polimerowych w wyniku wyciągania z zawiesiny polimerowej ultracienkich włókien pod wpływem przyłożonego wysokiego napięcia. Drugą przedstawioną metodą otrzymywania materiałów kompozytowych jest wytwarzanie jednolitych warstw poprzez nakropienie i odparowanie rozpuszczalnika. Wybór obu technik opierał się na ich skalowalności, kompatybilności z różnymi matrycami polimerowymi i możliwości zachowania właściwości przełączalnych wprowadzonych struktur koordynacyjnych.

W badaniach wykorzystano szereg technik umożliwiających kompleksowe wyznaczenie właściwości strukturalnych i magnetycznych otrzymanych materiałów kompozytowych. Mikroskopia elektronowa i dyfrakcja rentgenowska zapewniły szczegółowy wgląd w morfologię i zachowanie struktury krystalicznej próbek. Ponadto zastosowano spektroskopię wibracyjną w celu zbadania stabilności chemicznej układów funkcjonalnych po użyciu techniki wykorzystującej wysokie napięcie do przygotowania materiałów. Synchrotronowa spektroskopia absorpcji promieniowania rentgenowskiego, spektroskopia Mössbauerowska oraz magnetometria SQUID zostały wykorzystane do zbadania zjawisk przełączania spinów i przeniesienia ładunku. Uzupełniające analiza termiczna oraz eksperyment in situ indukowanego przejścia pod wpływem ciśnienia dodatkowo wykazały odporność i reaktywność kompozytów w warunkach odpowiadających potencjalnym zastosowaniom.

Badania zawarte w niniejszej rozprawie dowodzą, że wrażliwe na bodźce zewnętrzne magnetyki molekularne, zwykle podatne na kruchość i degradację w określonych warunkach przechowywania, można skutecznie osadzić w matrycach polimerowych bez utraty ich przełączalnych właściwości. Trójwymiarowe maty złożone z elektroprzędzonych włókien charakteryzują się zarówno wysoką odpornością mechaniczną, jak i szybką odwracalną reakcją na zmianę warunków otoczenia, podczas gdy warstwy wykonane metodą nakrapiania umożliwiają szybką detekcję. Podsumowując, badania wchodzące w tematykę tej rozprawy przedstawiają metodologię wytwarzania materiałów kompozytowych opartych o matrycę z polimerów organicznych oraz układów magnetyków molekularnych reagujących na bodźce zewnętrzne, które mogą zostać wykorzystane w inteligentnych urządzeniach i materiałach przełączalnych nowej generacji.

Abstract

Switchable molecular magnets represent a compelling class of coordination compounds, whose magnetic states may be modulated reversibly in response to external stimuli such as temperature, pressure, or irradiation. The combination of precise molecular design and functional responsiveness renders them particularly promising for applications in sensing, data storage, and adaptive textiles. The integration of these switchable entities within polymer hosts not only enhances mechanical robustness and processability but also enables composite materials to exhibit multifunctional performance.

The following thesis outlines the development and characterisation of a series of polymer-based composite materials incorporating three prototypical coordination systems: micro- and nanoparticles of Prussian Blue Analogues (PBAs), which display long-range magnetic ordering; iron(II) spin-crossover (SCO) nanoparticles, which undergo temperature-driven high-spin to low-spin transitions; and a bimetallic nickel–iron charge-transfer chain exhibiting reversible metal-to-metal electron transfer under thermal or mechanical stimuli. Each of these systems demonstrates a distinct switching mechanism, thus providing a broad platform from which to further investigate the interplay between molecular architecture and composite behaviour.

The incorporation of functional fillers into polymer matrices was primarily achieved through the utilisation of solution-based processing methodologies, with a particular focus on electrospinning and drop-casting techniques. Electrospinning is a process that facilitates the formation of flexible, non-woven fibre mats by drawing polymer–particle suspensions into ultrafine filaments. Alternatively, the fabrication of uniform films was enabled by drop-casting. The selection of both techniques was based on their scalability, compatibility with a variety of polymeric hosts, and capacity to preserve the intrinsic switching properties of the embedded materials.

A comprehensive approach to characterisation techniques was adopted for the purpose of extracting the structural, electronic, and magnetic properties of the resulting composites. Electron microscopy and X-ray diffraction techniques provided detailed insight into the morphology and phase integrity of the samples. In addition, vibrational spectroscopies were employed to probe the chemical stability of the functional systems following the implementation of high-voltage composite preparation techniques. Synchrotron X-ray absorption spectroscopy, Mössbauer spectroscopy, and SQUID magnetometry were employed to interrogate the spin and electron transfer switching phenomena. Complementary thermal analyses and in situ pressure-induced experiments further demonstrated the composites' resilience and responsiveness under conditions corresponding to the anticipated applications.

The investigations demonstrate the potential for the integration of stimuli-responsive molecular magnets, which are often characterised by fragility and degradation under certain conditions, into polymer matrices without compromising their switchable function. Electrospun fibre meshes exhibit both mechanical flexibility and rapid, reversible response to external triggers, whereas drop-cast films afford spatially resolved sensing capabilities. Collectively, this research establishes methodology for the fabrication of stimuli-responsive magnetic composites, which can be applied to next-generation smart devices and adaptive material systems.

Table of contents

1. Introduction

1.1 Functional coordination structures

Coordination polymers (CPs) are a class of extended inorganic–organic hybrid materials formed by linking metal centres with multidentate organic ligands into one-, two-, or three-dimensional networks. The "bottom-up" assembly process, in which discrete building blocks preserve their structural integrity throughout the reaction, enables exquisite control over both the topology and functionality of the resulting frameworks. Historically, the primary interest in CPs was in their structural properties as solids. However, in recent years, these materials have emerged as highly designable substances whose properties can be tuned by the selection of metal, ligand design, and synthetic conditions[1].

The design of molecular materials has the capacity to induce a variety of features, including but not limited to magnetic properties[2], porosity[3,4], non-linear optical activity[5], conductivity[6], chirality[7], reactivity to changes in external conditions[8–10], or susceptibility to chemical stimuli[11,12]. These features can result in the production of functional coordination structures. A prime example of this phenomenon is provided by coordination polymers, which are known as molecular magnets[13]. The potential for crystal engineering to chemically design structures of desired architecture has been widely exploited in order to induce magnetic properties in the materials. The utilisation of a modular approach has been demonstrated to facilitate the assembly of paramagnetic metal ions, which possess unpaired electrons in d or f orbitals, and/or organic radicals, which possess unpaired electrons in p orbitals. These entities are connected through the utilisation of appropriate ligands. Consequently, the paramagnetic centres exhibit the capacity to interact magnetically with each other at temperatures lower than a certain threshold. The occurrence of long-range magnetic ordering is a consequence of quantum-mechanical super-exchange phenomena resulting from the overlap of the relevant orbitals of paramagnetic centres and the bridging ligands. The nature of the ordering is contingent upon the electronic configuration of the metal centres, the ligand's nature, and the connection's geometry. The first molecule-based ferromagnet to be synthesised at a temperature below 16 K was a one-dimensional chain $[Fe^{III}(C_5Me_5)_2]^+[TCNE]^-$ prepared by Miller et al. (1988)[14]. Since then, various examples of molecular magnets have been shown, starting from three-dimensional Prussian Blue Analogues (PBAs) with long-magnetic ordering above 300 K[15,16] or exhibiting photo-induced magnetism[17,18], through two-dimensional layered structures[19,20], one-dimensional chains with Single Chain Magnet (SChM) behaviour[21], down to zero-dimensional clusters exhibiting Single Molecule Magnet (SMM) behaviour shown by Sessoli et al.[22–25], directing the research in molecular magnetism towards spintronics applications[26–30].

Another noteworthy feature of coordination polymers that derives from their architecture is porosity, which manifests in the form of voids or channels within crystallographic structures[31]. The capacity of CPs to be constructed with precise pore geometries and tuneable sizes has been

well documented. The combination of ligands of varying lengths and rigidity has been demonstrated to result in the transformation of structures. Starting from rigid metal-organic frameworks (MOFs), which are characterised by permanent porosity and channels and cavities that are stabilised following the removal of solvent (an ideal condition for catalytic purposes)[32,33]. This is followed by more dynamic porous structures, which manifest the "breathing" effect of the crystal lattice[34–36]. In such instances, the removal or incorporation of solvent/guest molecules gives rise to structural changes that may also affect other properties of the material, for example magnetic properties (in the solvatomagnetic effect)[37]. The conjugation of porosity and magnetic properties in a single material was presented by Oliver Khan and colleagues in 1999[38]. The study demonstrated the impact of solvent molecules on the structural alterations of the coordination framework. In systems referred to as "magnetic sponges," a reversible polymerization process was observed upon the removal or absorption of water molecules into the crystal structure. The magnetic properties of the sponges were found to vary at each stage of structural reformation.

As a result, in the field of coordination polymers, a category of dynamic molecular crystals emerged, wherein the properties exhibited by the material can be (reversibly) switched by alterations in external conditions (schematic representation in Figure 1.1.1). As Sato has reviewed[39], dynamic crystals harness mechanisms such as thermally or photoinduced spin state transitions, redox state switching of molecular components, guest-molecule induced reconfiguration of crystal structure, stimuli-induced molecular reorientation, and many more. Mechanisms found in dynamical crystals have the capacity to trigger abrupt, often hysteretic changes in magnetism, conductivity, polarization, optical properties, or mechanical strain. For instance, a significant number of octahedral Fe^{2+} complexes have been observed to reversibly interconvert between low-spin and high-spin states when exposed to heating or light irradiation. This phenomenon results in the material becoming bistable over a finite temperature range, thereby conferring memory and switching capabilities. Through the judicious selection of ligands and the meticulous design of crystallographic structures stemming from a modular approach, such dynamic CPs manifest as stimuli-responsive solids, thereby exhibiting the remarkable property of transforming molecular-level electronic changes into observable shifts in macroscopic properties.

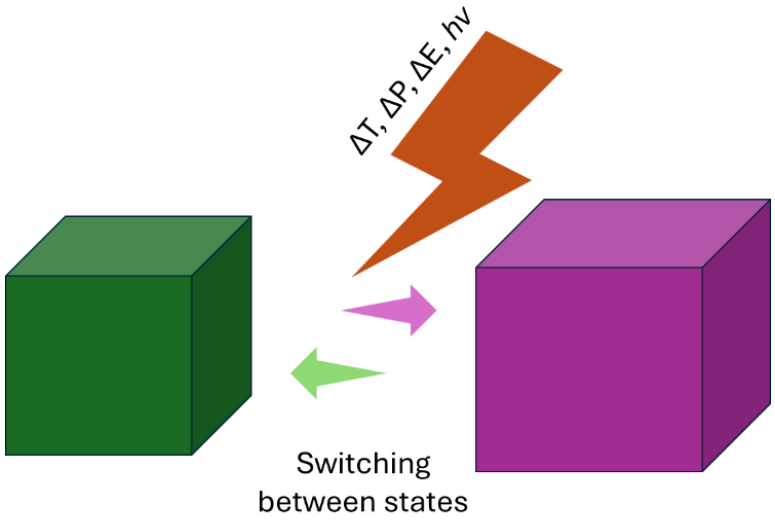

Figure 1.1.1 Schematic representation of a dynamic molecular crystal and its switching properties under external stimuli[39].

In the context of dynamic coordination polymers, Prussian Blue Analogues (PBAs) are of particular significance due to their multifunctional nature. Structurally, PBAs are cyano-bridged frameworks of general formula $AM^{2+}[M'^{3+}(CN)_6]_x \cdot zH_2O$, where M^{2+}/M'^{3+} can be various transition metal pairs (e.g., Mn^{2+}/Fe^{3+}, Co^{2+}/Cr^{3+}, V^{2+}/Cr^{3+}, Ni^{2+}/Cr^{3+}, Ni^{2+}/Fe^{3+}, Fe^{2+}/Co^{3+})[40,41], and A is an alkali cation or vacancy that occupies interstitial sites. Depending on the degree of vacancy ordering, the framework may adopt a face-centred cubic arrangement with alkali ions in tetragonal sites, or a defected variant with coordinated water molecules, shown schematically in Figure 1.1.2. The linear cyano-bridges facilitate strong super-exchange, often yielding long-range magnetic ordering (e.g., Curie temperature above 300 K in V^{2+}/Cr^{3+} PBAs[42]). Furthermore, certain PBAs have been observed to undergo thermal charge-transfer phase transitions (eg, Mn^{2+}-NC-Fe^{3+} ↔ Mn^{3+}-NC-Fe^{2+}), accompanied by lattice distortions and abrupt colour changes[43], or pressure-induced increase of the critical temperature of magnetic ordering (Mn^{2+}/Mn^{3+})[44]. Relevant from the technological point of view is photomagnetism exhibited by PBAs, such as Co^{2+}/Fe^{3+} analogues, as a consequence of photoexcitation, which generates ferromagnetic Fe^{3+}-CN-Co^{2+} states from paramagnetic precursors at cryogenic temperatures[45]. The water content modulation and alkali-ion selection in the PBA structures offer further opportunities for manipulation. For instance, humidity-sensitive magnetic properties were found in the Co^{2+}/Cr^{3+} system, where rearrangements of coordinated and zeolitic water modified super-exchange pathways. With further modifications of the lattice by the addition of Mn^{2+} ions, ferroelectric-ferromagnetic coupling was achieved[12]. Finally, PBAs have been shown to support proton conduction via connected water networks, leading to spin-ionic coupling wherein magnetostriction alters hydrogen-bond networks and thus proton conductivity[46]. Collectively, PBAs serve as paradigms of multifunctionality, combining magnetic, optical, ionic, and electronic phenomena within a single coordination framework.

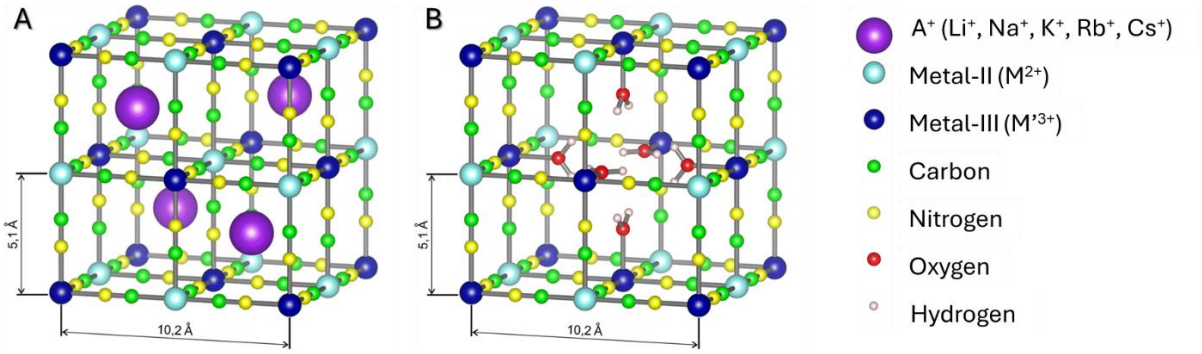

Figure 1.1.2 Crystallographic structures of PBAs: face-centred cubic arrangement with incorporated alkali ions (A) and defected system with coordinated water molecules (B)[47].

A remarkable degree of structural and electronic tuneability found in the field of coordination polymers renders them as highly promising candidates for a broad range of applications. In the fields of molecular electronics and spintronics, dynamic CPs with switchable magnetism have been demonstrated to enable bistable memory elements operating at the nanoscale[48]. Furthermore, CPs with luminescent lanthanide or d^0/d^{10} centres are useful in optical sensing[49,50], while electrically conductive frameworks are being explored for use in batteries or supercapacitors[51]. In the domains of gas storage and separation, MOFs play a leading role as they may exhibit high surface areas and well-defined pore structures, which confer them with selective adsorption capabilities[52]. The modulation of these properties can be further enhanced through the utilisation of framework flexibility or ligand functionalisation strategies. In the context of heterogeneous catalysis, immobilized metal centres embedded in porous architectures have been shown to mimic enzymatic pockets, thereby offering size and shape selectivity, as well as facilitating mass transport[33,53,54]. The capacity of CPs to undergo structural transitions upon guest uptake is a key advantage in membrane or sensor applications[55,56]. Finally, biomedical applications of CPs, ranging from theranostic agents[57] to MRI contrast agents[58], are beginning to emerge as researchers increasingly exploit the chemical modularity and biocompatibility of certain CP families. In each case, the combination of modular approach in compound engineering and possibilities to merge multiple properties in one material affords a degree of design flexibility that is unparalleled by conventional solid-state materials.

1.2 The scope and goal of the thesis

The theme of the following thesis lay in coordination compounds, with a focus on the systems characterised by well-defined bistability, embedded into an organic polymer matrix in the form of electrospun fibres and drop-casted foils. The thesis describes the preparation methodology of both polycrystalline fillers and their appropriate polymer composites, basic characterisation, and the overall evaluation of the differences between composites and their starting elements. The experimental part of the thesis is divided into three parts, each treating a different family of coordination compounds and composite materials prepared on their basis.

The first chapter is devoted to the preparation of electrospun fibres based on micro- and nanoparticles of two families of Prussian Blue Analogues (PBA). Due to their straightforward synthetic routes and wide range of possible metal combinations, these structures have been extensively studied from the early days of molecular magnetism research to the present. Starting from the standard examples of $Ni_3[Cr(CN)_6]_2 \cdot nH_2O$ (**NiCr**) and $Ni_3[Fe(CN)_6]_2 \cdot nH_2O$ (**NiFe**) structures[59,60], which in fact do not show any switchability and bistability, however, they served as an ideal introduction to the methodology of electrospun fibres preparation. The synthesis of both systems in the form of well-defined nanocubes has been described, as well as the characterisation of their structural, spectroscopic, and magnetic behaviour. At the same time, the preparation of polyvinylpyrrolidone (**PVP**) fibres doped with both coordination structures has been presented, with the focus on their resulting properties and the impact of the composite preparation. The thesis then delves into the preparation of electrospun fibres based on the flagship PBA structure showing metal-to-metal charge transfer (MMCT) transition, with the general formula $Rb_xMn[Fe(CN)_6]_{(x+2)/3} \cdot nH_2O$ (**RbMnFe**)[61,62]. Again, the synthetic protocol for one example of sub-microparticles is presented together with a description of their properties, with a focus on the magnetic bistability. The production of electrospun fibres of PVP polymer with added functional filler is shown, and their properties are characterised based on optical and electron microscopy, Raman spectroscopy, and magnetic measurements, and the effect of particles embedding into the organic matrix is discussed. First example of a composite based on MMCT additive (where the filler was stable over a wide range of external conditions).

The second chapter is devoted to the one of more elaborated examples of spin crossover (SCO) compounds, namely one-dimensional $[Fe(Htrz)_2(trz)](BF_4)$ (Htrz = 1,2,4-1H-triazole) (**FeTrz**) coordination chain, which exhibits spin transition above room temperature (~350 K), making it a molecular structure quite relevant in the development of molecule-based electronics[63–65]. More importantly, it has been shown that tuning of the hysteresis range can be done by varying particles dimensions, without losing the bistable region even for the smallest synthesised nanoparticles. At the beginning of the chapter, a detailed characterization of particles of various sizes, ranging from nano- to microscale, synthesized via the reverse micelle technique, was presented. The focus was placed on comparing the size-dependent spin crossover (SCO) effect using Mössbauer spectroscopy, X-ray absorption spectroscopy (XAS), and magnetic measurements. In the latter part, the preparation of PVP electrospun fibres and drop-casted foils doped with FeTrz nanoparticles has been presented, and the effect of the organic matrix upon the spin transition has been discussed, based on calorimetric and magnetic measurements. Part of the

material preparations and characterisation described in this chapter have been performed in collaboration with Eugenio Coronado's group from the University of Valencia, as a result of an international scholarship exchange for doctoral students (STER and PROM) from the NAWA agency.

The last experimental chapter is fully devoted to a multi-functional coordination complex, $\{NH_4[Ni(cyclam)][Fe(CN)_6]\cdot 5H_2O\}_n$ (cyclam = 1,4,8,11-tetraazacyclotetradecane) (**NiFe-chain**), where metallic moieties have been bridged by CN-ligand, forming a one-dimensional chain[66]. It is an extraordinary example, as it exhibits three phases stable within a certain range of external conditions; however, they can be reversibly interconverted by changing temperature, humidity, or applying pressure. It is an example of a coordination complex with MMCT properties, switching within room temperatures and exhibiting thermal hysteresis in the range 4 °C to 37 °C, with very distinct changes in optical, spectroscopic, and magnetic properties, making it a fine representative of a versatile molecular sensor. The first part of the chapter elaborates more on the characteristics of the crystalline structure and the process of top-down miniaturization, starting from finely formed single-crystals, and resulting in powder with micro- and submicroparticles. The influence of particle size on the general properties of the compounds is described. The chapter then follows the preparation method-ology of electrospun fibres with embedded particles within poly(ε-caprolactone) (**PCL**) or poly(2-vinylpiridne-co-styrene) (**P2VP-PS**) organic matrices, making it a first example of electrospun materials with MMCT additive, where the filler shows limitations in stability under certain conditions (recrystallization in water/alcohol conditions). The characterisation of the composites' properties is described in comparison to the powdered sample, and the issue of **NiFe-chain** fragility to water is elaborated based on X-ray diffraction measurements. The last subsection of the third chapter presents the preparation of drop-casted foils containing **NiFe-chain**. With this form of composite material, the switchability of the functional filler upon applying external pressure is elaborated, with the analysis of the MMCT transition in the pressed drop-casted foil by XAS spectroscopy, explored at the synchrotron radiation centre.

Overall, the goals of the presented thesis are:

- The presentation of a scalable and adaptable method for organic polymer composites doped by functional coordination structures, of different shapes and diameters.
- Showcasing the importance of studying the influence of organic polymer matrix on the functionalities of the dopants, by different preparation methodologies.
- The elaboration on the composites preparation for two types of coordination compounds switchability (SCO and MMCT), without loss of their sensing and switching abilities.
- Overcoming the limitations of powdered switchable coordination compounds by preparing more scalable materials that are easier to implement into real working devices.

The hypothesis of the following thesis is as follows: **it is possible to design and prepare switchable molecular compounds within an organic polymer matrix in the form of electrospun fibres and drop-casted foils, without the loss of coordination compounds' functionality.**

The research shown in the dissertation incorporates findings that were partially conducted as a part of the NCN grant OPUS 22, titled: “Switchable materials based on complex ions in nano- and micro- scale”, led by dr hab. Beata Nowicka from the Faculty of Chemistry at Jagiellonian University in consortium with dr hab. Magdalena Fitta at the Institute of Nuclear Physics, Polish Academy of Sciences.

1.3 Bistability in molecule-based materials

The concept of bistability, defined as the capability of a system to reversibly alternate between two distinct states in response to external stimuli, has attracted significant attention from researchers across multiple fields, including chemistry, physics, material engineering, and nanotechnology. This is primarily due to its relevance in the development of next-generation molecular electronics, memory devices, and responsive materials[67]. In this context, molecule-based coordination compounds exhibiting bistable behaviour are of particular interest. This is due to their intrinsic nanoscale functionality and the physical properties that can be tuned. In the field of molecular magnetic materials, the process of switching between two electronic states is contingent on the interplay of electronic structure, molecular geometry, intermolecular interactions, and external stimuli[68]. A plethora of methodologies have been documented within the domain of coordination chemistry to achieve switchability. Significant research endeavours have been prompted by variations in electron configuration, encompassing spin crossover (SCO) and electron-transfer-induced valence tautomerism, which occurs during electron transfer between two metal ions and is designated as metal-to-metal charge transfer (MMCT). Even though both phenomena yield two thermodynamically accessible states that differ significantly in terms of spin, colour, volume, and other physical properties, their chemical and physical origins are distinct. In the context of embedding such bistable compounds into organic polymer matrices, which falls within the scope of the presented thesis, it is essential to understand the microscopic driving forces that enable SCO and MMCT, as well as the cooperative interactions that give rise to sharp, hysteretic switching.

1.3.1 Spin crossover (SCO) effect

Spin crossover compounds, typically involving (pseudo)octahedral complexes of $3d^4$ – $3d^7$ transition metals[69] such as Cr(II), Mn(II), Mn(III), Fe(II), Fe(III), Co(III), and Co(II), exhibit bistability due to a thermally or optically induced transition between high-spin (HS) state with maximum number of unpaired electrons and low-spin (LS) state with minimum number of unpaired electrons (Figure 1.3.1A). The spin transition originates from a delicate balance between ligand field stabilization energy and spin pairing energy, explained based on ligand field theory[70]. Most 3d metal complexes exist only in one stable electron configuration, independently of external conditions. For particular octahedral complexes, usually with 6 nitrogen atoms as donors, the transition from LS to HS states is possible due to the decrease of ligand field strength in respect to spin-pairing energy leading to the increased population of higher-energy e_g orbitals with concomitant depopulation of lower-energy t_{2g} orbitals, as a response to small external perturbations. For most commonly used d^6 Fe(II) complexes, this transition involves conversion from a diamagnetic LS state with $(t_{2g})^6(e_g)^0$ configuration into a paramagnetic HS state, with electronic configuration of $(t_{2g})^4(e_g)^2$. Together with the LS to HS transition in electron configuration, the metal-ligand bond length increases, due to the antibonding character of the e_g orbitals (Figure 1.3.1B). An increase in temperature stabilizes the high-spin (HS) state, which is entropically favoured due to greater electronic and vibrational contributions. In contrast, the low-spin (LS) state is enthalpically favoured, characterized by stronger metal–ligand bonding and a smaller molecular volume, making it more stable at lower temperatures and under

increased pressure. Upon switching, SCO materials undergo dramatic changes in bulk properties such as magnetic susceptibility, colour, and electrical conductivity. Apart from changes in temperature and pressure, other external stimuli that lead to spin transition in SCO materials are adsorption/desorption of guest molecules and light or X-ray irradiation[13].

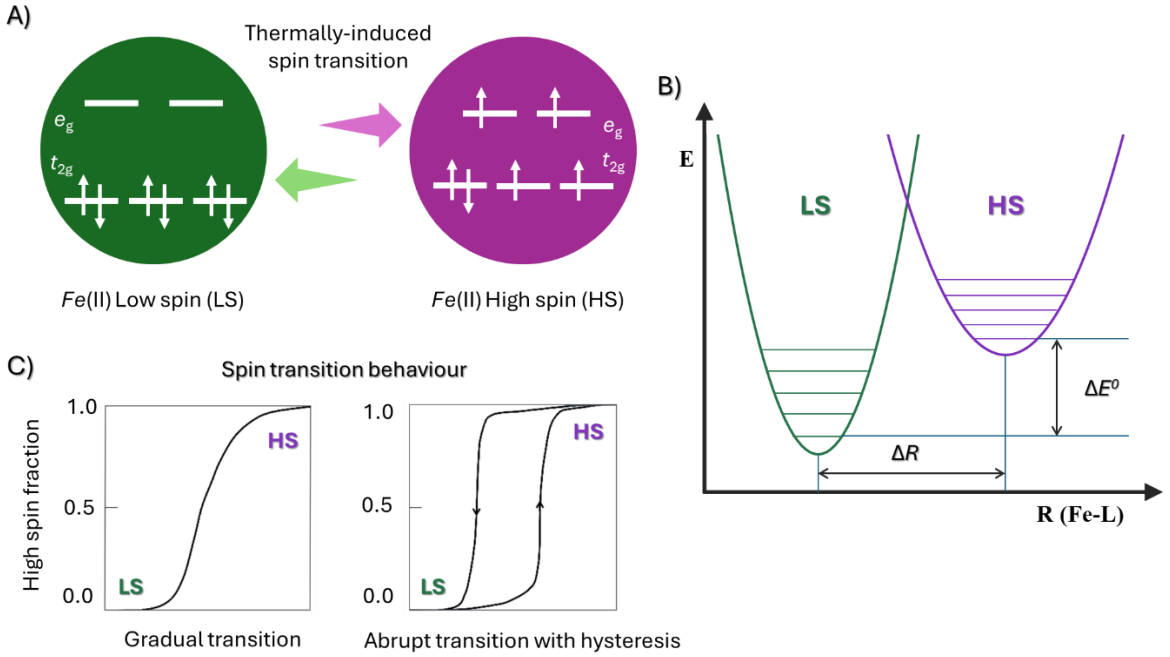

Figure 1.3.1 (A) Electron configuration for octahedral d-metals, example of Fe(II). (B) Potential wells for LS and HS. (C) Examples of the gradual SCO with hysteresis[39].

The change in electron occupancies of t_{2g} and e_g orbitals is also possible through higher energy excited states to photo-induce LS to HS conversion. Known as the light-induced excited spin-state trapping (LIESST) effect, it showcases the close entanglement of electronic and vibrational phenomena in SCO. Irradiation promotes the molecule to excited states that decay on the picosecond timescale into the HS potential well, and thus traps the system in a metastable HS state at low temperatures. The reverse decay can be thermally induced or driven by light of a different wavelength. This ability to photo-switch spin states within picoseconds and to trap them for seconds to hours at low temperatures opens avenues for ultrafast optical memory and molecular photonics[71].

The memory effect in SCO materials, which is most commonly manifested as a temperature hysteresis between LS to HS and HS to LS transitions, is a characteristic feature of cooperative behaviour[72,73]. This effect underlies the potential of these materials as molecular bistable devices. In bulk SCO samples, the presence of elastic interactions, arising from change in bond length between metal and ligand (approximately 0.2 Å for Fe(II)-N bonds), is evidenced, with each molecule behaving as an elastic inclusion whose volume misfit strains in the surrounding lattice are observed (Figure 1.3.2). Local distortions propagate via the crystal's elastic network, thereby effectively coupling neighbouring molecules. Consequently, once a critical temperature is reached, the lattice undergoes a collective first-order transition rather than a gradual, Boltzmann-like conversion. The hysteresis effect is characterised by non-coincidence of LS to HS

conversion (during the heating process) with the HS to LS transition (during the cooling process). The bistable temperature window provides intrinsic memory of the material's thermal history and enables the design of molecular switches and devices. These range from photonic memory elements to mechanical actuators, which can stably retain either spin states without a continuous power supply. The ability to engineer materials exhibiting room-temperature hysteresis has been an important endeavours in the field of SCO research. By optimising intermolecular cooperativity through ligand design, crystal packing, and nanostructuring, the fundamental foundations for information storage applications have been laid.

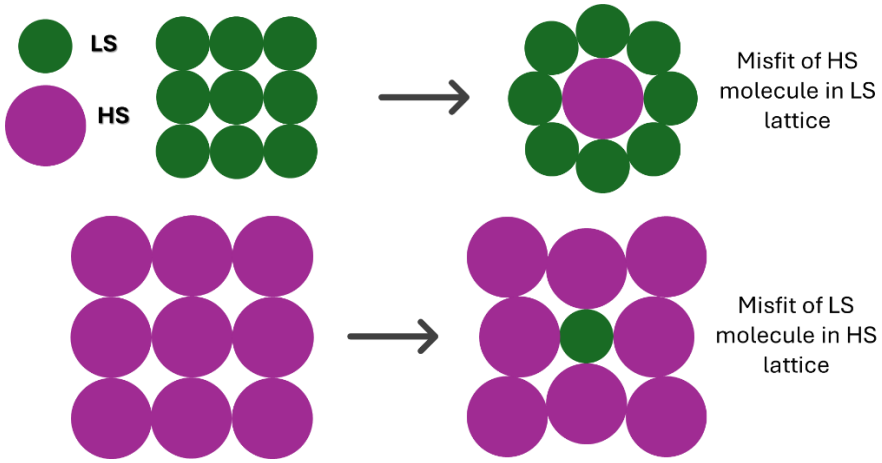

Figure 1.3.2 Scheme of the misfit of the LS molecule in an HS lattice.

However, it has been demonstrated that the nanoscale reduction of SCO materials can induce substantial size-related alterations[74], which can significantly modify or even eliminate the memory effect phenomenon (examples presented in Figure 1.3.3). As the dimensions of particles are reduced, the significance of surface and interface contributions to the free energy is enhanced, which, in general, results in the flattening of the spin-transition curves and the reduction or elimination of thermal hysteresis. A significant number of experiments have been conducted on systems of varying dimensionality, and it has been observed that nanoparticles frequently manifest a downshift in transition temperatures, a more gradual transition over a broader temperature range, and the presence of a residual high-spin fraction at low temperatures. These phenomena have been attributed to a weakened cooperativity and surface-stabilised HS states. It is important to note that, in certain coordination systems, there is an opportunity for hysteresis retention for particles measuring a few nanometres; however, for most nanoscale SCO assemblies, finite-size effects must be taken into consideration. In this view, successful integration into devices is a matter of careful control of particle crystallinity, surface chemistry, and matrix embedding, in order to preserve essential memory behaviour at reduced dimensions.

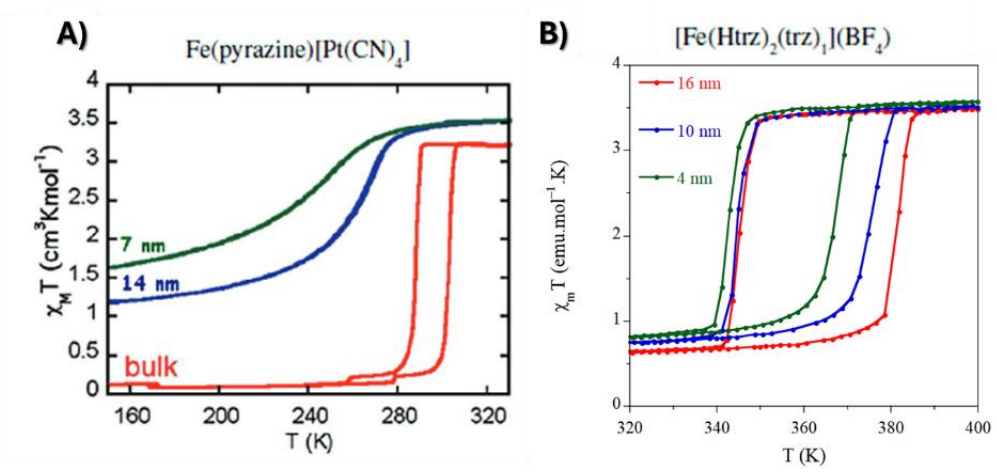

Figure 1.3.3 Examples of changes in magnetic susceptibility when going from bulk SCO to nanoscale. (A) The example with the elimination of hysteresis and a gradual transition[75]. (B) The example where the hysteresis has been retained[76].

1.3.2 MMCT materials

The bistability of MMCT coordination compounds stems from electron transfer between two distinct metallic centres, which are typically linked by a bridging ligand. This results in two valence isomers that differ in their electronic, magnetic, and structural properties. In the literature, cyanide linkers with strong σ-donor and π-acceptor properties have served as ideal channels for electron transfer[77]. Coordination systems originating from Prussian Blue Analogues (PBAs) with different compositions and dimensionalities have been the most prevalent in the field. Following the canonical example of the cyano-bridged Fe-CN-Co PBA system, the paramagnetic high-temperature phase Fe^{III}(LS)-CN-Co^{II}(HS) (S_{Fe} = 1/2, S_{Co} = 3/2) undergoes an electron transfer upon cooling, resulting in the diamagnetic low-temperature phase Fe^{II}(LS)-CN-Co^{III}(LS) (S_{Fe} = S_{Co} = 0)[78], presented schematically in Figure 1.3.4. Apart from the simple oxidation change of both metal centres induced by the electron transfer change, this system exhibits an additional spin transition at the Co centre. This phenomenon is known as electron-transfer-coupled spin transition. In addition to 3d metal assemblies, such as Fe/Fe, Fe/Mn, and Fe/Ni, studies on MMCT systems have also been extended to 4d and 5d metals (Mo, W, and Os), together with 3d metals, to form MMCT bimetallic coordination assemblies[79]. This underscores the potential for designing bistable coordination compounds, ranging from three-dimensional networks to low-dimensional clusters.

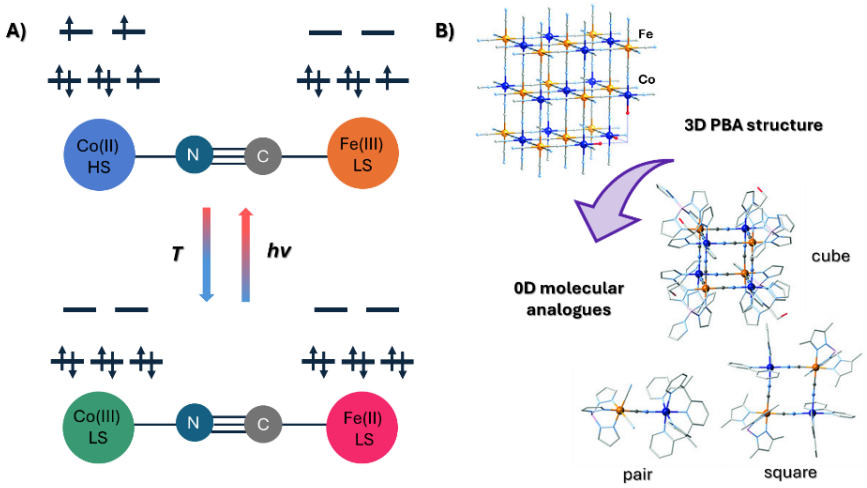

Figure 1.3.4 Scheme of the MMCT conversions for FeCo together (A) with structure visualizations[77] of Fe/Co combinations with different dimensionality (B).

Similar to SCO materials, electronic switching in MMCT systems can be toggled by various external stimuli, such as temperature, light, or pressure. Unlike SCO, which manifests bistability through a change in spin multiplicity on a single metal, MMCT assemblies involve charge redistribution between two sites, inducing redox changes and spin state switching simultaneously. These transitions consequently lead to differences in cell parameters, with the difference in bond length being up to 0.1 – 0.2 Å per metal site, due to the (de)population of the antibonding e_g orbitals[80,81]. These unique behaviours of volumetric thermal expansion (positive, negative, or zero) are an interesting area for development in the context of microscale or nanoscale actuators[82]. Changes induced by MMCT conversion can be observed optically as the intervalence charge-transfer bands shift, and noticeable thermochromism occurs. Other extensively analysed properties upon valence switching include magnetic susceptibility, which is accompanied by thermal hysteresis indicating a first-order transition, and switchable dielectric permittivity derived from rapid dipole reorganisation (Figure 1.3.5).

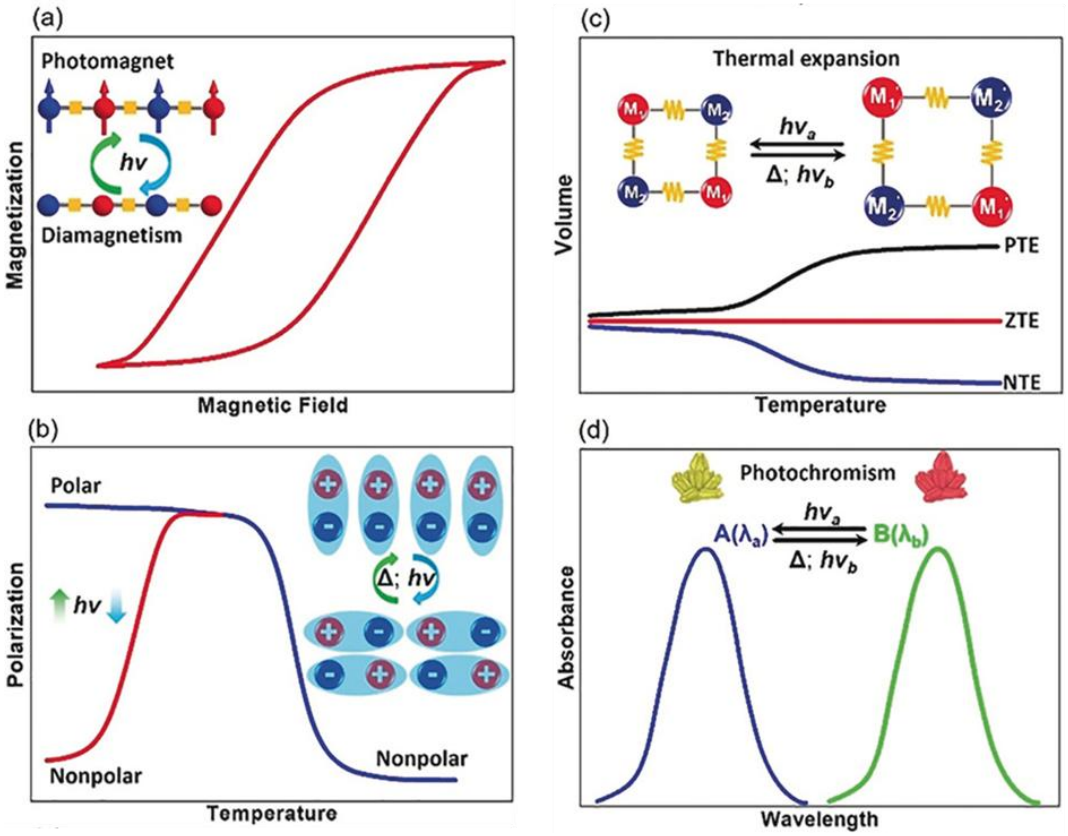

Figure 1.3.5 Schematic illustration of MMCT-induced changes in magnetism, electricity, thermal expansion, and photochromism[79].

The discovery of a reversible, photoinduced MMCT transition at cryogenic temperatures has played a crucial role in the further development of systems for use in optical data storage. For example, irradiation of the diamagnetic phase of the FeCo PBA system leads to ultrafast conversion into ferromagnetic states. Relaxation back to the ground state can occur thermally or under a second light stimulus, providing an excellent example of the reverse MMCT effect and affording bidirectional optical and magnetic switching[83]. This makes MMCT materials promising candidates for multifunctional, light-driven actuators.

1.4 Bistable materials embedded in a polymer matrix

The integration of switchable molecule-based compounds within functional devices necessitates a fabrication methodology for processable materials that can be effectively handled and integrated without compromising functionality, a prospect that currently remains challenging. One of the suggested approaches has been based on producing polymer composites, which in simple words can be described as multi-phase materials composed of organic polymer in the role of the matrix and bistable coordination compounds as fillers of lower concentration. According to recent literature[84], several approaches have been made, so far exploring SCO-based composites, and one can find examples of developed functioning actuators or sensors, while there is a lack of examples of composites based on CT compounds.

One of the suggested approaches involves using soluble SCO complexes or their precursors and incorporating them into polymers through solution-based methods. For example, Fe(II) complex with Schiff base ligand was dispersed into a polystyrene sulfonate (PSS) matrix by co-dissolution in water, followed by solvent evaporation, leading to films suitable for optical and photophysical studies[85]. Chen et al. demonstrated that mixing precursors of Fe(II) - aminotriazole (NH_2trz) system with polyvinylpyrrolidone (PVP) results in organised microstructure due to the strong hydrogen bonding forming between polymer and SCO complex, shifting the transition temperatures into higher regime, what highlighted the potential for fine-tuning SCO behaviour through supramolecular interactions with the matrix. By designing a highly soluble Fe(II)-SCO compound, Basak et al.[86] were able to shape the material into rectangular stripes within polystyrene (PS) using lithographic micro-pattering, which resulted in a flexible polymer composite with observable optical diffraction phenomena. Soluble SCO compounds have also been implemented into polymer matrices with the use of the electrospinning technique. With the creation of fibrous structure, excellent for the development of wearable devices or the development of optical waveguides, the first Echeverria et al.[87] showed the possibility of using organic polymer and SCO compounds, both soluble in the same solvent. The idea was later elaborated by the group of Franz Renz, where different polymer matrices were tested and differences in the SCO behaviour were recorded[88] Also noteworthy is the example of coaxial electrospinning of $[Fe(atrz)_3](2ns)_2$ in poly(methyl methacrylate) (PMMA) matrix and outer shell of pure PMMA, which were characterised by higher resistance to water rinsing[89] (shown in Figure 1.4.1A).

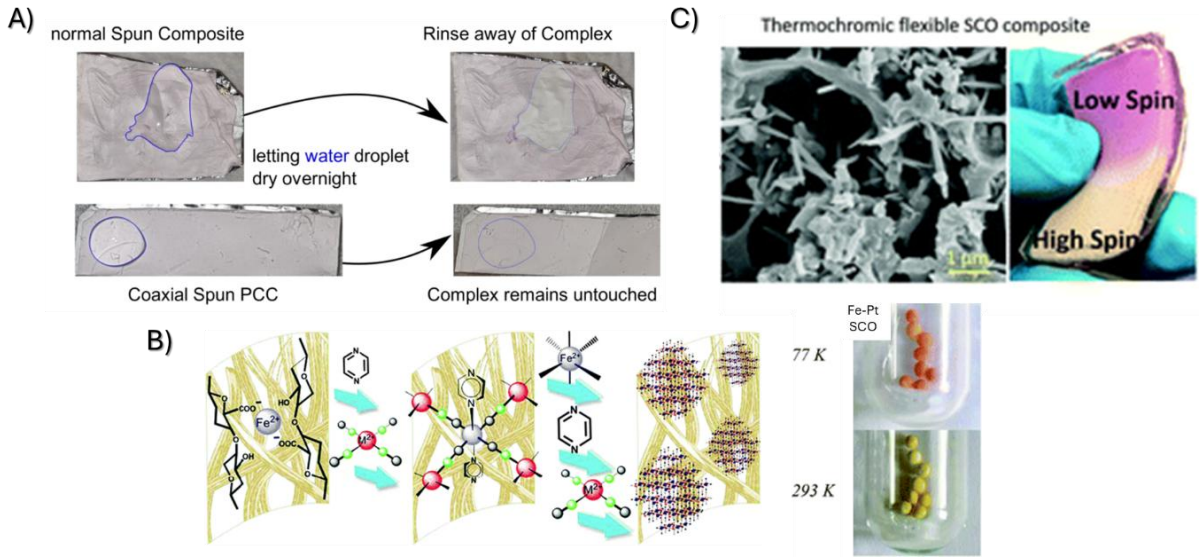

Figure 1.4.1 (A) Example of soluble SCO system incorporated into PMMA electrospun polymeric fibres showcasing increased resistance to water rinsing, after introduction of core-shell electrospinning[89]. (B) Schematic representation of SCO nanoparticle sequential growth inside alginate beads, together with photographs showing their colour changing properties due to thermally induced SCO[90]. (C) SCO nanoparticles immobilized within flexible microporous silica structure, showcasing a drastic colour changes pink (LS) and yellow (HS) depending on the thermally-induced spin state[91].

In the approach for SCO particles miniaturization, several attempts in synthesising SCO nanoparticles within a matrix have been undertaken. For example, by immersing a hard template – silica monolith, within precursor solutions (iron(II) salt and triazole ligand), SCO nanoparticles of 3.2 nm average size have been synthesised within pores. Although SCO properties were only partially reversible, the appearance of wide thermal hysteresis was recorded[92]. In another example, naturally occurring polymers have been used in the synthetic protocol to obtain ultrasmall SCO nanoparticles of the Hofmann clathrate family. In a multi-step sequential assembly of the precursors 3D SCO coordination polymer has been homogenously immobilised within chitosan (average size: 2.8 nm)[93] and alginate (average size: 3.2 nm)[90] beads (shown in Figure 1.4.1B). The immobilization of SCO nanoparticles was also performed within a flexible microporous silica network, where islands of SCO crystalline needles and spherical silica nanoparticles have been located within an amorphous SCO network, dispersed in the organosilica matrix. The resulting composite material showed stunning macroscopic thermally-induced colour change, and due to the additional hydrophobic coating, it displayed long-term stability[91] (Figure 1.4.1C).

A second route in SCO-composite fabrication methodology involves mixing polymers with presynthesised SCO powders (from micro- to nanocrystals), leveraging physical dispersion techniques to form functional composites. This approach opens more possibilities as almost all available compounds can be processed (both soluble and insoluble) and allows for better control over the bistable properties of the fillers, because of the known particle morphology. The issue of particle aggregation and their homogeneous distribution across the polymer matrix must be taken into account. Despite this obstacle, examples one can find in literature prove their potential in developing multi-functional devices.

A prime example was reported by Shepherd et al., where they pointed out the possibility of using strain associated with the SCO spin transition in the production of mechanical work, by preparing a PVP and PMMA actuating bilayer with embedded SCO particles[94] (shown in Figure 1.4.2A). The idea was later advanced by addition of Ag particles into one of the layers to observe electro-thermal actuation, and under alternating current the variations of the tip position of composite cantilever was recorded, without noticeable fatigue over few hundreds of actuating cycles, paving the way for "artificial muscle" preparation based on SCO compounds[95] (in Figure 1.4.2B). Another example of exploring the spin transition-induced changes in volume was presented in SCO-composite films constructed with bistable nanoparticles and piezoelectric poly(vinylidene fluoride-co-trifluoroethylene) – P(VDF-TrFE), as a polymer matrix, leading to electrical response upon spin switching[96]. It was further developed to harness both the piezo- and pyroelectric properties of both filler and polymer matrix with the perspective of thermal energy harvesting[97]. Drop-casting technique for composite films development was also used in production of thermochromic cellulose composite with SCO compound – $[Fe(Htrz)_2(trz)](BF_4)$, which allowed for preparation of paper-like sheets, which could be locally heated or cooled to form different patterns, posing as a prospect for rewritable paper materials[98].

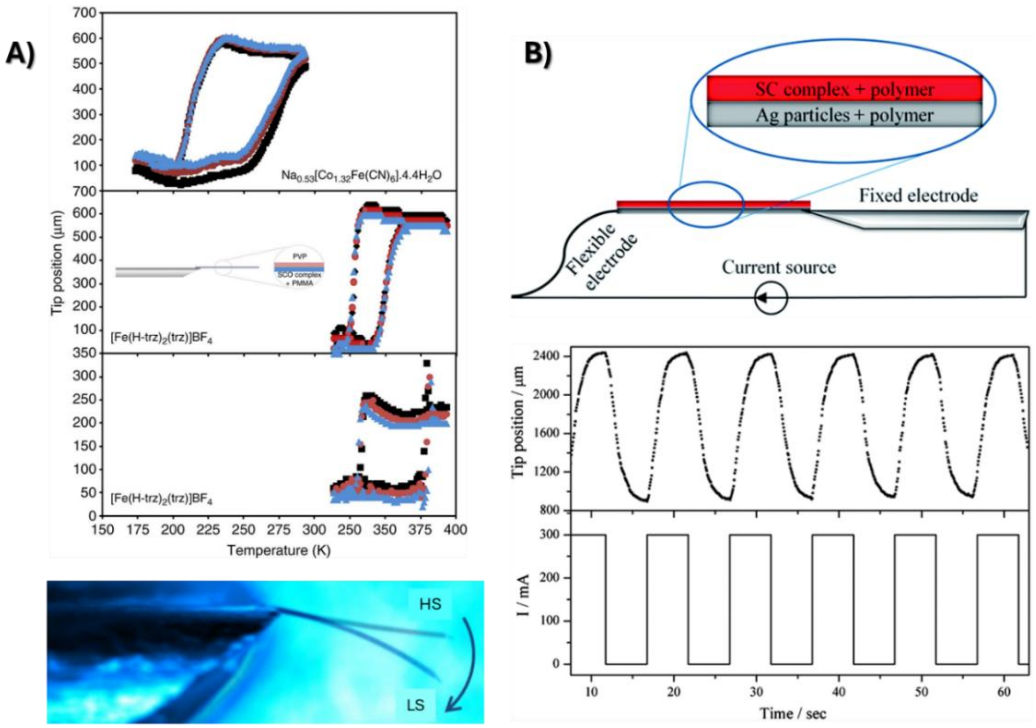

Figure 1.4.2 (A) Recorded movement of actuating bilayers in the function of temperature, with the presence of thermal hysteresis corresponding to the properties of chosen SCO materials. Additionally, the image below shows the actual change of tip position depending on the spin state (HS or LS) of the filler[94]. (B) Presentation of the SCO-based bilayer composite within a measuring system, where the layer's tip movement was recorded over several cycles in response to applied alternating current[95].

The use of a spray-coating technique was also elaborated by Manrique-Juarez et al. for thermally-driven actuation in micro-electro-mechanical systems (MEMS). They have embedded $[Fe(Htrz)_2(trz)](BF_4)$ nanoparticles within epoxy resin (SU-8) onto a silicon cantilever, which

showed abrupt bending at spin transition temperatures within a stable range of movement amplitude[99] (Figure 1.4.3A). Actuation property was presented in a very eye-catching example of a flower, whose petals could reversibly open and close, accompanied by colour change, in response to temperature change, presented in Figure 1.4.3B. Recently, polymers doped with SCO fillers have been making their way in the field of 3D printing actuators, with the possibility of changing the shape of printed material over time. With the stereolithography approach, variously shaped objects have been presented (see the Eiffel tower presented in Figure 1.4.3C), together with evaluation of their actuation performance, a goal that is not reachable by other means[100,101].

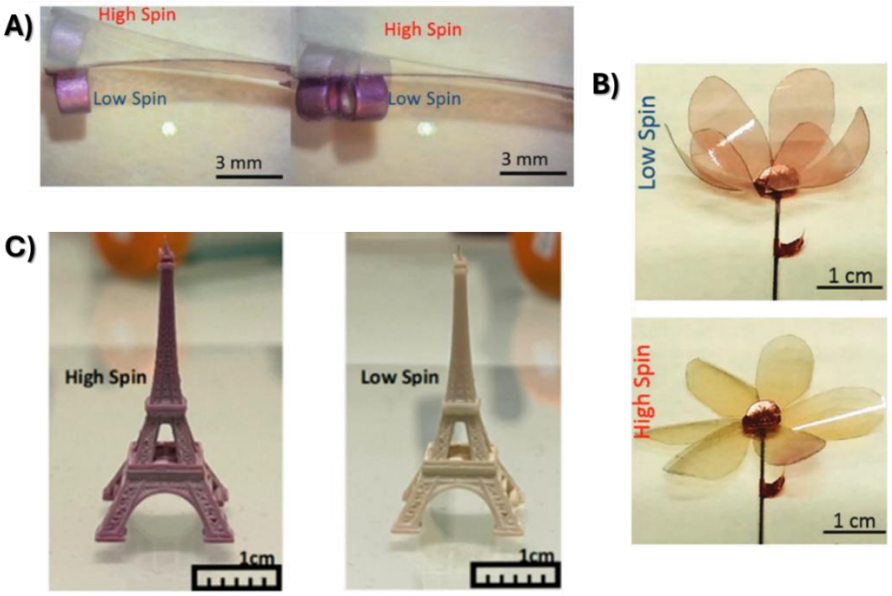

Figure 1.4.3 Examples of SCO-based composites: (A) a thermally driven actuation of spray-coated layers of SCO particles embedded in epoxy resin, illustrating the capacity to modify its position despite the additional load at the end; (B) a photographic depiction of the actuation properties of an SCO-based composite under spin state switching, elucidating the transition of unit volume between LS and HS states[99]; (C) an example of 3D-printed SCO-based composite in the form of an Eiffel Tower, showcasing the capability to undergo spin transition by means of a colour change[101].

In the literature, few examples can be found where the property of the SCO compound react to the presence of certain vapours in the atmosphere, starting with different amounts of water molecules. Apart from recorded response in magnetic behaviour, there have been proposed to fabricate bistable composite materials, which would change colour when exposed to HCl, HNO_3 or NH_3 vapours, making them vapochromic detectors[102] (see Figure 1.4.4A). Again, straightforwardly drop-casted films already showed some potential with potential application; however, the use of electrospun composites with fillers sensitive to the presence of those compounds has been elaborated (presented in Figure 1.4.4B)[103]. With drastic colour changes, fibres pose an interesting alternative to simple composite films, which, due to their fibrous structure, already act as a filter, increasing their applicability in sensing the freshness of meat, which releases ammonium while it goes bad, which is important from the point of food production[104].

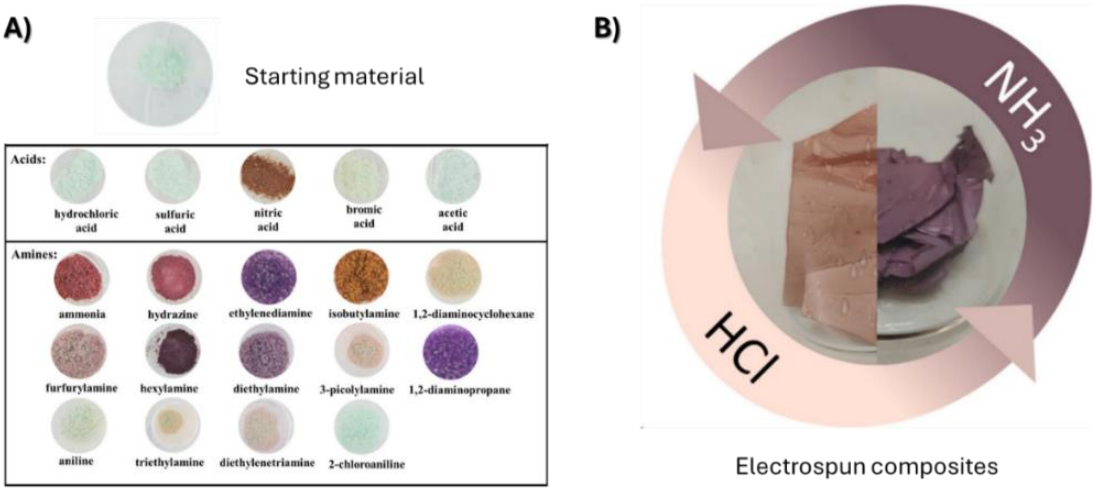

Figure 1.4.4 (A) Images taken after exposition of vapour-sensitive complex to several acids and amines with observable colour changes[102]. (B) Example of incorporation of vapour-sensitive material into electrospun fibre matrix[103].

2. Measurement methods and research techniques

2.1 Electron microscopy (SEM, TEM)

Electron microscopy is the primary characterization method to gain a basic understanding about studied materials on the micro- (Scanning Electron Microscopy – SEM) to nano- (Transmission Electron Microscopy – TEM) scale. It is an excellent method to observe magnified objects and their surface, and gain information about their morphology and composition. The principle of creating a magnified image in electron microscopy is based on similar rules to optical microscopy. Visible light is replaced by a beam of electrons accelerated by an electric field, and optical lenses by electromagnetic lenses.

In the microscope column, the electron beam necessary for imaging is created at the electron gun in the condition of high vacuum. Electrons from the emitter are being accelerated in an electric field to gain appropriate energy, according to the relation: $E = eU$, where e is the charge of the electron and U is the voltage between cathode and anode. The electron beam that scans the specimen is then formed by the system of focusing coils, which change the course of the electrons with a suitably shaped magnetic field. After the contact of the accelerated electron beam with a fragment of the specimen, different effects take place. Signals resulting from the interactions of electrons and matter are then recorded by the apparatus, and an image is produced. It is worth noting that in transmission electron microscopes, the electrons pass through the examined sample, and they are the source of the signal to create an image. For this reason, in TEM imaging, the thickness of the specimen is highly limited (< 0.1 μm), and electron beams with higher accelerating voltages are used. Thus, the high resolution of the image corresponds to the wavelength (note how it is connected to accelerating voltage) of the electrons and the diameter of the beam.

The signal responsible for the creation of the image in SEM is based on the effects that take place at different penetration depths of electrons with the sample matter shown in the scheme in Figure 2.1.1.

In scanning electron microscopy, as the name suggests, the electron beam scans across the surface of the sample, producing secondary and backscattered electrons, which are then detected and converted into an image. Secondary electrons (SE) are created by inelastic interactions of the primary beam with the electrons of individual atoms of the sample. SE originate from the atoms of the sample, and their emission occurs near the surface of the sample due to their low energy (below 50 eV), much lower than the energy of the incident beam. The signal contrast obtained from the SE is related to the topology of the sample. The edges and borders emit more secondary electrons, thus those areas are characterized by higher brightness, allowing for the interpretation of the material's morphology. Additionally, to derive more information about the specimen with detection of SE, the manipulation of the accelerating voltage can be useful. With a low initial voltage, the electron beam scans the surface of the specimen, giving valuable

information about the topography of the sample. Increasing the voltage makes it possible to gain access into deeper parts of the specimen.

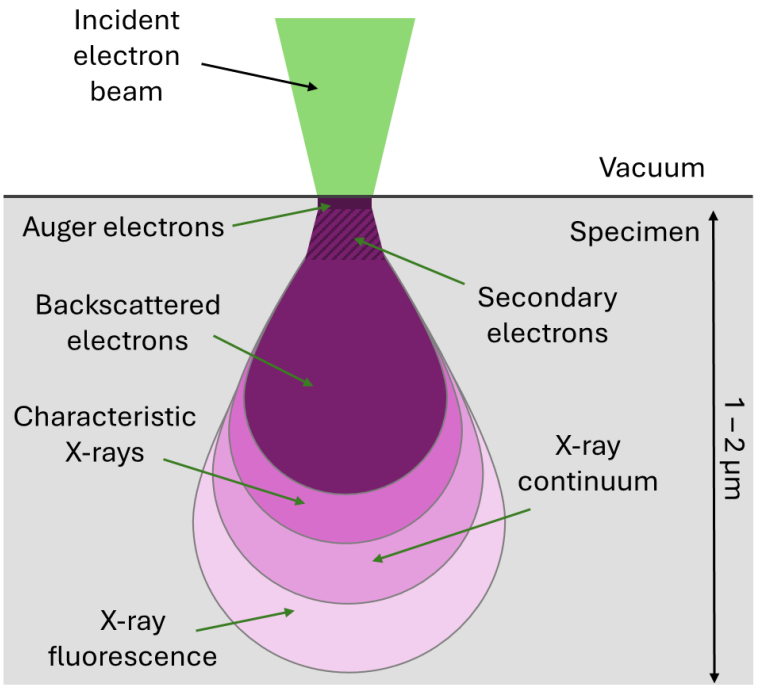

Figure 2.1.1 Types of signals in electron microscopy depending on the penetration depth.

Backscattered electrons (BSE) are the other type of detected electrons during image acquisition. They are electrons from the incident electron beam, which underwent elastic scattering on the atomic nuclei of the samples and left the specimen with almost no energy loss, so the name backscattered. BSE originate from much deeper regions within the sample volume compared to SE. As the probability of backscattering events increases with atomic number, heavier atoms (Fe, Pt) present in the specimen produce a higher signal compared to lighter elements (C, N). Therefore, contrast present in images with BSE detection derives from the chemical composition, allowing for the chemical characterization of the components in the composite materials at different depths of the sample. However, the images do not give a 3D visualisation of the specimen, so the depth information is lost during the measurement. Additionally, to be able to work with BSE, more sophisticated detectors are needed in SEM microscopes, so more commonly in the microscopes, SE are the source of the signals.

Irradiating a sample with an electron beam induces other effects, such as the emission of characteristic radiation of the elements composing the material. When the beam of high-energy electrons strikes the surface, it causes the specimen atoms to be excited, and they emit characteristic X-rays. Then in the detector, like an EDS (Energy Dispersive Spectroscopy) detector, the number of radiation quanta of the same energy are counted as they are proportional to the amount of the elements in the specimen. The information about each element is calculated based on the peak area and derived from the energy histograms. Due to the weak absorption of X-ray radiation by matter, the information given from EDS analysis derives from the whole volume of the fragment of the studied sample irradiated with an electron beam.

SEM images of microparticles and composite materials were collected at IFJ PAN using Tescan Vega 3 SEM equipped with an X-ray energy dispersive spectrometer EDAX Brucker with a secondary electron (SE) detector. Imaged samples were drop-casted or electrospun directly onto cleaned Si(100) wafers in small batches to minimalize the charging effect and were measured without additional coating. Moreover, for **NiFe-chain** microcrystals and composite fibers, images were taken at the Institute of Geological Studies, Jagiellonian University in Kraków as a result of collaboration with dr hab. Beata Nowicka, prof. UJ at the Faculty of Chemistry. The samples were measured at a Hitachi S-4700 scanning electron microscope with a Thermo Scientific microanalysis system, with the use of a secondary electron (SE) detector and a backscattered electron (BSE) detector (YAG). Before measurements, the specimens were coated with additional conductive layers of gold for SE detection and carbon for BSE detection.

TEM imaging of **FeTrz** nanoparticles and composite materials was performed at the Institute of Molecular Science (ICMol) of the University of Valencia, Spain, within the collaboration with dr Alicia Forment-Aliaga and Alejandro Garcia-Reguiero, with the use of JEM-1010 TEM operating at 100 kV. Nanoparticles were drop-casted from methanol suspensions onto Cu grids with a formvar/carbon layer, and electrospun fibers were directly electrospun in small amounts on the Cu grids. Additionally, for **RbMnFe** and **NiFe-chain** composites together with **FeTrz** nanoparticles, TEM imaging was performed at the Institute of Metallurgy and Material Engineering, Polish Academy of Sciences in Kraków, in collaboration with dr hab. Paweł Czaja using a Tecnai G2 operating at 200 kV transmission electron microscope fitted with an energy dispersive X-ray (EDX) microanalyzer coupled with a high-angle-annular dark-field detector (HAADF).

SEM and TEM images size distribution of NPs and microcrystals, and the diameters of composite electrospun fibers were determined with the use of ImageJ software[105].

2.2 Optical spectroscopy

2.2.1 Infrared spectroscopy

A chemical analysis technique that takes advantage of the interaction between infrared light (wavelengths from 780 nm to 1 mm) and matter. It allows to obtain the information about the existence of specific chemical bonds in the studied materials. The principle of the IR measurement lies in the fact that the frequency of vibrations of the individual chemical bonds lies in the infrared range of the electromagnetic spectrum. And so when a compound is irradiated with IR light, the molecule absorbs specific frequencies that match the vibrational energy between neighbouring atoms. As a result, it causes excitation of the respective vibrational mode, which can be associated with a particular bond type in the sample. For a molecule to be observed in IR spectroscopy, the vibrational mode must be associated with the changes in the permanent dipole. As IR is a technique based on absorption, the detection of the specific bonds manifests itself as a decrease in the intensity of incident radiation in the function of frequency represented as cm^{-1}.

Infrared spectroscopy measurements were performed on powdered samples at the Faculty of Chemistry, Jagiellonian University in Kraków, within the collaboration with dr hab. Beata Nowicka, prof. UJ. Fourier-transform infrared spectra were collected with the use of an ALPHA II FTIR Brucker spectrometer in the attenuated total reflectance mode in the 4000-400 cm^{-1} range, without KBr pellets.

2.2.2 Raman spectroscopy

A non-destructive chemical analysis method that probes molecular vibrations to provide a molecular fingerprint of materials. Raman is based on the inelastic scattering phenomenon, which takes place after irradiating the sample with a high-intensity laser light source. By irradiating the sample, the oscillating electromagnetic field of a photon induces a polarisation of the molecular electron cloud. This leaves the molecule in a higher energy state, with the energy of the photon transferred to the molecule. It can be considered as the formation of a very short-lived complex between the photon and molecule, which is commonly called the virtual state of the molecule. The virtual state is unstable, and the photon is re-emitted almost immediately, as scattered light (visualisation presented on the Jabłoński Diagram in Figure 2.2.1).

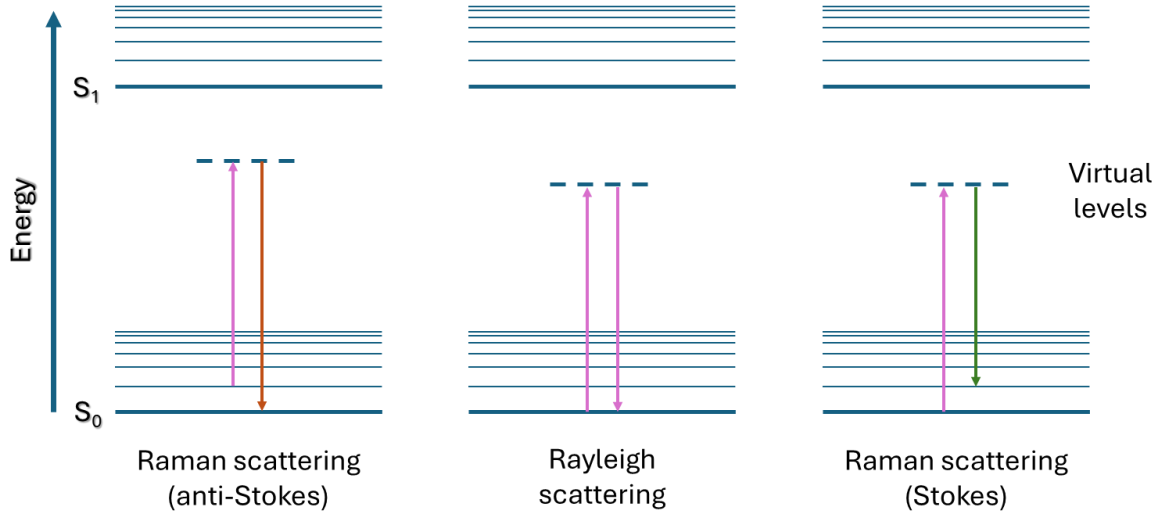

Figure 2.2.1 Jabłoński Diagram showing the origin of Rayleigh, Stokes, and anti-Stokes Raman scatter.

In most scattering events, Rayleigh scattering occurs when the molecule returns to its ground vibrational state. As this is an elastic scattering, its energy is conserved after the interaction with the photon. The scattered photon is of the same energy (wavelength) as the incident photon. Being a dominant process, it is around 10^7 times more intense than inelastic scattering.

In a much rarer event, Raman scattering occurs, which is an inelastic scattering process with a transfer of energy between the molecule and the scattered photon. If a photon loses energy by exciting the molecule from the ground state to a higher vibrational level, the wavelength of the photon increases, which is called Stokes Raman scattering. Inversely, if a photon gains energy, the molecule relaxes to a lower vibrational level. The wavelength of the photon decreases, and Raman scattering is called anti-Stokes. Due to the Boltzmann distribution for the ensemble of molecules, the majority of molecules will be in the ground vibrational level. Therefore, statistically, Stokes scattering is a more probable process, which results in the lower intensity of the anti-Stokes Raman light.

To detect measurable intensity of the scattered radiation, which is 4-8 orders of magnitude lower than the intensity of the excitation, a strong radiation source is required, as well as a sensitive detection system. The answer is to use a laser source to excite, due to its characteristics – monochromaticity and high beam intensity. The resulting spectrum is a function of the scattered radiation dependent on the frequency, called Raman shift, and expressed in cm^{-1}, with intensity expressed in conventional units related to some chosen standard. Raman spectroscopy depends on a change in the polarizability of a molecule, whereas IR spectroscopy depends on a change in the dipole moment. Raman spectroscopy measures relative frequencies at which a sample scatters radiation, unlike IR, which measures absolute frequencies at which a sample absorbs radiation.

Raman measurements were performed at IFJ PAN with the help of dr Marzena Mitura-Nowak, using a Confocal micro-Raman spectrometer, Nicolet Almega XR, equipped with a laser 532 nm. For the measurement, microcrystals were drop-casted from a methanol/chloroform suspension onto a Si(100) wafer, and composite materials were directly deposited on the

Si(100) wafer, similarly to SEM imaging. During measurement, 1% laser power was used to minimise the burning effect on the powdered samples, whereas for composite materials, 10% laser power was used.

2.3 X-ray diffraction (XRD)

The analysis of the structure of the investigated material at the atomic or molecular level (study of crystal structures and atomic spacing) may easily proceed during the X-ray diffraction measurements (XRD). When the electromagnetic radiation with a wavelength on the order of nanometres strikes the matter, the crystalline substance acts as a three-dimensional diffraction grating.

The principle of X-ray diffraction is to measure the intensity of scattered radiation as a function of outgoing direction (angles) due to the interference of reflected X-rays from the individual planes of the crystalline structure (Figure 2.3.1).

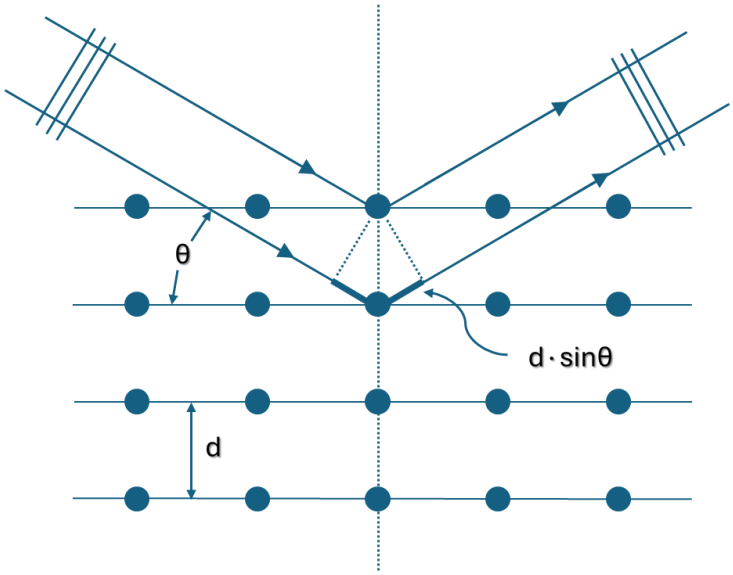

Figure 2.3.1 The scheme of x-rays interacting with the crystal structure.

The constructive interference of the reflected rays occurs when the difference in optical paths of the incident and reflected rays is proportional to the diffraction angle (θ) and the lattice spacing in a crystalline sample (d). The diffraction maxima are observed when Bragg's law is satisfied:

$$n\lambda = 2d_{hkl}\sin\theta, \tag{1}$$

where n is an integer and λ is the wavelength of the X-ray beam. The interplane distance d_{hkl} is described by the Miller indices (hkl).

XRD gives information about the crystallinity of the studied materials, as diffractograms of samples with crystalline structures show clear maxima, while amorphous materials (some organic polymers or glasses) present broad diffraction bands. Due to the additive nature of the diffraction pattern, composite materials can be characterized straightforwardly. The obtained diffraction pattern represents a summarized count for both types of components in the composite material, especially when one is a crystalline structure and the other shows amorphous characteristics.

Powder X-ray diffraction data on microcrystals, nanoparticles, and composite materials were collected in IFJ PAN by dr Marcin Perzanowski and dr Aleksandra Deptuch on a Panalytical X'PERT PRO diffractometer equipped with a Cu-Kα radiation source using Bragg-Brentano geometry. The room temperature data for powder and composite materials were recorded over varied 2θ (within 5°-90°). Composite materials were directly prepared (electrospun) onto the Si(100) wafers with a size of 1.5 × 1.5 cm, with ensured homogeneity of the samples. Additional high-temperature measurements (at 400 K) were performed with the use of the TTK-450 Anton Paar attachment. For the low-temperature measurement (at 150 K), it was performed at AGH University of Krakow in collaboration with dr hab. Łukasz Gondek, prof. AGH with the use of the Panalytical X'PERT PRO diffractometer. Lattice constants were determined for powdered and composite samples by dr Naveen Kumar Chogondahalli Muniraju at IFJ PAN by performing full-pattern Le Bail fit with the use of Mag2Pol software[106] with subsequent structures visualisations.

2.4 Magnetometry (MPMS SQUID)

To study the magnetic properties of the material, a magnetometer is utilized, where the studied substance is placed into and its response to the applied magnetic field is observed. The accuracy of the obtained signal is greatly determined by the precision of the measuring element in the magnetometer. The study presented in the following thesis contains results obtained from the MPMS XL7 magnetometer equipped with the *Superconducting Quantum Interference Device* (SQUID).

Principles of the magnetic measurements in MPMS SQUID

SQUID is a very sensitive measurement system in studying materials with weak response to changes of magnetic field, where the effect of quantisation of magnetic induction flux in a superconducting ring and the Josephson effect are used. The latter one is a phenomenon which involves the tunnelling of electrons at the Josephson junction – two superconductors separated by a spacer made of an insulator. The BCS (Bardeen-Cooper-Schrieffer) theory posits that the current carriers in superconducting materials are Cooper pairs, which are pairs of electrons with opposite spins. During the flow of current through the Josephson junction, it is observed that the wave functions of the Cooper pairs interfere with one another. This interference is possible due to the electrons moving along two possible equivalent paths (*a* or *b*) with the phase differences, as shown in Figure 2.4.1.

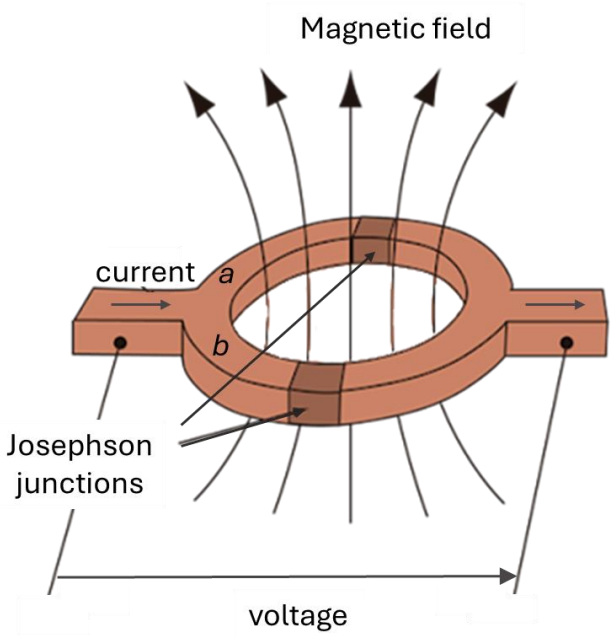

Figure 2.4.1 Scheme of SQUID interferometer.

The phase difference of the electron pairs is dependent on the change in magnetic field flux (Φ). The total current flowing through the junction is defined as the Cooper pair current. Josephson's First Law describes its intensity (I) as being dependent on the phase difference of the Cooper pairs' wave function (φ) and the critical current of the junction (I_c) in the following equation:

$$I(t) = I_c(t)\sin(\varphi(t)). \quad (2)$$

The critical current of the junction exhibits strong dependence on both temperature and magnetic field. A change in the flux encompassed by the SQUID element induces a change in both the current flowing through the device and the induced current in the ring.

Apart from the SQUID element, the principal components of a SQUID-type magnetometer are a superconducting magnet and superconducting detection coils. The superconducting magnet (solenoid made from superconducting material) is positioned within a dewar filled with liquid helium, which generates a homogenous magnetic field along the axis of the coil. The superconducting detection coil is a single superconducting rod, arranged in a gradiometer configuration and positioned within the homogeneous magnetic field.

The measurement performed in the SQUID-type magnetometer involves the movement of the sample (placed in a drinking straw) along the detection coil (Figure 2.4.2). As the sample moves, its magnetic moment induces an electric current in the detection coil. Given that the detection coil and the SQUID element constitute a closed loop, any modification to the magnetic field flux within the detection coil leads to the proportional alteration of the electrical current that flows through the detection circuit.

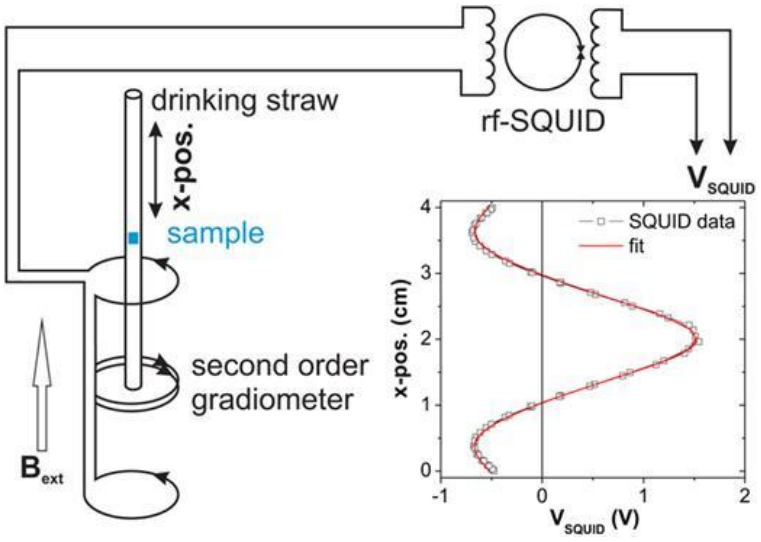

Figure 2.4.2 Scheme of the measurement in SQUID-type magnetometer[107].

Magnetic measurements with the MPMS SQUID magnetometer

The basic parameters describing the properties of the tested material are the magnetic moment *M*, called magnetisation, and the magnetic susceptibility χ in the units of mass, volume, or the mole of the substance. The following equation shows how these quantities are related to each other through the external magnetic field *H*:

$$M = \chi H. \quad (3)$$

According to the above equation, magnetic susceptibility is a parameter that describes the ability of the system to become magnetised under the influence of an applied external magnetic field. The measurement of the direct current (DC) magnetic susceptibility (χ_{DC}) gives insight

into the static magnetic properties of the material. It is determined by the value of magnetisation during the change of temperature within a certain range and at a constant value of the magnetic field, so the measurement is performed under equilibrium conditions. Additionally, the magnetic measurement can be performed at a constant temperature with changes in the value of the field induction. In this approach, it is possible to determine saturation magnetisation (M_{sat}) or coercivity field (H_c), which are the parameters often used to describe the magnetic systems.

The measurement of magnetic susceptibility can also be collected with an alternating current (AC) applied field. In this configuration, the magnetic moment of the sample is changing due to the application of the field that oscillates with small amplitudes (H_{AC}). The time-dependent magnetization of the sample provides insight into the material dynamics and the alternating magnetic susceptibility (χ_{AC}) can be divided into two components: real (χ') responsible for the response of the material to the H_{AC} field and imaginary (χ''), which corresponds to the absorption of the energy by the sample due to the relaxation processes. In an AC measurement, the response can depend on the time-varying temperature, constant field induction, or the frequency at which the field is alternated.

Magnetization data for powder samples and their respective composite materials were collected at IFJ PAN with a Quantum Design MPMS XL-7. DC magnetic susceptibility measurements were performed under an applied magnetic field of 1000 Oe in the temperature range between 2 K and 400 K, depending on the sample's properties. The dependence of the magnetisation upon magnetic field was performed at a constant temperature of 2 K within ± 5 T. The diamagnetic contributions were corrected using Pascal tables. For the composite samples, the correction of magnetic susceptibility was performed using the Curie-Weiss law, elaborated in Chapter 4.2. Depending on vacuum sensitivity, samples measured as powders and composite materials were properly wrapped and placed onto the measuring straw.

2.5 Differential scanning calorimetry (DSC)

Differential Scanning Calorimetry (DSC) is an analytical technique used to study the thermal properties of materials by extracting information on the influence of temperature on specific physical properties. In principle, it is based on the measurement of the amount of heat released or absorbed by the sample during heating or cooling. It is a direct method to determine the enthalpy of the interested process, in particular the temperature of phase transition, including glass transition temperature, fusion and crystallization events, or to establish phase diagrams for various chemical systems.

During DSC measurement, the instrument determines the temperature and heat flow associated with material transition as a function of time and temperature. With the change of temperature, the heat quantity radiated or absorbed by the sample is measured as a difference in temperature between the sample and the reference. DSC serves as a thermodynamical tool for direct measurement of the heat energy uptake in exo- and endothermic events. The resulting DSC curves of heat flux as a function of temperature can be used to determine the values of enthalpy (ΔH) of the transitions and the change in heat capacity (ΔC_p) associated with the changes occurring during the phase transition processes.

Differential scanning calorimetry measurements were carried out at the Institute of Molecular Science (ICMol) at the University of Valencia within the collaboration with dr Alicia Forment-Aliaga and Alejandro Garcia-Reguiero. The measurements of powdered samples and composite materials cut beforehand into smaller fragments to fit the measuring vessels were performed using a Mettler Toledo DSC 821e model at a scan rate of 10 K/min, in the heating and cooling modes, that operates in the temperature range -25-500°C equipped with liquid nitrogen cryostat and a 200 W furnace.

2.6 Dynamic vapour sorption measurements (DVS)

Sorption measurements are a type of analysis to establish the degree of porosity of the given material and its ability to capture guest molecules (mostly water) from the nearest environment on the surface (adsorption) or by incorporating them into the body of the material (absorption).

To study the sorption process, the Dynamic Vapor Sorption apparatus (DVS) can be used. It is based on a gravimetric sorption technique, which means that it measures the change of the sample mass on a time scale, giving information on how quickly and how much of a solvent was absorbed by the sample. The measurement is performed by varying the vapor concentration (a specified relative humidity or partial pressure) over the sample suspended from the weighing mechanism in a controlled environment, as it continuously measures the induced change in sample mass with the use of an ultra-sensitive microbalance. While water vapor is most commonly used, the technique can also be employed with a wide range of organic solvents (e.g. methanol, acetone, chloroform).

In general, the vapor sorption measurement gives an insight into the kinetics of sorption-desorption of solvent over time at a constant temperature. From that, isotherms can be derived showing the equilibrium amount of vapor sorbed as a function of steady state relative vapor pressure (for water expressed as relative humidity) at a constant temperature. In the DVS measurement, the sample is exposed to a series of step changes in relative humidity, and the mass change is monitored as a function of time. The difference between water vapor intake in sorption and desorption mechanisms is observed with the existence of hysteresis in isotherms. The characteristics of sorption-desorption curves and also the shape and location of the hysteresis give information about sample porosity and sorption mechanism (absorption or adsorption of guest molecules).

The process of controlled sorption and desorption of water molecules for powder and composite materials was performed using a Surface Measurement System Dynamic Vapor Sorption DVS-Resolution apparatus at the Faculty of Chemistry, Jagiellonian University in Kraków, Poland, within the collaboration with dr hab. Beata Nowicka, prof. UJ and mgr Gaja Wota. The water sorption isotherms were measured at 25 °C in the range 0–96% RH of water vapor with a 2% step. At each step, the sample weight was equilibrated ($dm/dt = 0.001\%\ min^{-1}$).

2.7 X-ray absorption spectroscopy (XAS)

X-ray absorption spectroscopy (XAS) is typically a synchrotron radiation-based technique that probes specific elements in the material to provide information about the local electronic and structural properties around an atom, which absorbs X-rays at energies near and above the core level binding energies of that particular atom.

The basis of XAS measurement lies in the occurrence of the photoelectric effect due to the absorption of electromagnetic radiation by the atoms in the sample. As a response, electrons within the sample are given enough energy to be emitted from the material as photoelectrons. The atoms absorb X-rays at certain energies, called absorption edges, which are specific for particular atomic species. In principle, XAS is a measurement of the transition of electrons of the atom from core electronic states to unoccupied states above the Fermi energy, and then to the continuum.

XAS spectrum is characterized by the energy (E) of the incident radiation and the intensity expressed by the absorption coefficient ($\mu(E)$). The obtained spectra are composed of the following characteristic regions: pre-edge region, absorption edge, and the post-edge region, marked accordingly on Figure 2.7.1.

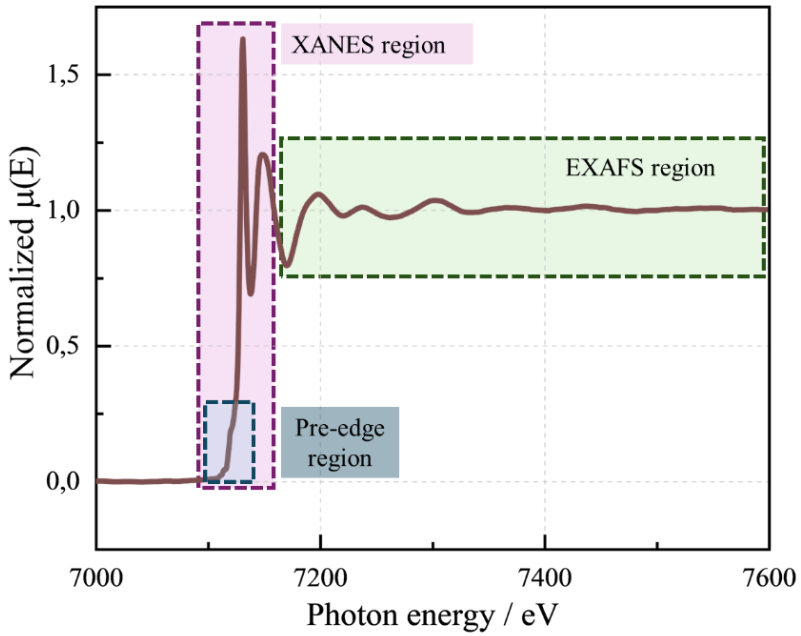

Figure 2.7.1 Example of the XAS spectrum at Fe K-edge with marked regions.

X-ray Absorption Near Edge Structure (XANES) showcases absorption fine structure close to the absorption edge. It is referred to the pre-edge region, around 10 eV below the absorption edge, and the post-edge region up to ~60-100 eV above the edge. Due to the fact that the lowest unfilled electronic levels of an absorbing atom are strongly affected by the change of the oxidation states and the local atomic coordination environment, XANES technique may provide necessary information about the studied elements in the material. It is particularly interesting for the transition metal ions, as in XANES measurement it is possible to define their oxidation

and spin state, coordination geometry, nature of coordinated ligands crystal field splitting, or the density of unoccupied electronic states.

According to selection rules for the XANES spectra, the transition of a core electron to the lowest unoccupied valence state is allowed by the dipole moment approximation ($\Delta l = \pm 1$ and $\Delta J = 0, \pm 1$). For K-edge XANES, they represent the transition from the 1s orbital to np orbital, whereas for L-edge, the spectra show the transition of 2p electrons to nd orbitals. The pre-edge peaks characterised by much weaker intensity represent transitions forbidden by the dipole selection rules, however, allowed by the quadrupole moment interactions and/or orbitals mixing. In the K-edge region, they present transitions 1s → nd, and for the L-edge region, 2p → nf.

The latter part of the XAS spectrum, starting from ~50 eV up to ~1000 eV above the absorption edge, relates to the transitions of the core electrons to the continuum. Named as Extended X-ray Absorption Fine Structure (EXAFS), this region is characterized by the oscillations in the XAS spectrum, originating from the backscattering of a high-energy photoelectron on the surrounding atoms and from the constructive and destructive interference of the scattered waves with the original spherical photoelectron wave. EXAFS serves as a very sensitive probe of the local structure of the studied element and its surrounding atoms, as it allows to extract qualitative information about the radial distance and the number of neighbours, in the close distance to the scattering atom.

To model EXAFS oscillations, the photoelectron wavenumber k is defined by the photon energy (E) and the energy of the absorption edge (E_0):

$$k = \sqrt{\frac{2m_e(E-E_0)}{\hbar}}. \tag{4}$$

The EXAFS equation is represented as a sum over possible scattering paths (neighbouring atoms on the j^{th} shell from the absorbing atom):

$$\chi(k) = \sum_j \frac{N_j S_0^2}{kR_j^2} F_j(k) e^{\frac{-2R_j}{\lambda_j(k)}} e^{-2k^2\sigma_j^2} \sin[2kR_j + \Phi_j(k)]. \tag{5}$$

Equation (5) can be interpreted in terms of the underlying physical process behind EXAFS oscillations. The number of neighbouring atoms in shell j (degeneracy) is represented by the coordination number N_j, whereas the distance from the absorber to the nearby atoms in shell j is noted as R_j. The $F_j(k)$ factor accounts for the scattering amplitude of the photoelectron by nearby atom j at a distance $2R_j$. The phase shift noted as $\Phi_j(k)$ is incorporated due to the phase change of the photoelectron wave after scattering. $F_j(k)$ and $\Phi_j(k)$ are dependent on the atomic number Z of the scattering atom, allowing for the determination of the neighbouring species. S_0^2 stands for the amplitude reduction factor, which accounts for multi-body effects and the relaxation of the absorbing atom, due to the creation of the core hole. This factor is weakly energy dependent, however strongly correlated with coordination number N_j, and is approximated by a constant, taking values from 0.6 to 1. The factor responsible for the suppression of EXAFS oscillations, due to the inelastic photoelectron scattering and the decay of the core hole, is in the expression containing the mean free path of the photoelectron $\lambda_j(k)$ in the exponent.

The differences in the local surrounding of the absorbing atom, occurring as a result of thermal vibrations and static disorder, are encompassed by the expression containing parameter σ_j^2, known as the Debye-Waller factor, which derives from the mean square radial displacement in the distance for the j^{th} shell. The local probing for only nearest atomic shells in EXAFS lies in the values for the mean free path $\lambda_j(k)$, which is of the order of several Å and in the decrease of scattering probability as the square of the distance R_j^2 to the neighbouring scattering atoms, making EXAFS a much weaker probe over longer distances from the absorbing atom.

In the EXAFS analysis, the Fourier Transform of this expression is taken into frequency space, resulting in a radial distribution function, where the appearing peaks correspond to the most likely distances of the neighbouring atoms. In the curve fitting of EXAFS signal, local structural parameters of the first few atomic shells from the absorbing atom can be extracted, such as radial distance and the number of scattering atoms, together with the radial displacement factor.

Temperature-dependent XAS measurements at ASTRA beamline in SOLARIS synchrotron

For XAS experiments with temperature dependence, performed at the ASTRA beamline in the National Radiation Centre SOLARIS in Kraków, it was necessary to construct a compatible sample holder, which would allow temperature regulation in the necessary temperature regime. This task was undertaken in the collaboration with the group of dr hab. inż. Wojciech Tabiś at AGH of Krakow. The custom-made sample holder is presented in Figure 2.7.2A, including its installation on the ASTRA beamline in SOLARIS.

In detail, the custom-made sample holder was designed for temperature control in the range 150-440 K, where cooling (via liquid nitrogen, LN) was applied to the sample in the manner of a cold finger. As it is visible in Figure 2.7.2A, the holder consists of a 3D printed container for liquid nitrogen made up of two vessels between which cotton wool has been inserted for insulation purposes. A copper rod supplying cooling power to the sample has been immersed in LN, and on the other end, a copper plate has been attached, containing space for mounting the sample. The temperature stabilisation was possible thanks to the heater installed next to the sample area, with a Pt-100 temperature sensor next to it, attached to the copper holder. Set point temperature of the holder was encoded through Lakeshore PID temperature controller, according to the calibration curves, which were carried out on samples in different forms: as boron nitride pellet (Figure 2.7.2B) or as a powder in a polyethylene (PE) bags sealed under ammonium chloride solution (Figure 2.7.2C), before the assigned beamtimes.

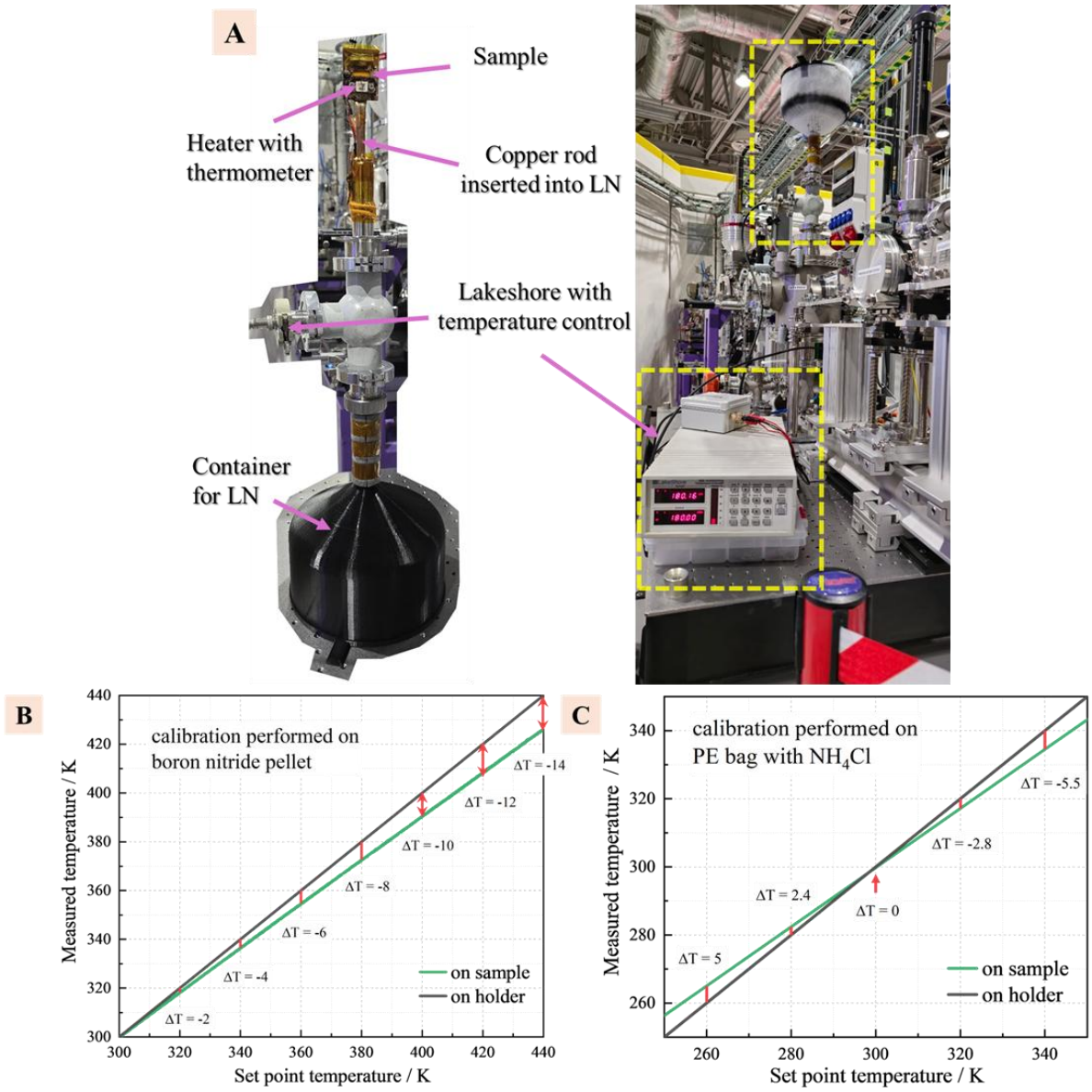

Figure 2.7.2 (A) Photograph of the custom-made sample holder for temperature-dependent measurements at ASTRA, with a picture after proper positioning at the beamline during XAS measurements. (B, C) Temperature calibration curves for the custom–made sample holder, performed on two types of samples: a boron nitride pellet and a polyethylene pocket filled with 2M NH_4Cl solution.

XAS experiments performed on Fe and Ni K-edges described within the framework of this thesis have been performed at the ASTRA beamline of the SOLARIS National Synchrotron Radiation Centre in Kraków, Poland, within 4 consecutive allocated beamtimes, with the help of beamline scientists, dr Alexey Maximienko and mgr Grzegorz Gazdowicz. In the measurement both powdered samples and polymer composite foils have been analysed, with the former prepared as a pellet dispersed in boron nitrate or sealed in polyethylene (PE) bags under ammonium chloride solution (NH_4Cl) necessary for material stability, and the latter sealed in PE bag after ensuring full hydration, without addition of solvent. All spectra were recorded in transition mode using a Ge(220) modified Lemonnier-type double crystal monochromator. The resultant monochromatic beam, with dimensions of 10 × 1 mm at the sample position, where shaped by slits, to ensure sample homogeneity at the measurement spot with the help of an X-

ray camera. To facilitate calibration and alignment at the stage of data analysis, during the course of each scan, the Fe or Ni reference foils were measured simultaneously. Samples in the form of pellets, powder immersed in solution in a PE bag, or composite foil have all been mounted onto the custom-made sample holder described above and were measured in the temperature range of 240-440 K. As a setpoint temperature, data from the calibration curves was used (Figure 2.7.2Bb). The processing and analysis of the data were conducted utilizing the Demeter software package[108] with the exception of background fitting in the pre-edge region, which was performed using the Larch software package[109]. In the course of the normalisation process, the position of the edge was determined as the point at which $\mu(E) = 0.5$ in the normalised spectra.

2.8 Mössbauer spectroscopy

Mössbauer spectroscopy is a highly precise nuclear-resonance technique that uses recoil-free emission and absorption of gamma rays (Mössbauer effect) in a solid matrix to provide unique insights into the local electronic and magnetic environments of Mössbauer-active isotopes. The resonance absorption that lies behind the Mössbauer effect take place, when a ^{57}Fe nucleus (source) in the excited state (E_e) with a mean lifetime of typically 100 ns emits a photon (a γ-ray), which is then absorbed by another ^{57}Fe nucleus (absorber) in the ground state (E_g), resulting in a transition of the second Fe nucleus to the excited state defined by energy E_e. The subsequent transition back to the ground state takes place by the re-emission of a photon of energy, a γ-quantum, which has been schematically presented in Figure 2.8.1. The resonance absorption may only take place when the emission and absorption lines overlap, which cannot happen to the freely moving atoms or molecules (as in gases or liquids), which lose energy due to the recoil effect. For atoms and molecules in the solid state, recoilless emission and absorption of γ quanta are possible, as atoms are bound to each other in the crystal lattice, and upon emission or absorption of γ-rays, there is a probability that no phonons are created, disturbing the lattice, leading to recoil-free events.

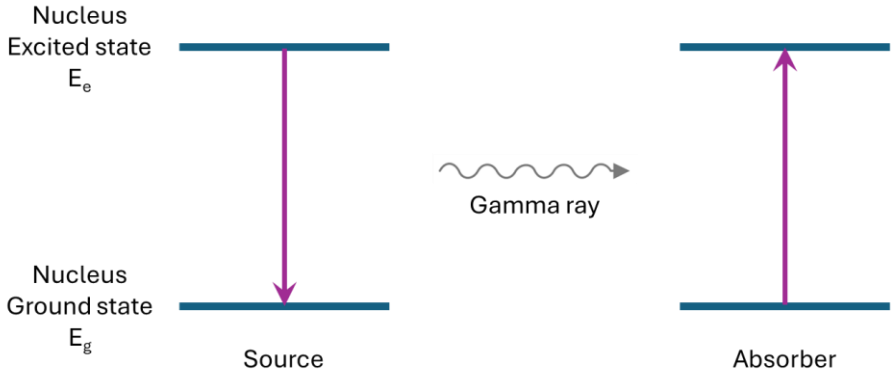

Figure 2.8.1 Scheme for the recoilless nuclear absorption or emission of a gamma ray.

The Mössbauer spectrum shows the relation of relative energy transmission as a function of Doppler velocities of the source (for ^{57}Fe in several mm/s). During the measurement the source is moving toward and away from the sample in an oscillating manner in order to change the energy of γ-ray, by exploiting the Doppler shift, and thus put into a resonant state the source and the absorber, which due to the differences in local environment exhibit a tiny mismatch in the nuclear energy levels.

Mössbauer spectroscopy allows to probe certain elements (most commonly Fe) and give details of their electronic structure, on the basis of hyperfine interactions, which are the result of modifications of the energy states of the atom due to the interactions of the atomic shell with the nucleus. In the Mössbauer spectrum, three kinds of hyperfine interactions may be observed, namely electric monopole, electric quadrupole, and magnetic dipole interactions. The first one originates from Coulomb interactions between protons of the nucleus and neighbouring electrons (mainly from the s orbitals), which penetrate the nuclear field, and is characterised by the isomer shift parameter (δ). The values of isomer shift give information on the oxidation and

spin state of probed atoms and elaborate on their bonding properties, such as character of bonds (covalency) or electronegativity of ligands. The difference in isomer shifts depending on oxidation and spin state for iron compounds is depicted in Figure 2.8.2. The next hyperfine interaction comes from the electric quadrupole interaction between the nuclear quadrupole moment and an inhomogeneous electric field at the nucleus. In the spectrum, it is observable as a quadrupole splitting parameter (ΔE_q), providing information about oxidation and spin state of the studied atoms, as well as details about molecular symmetry determined by electronic structure and nearby lattice surroundings. The final hyperfine interaction observed by magnetic splitting parameter (ΔE_M) derives from the interaction of the nuclear magnetic dipole moment and a magnetic field, and thus provides clues on the magnetic interactions that occur in the studied material.

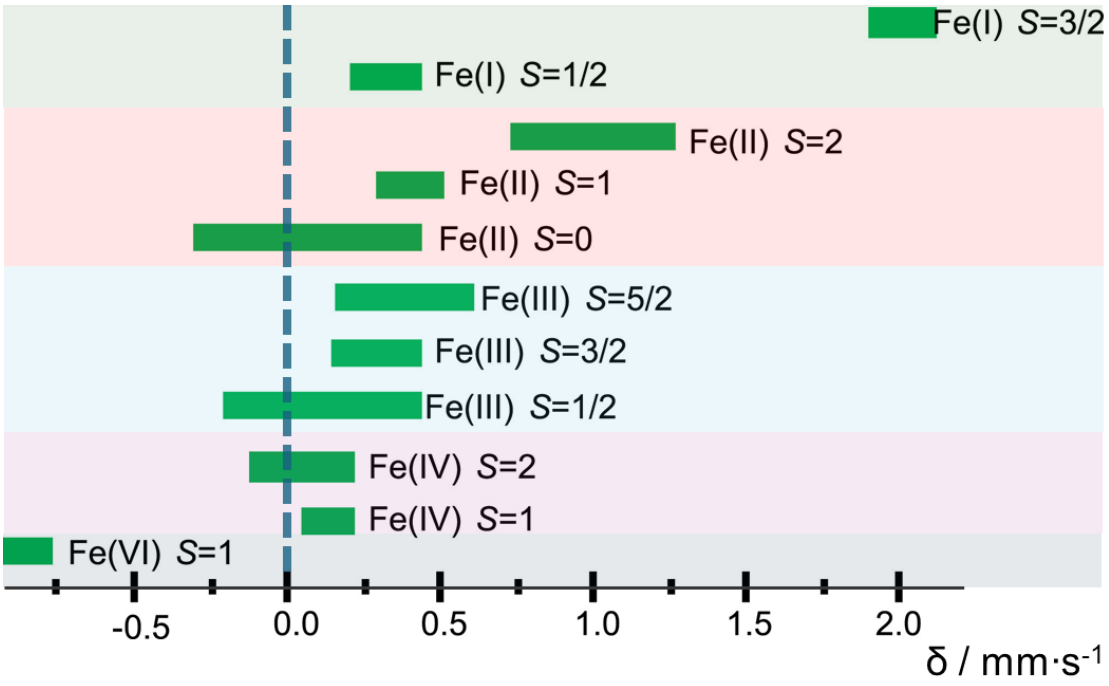

Figure 2.8.2 Ranges of isomer shift (δ) for Fe-compounds at different oxidation and spin states[110].

The Mossbauer absorber was prepared in powder form by mixing 25 mg of **FeTrz** powders with the BN carrier. The thickness of the absorber amounted to 19 mg/cm^2. Mössbauer transmission measurements for 14.41-keV transition in 57Fe were performed using a conventional constant acceleration spectrometer operated in the round-corner triangular mode and equipped with the LN Kr-filled proportional detector. A commercial 57Co(Rh) source kept at room temperature was applied. A Cryogen-free Mössbauer cryostat was used to maintain the absorber temperature. The geometry, count-rate and single channel analyzer window borders were kept constant during all measurements constituting a single uninterrupted series with increasing subsequent temperatures within the range RT-440 K. Additional spectra were collected at 200 K. The velocity scale was calibrated by a α-Fe foil. The data were processed within the transmission integral approximation by the PMOS software. The Mössbauer experiment and the subsequent data analysis were performed at by dr Kamila Komędera and dr hab. inż. Damian Rybicki at AGH University.

3. Techniques and polymer matrices chosen for composite preparations

3.1 Electrospinning

It is a versatile technique for material preparation in the form of long fibres of minimized fibre diameters by application of high voltage to the solution based on organic polymers. The simplicity of the method comes from the few strains given on the preparation methodology, and at the same time, opens up a lot of possibilities for modification of the process at various steps of the process[111,112].

Typically, for the material to be electrospun, it has to be prepared in the form of a solution, with the basic component being an organic polymer. Several parameters during the whole sample preparation can be manipulated to obtain electrospun fibres with different morphology and functionality. The choice of polymer matrix and solvent plays a key role in the final material, as they influence other necessary parameters, such as concentration of the solution and the voltage at which the polymer solution can be effectively electrospun. Additionally, by preparing composite polymer fibres, the order in which the filler compound is introduced into the polymer influences the final product and its properties.

3.1.1 Electrospinning process

The electrospinning setup is composed of several basic components presented in Fig. 3.1.1.

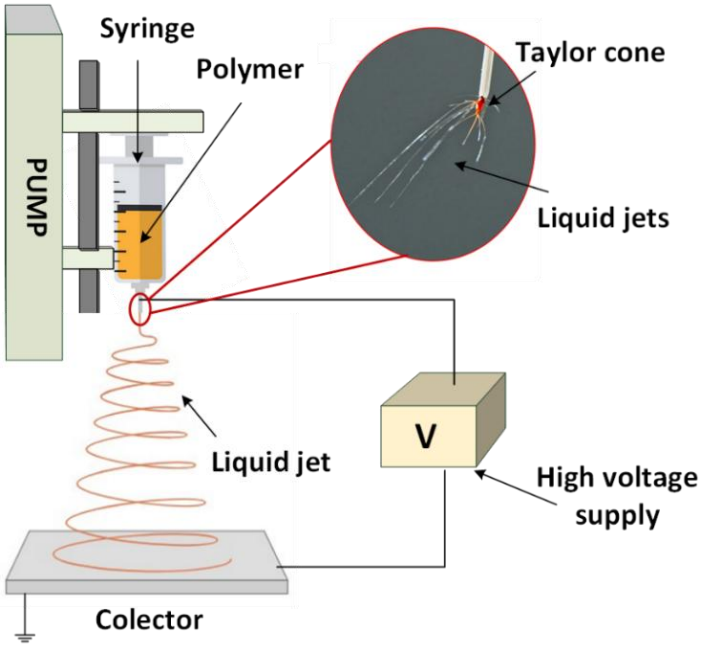

Figure 3.1.1 Electrospinning setup.

Firstly, polymer solution is introduced into a syringe attached to the pump, pushing the solution during the whole process with a constant flow rate and a needle connected to the high voltage generator. At a certain distance from the needle, the grounded metallic collector is situated onto which the fibres are being deposited during the process. For reproducibility of the material preparation, the setup is located in the locked chamber to have control over the temperature and humidity in the space where fibres are formed.

To understand the process itself, it is essential to acknowledge what happens to the droplet of polymer solution after introduction into the needle, when high voltage is applied (Figure 3.1.2). When a spherically charged droplet of conducting liquid is placed in a vacuum, it is in an equilibrated state as it experiences two forces: (1) a repulsive force meant to disintegrate the droplet, and (2) surface tension, whose role is to hold the droplet in the spherical shape. In the electrospinning process, a high voltage is applied to a liquid droplet at the tip of the spinneret. The droplet starts to elongate, forming a conical shape known as a "Taylor cone". This behaviour is caused when electrostatic repulsion (1) overcomes surface tensions (2)[113].

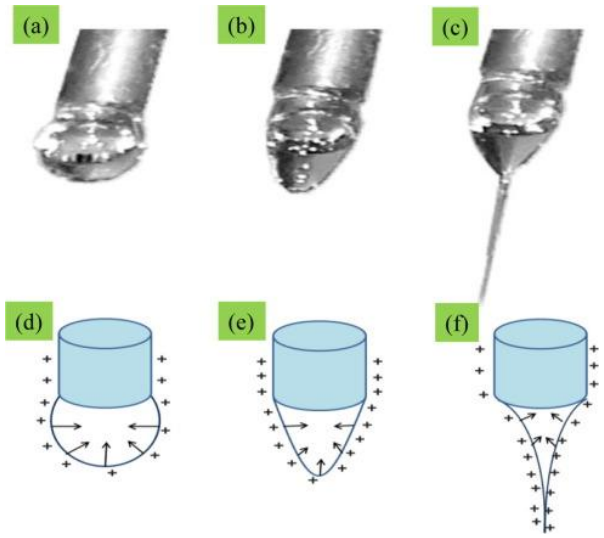

Figure 3.1.2 (A-C) Deformation of polymer droplet with further formation of Taylor cone after application of high voltage to the polymer solution. (D-F) The schematic representation of the mechanism imbalance between electrostatic repulsion and surface tension on the droplet's surface, with the subsequent creation of a conical shape with the increase of applied voltage[114].

The generated jet starts to orient in the direction of the counter electrode. In the distance between the needle and collector, the solvent starts to evaporate, the jet starts to elongate due to the Coulomb repulsions, and polymer strands begin to solidify. At that point, the ejected fibres start to diminish their diameter, ranging from micro to nanometres, and get deposited in the form of solid materials (fibrous mesh) on the counter electrode.

Even though the process itself is simple to perform and relatively fast, the theoretical explanation of the behaviour of the fibres on the way to the collector is quite complex. The scheme in Figure 3.1.3 presents certain characteristic regions of the fibre formation.

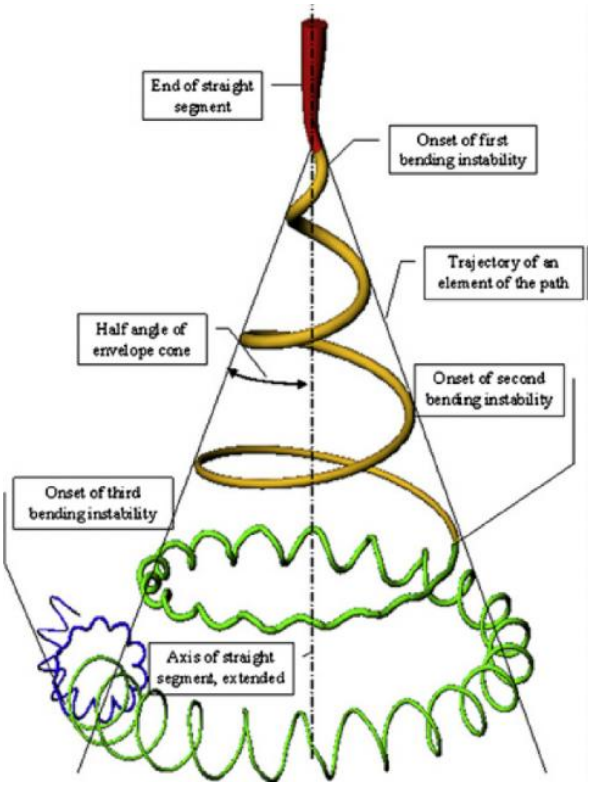

Figure 3.1.3 Diagram showing onset and development of bending instabilities[115].

With the fibre formation, bending instabilities play an important role. The first part of the jet is a straight segment, with the flow direction parallel to the axis of the jet, along the instantaneous path of the jet. Under the influence of the charge carried within the jet, the bending perturbation begins and starts to grow rapidly into a coil. In the bending segment, the elongation increases more rapidly, which influences the reduction in diameter. The longer the path the jet has to follow towards the counter electrode, the number of electrical bends increases, causing the jet to coil, with trajectories of each of those short segments becoming almost perpendicular to its own axis[116].

3.1.2 Parameters influencing the electrospinning process

During electrospun fibre preparation, several parameters can significantly influence the process itself, as well as the morphology of the product and its properties[117]. The following parameters have been divided into three groups according to their nature: (i) material parameters, (ii) parameters of the process, and (iii) environmental conditions.

Material parameters:

- Polymer and its properties

During selection of the polymer serving as a matrix for the electrospun fibres, the molecular weight of the polymer plays an important role, as it has a significant effect on the rheological properties (viscosity and surface tension), as well on the electrical ones such as conductivity and dielectric strength of the prepared polymer solution. The higher the molecular weight, it is generally easier to produce uniform fibres, as the polymer solution has appropriate viscosity to

generate fibres. In comparison, for the low molecular weight polymer solution, during the electrospinning, there is a tendency to produce beaded structures, related to the instability of the jet of the polymer solution.

- Solution concentration

For the successful electrospinning of the chosen polymer solution, optimization of the concentration of the polymer is an important step, as it influences the spinning abilities of the solution in the fibre production. What's more, it introduces a balance between the viscosity and surface tension of the solution in the electrospinning needle. At low concentrations of the polymer, instead of the fibres, the droplets are formed as a result of surface tension. On the other hand, at concentrations higher than optimal, the viscosity of the solution is too high, which prevents the fibre formation. While optimizing the concentration, it is important to note that generally, when increasing the polymer concentration, the fibres become more uniform with increasing diameter. The lower the polymer concentration, the thinner the fibres are produced; however, at this concentration regime, additional beads can appear along the fibres. To prevent the formation of the beads, one can increase the electrical conductivity of the solution, which could lead to the formation of very thin fibres.

- Volatility of solvents

During the electrospinning process, in the distance between the needle and the collector, fibres are formed due to the process of solvent evaporation. As one can assume, solvent vapor pressure plays a vital role in determining the rate of evaporation and, as a result, the drying time at fibre formation. At first, it may be a trivial role; however, the evaporation of the solvent influences the process of phase separation at the moment when the jet undergoes the thinning process. As a result, the relation between the solvent volatility and fibre diameter can be extracted, because fibres with diminished diameters can be produced by choosing a less volatile solvent.

Processing parameters

- Applied voltage

Adjusting the voltage applied to the needle filled with polymer solution is essential to the fibre formation, as the electrospinning will take place when the value of the voltage exceeds a certain threshold. The increase of applied voltage (in the range of a few kV) results in a higher electrostatic force on the solution, leading to a decrease in fibre diameter. Moreover, the value of applied voltage modifies the polymer solution during the formation of the drop's shape at the tip of the needle. This has an effect on the structure and morphology of the produced fibrous mesh. Additionally, the occurrence of beads along the fibre axis can be controlled by adjusting the spinning current.

- Flow rate

This parameter corresponds to a constant rate at which polymer solution is pumped into the needle tip in order to refill the cone. Adjusting the flow rate of the polymer solution into the syringe not only influences the material transfer rate but also the jet velocity. The optimal value of the flow rate of polymer corresponds to the ejection speed of the solution at the needle tip.

- Collector – geometry and distance from the needle

In general, a collector is a grounded metal plate onto which fibres produced in the described process are deposited chaotically. With the increased interest in the electrospinning process, various types of collectors have been introduced, often with specific geometries to influence the spatial distribution of the fibrous mesh; these include parallel plates, rotating disc, rotating drum, or a grid. In the case of a rotating drum, the mechanical stretching induces the alignment of the fibres, which leads to the electrospun mat with better mechanical properties[114].

Another parameter that greatly influences the structure and morphology of electrospun fibres is the distance between the needle and the collector. Adjusting this parameter is important due to the influence on the evaporation and deposition time, so in general, on the fibre formation. At short distances, the stream of polymer jet will have a limited time to dry, which could result in thicker fibres with residual solvent inside. Contrary, the longer the distance between the needle and collector, the electric field intensity is reduced, affecting the development of the jet stream at the needle tip. To overcome this effect and allow for the successful fibre formation, it is necessary to increase the applied voltage.

Environmental parameters

- Temperature

The temperature at which the electrospinning process is performed is another parameter that should be noted. As the solvent vapor pressure is temperature-dependent, as well as the rheological properties of the polymer, the properties of polymer solutions are also influenced by temperature.

- Humidity

The control over relative humidity in the electrospinning chamber is another environmental condition, which in fact may significantly influence the effective spinnability of the polymer solution, as well as the morphology and dimensions of fibres. In general, the electrospinning process is optimally performed when relative humidity is in the region of 40-55%, as for highly humid conditions, the process itself is much more challenging to perform[118].

3.2 Drop-casting from suspension

A straightforward technique for processing materials suspended in the suspension into a solvent-free sample, by casting the suspension onto the surface and allowing for evaporation of the solvent (Figure 3.2.1). The final form of the sample strongly depends on the form onto which the suspension was spread (mainly its area). As in principle the method is a simple approach, there is not much room for modifications to produce samples of better quality; however, the lack of specific equipment makes it a desirable technique in the prototypical formation of the functional composite foils.

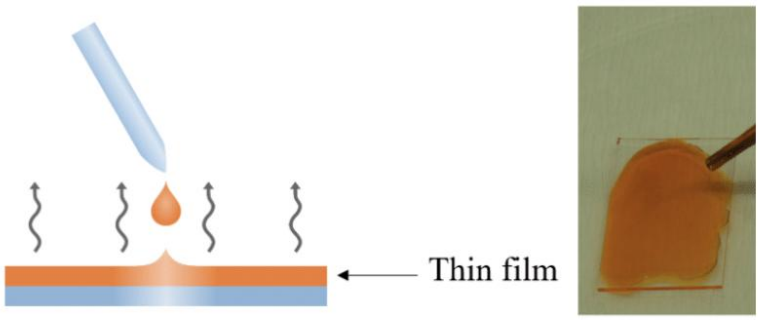

Figure 3.2.1 Scheme of drop casting method[119].

It is most commonly used as a method for sample preparation in the form of thin films, for chemical and physical characterization (SEM, TEM, AFM). Additionally, it is a coating method that is quite useful for depositing nanoparticle dispersion over relatively small areas of the substrates (~1cm^2). Characteristics of the as-produced films, such as film thickness and the coated area, strongly depend on the parameters that can be easily tuned: the volume of the dispersion and the particle concentration, as well as the substrate surface.

The preparation of the composite thin films by the drop-casting method differs in a way from the traditional substrate coating. Using an organic polymer as a matrix in the film production process imposes limitations on the final product. The thickness of the as-produced foils is much greater, and the concentration of the functional particles spread in the matrix, as well as the organic itself, influences the homogeneity of the final foil. Usage of volatile solvents is most commonly advised to minimize the time for sample preparation and additional effects, such as aggregation; however, the rate of evaporation as well as the drying process have a strong influence on the morphology of the final composite film.

Apart from simply coating the surface with the drop-casting method, this technique may be utilized for the production of substrate-free foils. With this approach, the organic polymer matrix plays a crucial role, as its mechanical properties after solvent evaporation depend on whether it is possible to detach the composite film in a solid form from the substrate.

In the following research, this technique served as a comparative method for composite preparation to the electrospinning process, due to the lack of control over the dispersion and aggregation of the additive functional particles (section related to FeTrz-NP in the PVP matrix). On the other hand, this method was utilized as a way to produce a prototypical reusable composite pressure sensor in a simple and quick manner at laboratory scale (section related to NiFe-chain foil).

3.3 Characteristic of the polymer matrices

In the following thesis, three polymers that have been selected as the matrices for the formation of composite materials, namely: poly(ε-caprolactone) (**PCL**), poly(*N*-vinyl-2-pyrrolidone) (**PVP**), and the copolymer poly(2-vinylpyridine-co-styrene) (**P2VP-PS**). Their chemical structure is presented in Figure 3.3.1, while the comparison of their physicochemical characteristics is summarised below in Table 3.3.1.

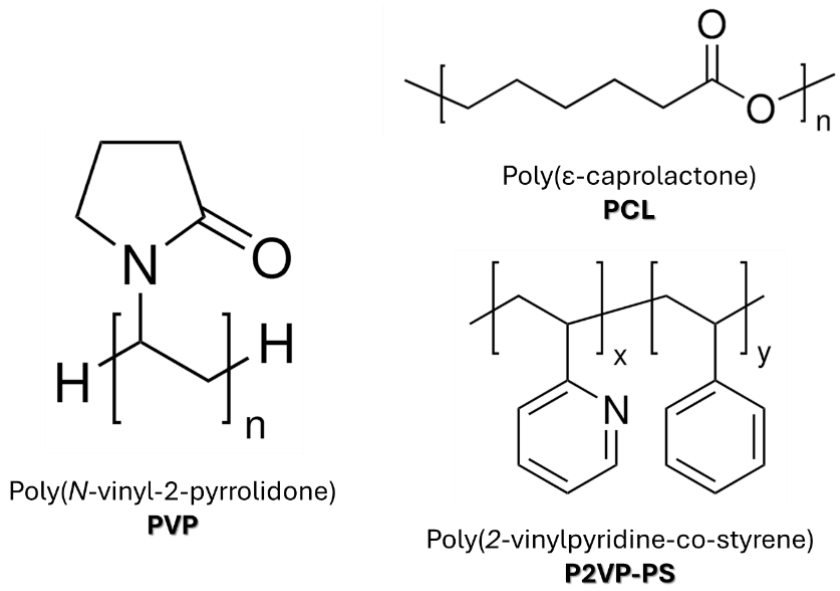

Figure 3.3.1 Chemical structures for the chosen polymers: PVP, PCL, P2VP-PS.

Firstly, PVP is an amorphous, water-soluble, hydrophilic, and chemically inert polymer, distinguished by its pronounced biocompatibility, thermal stability with a relatively high glass transition temperature ($T_g \approx 180°C$). In the field of coordination polymers and metallic nanoparticles, it is distinguished for its abilities as a coating agent for NPs. For example, PVP with low molecular weight has been widely used in metallic/ metallic oxide nanoparticles formation and stability (eg. Ag, Fe_3O_4, ZnO, Pt)[120–122]. Additionally, it has been employed in the preparation and stabilization of PB and PBA NPs[123–125]. In the electrospinning community, PVP is recognised for its versatility, favourable solubility in polar solvents, and capacity to be utilised in the fabrication of core-shell structures in conjunction with polymers of varying molecular weights[126,127]. In addition, PVP polymer has been employed in the preparation of conductive composites through the incorporation of diverse conducting fillers[128,129].

The second of the chosen matrices is PCL, a semi-crystalline aliphatic polyester, valued for its biodegradability, low glass transition temperature ($T_g \approx -60°C$), mechanical strength, and relatively low melting temperature (60°C). PCL is known for its hydrophobicity, due to the presence of aliphatic chains within monomers, which reduces its affinity to water. And so, PCL is insoluble in water and alcohols, but soluble in various organic solvents such as dichloromethane, chloroform, and toluene. It is a chemically inert polymer, and it has been proven to be a staple biodegradable and biocompatible cost-effective material, that has found many applications in drug delivery systems, packaging, and the antimicrobial field, such as medical

implants, wound dressing, and tissue engineering[130,131]. Within the field of electrospinning, it has been widely used[132], especially as a polymer blend[133] or with the incorporation of specific drugs[134], making it an ideal wound dressing material with the ability to gradually release the drug into an infected area.

Lastly, a block copolymer P2VP-PS has been selected as a polymer matrix. It is a polymer composed of 2-vinylpyridine units and styrene segments, each imparting properties onto the copolymer. P2VP-PS shows amphiphilic properties, with hydrophobic styrene units and 2-vinylpyridine hydrophilic parts. The presence of styrene mers adds rigidity and mechanical reinforcement to the copolymer properties. As for the poly(2-vinylpyridine), it is pH dependent, due to the ability of nitrogen in the aromatic ring to be protonated[135,136]. Additionally, due to the presence of a pyridine ring, it shows potential in coordination and confinement of nanoparticles[137,138], as it was shown for Au NPs[139,140] and silica NPs[141], or iron(II) spin-crossover coordination polymer NPs with poly(4-vinylpyridine) analogue[142–144]. In contrast to PVP and PCL polymers, P2VP-PS copolymer has not been as widely studied in the formation of composite materials, especially in the form of electrospun fibres[145]. Nevertheless, the amphiphilic character of the polymer has recently been making its way in biomedical applications (eg, drug release systems)[146], in filtration membranes preparation[147], or microgel formation.

Table 3.3.1 Comparison of physicochemical characteristics of chosen polymer matrices and their potential application usage.

Polymer	**Poly(*N*-vinyl-2-pyrrolidone)**	**Poly(ε-caprolactone)**	**Poly(2-vinylpyridine-co-styrene)**
Symbol	PVP	PCL	P2VP-PS
Molecular weight	360 kDa	80 kDa	220 kDa
Glass transition temperature	~180 °C	-60 °C	~100 °C
Melting temperature		60 °C	
Reactivity	Chemically inert, non-toxic	Chemically inert, non-toxic	Contains reactive pyridine groups
Crystallinity	Amorphous	Semi-crystalline	Amorphous
Amphiphilicity	Hydrophilic	Hydrophobic	Amphiphilic
Solubility	Soluble in water, alcohols (methanol), and other polar solvents (chloroform, DMF, acetone) Insoluble in hydrocarbons and oils	Soluble in organic solvents (chloroform, dichloromethane, toluene) Insoluble in water and alcohols	Soluble in organic solvents (chloroform, methanol, DMF, THF, toluene) Insoluble in water
Other properties	Highly hygroscopic, pH stable	Biodegradable, Biocompatible, Flexibility,	pH responsiveness
Applications	Coating agent for NPs; Stabilizer for drugs; Wound dressing and tissue engineering; Coatings and adhesives	Drug delivery; Tissue engineering, and wound dressing; Packing	Stabilizing agent for NPs; Drug release systems, Coatings and adhesives; Filtration; Microgels formation

4. Composites based on PBA micro- and nano-particles

The following chapter will focus on the 3D coordination structures known as Prussian Blue Analogues (PBA) with a general formula $A_zM_x[M'(CN)_6]_y \cdot nH_2O$, where M and M' are transition metals and A is an alkali metal. It is dedicated to two different sub-families:

1) $Ni_3[M(CN)_6]_2 \cdot nH_2O$, where (M = Fe, Cr) with intercalated Na^+ cations;

2) $Rb_xMn[Fe(CN)_6]_{(x+2)/3} \cdot nH_2O$ with Rb^+ cations, being an example of a composition showing thermally-induced charge transfer (CT) process, involving metal centres.

In both sub-chapters, synthetic protocols for preparing bulk samples and their corresponding electrospun fibre composites are presented. The characterization of prepared materials is based on particles and fibre morphology derived from SEM imaging, followed by spectroscopy (IR and Raman) and structural (XRD) characterization. In both cases, the magnetic characterization is discussed in the final section.

4.1 Cubes of $Ni_3[M(CN)_6]_2 \cdot nH_2O$, where (M = Fe, Cr) introduced into organic polymer electrospun fibres

The first part of the PBA-related chapter is devoted to nickel hexacyanochromate(III) with formula $Ni_3[Cr(CN)_6]_2 \cdot nH_2O$ (hereafter referred to as **NiCr**) and nickel hexacyanoferrate(III) with formula $Ni_3[Fe(CN)_6]_2 \cdot nH_2O$ (hereafter referred to as **NiFe**), which have been studied as freshly synthesized nanoparticles and have been incorporated into the organic polymer matrix in the form of electrospun fibres. The interest in these PBA compositions comes from the simplicity of synthesis and, at the same time, the possibility of obtaining particles of defined morphology. Despite great similarities between both structures, they present differences in magnetic properties, which have been studied with a focus on their topology (nanoparticles, thin films, nanorods)[59,148] or mixed compositions[60]. The results presented in the following sub-sections have been partially published in *Acta Physica Polonica*[149].

Generally, PBA structures are characterised by relatively simple bulk synthesis performed through co-precipitation. It is a direct reaction of chosen precursors, and depending on the lower solubility of the product in aqueous conditions, the PBA structure is obtained. As interest in obtaining well-defined particles of nanoscale dimensions emerged, several synthetic approaches have been presented in the literature to govern the co-precipitation process[150]. Some examples include using templates, adding organic polymers, or using other stabilizing agents. The last group, led by the addition of citrate salts, appeared as one of the most elegant pathways, as it resulted in homogenous growth particles with tuneable dimensions, dependent on conditions easily manipulated during synthesis.

Synthesis of **NiFe** and **NiCr** nanoparticles

The preparation of chosen PBA nanoparticles based on Ni^{2+} salt and $[Cr(CN)_6]^{3-}$ or $[Fe(CN)_6]^{3-}$ was performed according to the modified literature protocol[151] with the use of citrate anion as a stabilization agent. Detailed amounts of substrates used for both syntheses are presented in Table 4.1.1. The procedure to obtain both types of nanoparticles was comparable, with the difference in the source of cyanometallates (Cr or Fe).

In the initial vial, nickel(II) salt was introduced in the form of nickel(II) nitrate hexahydrate, together with trisodium citrate tetrahydrate as a stabilizing agent. They were dissolved in 40 ml H_2O with the use of magnetic stirring. In the second beaker, cyanometallate salt was placed: $K_3[Cr(CN)_6]$ or $K_3[Fe(CN)_6]$, and then dissolved in the same amount of distilled water. Following the combination of the two solutions, the resulting mixture was subjected to magnetic stirring for 48 hours at room temperature (20 °C). The final product was separated from the supernatant by centrifugation at 9000 rpm for 15 min at a constant temperature of 10 °C. The cleaning protocol by centrifugation was performed three times to wash away any residues from the substrates. It was comprised of a series of washing the product with distilled water, followed by centrifugation with the same parameters (9000 rpm, for 15 min, at 10 °C). The resulting solid (light blue for **NiCr**, and orange for **NiFe**) was then subjected to vacuum drying at 40 °C for 20h.

Table 4.1.1 Synthetic details for **NiCr** and **NiFe** NPs.

Substrate	H_2O volume	**NiCr**	**NiFe**
Nickel(II) nitrate hexahydrate	40 ml	1.2 mmol (0.350 g)	1.2 mmol (0.350 g)
Trisodium citrate dihydrate		1.8 mmol (0.529 g)	1.8 mmol (0.529 g)
$K_3[Cr(CN)_6]$	40 ml	0.8 mmol (0.260 g)	-
$K_3[Fe(CN)_6]$	40 ml	-	0.8 mmol (0.263 g)
Stirring time (temperature)		48 h (20 °C)	48 h (20 °C)

Preparation of electrospun composite fibres

During the fabrication of composite materials in the form of electrospun fibres incorporating freshly synthesized PBA nanoparticles, careful selection of both the polymer matrix and the solvent system was crucial to ensure successful fibre formation and nanoparticle integration. Accordingly, an organic polymer called poly(*N*-vinyl-2-pyrrolidone) (**PVP**) was chosen with an average molecular weight of M_w = 360 kDa. In the solution preparations, methanol was used as the solvent, as it is capable of entirely dissolving PVP within several hours, without any extensive heating.

Before the fabrication of composite material, pure PVP electrospun fibres needed to be obtained for a comprehensive characterization of the polymeric matrix. During the preparation of the electrospinning solution, PVP 360 was dissolved in methanol to a polymer concentration of 12 wt%, following a protocol established in the literature[152].

In the case of PBA NPs loaded composites, the procedure for electrospinning solution preparation was as follows. For both types of PBA NPs, 43.00 mg of freshly synthesised powders were redispersed in 3 ml of methanol. To ensure a high degree of homogeneity, the dispersion was sonicated with the use of an ultrasound homogenizer probe (Sonoplus GM 4200, Bandelin electronic GmbH & Co. KG) operating at 30% power amplitude without pulsation for 2 min. Then, the appropriate amount of PVP 360 (~ 0.33 g) was introduced to give a solution with the PVP polymer concentration equal to 12 wt%. To maintain the dispersion of PBA NPs and at the same time allow for the slow dissolution of PVP, the mixture was immediately placed onto the gyromixer for approximately 3-4 hours for the complete dissolution of the polymer, before performing electrospinning. The prepared electrospinning solutions are presented in Figure 4.1.1.

Figure 4.1.1 Photographs of the polymer solutions prepared for electrospinning.

For the electrospinning process, the polymer solution, either pure PVP or PVP with added PBA nanoparticles, was loaded into a plastic syringe and electrospun using custom-built electrospinning equipment. The flow rate of the polymer solution was controlled by the syringe pump at 1.5 ml/h. The electrospinning of PVP with and without the PBA fillers was performed with a voltage of 11 kV, at room temperature (~20 °C) with relative humidity ranging from 46−52% RH. The fibre mats were collected on a metallic plate collector randomly, at a constant distance from the tip of the needle to the grounded collector equal to 10.5 cm.

4.1.1 Morphology of NPs and electrospun fibres

The synthesis of PBA nanoparticles based on the trisodium citrate salt as a capping agent resulted in well-defined particles with a cubic shape (see Figure 4.1.2). Interestingly, measured diameters of cubes and resulting size dispersions showed that the average particle size of **NiFe** cubes is three times larger than **NiCr** (238 ± 37 nm and 80 ± 17 nm, respectively), despite the similarities in the synthetic protocol.

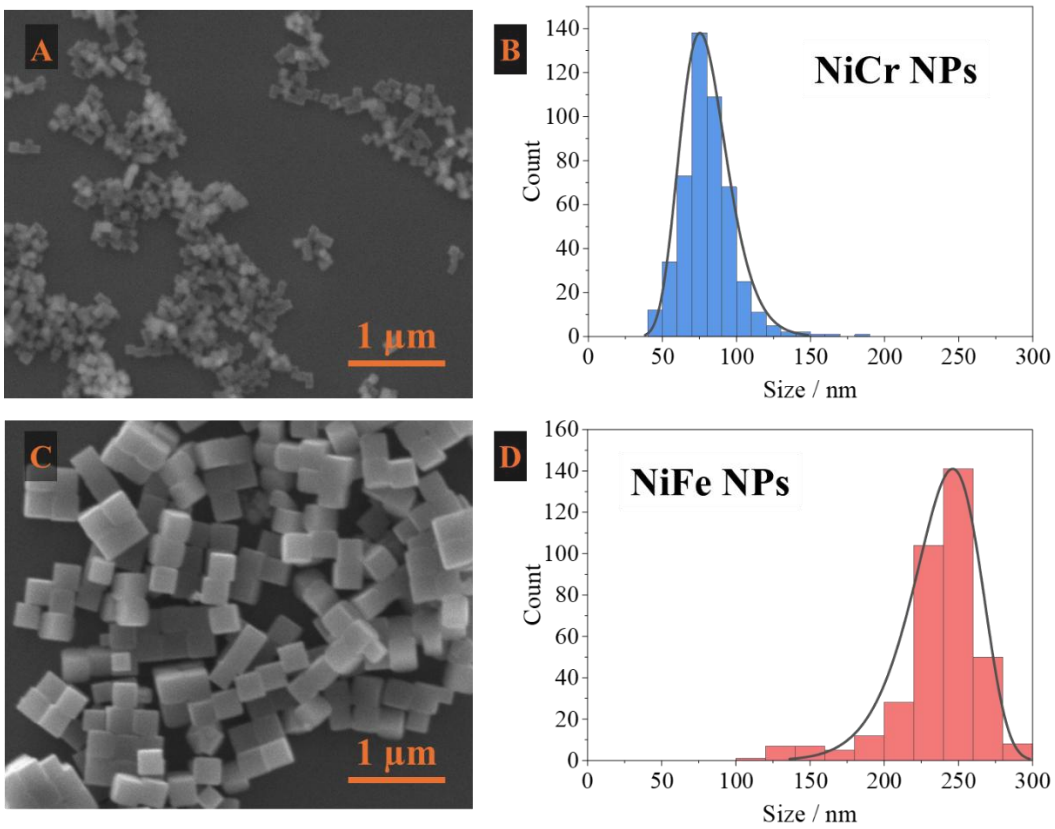

Figure 4.1.2 SEM image of **NiCr** NPs (A), with lognormal distribution curve (B); SEM image of **NiFe** NPs (C), with Weibull distribution curve (D).

The electrospinning process was employed for the preparation of PVP-based composites with incorporated PBA particles at a concentration of 11.0 wt.% (**NiFe/PVP**) and 11.9 wt.% (**NiCr/PVP**) yielded materials of two distinctive colours, corresponding to the initial solutions: light orange for **NiFe** and white for **NiCr** (Figure 4.1.3).

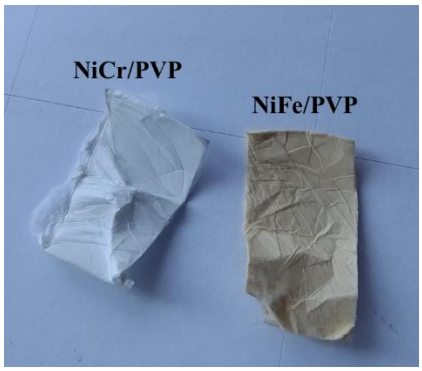

Figure 4.1.3 Photographs of the obtained electrospun mats.

SEM imaging performed on the freshly deposited fibres on a silicon wafer at an accelerating voltage of 20.0 kV, without any additional coating with a conducting layer, allowed the analysis of the fibre's morphology, with an emphasis on the embedded particles and their displacement within the fibres, as illustrated in Figure 4.1.4. In both cases, the PBA nanocubes are visibly incorporated into the electrospun fibres, without any relevant breakage of the fibres due to the material agglomeration. Apart from this similarity, there are also some significant

morphological differences between the two materials. For the larger **NiFe** nanocubes in the **PVP** matrix, the average diameter of the electrospun fibres is measured at 0.69 ± 0.15 µm, while the incorporation of nanocubes resulted in thickened fibre fragments with diameters reaching the value of 0.97 ± 0.18 µm. Conversely, composite material containing **NiCr** particles within the polymer matrix exhibits a reduced average fibre diameter of 0.56 ± 0.12 µm, with the areas of nanocubes aggregation leading to fibre thickening up to 0.70 ± 0.14 µm. Notably, the broadening effect of fibre diameters amounts to approximately 40% for the **NiFe/PVP** composite and 25% for the **NiCr/PVP** electrospun composite.

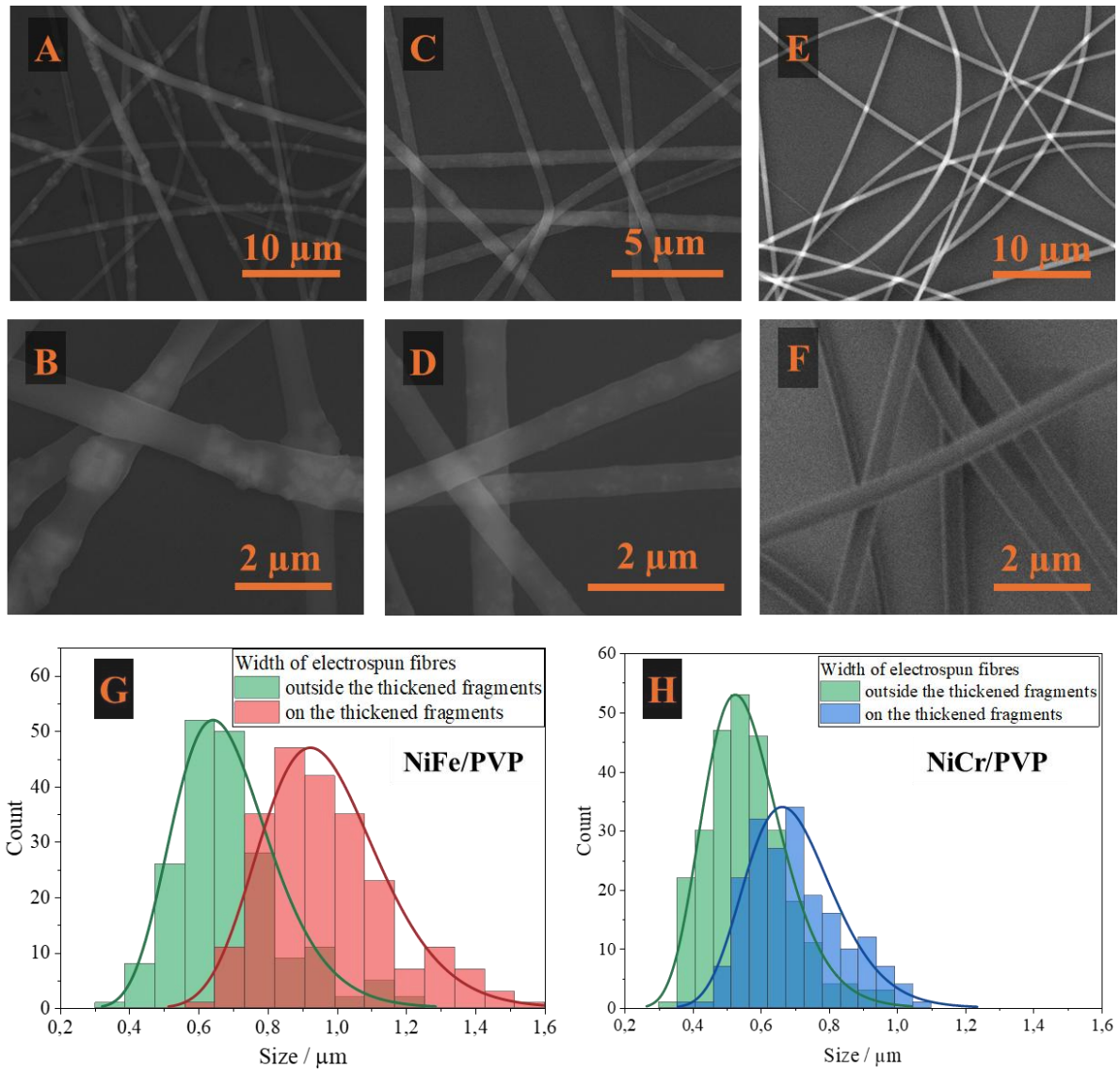

Figure 4.1.4 The SEM pictures of the electrospun fibres for **NiFe/PVP** (A, B) and **NiCr/PVP** (C, D) and undoped **PVP** (E, F) fibres for comparison.

EDS mapping, as depicted in Figure 4.1.5, substantiates that the thickened segments of the fibres arise from the incorporated nanocubes. It is important to note that the quality of the mapped fragments provides only a rough estimation of the nanoparticles' placement. The mapping reveals that elements such as Ni, Fe, and Cr – representative of the PBA nanoparticles – are more concentrated in regions associated with nanocubes placement compared to areas

devoid of particles, where carbon mapping was performed. Additionally, regions rich in PBA NPs exhibit a high carbon content, likely attributed to the polymer coating. This observation further corroborates that the fillers, even when aggregated, are embedded within the **PVP** fibre matrix rather than residing on its surface.

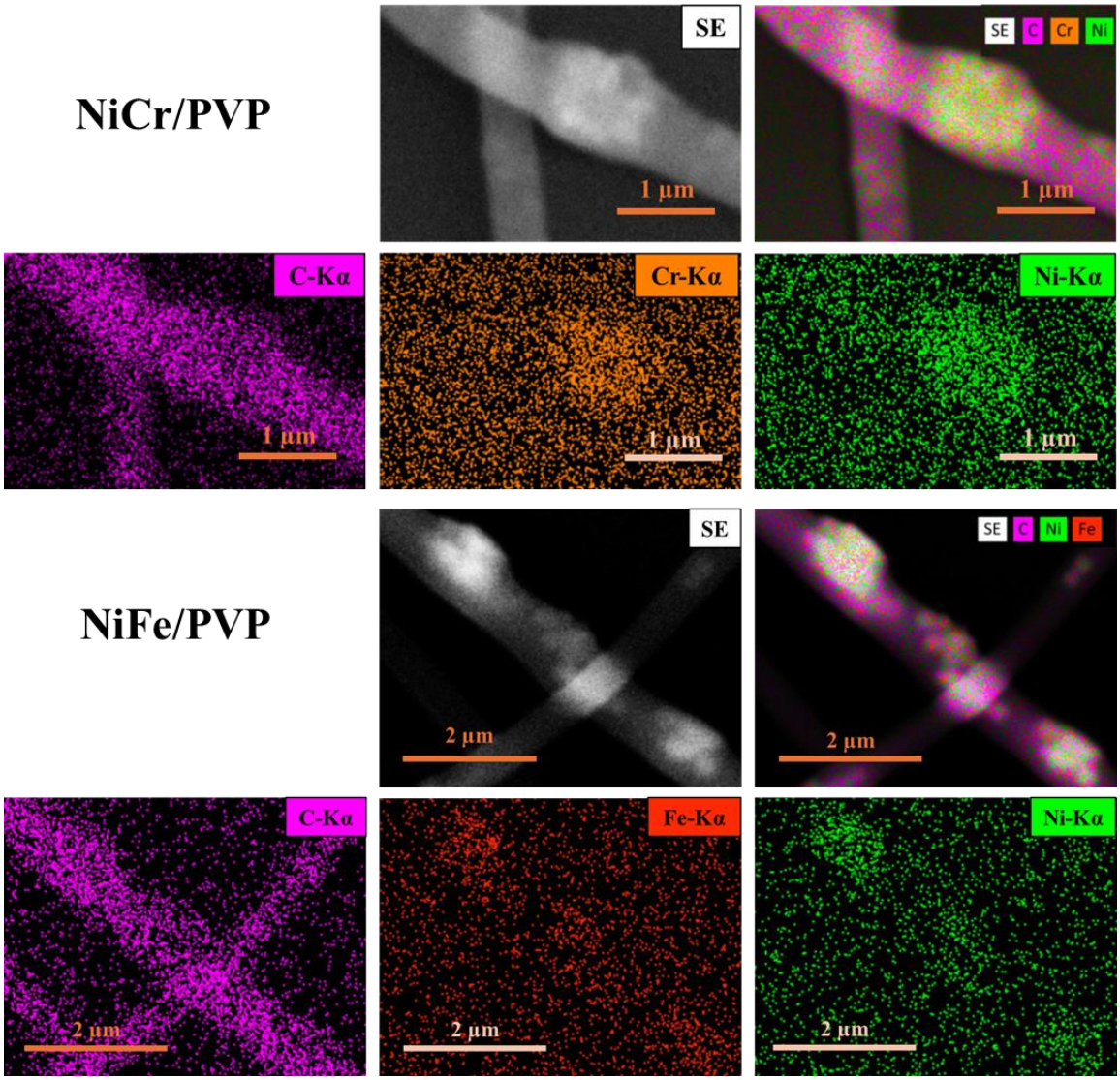

Figure 4.1.5. Elemental mapping of PVP nanofibres loaded with 12 wt.% **NiCr** (upper panel) and **NiFe** (lower panel) nanoparticles by EDS.

Importantly, the presence of these cubic particles does not compromise the structural integrity of the fibres, given that their dimensions are significantly smaller than the diameters of the fibres themselves. Although the distribution of nanocubes along the fibres is not entirely homogeneous for both composite types, the reduced size of the **NiCr** nanocubes contributes to an improved fibre morphology. This enhancement in morphology may have implications for the mechanical properties of the resulting composite materials.

4.1.2 Spectroscopic and structural analysis

To confirm the purity of the obtained PBA NPs, infrared spectroscopy was performed, and the results have been depicted in Figure 4.1.6. Both studied structures show distinct peaks around 2170 cm^{-1}, more precisely 2166 cm^{-1} and 2171 cm^{-1}, which are attributed to the CN stretching vibrations of Fe^{3+}–C≡N–Ni^{2+} and Cr^{3+}–C≡N–Ni^{2+} bonds, respectively. Additionally, for the Fe-based PBA, a weaker bond is observed at 2098 cm^{-1}, suggesting a partial reduction of Fe^{3+} to Fe^{2+} species in the sample[59].

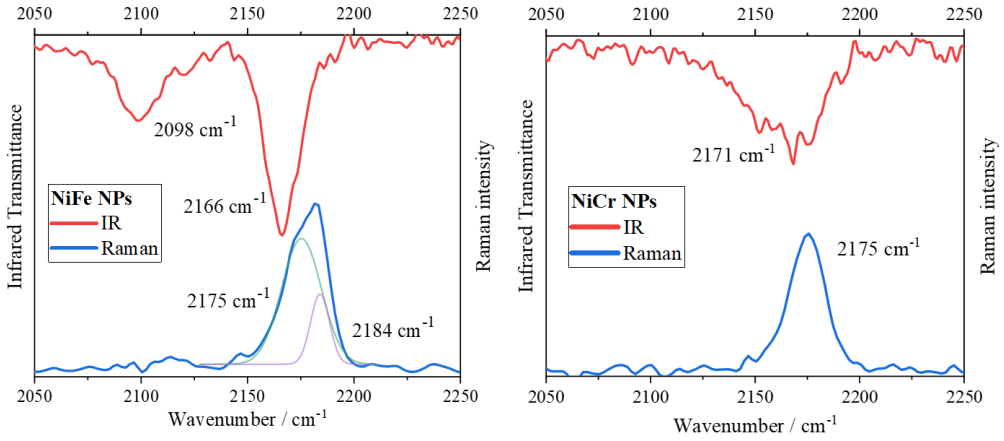

Figure 4.1.6 The comparison of IR (red) and Raman (blue) spectra in the ν(CN) region of **NiFe** (left) and **NiCr** (right) bulk samples

To obtain information about the chemical stability of the PBA fillers after introducing them into electrospun **PVP** fibres, Raman spectroscopy was employed. It has proven to be an ideal technique for studying the characteristic bonds of both the matrix and the embedded particles in the composite materials in different forms (films, fibres, etc.)[143,153–155]. For the studied composite fibres, the measurement was performed on the electrospun fibres deposited onto the Si(100) wafer, similarly to the SEM imaging.

In the case of powdered samples, Raman spectroscopy is not as common, due to the use of a laser beam, which burns through the sample relatively quickly, in contrast to non-invasive infrared spectroscopy. However, the measurement is possible with appropriate parameters, such as short exposure time and minimal laser power. As for the PBA structures and their characteristic cyano-bonds, the Raman spectrum also shows C≡N stretching vibrations in the 2000-2300 cm^{-1} wavenumber region[156], although they may not correlate with the number and location of the bands in IR. The spectra recorded for Ni-CN-M displayed similar characteristics – a single band at 2175 cm^{-1} (**NiCr**) or a deconvoluted double band at 2175 cm^{-1} and 2184 cm^{-1} (**NiFe**), illustrated in Figure 4.1.6.

The comparison of Raman spectra recorded for both types of PBA NPs, together with their appropriate composites and spectra for the undoped PVP matrix, has been depicted in Figure 4.1.7. In general, the Raman spectra of composite fibres feature both CN stretching vibrations at 2000 cm^{-1}, with the addition of characteristic bands in three regions (around 1000, 1500, and 3000 cm^{-1}, marked with frames) originating from the **PVP** polymer matrix[157,158]. In detail, PVP characteristics derive from: strong vibrations at 938, 954, and 972 cm^{-1} from C-C ring

breathing; weaker bands at 1419, 1440, and 1490 cm^{-1} assigned to CH_2 scissor vibrations; and bands at 1658 cm^{-1} originating from C=O in the amide bond. The last region with strong bands below 3000 cm^{-1} comes from C-H band vibrations. Detected CN vibration bands do not show any relevant shift, however in the case of **NiFe** apart from the predominant peaks at 2175 and 2184 cm^{-1}, two weaker bands appear centred at 2145 cm^{-1} and 2109 cm^{-1} most probably due to the partial reduction of Fe, similarly to the IR spectrum recorded for the bulk sample.

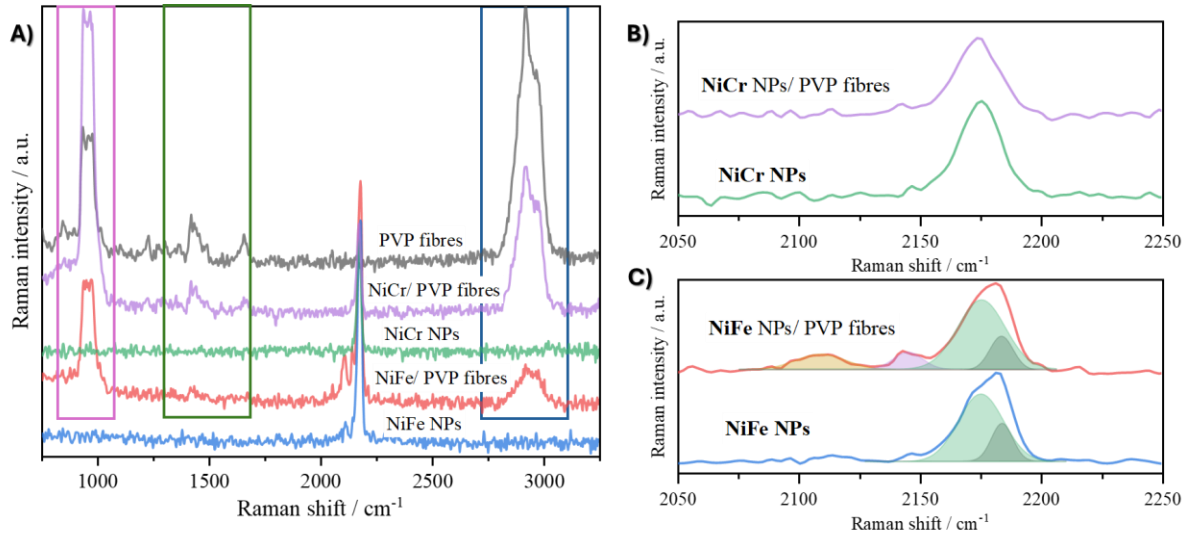

Figure 4.1.7 A) Raman spectra of composite fibres of **Fe-CN-Ni/PVP** (top) and **Cr-CN-Ni/PVP** (bottom) with appropriate bulk samples. Selected areas include regions of characteristic vibrations of PBP fibres. B), C): enlargement of Raman spectra in the ν(CN) region.

X-ray diffraction studies were initially conducted on the freshly synthesized PBA nanoparticles to verify the structural purity, given the modifications made to the original literature synthesis protocol. All the observed peaks of PXRD patterns for both materials were indexed with the cubic space group *Fm-3m*, without any noticeable impurity peaks in either compound. The LeBail fit was performed in the full-pattern range for both structures (presented in Figure 4.1.8). The obtained cubic unit cell parameters equal to 10.2307(6) Å for **NiFe** and 10.4985(5) Å for **NiCr** are consistent with the literature data[151,159].

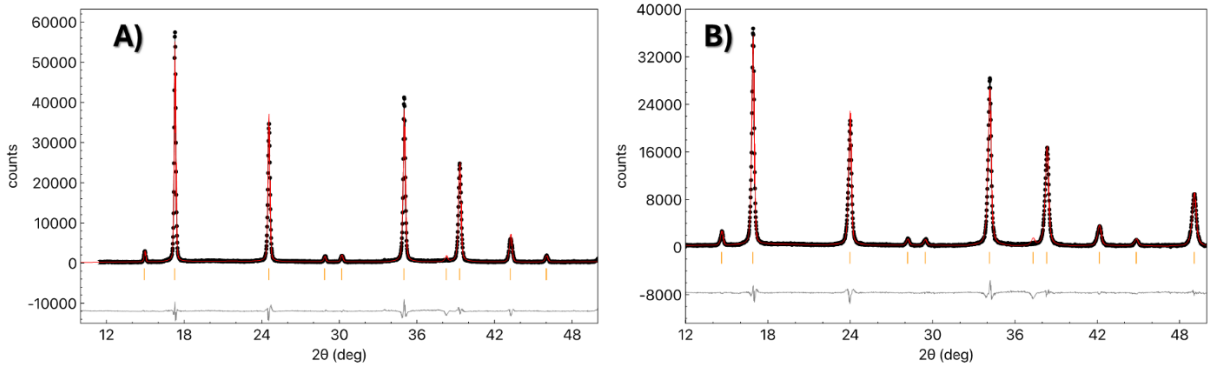

Figure 4.1.8 X-ray diffraction data of (a) **NiFe** NPs and (b) **NiCr** NPs. The black circles are the experimental data, and the red curve is the profile calculated using the Le Bail method.

To compare the structures of incorporated PBA NPs in the electrospun fibres with pure powdered samples, XRD measurement has been performed on the freshly prepared composites. For a homogenous and relatively flat surface of the fibre material, it was necessary to deposit the fibres onto a substrate, which could be transferred into a diffractometer without any additional preparations. Si(100) wafers of 1.5 cm × 1.5 cm dimensions have been chosen, as they do not interfere with collected diffractograms in the chosen 2θ range (Si(100) usually has a peak at 2θ = 69.25^0). The only drawback of the selected substrate was the appearance of the Si(200) reflection at the peak at 2θ = 33^0. Although it is a forbidden reflection, it is quite often encountered in diffraction measurements, where a silicon wafer is chosen as a substrate[160].

Firstly, XRD measurements have been performed on **PVP** fibres without any additives, as presented in Figure 4.1.9. The amorphous character of the PVP polymer chains is observed, as on the diffractogram two broad peaks can be identified at 2θ equal to 11.057º and 21.342º. According to the literature, the appearance of those two regions may be associated with the two distinct amorphous phases of PVP, originating from a difference in PVP polymer chains' length and orientation[161,162].

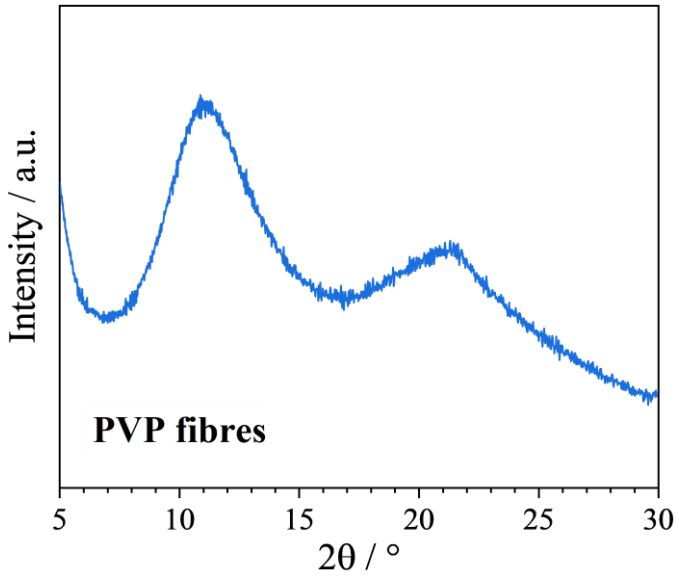

Figure 4.1.9 The XRD pattern measured for **PVP** fibres without any additives.

Figure 4.1.10 presents superimposed data of pure PBA structures in both forms and after embedding PBA NPs into PVP fibres. Above the amorphous characteristics of PVP of low intensity, the diffractograms of **PBA/PVP** composites show distinctive XRD peaks derived from PBAs structures. Due to the presence of all PBAs peaks and their high intensity relative to the polymer matrix signal, it can be assumed that the composite prepared in the electrospinning process contains a high loading of the PBA-type nanocubes in the PVP fibres. In the case of the **PVP** matrix-derived peaks (marked in with blue arrows), their position changes to 11.128º and 20.512º for **NiFe/PVP** and to 11.264º and 20.597º for the **NiCr**-based composite fibres.

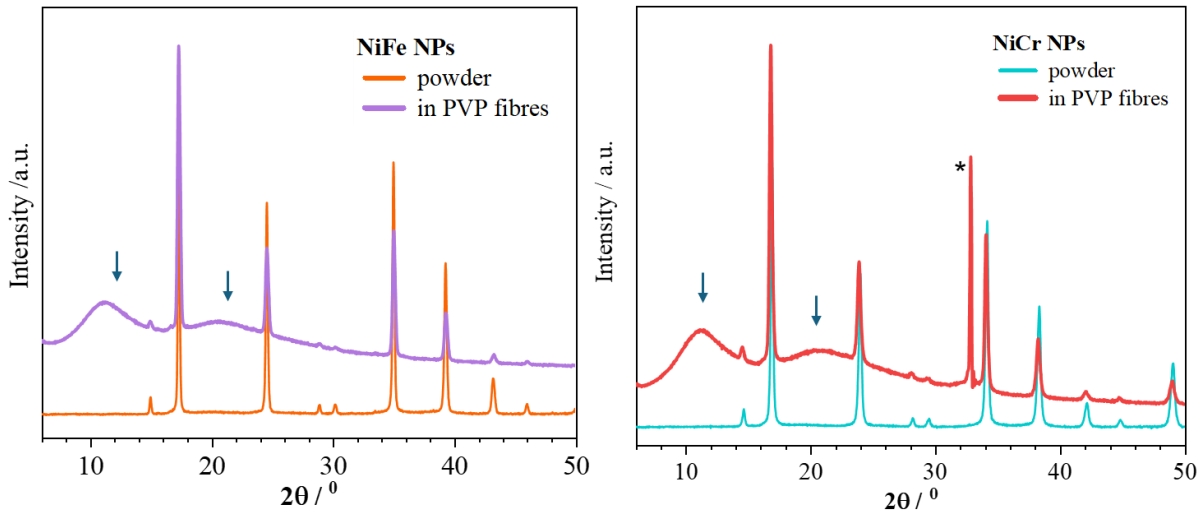

Figure 4.1.10 The XRD pattern measured for the **PBA** bulk sample and composite fibres of **PBA/PVP** with blue arrows marking peaks derived from **PVP** matrix and an asterisk originating from Si(100) substrate.

While comparing both patterns of composite fibres to relevant powder samples, a slight shift in the position of PBA peaks was noticed. The fitting of the recorded diffractogram of PBA structure in the composite fibres with the LeBail method (Figure 4.1.11) showed a slight decrease in the cell parameters to 10.2212(3) Å for **NiFe** and 10.4933(4) Å for **NiCr**. Comparing these results to powdered samples, the decrease in cell parameters is equal to 0.09% and 0.05%, respectively.

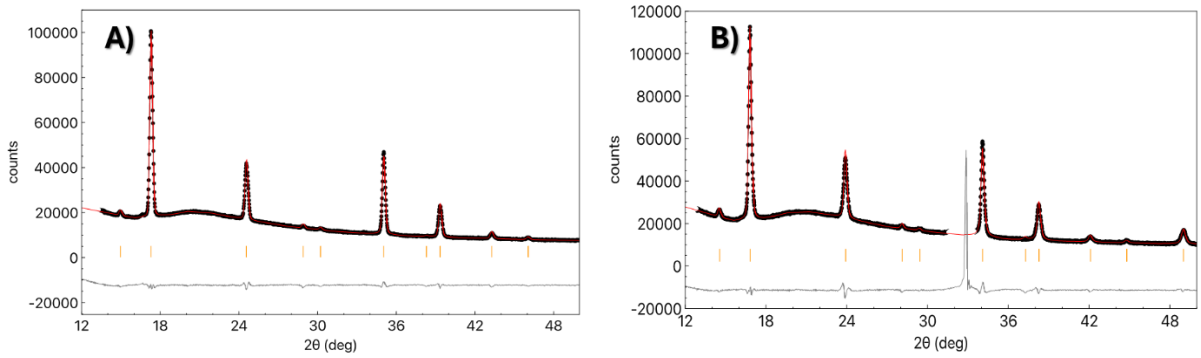

Figure 4.1.11 (A) **NiFe/PVP** composite, (B) **NiCr/PVP** composite. The black circles are the experimental data, and the red curve is the profile calculated using the Le Bail method.

4.1.3 Magnetic properties of PBA nanocubes and their composites

To comprehensively characterize the properties of the synthesized PBA nanoparticles and their composite electrospun fibres, their magnetic behaviour was investigated, with determined parameters summarised at the end of the subsection in Table 4.1.2. Magnetization measurements were conducted as a function of the external magnetic field at a temperature of 2 K to assess their magnetic response under low-temperature conditions. The resulting magnetic hysteresis curves for both the powdered nanoparticles and the composite electrospun fibres are presented

in Figure 4.1.12, providing insight into their coercivity, remanence, and overall magnetic properties.

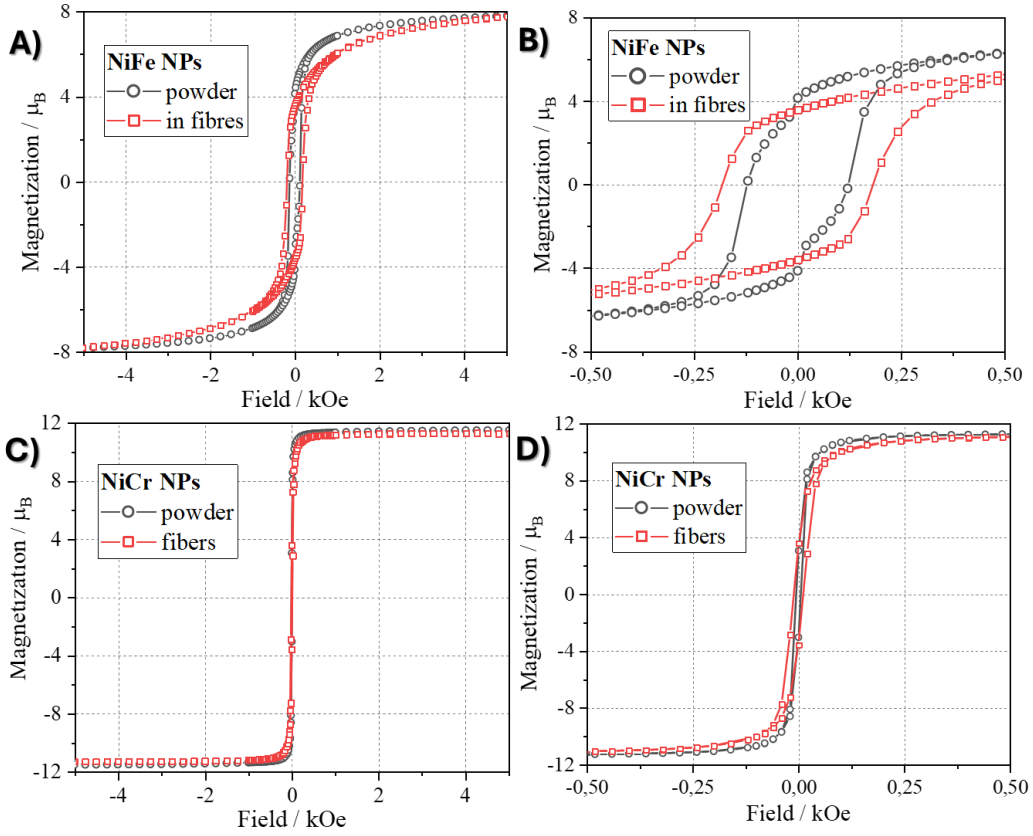

Figure 4.1.12 The comparison of magnetization curves for **NiFe** (upper panel) and **NiCr** (lower panel) in the form of the powder and respective composite fibres at a constant temperature of 2 K.

For both PBA compounds, a significant difference is observed in the width of the hysteresis loops. The **NiFe** compound displays a wider hysteresis with a coercive field of 120 Oe, while the **NiCr** compound shows a much narrower hysteresis with a coercive field of 5 Oe. The saturation of magnetization of the Cr-based compound reaches 11.3 μ_B, which is slightly lower than the theoretical value of 12 μ_B. This corresponds to the ferromagnetic coupling between three spins: Ni^{II} ($S = 1$, $g_{Ni} = 2$) and two Cr^{III} ($S = 3/2$, $g_{Cr} = 2$). The saturation of magnetization of the Fe-based compound comes to the value of 7.8 μ_B. This value is consistent with that expected ($8\mu_B$) for three Ni^{II} ($S = 1$, $g_{Ni} = 2$) ions and two Fe^{III} ($S = ½$, $g_{Fe} = 2$) ions and suggests the presence of ferromagnetic interactions.

To extract the amount of the embedded PBA NPs into the PVP polymer fibres, the values of the saturation of magnetization of the composites have been matched to the values of pure compounds, by multiplying the mass of the measured fibre samples by the percentage of magnetic particles. The obtained values are 10.5% and 11.25%, respectively, for the **NiFe** and **NiCr**. These results are slightly lower compared to the initial concentration of 11.0% and 11.9% (for **NiFe/PVP** and **NiCr/PVP**, respectively) set during the preparation of the materials, without any significant differences related to the different sizes of nanoparticles. Additionally, the field dependence on magnetization showed differences in the hysteresis widths between the pure PBA compounds and after incorporating them into the electrospun fibres. For both, the

hysteresis widens; however, for the **NiFe** it is much more pronounced as the coercive field reaches a value of 185 Oe, whereas for the **NiCr** it is equal to 10.5 Oe.

The study of the thermomagnetic behaviour of nanocomposites and nanoparticles was performed by DC susceptibility under zero-field-cooled (ZFC) and field-cooled (FC) conditions in an external field of 100 Oe (Figure 4.1.13). The rise of χ_{dc} at low temperatures observed for both nanoparticle types confirms the transition to the long-range ordered state with a high magnetic moment value. The critical temperatures of the films were determined from the minimum of the dχ/dT derivative and are equal to $T_C = 22.7$ K and $T_C = 77.3$ K for **NiFe** and **NiCr** samples. The values of critical temperatures determined for composites are very similar to the values observed for their bulk counterparts and are equal to 23.3 K and 77 K for **NiFe/PVP** and **NiCr/PVP,** respectively. Moreover, all investigated samples show significant hysteretic behaviour between ZFC and FC curves. The bifurcation point (T_{split}), determined based on the difference between $\chi_{FC} - \chi_{ZFC}$, corresponds to the critical temperatures of the studied materials.

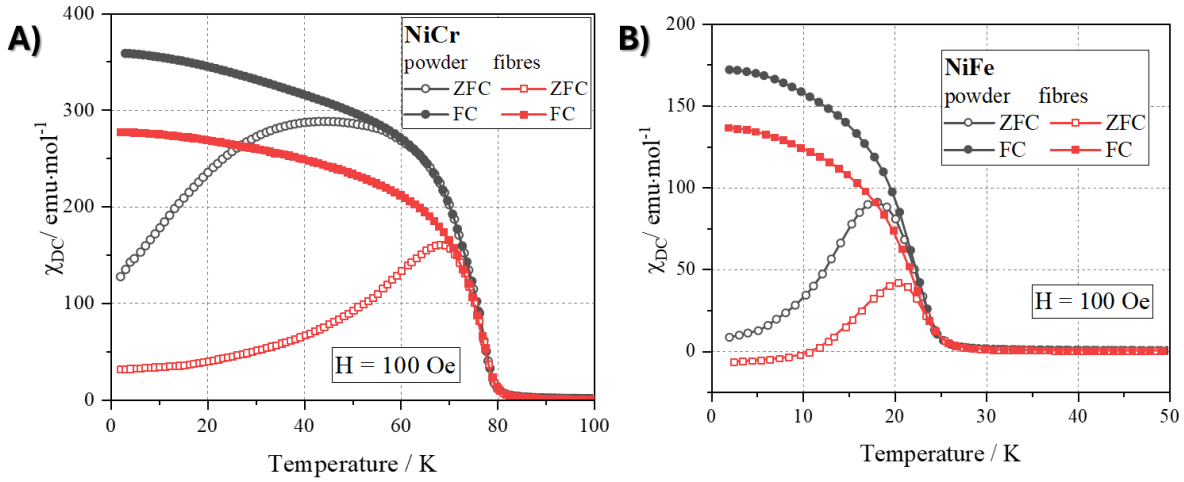

Figure 4.1.13 The comparison of DC magnetic susceptibility curves as a function of temperature for powder samples (black) and fibres (red) for both structures: **NiCr** (left) and **NiFe** (right).

Table 4.1.2 The comparison of parameters collected from M(H) and χ(T) measurements for powder and fibre form of **NiM**.

System	Form	T_C / K	H_C / Oe	M_S / μ_B	calc. wt%	wt% from synthesis
NiCr NPs	powder	77.3	5	~11.3	-	-
$Na_{0.125}Ni_3[Cr(CN)_6]_2 \cdot 10.8H_2O$	fibres	77.0	10.5	-	11.25	11.9
NiFe NPs	powder	22.7	120	~7.8	-	-
$Na_{0.125}Ni_3[Fe(CN)_6]_2 \cdot 11.75H_2O$	fibres	23.3	185	-	10.5	11.0

4.2 Switchable PBAs from $Rb_xMn[Fe(CN)_6]_{(x+2)/3}\cdot nH_2O$ family embedded in electrospun fibres

The second sub-family of Prussian Blue Analogue of interest in the following thesis is $Rb_xMn[Fe(CN)_6]_{(x+2)/3}\cdot nH_2O$ (**RbMnFe**) with intercalated Rb^+ cations in the structure. Among other PBA compounds, it particularly stands out as it is intrinsically highly multifunctional. Depending on the composition and relative proportions of its components, the **RbMnFe** compound can exhibit switchable behaviour driven by metal-to-metal charge transfer, offering promising potential for application in switchable electronic or magnetic devices. Within a certain composition range, **RbMnFe** particles present a change between two electronic configurations in response to external stimuli. This change alters the optical, structural, electrical, and magnetic properties. This switching ability, often accompanied by a hysteretic region, is due to the change of oxidation states between high-temperature (HT) Mn(II) – Fe(III) pairs to low-temperature (LT) Mn(III) – Fe(II) pairs (Figure 4.2.1). The reversible memory effect occurs around room temperatures and spans over a 100 K temperature range[163].

It is important to point out that the switching abilities of **RbMnFe** greatly depend on the composition, especially Rb^+ content. Due to the immense interest in this sub-family of PBAs, the synthesis of NPs has also been investigated to increase compound usability for modern-day technologies. However, several obstacles have been identified, such as large particle size distribution or high solubility of the aqueous media, partially due to the weaker stability of the Mn^{2+} bonding to the cyano-based components, in comparison to other metal ions (e.g., Ni(II)). Additionally, a clear size dependence of the particles on the switching abilities has been derived, with the disappearance of the CT process for particles smaller than 200 nm due to the reduced Rb content[164]. The results presented in the following subsections have been derived from research for which the corresponding manuscript has been submitted and is currently under review[165].

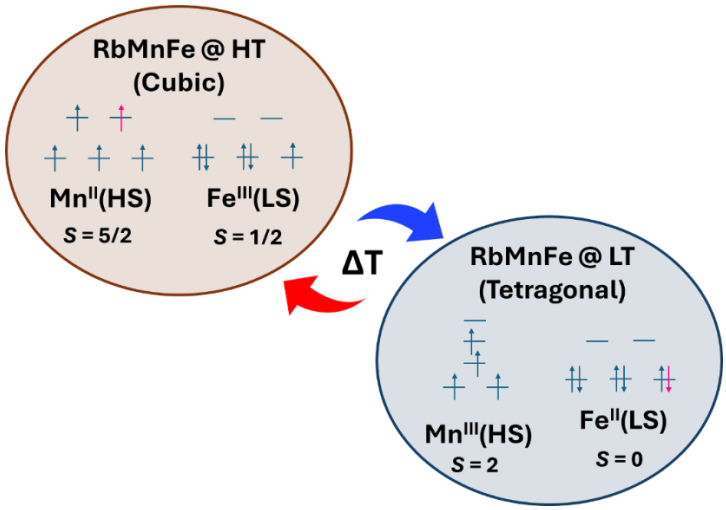

Figure 4.2.1 Schematic representation of CT in RbMnFe compound.

Synthesis of **RbMnFe** sub-microparticles

The synthesis of PBA particles, which exhibit a charge transfer process, was carried out following a literature protocol. This protocol specifically investigated the impact of various synthesis parameters on the final product and its charge transfer properties[164]. In preparations, no stabilizing agent or coating polymer was used. In the initial beaker, 5 mmol (0.604 g) of rubidium chloride was introduced, together with 5 mmol (1.647 g) of potassium hexacyanoferrate(III). They were dissolved in 5 ml H_2O with the use of magnetic stirring. Separately, in the smaller flask, 0.5 mmol (0.099 g) of manganese(II) chloride tetrahydrate salt was weighed and dissolved with magnetic stirring in 5 ml of distilled water. The entire volume of the solution containing Mn^{2+} ions was added drop by drop to the first beaker of the remaining components, and the resulting mixture was subjected to additional magnetic stirring for 5 min at room temperature (20 °C). The final product was separated from the supernatant by centrifugation, which was followed by a cleaning protocol with the use of centrifugation to wash away any residues from the substrates. The resulting brown solid **RbMnFe** was then subjected to air drying at room temperature for 48 hours.

Preparation of **RbMnFe**-based electrospun fibres

The composite material, consisting of electrospun fibres with embedded **RbMnFe** particles, was prepared using the previously described methodology for PBA nanoparticles. PVP was used as the polymer matrix to form the electrospun fibres. Likewise, 43.3 mg of freshly synthesised **RbMnFe** powder was introduced into the bottle and redispersed in 3 ml of methanol. For a high degree of homogeneity of the formed dispersion, the ultrasound homogenizer probe was used for 2 min without pulsation. Then, 0.336 g PVP 360 was introduced to give the electrospinning solution of PVP polymer equal to 12 wt.%. Taking into account the quantities of the components used, the nominal concentration of **RbMnFe** particles in the prepared solution was 11.4 wt.%, disregarding the mass of solvent that evaporates during further fibre preparation. To maintain the dispersion of **RbMnFe** particles and, at the same time, to allow for the slow dissolution of PVP, the mixture was immediately placed onto the gyromixer for approximately 3-4 hours for a complete dissolution of the polymer before performing electrospinning. The prepared electrospinning solution is presented in Figure 4.2.2.

Figure 4.2.2 Photograph of the polymer solution of **RbMnFe**/**PVP**/**MeOH**.

For the electrospinning process, the polymer solution containing incorporated **RbMnFe** particles was loaded into a plastic syringe and electrospun using homemade electrospinning equipment. The flow rate of the polymer solution was controlled by the syringe pump equal to 1.5 ml/h. The electrospinning of PVP was performed at a voltage of 11 kV, at room temperature (~20 °C) with relative humidity ranging from 46-52% RH. The fibre mats were collected on a metallic plate collector randomly, at a constant distance from the tip of the needle to the grounded collector equal to 10.5 cm. For SEM imaging, Raman, and X-ray diffraction characterization, the fibres have been collected straight on the Si(100) wafers of different dimensions, with appropriate amounts of the sputtered composite material.

4.2.1 Morphology of **RbMnFe** particles and their composite fibres

Similarly, as for the previous PBA NPs, SEM imaging was performed on the **RbMnFe** particles, which were specially redispersed and highly diluted in MeOH, and placed by drop casting onto the Si(100) wafer. Following the protocol for the preparation of **RbMnFe** particles presented above, the synthesis resulted in cubically shaped particles (see Figure 4.2.3). Contrary to the previous PBA structures, there is a much more evident disparity in the size of the obtained **RbMnFe** structures[166]. Measured diameters of particles resulted in size dispersions and average particle sizes of 0.666 ± 0.547 μm (length) and 0.431 ± 0.342 μm (width).

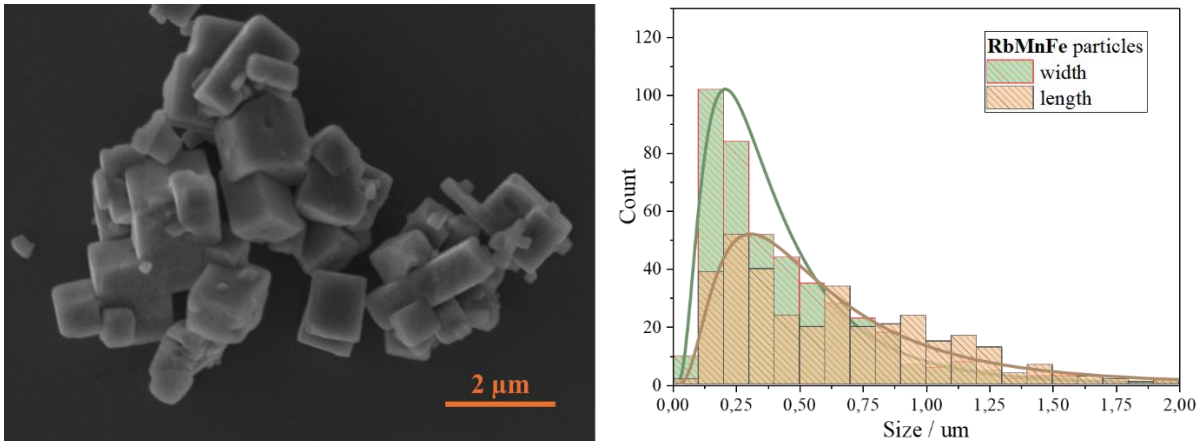

Figure 4.2.3 SEM images of synthesised **RbMnFe** particles (right) with size distribution performed with ImageJ software (left).

The electrospinning process used to prepare PVP-based composites with approximately 11 wt.% incorporated **RbMnFe** particles produced a material with a distinctive pale red-orange colour at room temperature. According to the presumable charge transfer properties of the embedded **RbMnFe** particles, the electrospun mat was immersed in liquid nitrogen (77 K) and immediately photographed with an optical microscope, presented in Figure 4.2.4. During the measurement, the colour change from pale red-orange to pale magenta was noticed, with an instant return to the original colour, as liquid nitrogen evaporated and the sample was reheated to room temperature[154].

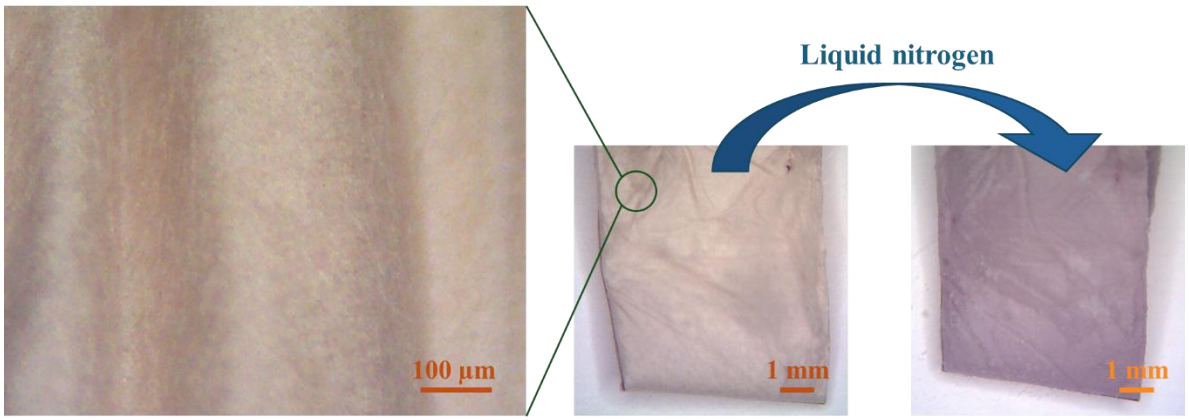

Figure 4.2.4 Photographs of the obtained electrospun mats and the corresponding images under the optical microscope. Freshly electrospun fibre mat imaged at RT (centre) and with magnified region (left; pale red-orange). Electrospun fibre mat imaged after cooling with liquid nitrogen (right; pale magenta).

SEM images of the composite fibres deposited directly on a silicon substrate were recorded at accelerating voltages of 1.0 kV and 20.0 kV, without any additional conducting layer coating, to explore different imaging areas. In particular, the fibre surface was observed at lower voltage, as well as its insides, with the emphasis on the placement of **RbMnFe** particles at higher voltage. Figure 4.2.5 presents the morphology of the fibres, where larger particles (marked with an orange frame) with the characteristic cubical shape or their agglomerations (marked with a green frame) can be easily spotted as they emerge from the polymer matrix region. Although the average size of the synthesized **RbMnFe** particles is more than twice that of the previously reported cubically shaped **NiFe** PBA nanoparticles, no significant fibre breakage was observed. Additionally, in the specified areas (A and B), a thin layer of PVP polymer appears to coat the regularly shaped particles.

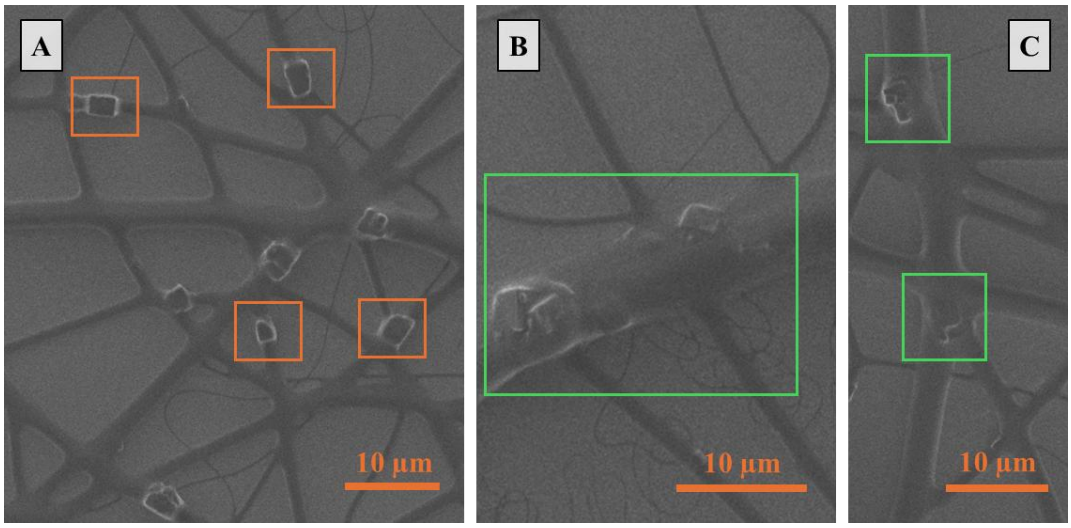

Figure 4.2.5 SEM images at 1.0 kV with embedded larger regularly shaped particles (A) and agglomerated particles (B and C).

Increasing the accelerating voltage to 20.0 kV enhanced the contrast between the organic polymer matrix and the inorganic **RbMnFe** particles, as shown in Figure 4.2.6. Compared to previous images, a significantly greater dispersion of RbMnFe particles within the polymer fibres

is observed, with the particles being notably smaller than the fibres themselves. Bright spots related to PBA particles are embedded in the regions of the fibres, which do not show any notable deformation. The average diameters of the electrospun fibres are measured at 0.728 ± 0.189 µm and 1.086 ± 0.464 µm, at the regions lacking and with the incorporated particles, shown in Figure 4.2.6 with orange and green markings, respectively. Worth noting is the average length of the **RbMnFe** particles equal to 0.713 ± 0.648 µm, which were successfully embedded into the fibre's structure without noticeable expansion of the fibre area, marked as an example with violet marking in Figure 4.2.6.

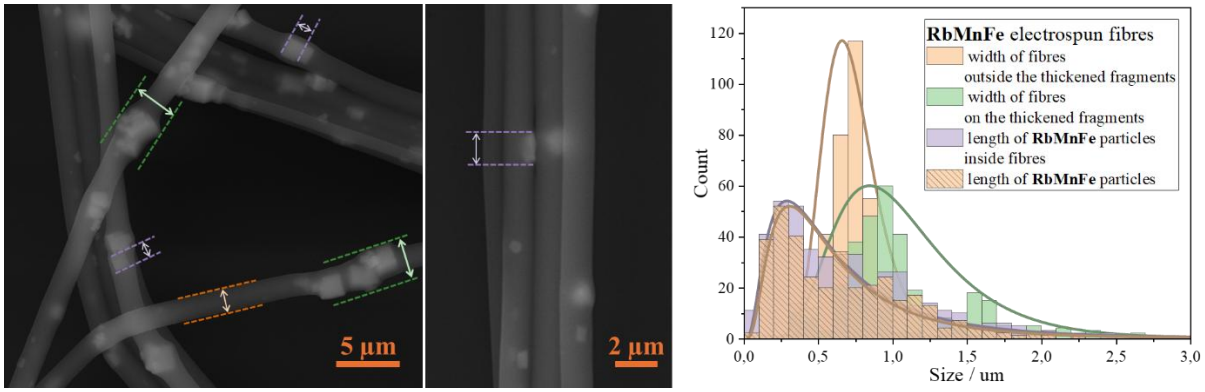

Figure 4.2.6 SEM images of **RbMnFe/PVP** fibres at an accelerating voltage of 20.0 kV with appropriate size distribution of the fibre's width on different areas and the incorporated particles inside fibres, performed with ImageJ software.

To confirm that the brighter spots in the electrospun polymer fibres relate to **RbMnFe** particles, EDS mapping of the individual elements was performed with a TEM equipped with a high-angle annular dark-field detector, as depicted in Figure 4.2.7. The resulting mapped image of Mn (green), Fe (magenta), and Rb (dark blue) agrees with assumptions that the bright spots inside fibres come from **RbMnFe** particles. In particular, a signal derived from rubidium atoms depicts the shape of embedded NPs, whereas, for manganese and iron, it is more blurred with several more intensive sites. Similarly to previously described PBA NPs, the regions rich in Fe, Mn, and Rb are also characterized by carbon (yellow) content. This aligns with observations from Figure 4.2.5, indicating that the polymer fibres maintain their integrity even in regions with a high concentration of nanoparticles.

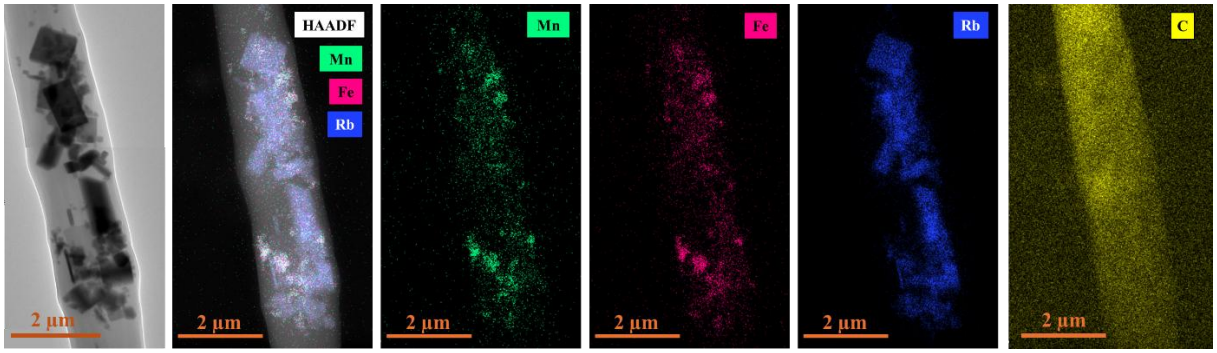

Figure 4.2.7 TEM image and EDS mapping of the composite fibre. Elements mapped: manganese (green), iron (magenta), rubidium (blue), and carbon (yellow).

4.2.2 Spectroscopic and structural characterisation

To verify the purity of the obtained **RbMnFe** bulk sample, infrared and Raman spectroscopies were conducted, with the results presented in Figure 4.2.8. In both methods, CN stretching vibrations of Fe−C≡N−Mn have been detected. For non-invasive IR, two bands appear, sharp and intensive at 2152 cm^{-1} and much broader and less intensive, centred at 2091 cm^{-1}. As the measurement was performed at room temperature, the recorded bands correlate to the following oxidation states of the metal ions: the former one to Fe(III)Mn(II), and the latter to Fe(II)Mn(II) impurity[164]. Regarding Raman spectra, a double band has been recorded at 2157 and 2166 cm^{-1} related to the high-temperature phase Fe(III)Mn(II). These observations are consistent with the literature[167,168].

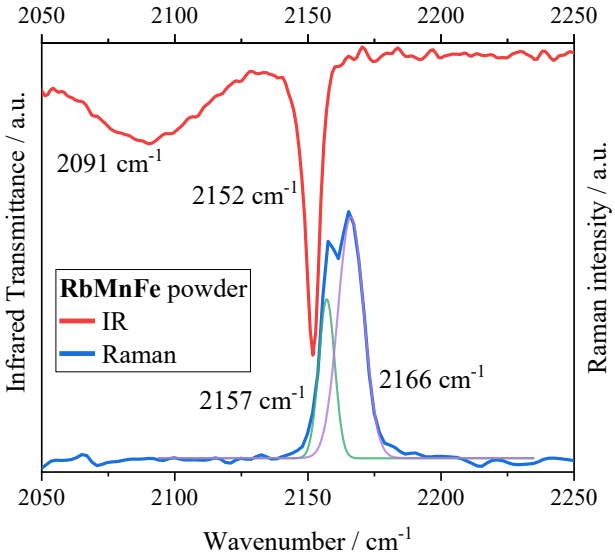

Figure 4.2.8 The comparison of IR (red) and Raman (blue) spectra in the ν(CN) region in the **RbMnFe** bulk sample.

To ensure that during the measurement of Raman spectra for composites the laser was pointing at the region with embedded **RbMnFe** particles, the image was taken with 50x magnification as presented in Figure 4.2.9A. As the particles themselves were brownish and the **PVP**-based fibres were transparent, the borders of individual **RbMnFe** particles or clusters could be spotted. In the spectra of composite fibres, two intensive bands related to CN stretching vibrations are apparent for bulk **RbMnFe** powder. Additionally, two weak CN stretching bands appear centred at 2080 cm^{-1} and 2120 cm^{-1}. According to the literature, they can be assigned to Fe(II)Mn(II) and Fe(II)Mn(III), respectively[168]. For the latter assignment, it shows the electronic configuration of metal centres in the low-temperature phase, however, the measurement for fibres was performed at 297 K, without prior irradiation. Their appearance may be due to the resonance effects caused by 532 nm excitation[168,169].

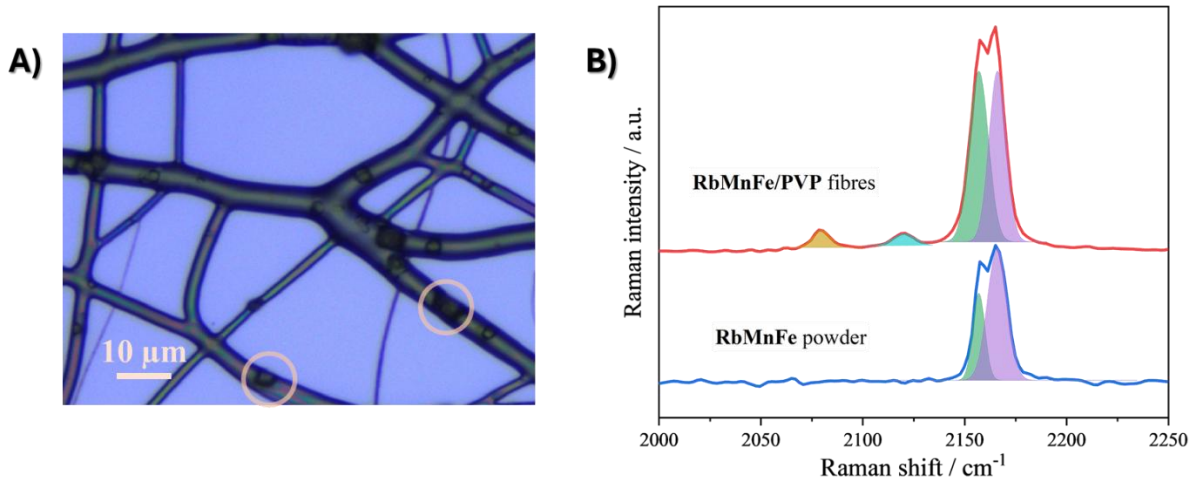

Figure 4.2.9 A) Photograph from the microscope attached to the Raman spectrometer. B) The comparison of Raman spectra in the ν(CN) region for composite fibres of **RbMnFe/PVP** and **RbMnFe** bulk sample.

Rubidium manganese hexacyanoferrate materials undergo charge transfer phase transitions between a high-temperature (HT) cubic phase, Mn^{II}(S = 5/2) – Fe^{III}(S = 1/2), and a low-temperature (LT) tetragonal phase, Mn^{III}(S = 2) – Fe^{II}(S = 0). These transitions are marked by significant thermal hysteresis. A Landau theory study revealed that the transition is driven by the coupling of CT instability with volume strain and the ferroelastic cubic-to-tetragonal phase change linked to the Jahn–Teller distortion around Mn^{III} sites[43].

Crystallographic analysis of synthesised **RbMnFe** powder measured at 300 K and 150 K showed significant lattice changes from the HT cubic phase to the LT tetragonal phase, consistent with the previous reports for bulk materials[170]. The structural parameters are summarised in Table 4.2.1 and diffraction patterns with Le Bail fit are presented in Figure 4.2.10, together with the visualisation of **RbMnFe** structures at both temperatures, showcasing intercalated Rb ions, which preferentially occupy one Wyckoff locations in both cubic and tetragonal structures.

Table 4.2.1 Summarised crystal structure parameters obtained from Le Bail fit for **RbMnFe** powder measured at two temperatures: 300 K and 150 K.

RbMnFe powder	**Cubic (HT)**	**Tetragonal (LT)**
Temperature / K	300	150
Space group	*F-43m*	*I-42m*
a / Å	10.5683(4)	7.0761(5)
b / Å	10.5683(4)	7.0761(5)
c / Å	10.5683(4)	10.5211(9)
Volume / Å^3	1180.37(7)	1180.37(7)

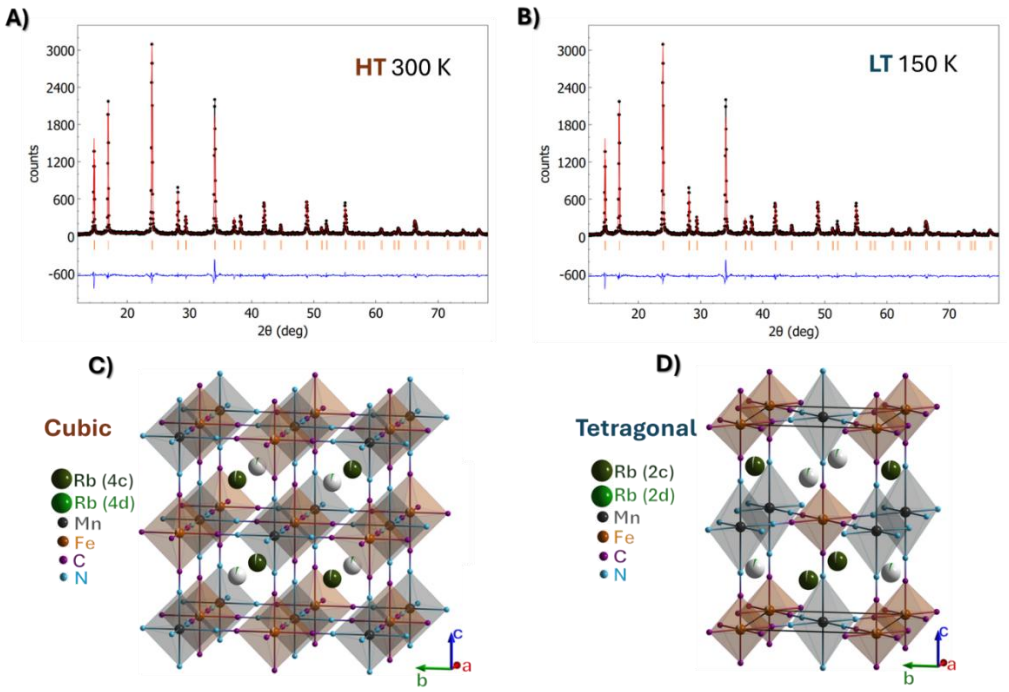

Figure 4.2.10 X-ray diffraction data and structure visualisation of **RbMnFe** bulk in HT cubic phase (A, C) and LT tetragonal phase (B, D) measured at RT and 150 K, respectively.

The X-ray diffraction measurement performed at room temperature on the composite electrospun fibres has been presented in Figure 4.2.11A, with superimposed data of the **RbMnFe** bulk sample together with pure **PVP** fibres. Similarly to **NiFe/NiCr** PBA composites reported in the previous subsection, the data collected for composite fibres consist of sharp peaks derived from the crystalline coordination structure of **RbMnFe** and the broad peaks of low intensity characteristic of the amorphous structure of **PVP** polymer. Fitting of the recorded peaks derived from the PBA structure of the composite fibres with the LeBail method (Figure 4.2.11B) showed a 0.06% decrease in the cell parameters to $a = b = c = 10.5612(2)$ Å, compared to the powdered sample. In the case of the **PVP** matrix-derived peaks, their position changes into 2θ equal to 11.16° and 21.29° (for the pure **PVP** fibres, their position are 11.06° and 21.34°, respectively).

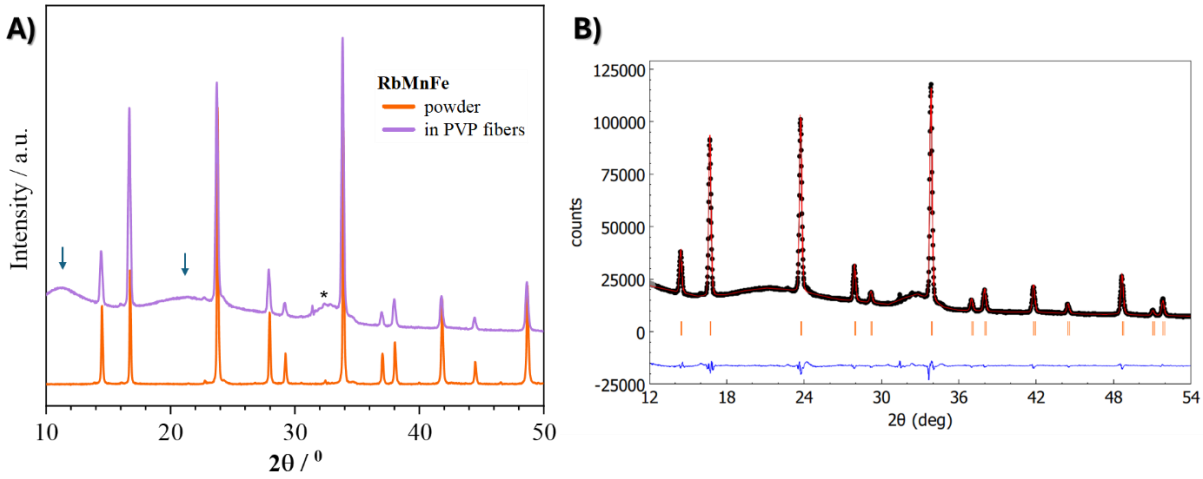

Figure 4.2.11 (A) The comparison of the XRD patterns of bulk **RbMnFe** NPs and their composite material, measured at RT. (B) The black circles are the experimental data of **RbMnFe/PVP** composite, and the red curve is the profile calculated using the Le Bail method.

4.2.3 Magnetic properties of **RbMnFe** cubes embedded into polymer fibres

The magnetic characterization of **RbMnFe** samples and their composites was based on two types of measurements. The dependence of magnetization as a function of external magnetic field in ± 5 kOe was performed at the temperature of T = 2 K. The dependence of magnetic susceptibility as a function of temperature was recorded at the applied field of 1 kOe in the 2-320 K range, with more detailed observations of charge transfer effect above 150 K.

Similar to the previous PBA composite examples, the magnetization measurements as a function of the magnetic field of **RbMnFe** composite fibres were compared qualitatively and employed to establish the real concentration of embedded particles in the fibres. The recorded dependence of magnetization on the magnetic field (Figure 4.2.12) for the powdered sample of **RbMnFe** follows the behaviour presented in the literature[61], without much difference. In comparison to the embedded particles, wider hysteresis appears for the composite material with the coercive field equal to 150 Oe, whereas for the powdered sample, it is 107 Oe. At the maximal applied field of 5 kOe, the magnetisation curve for the pure **RbMnFe** sample reaches the value of 2.93 μ_B. This quantity is much lower than the expected 4 μ_B but consistent with previously published data[163].

The percentage of the number of magnetic particles in the measured composite fibre mat sample has been extracted by matching the values of magnetization of the composites to the values of the powdered compound. The calculated value equals 11.5%, which is not far from the initial concentration of 11.4%, which was set during the preparation of the material. For the rest of the magnetic characterization of composite fibres with embedded **RbMnFe** particles, this calculated concentration was taken into account.

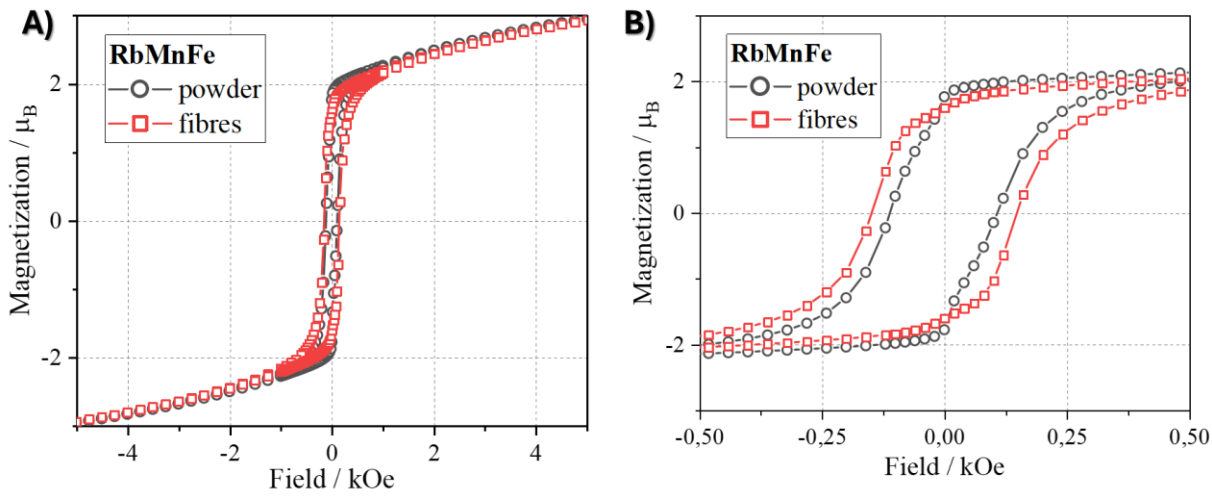

Figure 4.2.12 The comparison of magnetisation curves for **RbMnFe** in the form of the powder and composite fibres at a constant temperature of 2 K.

For the **RbMnFe** PBA, high-temperature measurements were of particular interest as they revealed a charge transfer effect accompanied by changes in the oxidation states of Mn and Fe in response to temperature variations. The magnetic susceptibility as a function of temperature is presented in Figure 4.2.13A, covering the entire recorded temperature range of 2 to 340 K. While decreasing the temperature, the magnetic susceptibility rises below 12 K for both powder and composite fibres, confirming the presence of ferromagnetic ordering in the lowest temperature range. On the other end of the curve presented on the enlarged fragment in Figure 4.2.13B, above 150 K, thermal hysteresis appears, originating from the charge transfer process, in the approximately similar temperature range for the powdered sample and after embedment in organic fibres. For the high temperature measurements, the paramagnetic contribution originating from the organic matrix has a far greater impact on the experimental data, which is observed with a higher inclination of the magnetic susceptibility curve for the composite fibre, as observed in Figure 4.2.13B.

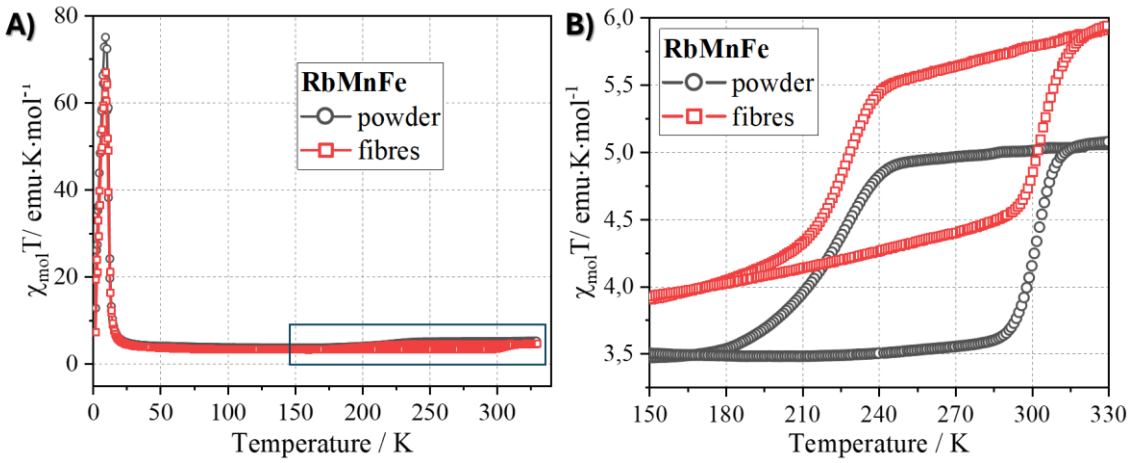

Figure 4.2.13 A) The comparison of DC magnetic susceptibility curves as a function of temperature for powder sample (black) and fibres (red) of **RbMnFe** measured at a constant external field of 1kOe with a 2 K/min sweeping rate. B) The enlargement of the high temperature range with thermal hysteresis originated from the charge transfer process.

To extract the magnetic signal of embedded NPs, the obtained data have been corrected experimentally using a Curie-Weiss law, according to the equation (6):

$$\chi = \frac{C}{(T-\theta)} + \chi_{\text{redisual}}\,, \tag{6}$$

where C is the Curie constant, θ is the Weiss constant, and χ_{residual} is the magnetic susceptibility of the residual temperature-independent paramagnetism. In practice, the residual corrections were performed by fitting the linear part on the $\chi(T^{-1})$ plots and subtracting the intercept values from the original magnetic moment data (see Figure 4.2.14A)[171]. The correction has been fitted on the linear fragment of the original data in the temperature range of 150-285 K. The corrected data of magnetic susceptibility as a function of temperature in the range 150-330 K is presented in Figure 4.2.14B.

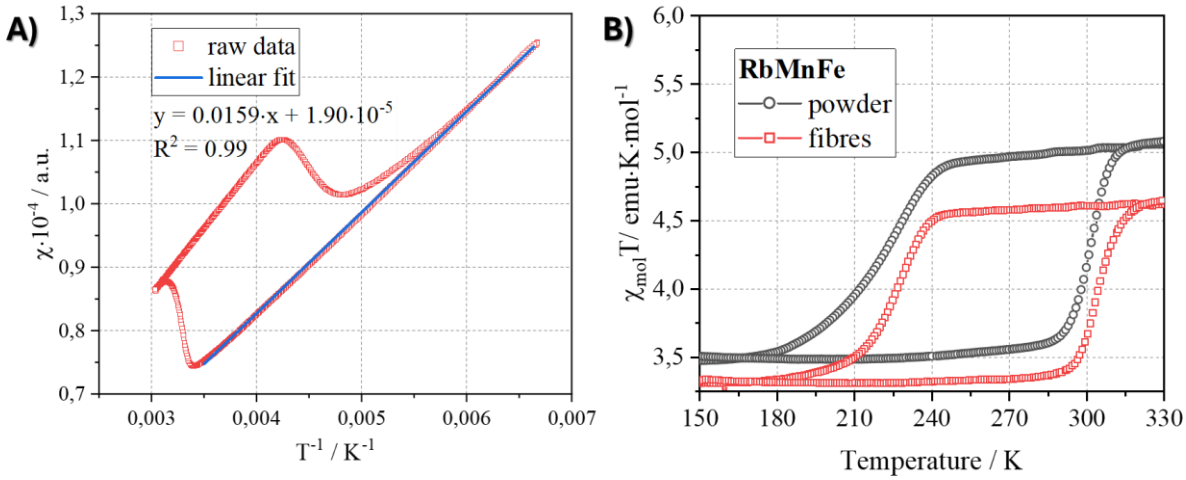

Figure 4.2.14 A) Plot of the magnetic susceptibility as a function of inverse temperature, with marked fitting area of the residual temperature-independent paramagnetism correction of **RbMnFe** composite fibres. B) The comparison of DC magnetic susceptibility curves as a function of temperature for powder sample (black) and fibres (red) of **RbMnFe** after employing the correction for the composite sample.

The transition temperatures extracted from the 1st derivative of the presented data for the powder sample and its relevant composite are only slightly different, with $T_{1/2}(\downarrow)$ and $T_{1/2}(\uparrow)$ equal to 228.8 K and 303.2 K for powder and 227.4 K and 302.3 K in the case of fibres. Therefore, the width of thermal hysteresis of the charge transfer process in **RbMnFe** changes from 74.4 K for loose powder to 74.9 K after embedment in the polymer fibre matrix. The values of $\chi_{\text{mol}}T$ recorded for high-temperature phase (at 320 K) and low-temperature phase (at 165 K) corresponding metal oxidation states of Mn(II) – Fe(III) and Mn(III) – Fe(II), respectively, have been presented in Table 4.2.2 together with other parameters collected from magnetic measurements. The discrepancies in magnetic susceptibility values between bulk and composite samples are especially apparent in the high-temperature phase derived from the applied correction to the composite sample.

Table 4.2.2 The comparison of parameters collected from $M(H)$ and $\chi T(T)$ measurements for powder and fibre form of **RbMnFe**.

Parameters	**RbMnFe** powder	**RbMnFe/PVP** fibres
H_C / Oe	107	150
M_S / μ_B	2.93	-
Calc. % (synthetic %)	-	11.5% (11.4%)
M_{rem} / μ_B	1.77	1.60
T_C / K	11.5	11.4
Thermal hysteresis ($T_{1/2}(\downarrow)$ to $T_{1/2}(\uparrow)$) / K	228.8 – 303.2	227.4 – 302.3
Width of thermal hysteresis / K	74.4	74.9
$\chi_{mol}T$ for HT phase (at 320 K) / emu·K·mol^{-1}	5.0	4.6
$\chi_{mol}T$ for LT phase (at 165 K) / emu·K·mol^{-1}	3.5	3.3

4.3 Summary of the chapter

In conclusion, this chapter focused on the preparation of composite materials consisting of PBA particles embedded within an organic polymer matrix in the form of electrospun fibres. The results presented in both sections demonstrate that pre-synthesized, cubically shaped PBA particles with varying compositions can be successfully incorporated into the polymer matrix without significantly altering their intrinsic structural or functional properties.

The electrospun composite fibres were examined using electron microscopy, allowing a detailed visualization of their structures. In comparison to other composites based on the soft matrix (such as chitosan or alginate matrix) independently of the NPs size, the electrospinning process does not lead to the NPs being attached to the organic polymer fibres on the surface, but rather results in fillers incorporated inside the matrix. The tendency of NPs to aggregate cannot be omitted; however, the limited diameter of the fibres minimizes this effect. Additionally, the initial concentration of NPs (10-11.5%) has no negative impact on the structure of fibres, as they do not seem to be much severed, and the materials on the macroscopic scale present themselves as 3D elastic materials, which can be easily modulated.

Further material characterization based on spectroscopic and diffraction methods showed no significant changes in the structure of the chosen PBA NPs as a result of the preparation process, where high voltage was used for fibre production. These observations were then complemented with SQUID magnetometry, providing insight into the magnetic properties of the fibres, without any additional steps taken in preparation for measurement of the composite samples. Based on low-temperature measurements of the field dependence of magnetisation, the NPs concentration in electrospun fibres has been calculated, providing values under assumed initial concentrations, without any major influence of the nanoparticle size. Additionally, for composite fibres with **RbMnFe** NPs, the methodology for extracting magnetic signals at high temperatures has been applied.

5. FeTrz SCO nanoparticles – spectroscopic studies and their composites

This chapter focuses on a one-dimensional (1D) coordination polymer based on iron centres, specifically $[Fe(Htrz)_2(trz)](BF_4)$ (where Htrz = 1,2,4-1H-triazole) (**FeTrz**), synthesized in the form of nanoparticles. This compound represents a stable example of a material exhibiting a thermally induced spin-crossover (SCO) transition at iron centres, occurring above room temperature. The chapter is divided into three main sections: (i) the preparation of the nanoparticles of desired dimensions, (ii) the investigation of size-dependent SCO effect on their spectroscopic and magnetic properties, and (iii) a comparative analysis of their behaviour when incorporated into an organic polymer matrix, either as electrospun fibres or drop-cast films.

Among the extensively studied SCO materials, **FeTrz** stands out as a particularly notable example due to its robust and wide thermal hysteresis near room temperature. A key advantage of this material is its ability to be synthesized as nanoparticles with precisely controlled diameters, while still preserving its characteristic memory effect. The motivation for in-depth studies of **FeTrz** nanoparticles stems from their strong potential for use in advanced SCO-based applications, including sensors, memory devices, and actuators. Investigating their structural, magnetic, and electronic properties offers valuable insights into how particle size, surface effects, and interparticle interactions influence SCO behaviour. Furthermore, a detailed understanding of the interplay between high-spin (HS) and low-spin (LS) states, along with the efficiency and reversibility of the SCO transition, is essential for optimising both the performance and long-term stability of these materials in practical applications.

5.1 Reverse micelle technique for the synthesis of nanoparticles

Nanoparticles of the **FeTrz** system were synthesized using a reverse micelle technique, following a previously reported protocol[172]. This method has been widely adopted in the synthesis of coordination compounds with well-defined nanoscale dimensions. In studies focused on developing reproducible synthetic procedures for the preparation of such nano-sized coordination structures, the reverse micelle approach has proven particularly effective for a range of materials, including FeTrz-based systems[76,173,174]. In general, it involves the formation of nanostructures through the interaction of the aqueous and organic phases. The process commenced with the formation of micelles, where the aqueous components are confined within a spherical structure formed by the organic surfactant in the organic phase. When the micelles containing separately a metal precursor and a ligand come into contact with each other, they react within the confinement of the micelles, which acts as nanoreactors[175,176] (shown schematically in Figure 5.1.1).

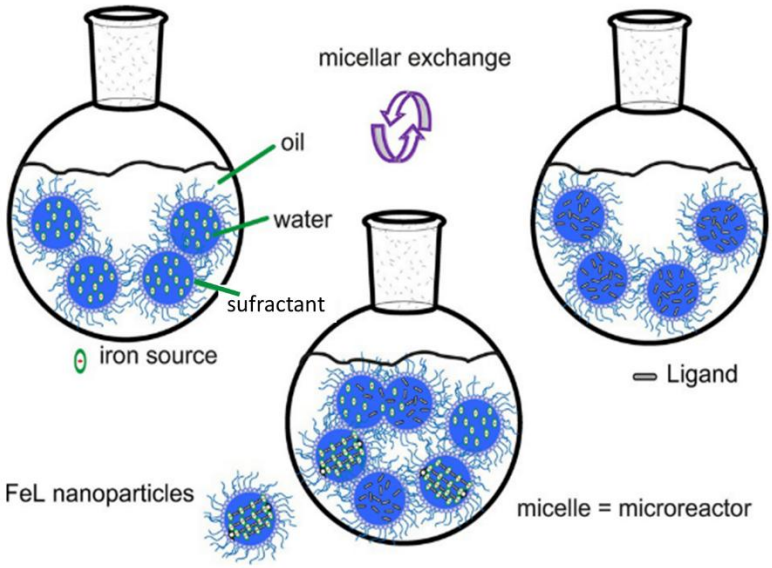

Figure 5.1.1 Schematic representation of reverse-micelle reaction[177].

For the formation of **FeTrz** NPs, an appropriate amount of metal precursor ($Fe(BF_4)_2 \cdot 6H_2O$) and ligand (Htrz) have been dissolved in separate vials in water, with the addition of tetraethyl orthosilicate (TEOS), forming the aqueous phases. Concurrently, a mixture of cyclohexane with Triton X-100 (surfactant) and *n*-hexanol (co-surfactant) constituted the organic phase. The detailed information on the proportion of the used reagents has been summarized in Table 5.1.1. The formation of nanoparticles encapsulated in a silica shell (NPs@SiO_2) with different sizes has been achieved by varying the ratios of the precursors (metal and ligand species; surfactant amounts) and the volume ratio of the aqueous phase to the organic phase. Additionally, adjusting the stirring time during the micelles formation and at the course of the reaction allowed for precise control over the size and morphology of the nanoparticles, which was shown to be critical for tailoring their SCO properties.

Table 5.1.1 Experimental conditions for the preparation of nanoparticles.

Nanoparticles/ sub-micro particles preparation	**FeTrz-1**	**FeTrz-2**	**FeTrz-3**	**FeTrz-4**
	Aqueous phase			
H_2O amount for micelle formation	0.5 ml	0.5 ml	0.5 ml	1 ml
$Fe(BF_4)_2 \cdot 6H_2O$	253 mg	210 mg	180 mg	180 mg
1,2,4-1*H*-triazole ligand	156 mg	130 mg	110 mg	110 mg
tetraethyl orthosilicate (TEOS)	0.1 ml	0.1 ml	0.1 ml	0.1 ml
	Organic phase			
Cyclohexane	7.5 ml	7.5 ml	7.5 ml	15 ml
n-hexanol	2.7 ml	1.8 ml	1.8 ml	3.6 ml
Trition X-100	2.7 ml	1.8 ml	1.8 ml	3.6 ml
	Synthesis time			
	2 h	12 h	48 h	48 h

Morphology of **FeTrz** nano- and microparticles

The morphology and average size of the synthesized nanoparticles were analysed using SEM and TEM techniques. Due to the nanoscale size of the **FeTrz-1/2/3** particles, TEM imaging was performed using a high-angle annular dark-field (HAADF) detector, while **FeTrz-4** particles were easily observable using SEM. The resulting particle images are shown in Figure 5.1.2, with energy-dispersive X-ray spectroscopy (EDS) analysis conducted on the first three types of particles. From the TEM images, well-defined rod-like particles can be clearly distinguished, with their characteristics becoming more pronounced as the particle size increases, particularly in terms of length. This size-dependent morphology is a characteristic feature of this family of compounds[64]. Additionally, the use of a silica shell, introduced during the synthesis to limit particle growth, is evident in the EDS maps, where the presence of silicon (Si) and oxygen (O) is observed at the particle boundaries, particularly for **FeTrz-1** and **FeTrz-2**.

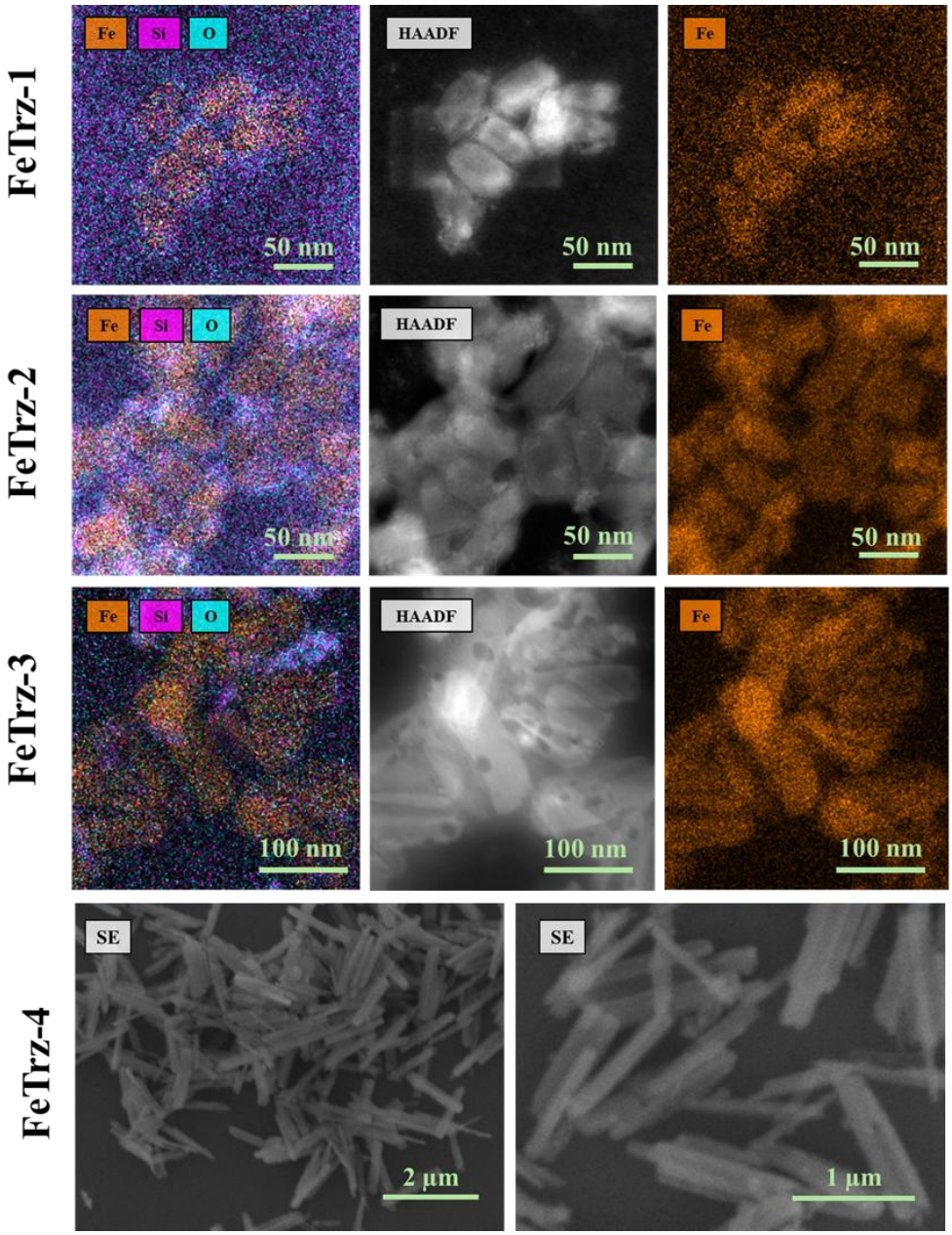

Figure 5.1.2 TEM and EDS imaging of **FeTrz-1/2/3** with SEM images of **FeTrz-4**.

The analysis of diameters of synthesised **FeTrz** particles performed with ImageJ software resulted in histograms presented in Figure 5.1.3. As expected, from **FeTrz-1** up to **FeTrz-4**, the differences in length and width of particles become more apparent, with the overall increase of particle size, what has been summarised in Table 5.1.2. For the smallest obtained particles, **FeTrz-1**, no difference between length and width was made, as the difference between them was negligible, and so their average diameter may be slightly overstated. Interestingly, for **FeTrz-2** and **FeTrz-3,** although the average length of particles doubles, the width-to-length ratio does not change much, compared to **FeTrz-4**. The observable changes in particles' length and width confirm that with the used synthetic protocol, particles of desired dimensions can be prepared by diversifying the amounts of precursors and the time of synthesis.

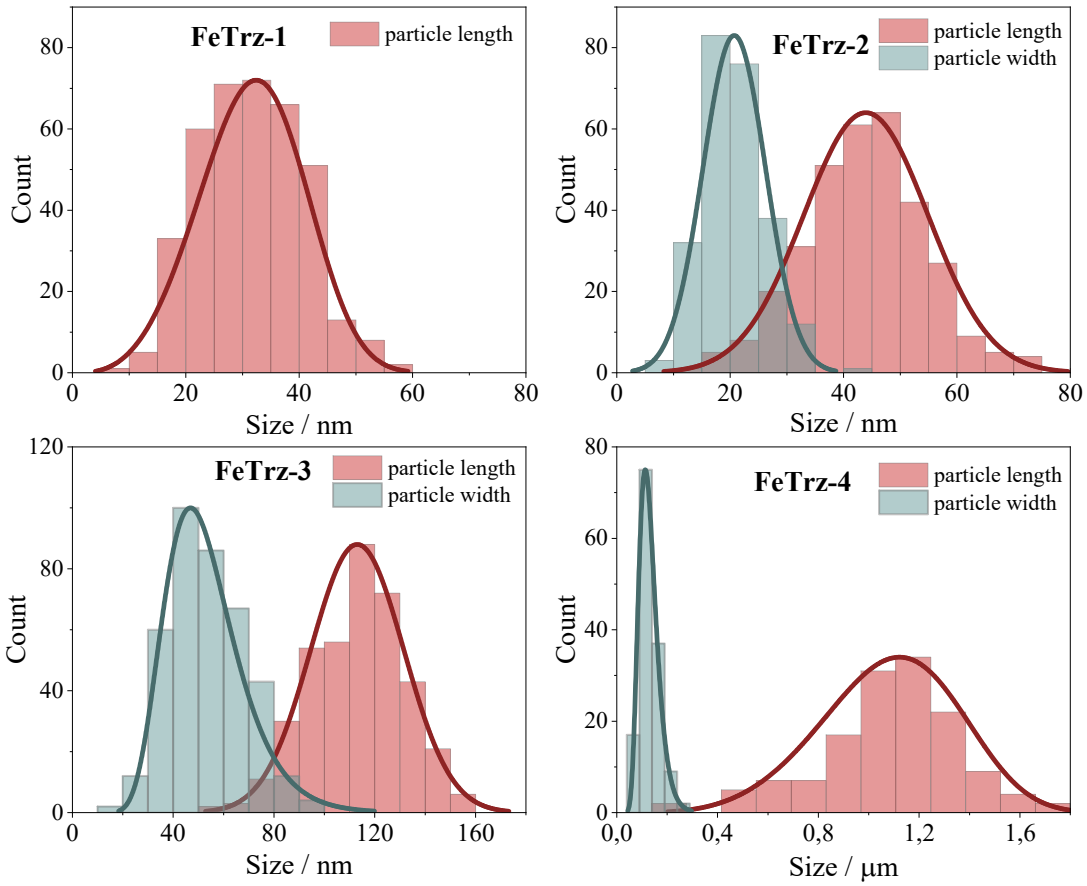

Figure 5.1.3 Histograms of **FeTrz-1/2/3/4** prepared based on TEM and SEM image analysis with ImageJ software.

Table 5.1.2 Summarised dimensions of synthesised **FeTrz** particles.

Parameter	**FeTrz-1**	**FeTrz-2**	**FeTrz-3**	**FeTrz-4**
length	37.6 ± 7.3 nm	44.0 ± 12.1 nm	119.6 ± 16.9 nm	1.095 ± 0.368 µm
width	-	20.7 ± 5.8 nm	53.1 ± 15.7 nm	129 ± 39 nm
width to length ratio	~ 1	0.48	0.44	0.12

5.2 SCO effect for nano- and microparticles – correlation of spectroscopic and magnetic properties

5.2.1 Magnetic properties and structural analysis of **FeTrz** nano- and microparticles

The thermal dependence of χT for the four samples is depicted in Figure 5.2.1. In all cases, thermal spin transitions are characterized by $T_{1/2}(\uparrow)$ and $T_{1/2}(\downarrow)$, which are defined as the temperatures for which 50% of both the LS and HS iron centres are present in the sample for the heating and cooling modes, respectively. Finally, ΔT represents the hysteresis width in all the spin transitions. The microcrystalline sample **FeTrz-4** exhibits an abrupt spin transition centred above room temperature with a large hysteresis of 38 K ($T_{1/2}(\uparrow)$ = 391 K and $T_{1/2}(\downarrow)$ = 353 K). Notably, the χT value at 300 K is equal to 0.59 emu·K·mol^{-1}, which is slightly higher than the typical range observed for Fe(II) in its singlet state (0.30–0.50 emu·K·mol^{-1}). With the reduction of particle size, the thermal hysteresis is shifted to the lower temperatures, and for the smallest NP sizes (**FeTrz-1** and **-2**), the χT value at 300 K is significantly higher than for **FeTrz-3** and **-4** and reaches values of about 0.9 emu·K·mol^{-1} (summarised parameters in Table 5.2.1). This anomalously high χT value has been previously reported for nanoparticles and is attributed to the presence of terminal Fe(II) complexes that remain in the high-spin (HS) state. Coronado et al.[178] have documented a similar phenomenon, observing that approximately 20% of the Fe(II) population remains in the HS state even when the material is expected to be in the low-spin (LS) configuration. This effect is likely due to the high surface area of the nanoparticles, which can lead to the incomplete coordination of Fe atoms, thereby stabilizing the HS state. A comparable effect has been reported by Tissot et al.[179] in their studies on confined spin-crossover (SCO) complexes. In their case, a fraction of Fe ions (around 20-25%) remained trapped in the HS state regardless of temperature. This behaviour is commonly observed in SCO solids with poor crystallinity, where structural disorder can hinder the complete transition to the LS state.

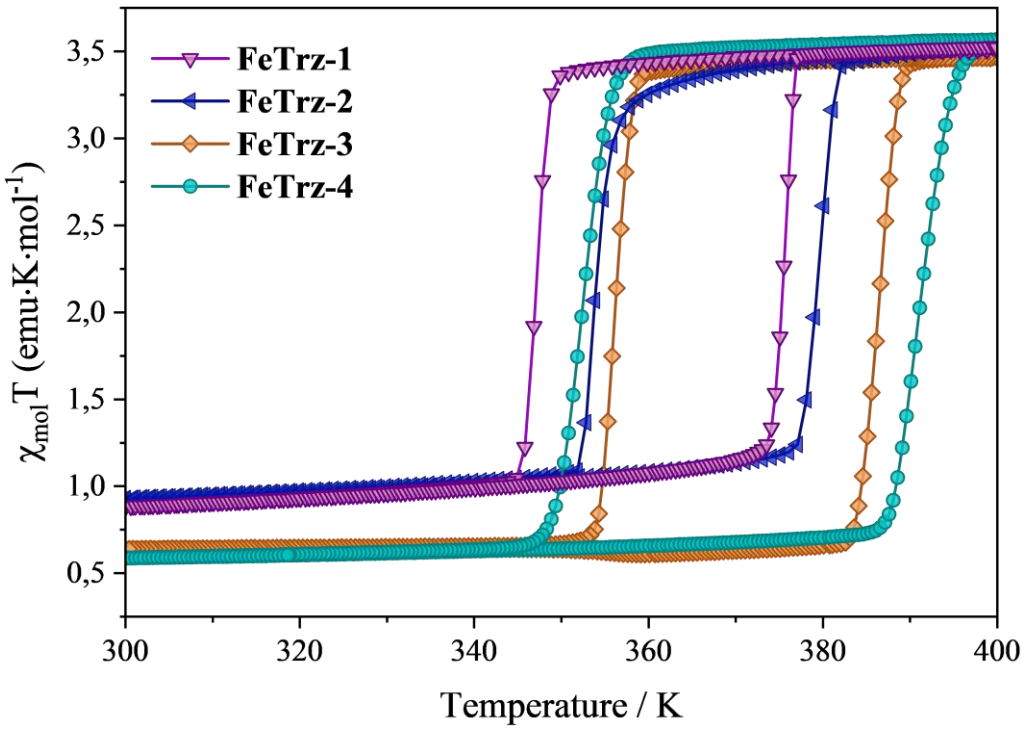

Figure 5.2.1 Magnetic susceptibility for nano- and microparticles of **FeTrz-1** to **-4**.

Table 5.2.1 Summarised parameters derived from magnetic susceptibility measurements for **FeTrz** nano- and microparticles.

Parameter	**FeTrz-1**	**FeTrz-2**	**FeTrz-3**	**FeTrz-4**
$T_{1/2}(\uparrow)$ / K	376	380	386	391
$T_{1/2}(\downarrow)$ / K	347	354	356	353
Thermal hysteresis width / K	28	26	30	38
$\chi_{mol}T$@300 K / emu·K·mol^{-1}	0.88	0.93	0.63	0.59
$\chi_{mol}T$@400 K / emu·K·mol^{-1}	3.52	3.53	3.46	3.57

Powder XRD patterns were recorded for the powder samples **FeTrz-1 – FeTrz-4** at room temperature and 400 K to analyse the changes in structure upon the SCO transition. The results are shown in Figure 5.2.2. For all studied materials, there is a volume expansion in transitioning from the low to high spin state, with corresponding shifts in diffraction peaks. However, only the microcrystalline sample **FeTrz-4** exhibits sharp reflections, while nanoparticle samples show peak broadening due to the small sizes of the crystallites.

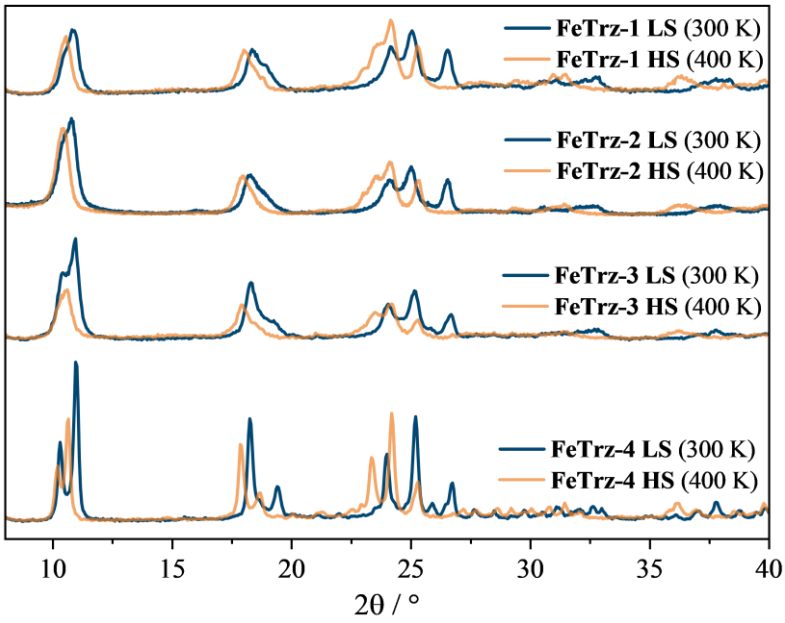

Figure 5.2.2 Powder XRD patterns of the complexes **FeTrz-1** – **4** in the 8-40° 2θ range.

The crystal structures of compound **FeTrz-4** were determined and refined at two distinct temperatures: 400 K, where the sample appears white and is in the HS state, and room temperature (300 K), where the sample appears pink and is in the LS state. The resulting X-ray diffraction patterns are of high quality (Figure 5.2.3), and the structural determination and refinement are reliable (Table 5.2.2), showing excellent agreement with previously published data[180,181].

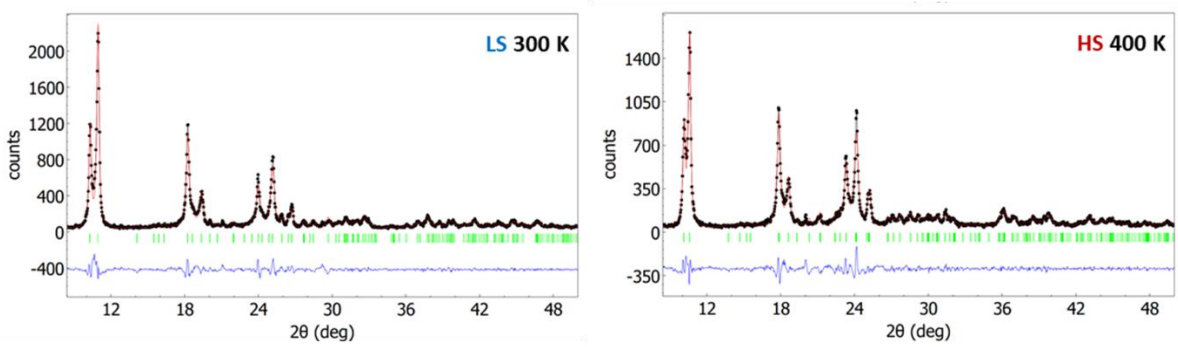

Figure 5.2.3 Experimental (black circles) and calculated (red line) diffraction patterns and the difference profile (blue line) of **FeTrz-4** in the LS state at room temperature (left) and in the HS state at 400 K (right).

Table 5.2.2 Summarised crystal structure parameters of **FeTrz-4** at two temperatures: 300 K and 400 K.

FeTrz-4	**Low spin**	**High spin**
Temperature / K	300	400
Space group	*Pnma*	*Pnma*
a / Å	17.215(2)	17.498(3)
b / Å	7.332(2)	7.805(3)
c / Å	9.178(1)	9.538(1)

In the structure of $[Fe(Htrz)_2(trz)](BF_4)$, the triazole ligands coordinate with the central iron (Fe^{2+}) ions. Symmetry operations result in the alignment of Fe^{2+} centres along the *b*-axis, connected through three bridging triazole ligands in alternating inverted positions (Figure 5.2.4). The triazole ligands generate ligand-field strengths around the Fe^{2+} ions that are sufficient to induce spin-crossover (SCO) behaviour. Additionally, these ligands offer chemical flexibility while maintaining the one-dimensional (1D) coordination chains of Fe^{2+} through triple N1,N2-bridged triazoles. The triazole-based system is characterized by its short, rigid, and strain-free structure, which contributes significantly to the stability of these 1D Fe^{2+} SCO systems in both their low-spin and high-spin states. This structural robustness underscores the unique suitability of triazole ligands for achieving stable SCO behaviour.

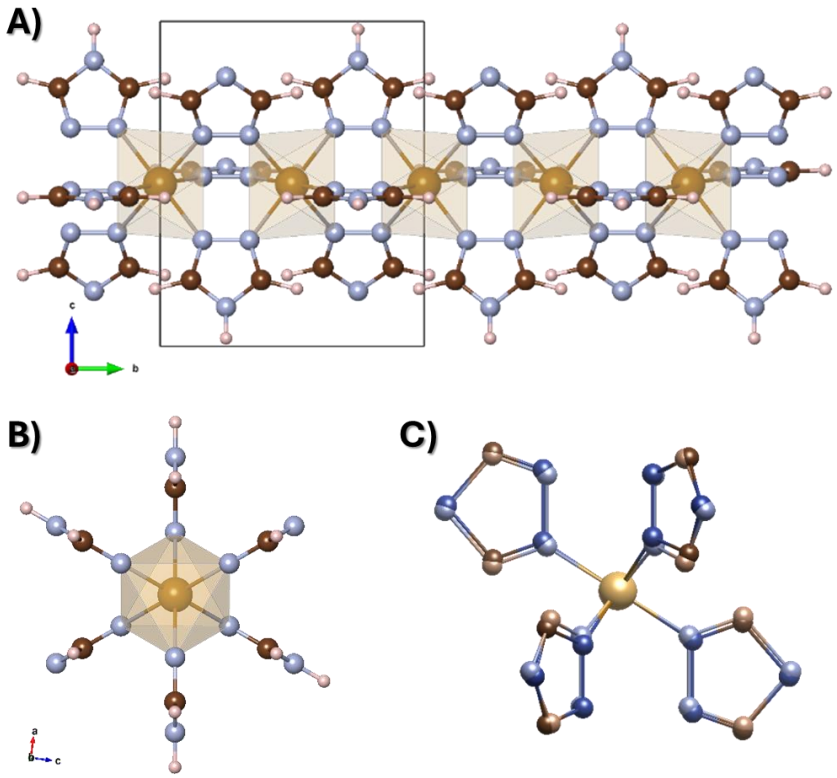

Figure 5.2.4 View of a segment of the [Fe(Htrz)2(trz)](BF4) chain along *a* (A) and *b* (B) axes with superimposed LS and HS structures within one Fe centre and the neighbouring triazole ligands (C).

5.2.2 Mössbauer spectroscopy

Mossbauer spectra of iron-containing solids provide information on the valence and electronic configuration of the iron ion, but also inform us of fine structural details for the sample under study. For Mossbauer spectroscopy measurement, two samples were selected, **FeTrz-1** and **FeTrz-4,** as these of the most significant size differences. The Mossbauer spectra were collected for both samples in the broad temperature range upon heating and cooling to obtain information about the changes in the spin state of iron. The results obtained for sample **FeTrz-1** are presented in Figure 5.2.5, and for **FeTrz-4** in Figure 5.2.6.

nanoparticles (**FeTrz-1**)

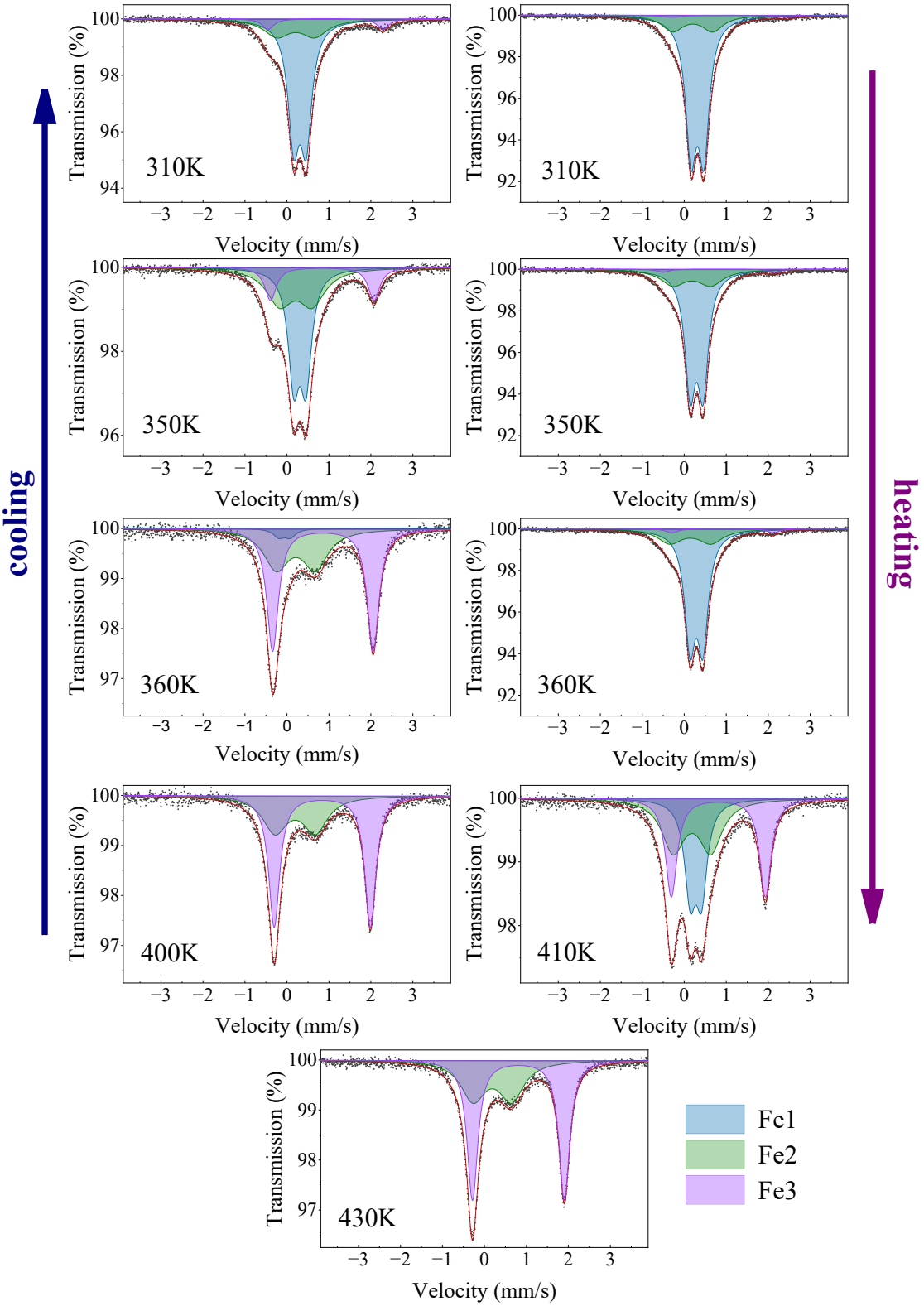

Figure 5.2.5 Selected ^{57}Fe Mössbauer spectra of **FeTrz-1** on heating and cooling modes.

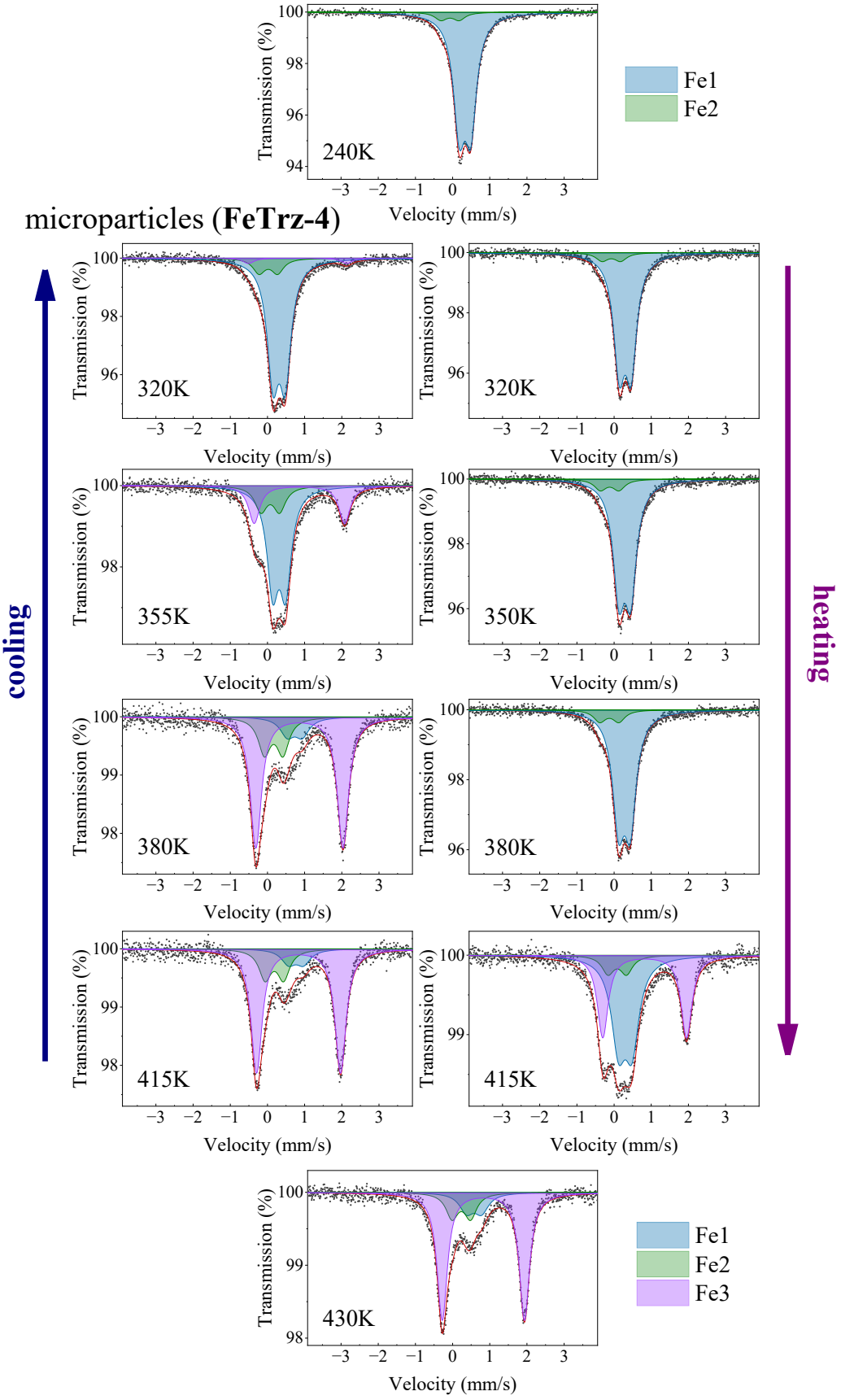

Figure 5.2.6 Selected ^{57}Fe Mössbauer spectra of **FeTrz-4** on heating and cooling modes.

At 320 K, the spectrum of **FeTrz-1** could be fitted best with two doublets: Fe1 (isomer shift $\delta = 0.4491$ mm·s^{-1}, quadrupole splitting $\Delta E_Q = 0.29839$ mm·s^{-1}) and Fe2 ($\delta = 0.3378$ mm·s^{-1}, $\Delta E_Q = 0.94725$ mm·s^{-1}). When the sample is heated up at 350 K, the third doublet appears, Fe3, with $\delta = 0.3378$ mm·s^{-1} and $\Delta E_Q = 0.94725$ mm·s^{-1}. At final temperature 430 K, the Fe1 doublet disappears and the spectra contains only Fe2 and Fe3 doublets. Upon cooling down to a low temperature, the Fe1 doublet appeared again at 360 K. When the temperature reached 320 K, only Fe1 and Fe2 doublets were observed. The temperature dependences of isomer shift and quadrupole splitting of **FeTrz-1** are presented in the left graph in Figure 5.2.7. The isomer shift value of Fe1 doublet corresponds to Fe(II) ions in the LS state, while Fe3 doublets have isomer shift values typical of Fe(II) in the HS state. Therefore, the redistribution of the area values of Fe1 and Fe3 doublets is caused by the spin crossover transition. Some surprise is the presence of Fe2, which can be assigned to Fe(III) in the HS state. The temperature dependence of the contribution of Fe1, Fe2, and Fe3 in Mossbauer spectra obtained for **FeTrz-1** is shown in Figure 5.2.8. The antagonistic and hysteretic behaviour of Fe1 and Fe3 confirms the presence of spin crossover phenomena[182,183].

A similar analysis was performed for sample **FeTrz-4**. The Mössbauer spectra of **FeTrz-4** were performed in the temperature range of 240-430 K (Figure 5.2.6). The change of an iron spin state as a function of temperature is clearly reflected in the Mössbauer spectra. As in the case of **FeTrz-1,** Mössbauer spectra contain three different doublets, Fe1, Fe2, and Fe3, corresponding to Fe(II) ions in LS, Fe(III) ions in HS, and Fe(II) ions in HS, respectively. The temperature-dependent contributions of Fe1, Fe2, and Fe3 in the Mössbauer spectra of **FeTrz-4** are presented on the right in Figure 5.2.7, with the antagonistic behaviour of Fe1 and Fe3 providing evidence for spin-crossover phenomena. Figure 5.2.8 summarises quadrupole splitting and isomer shift values from the spectral analysis. Upon cooling and heating, the hysteresis occurred in the temperature dependences of IS for Fe1 (Fe(II) in LS) and Fe2 (Fe(III) in HS), whereas there was no such behaviour in the change for Fe3 (Fe(II) in HS).

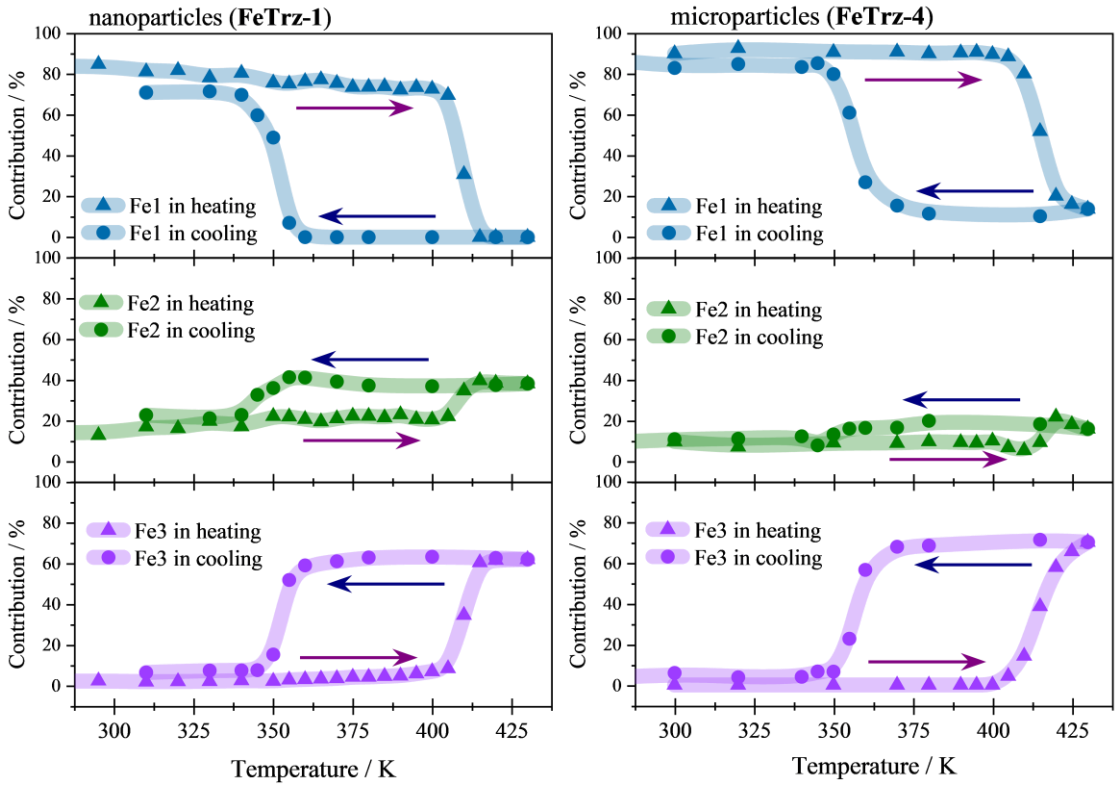

Figure 5.2.7 Temperature dependence of contributions of subsequent components Fe1, Fe2, and Fe3 resolved in Mössbauer spectra obtained for **FeTrz-1** (left) and **FeTrz-4** (right).

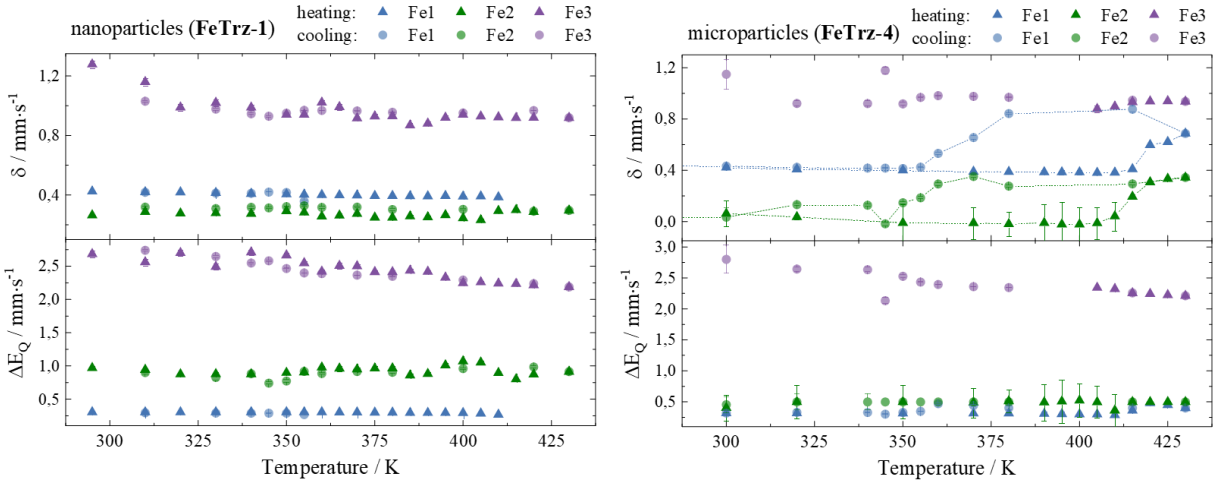

Figure 5.2.8 Left side: Temperature dependence of the isomer shift δ (top) and quadrupole splitting ΔE_Q (bottom) on cooling and warming modes of **FeTrz-1**, as resolved from Mössbauer spectroscopy. Right side: Temperature dependence of the isomer shift δ (top) and quadrupole splitting ΔE_Q (bottom) on cooling and warming modes of **FeTrz-4**, as resolved from Mössbauer spectroscopy.

5.2.3 X-ray absorption spectroscopy

To gain insight into the local atomic structure of the samples belonging to the family of Fe-triazole coordination chains, the X-ray absorption spectroscopy (XAS) was employed at the Fe K-edge, with the variable of temperature. Figure 5.2.9 shows Fe K-edge XANES spectra at limiting temperatures from temperature-dependent measurements for **FeTrz-1** and **FeTrz-4**,

together with data collected for iron(II) reference samples at room temperature: one LS reference – tris(2,2'-bipyridine)iron(II) tetrafluoroborate ($[Fe(bpy)_3](BF_4)_2$) and two HS references – iron(II) tetrafluoroborate hexahydrate ($Fe(BF_4)_2 \cdot 6H_2O$) and ammonium iron(II) sulphate hexahydrate (Mohr salt; $(NH_4)_2SO_4 \cdot FeSO_4 \cdot 6H_2O$). Following the behaviour recorded for references, spectra for **FeTrz-1** and **FeTrz-4** at 320 K can be assigned to Fe(II) in a low-spin state. Upon heating and reaching the highest temperatures, the main feature of Fe K-edge, determined by the allowed 1s → 4p electron dipole transition of **FeTrz-1** and **FeTrz-4,** shifts toward lower energy of photons by ~2.3 eV, when following the white line position. The explanation behind it derives from the distance increase between Fe and nearest-neighbour N atoms and the decrease of the crystal field force, which induces the transition of the iron ion from LS to HS. The reversibility of the shape and the Fe-edge shift for **FeTrz-1** and **FeTrz-4** were checked by performing two heating-cooling cycles.

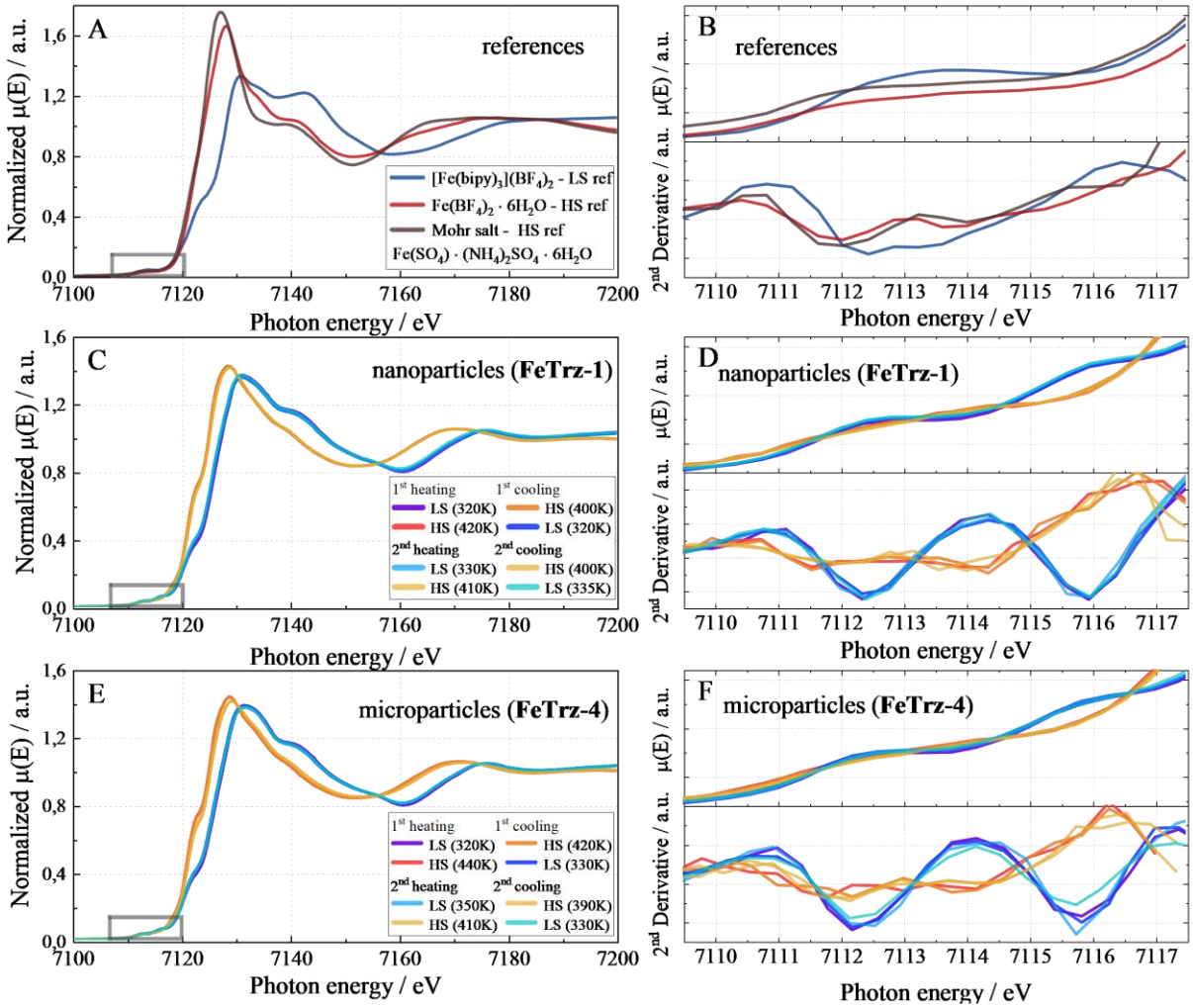

Figure 5.2.9 Normalized absorption coefficient at Fe K-edge for references (A), **FeTrz-1** (C), and **FeTrz-4** (E) for temperature-dependent measurements. Presented recorded XANES at the border temperatures are shown for two heating-cooling runs performed during the experiment. Marked with grey boxes are pre-edge regions, enlarged on the right, together with the 2nd derivative of absorption coefficient for references (B), **FeTrz-1** (D), and **FeTrz-4** (F).

In addition to the distinguishable XANES transition of the main feature of iron(II) when going from LS to HS state, in the pre-edge region of Fe K-edge spectra of **FeTrz-1** and **FeTrz-4,** small peaks or shoulders appear at approximately 7112 eV, corresponding to unallowed electric quadrupole 1s → 3d transitions. Although these transitions are generally weaker, they provide valuable insights into the local electronic structure of the metal centre. In particular, the pre-edge region is widely utilized in the literature as a diagnostic tool for determining both the oxidation and spin states of transition metal ions, such as Fe. By analysing the intensity, energy position, and shape of these pre-edge features, it is possible to gain crucial information about the electronic configuration and coordination environment of the metal centres. Since the samples of interest contain 6-coordinated Fe ions, the pre-edge features associated with octahedral symmetry show the lowest intensity[184]. This is because, in centrosymmetric environments, these features correspond to electric dipole forbidden transitions. Nevertheless, very weak pre-edge peaks are still experimentally detected, with electric quadrupole coupling being the most likely mechanism behind the observed intensity.

Figure 5.2.9 at panels B, D, and F presents an enlarged fragment of the pre-edge region marked with a grey frame on the XANES spectra. As a consequence of the low intensity, the disparities amongst the low and high temperature measurements are barely discernible. Nevertheless, the second derivative of the normalized absorption coefficient in the relevant energy region serves to enhance the distinctions amongst the spectra. In case of the reference samples, the LS compound is characterized by a single peak positioned at ~7112.5 eV, whereas HS reference samples show characteristics of two peaks positioned at ~7112 eV and ~7114 eV. As for the pre-edge region of **FeTrz-1** and **FeTrz-4**, they show similar behaviour for the high temperature spectra to HS references, however, the appearance of two peaks is less distinct compared to references. In the case of low temperature measurements of **FeTrz-1** and **FeTrz-4**, a clear peak positioned at ~7112.5 eV is observed, similarly to the LS reference spectra, together with an additional feature at ~7116 eV. According to literature, 1s → 3d pre-edge features are most typically assigned in the 7110 – 7115 eV region[185]. However, this higher energy feature, most probably assigned to the edge transition, has been observed in 6-coordinated structures based on Fe(II) and other members of the triazole ligand family[178,186].

To monitor the position of pre-edge features in the function of temperature from two temperature cycles for **FeTrz-1** and **FeTrz-4**, the background has been fitted as a combination of linear and Lorentzian functions in the Larch software package, and it was subtracted from the normalized $\mu(E)$ in the pre-edge region. The resulting features have been presented for nanoparticles (**FeTrz-1**) and microparticles (**FeTrz-4**) in Figure 5.2.10 A and B, respectively, for the first heating-cooling cycle. As observed from this temperature dependence, the transition from LS to HS is sharp for both samples. The pre-edge features were modelled by sums of Gaussian functions, and the peak energy positions have been summarized in Figure 5.2.10C (**FeTrz-1**) and D (**FeTrz-4**) according to the measurement's temperature. The difference in pre-edge position and splitting for LS and HS states of reference compounds (marked as lines on the graphs) and studied samples **FeTrz-1** and **FeTrz-4** can be explained based on ligand field theory and spin-allowed many-electron final states[185].

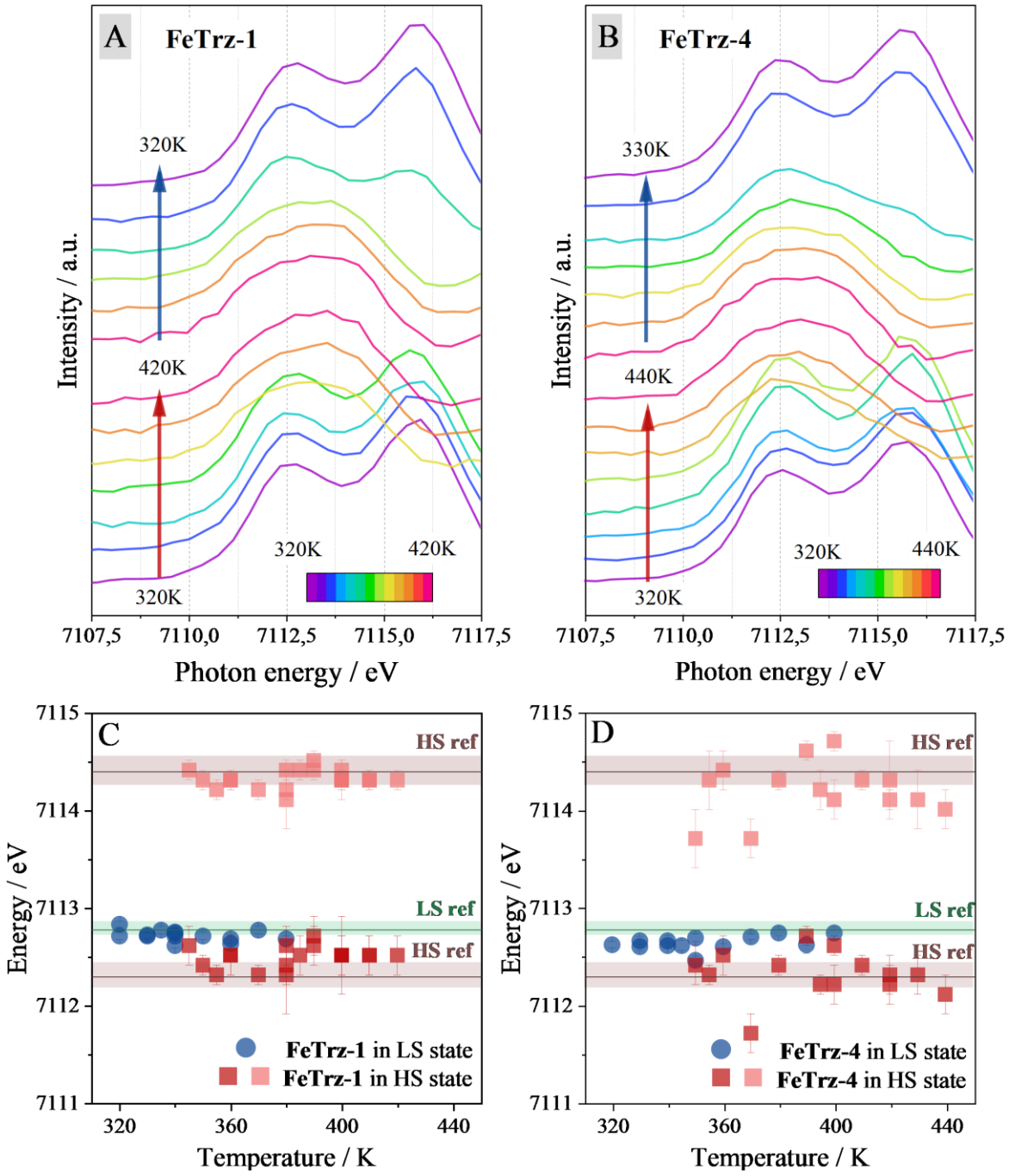

Figure 5.2.10 Extracted pre-edge region of normalized absorption coefficient at Fe K-edge for nanoparticles (A, C) and microparticles (B, D) for temperature-dependent measurements, together with analysis of pre-edge peaks position as a function of temperature with the position of reference pre-edge peaks.

Taking to the account the oxidation and the spin state of iron in the studied material, for Fe(II) in a low-spin state in an octahedral complex ground state is characterized by $(t_{2g})^0(e_g)^4$ hole configuration, and for that reason there is only one accessible one-electron allowed XAS final state $(t_{2g})^0(e_g)^3$ resulting in only one feature appearing in the pre-edge region. According to literature, for 6N coordination to the iron ion (e.g. $[Fe(bpy)_3]^{2+}$) the peak should be observed ~7112 eV, whereas for 6C coordination (e.g. $[Fe(CN)_6]^{4-}$) position of the peak is shifted by ~1 eV to higher energies. With the change of oxidation to Fe(III) in the low-spin state, there is an increase in the one-electron allowed final states, which leads to the observation of two pre-

edge features in the energy range 7110-7115 eV, separated by ~ 3 eV. In the case of Fe(II), the high-spin ground state in an octahedral ligand field has an electronic hole configuration of $(t_{2g})^2(e_g)^2$. Due to the transition of electron from 1s orbital into the 3d, it gives the excited hole configuration of $(t_{2g})^1(e_g)^2$ and $(t_{2g})^2(e_g)^1$, resulting in two very weak pre-edge features split by ~2 eV. For high-spin iron in 3+ oxidation, the ground state has a $(t_{2g})^3(e_g)^2$ configuration, and the promotion of the 1s electron into a 3d orbital produces two excited hole configurations, $(t_{2g})^2(e_g)^2$ and $(t_{2g})^3(e_g)^1$. It results in the appearance of two pre-edge features with splitting ~1.5 eV. It is also necessary to mention that the splitting of the two pre-edge features in the case of Fe(II) HS and Fe(III) HS is dependent on the ligand field strength. Considering the above without prior knowledge on the studied compounds, the distinction between low-spin Fe(II) and Fe(III) is more apparent with regard to high-spin counterparts, with the assumption of purely low or high states. However, for the studied nanoparticles and microparticles of **FeTrz** compound, the position of pre-edge features falls within the ranges defined by the reference samples, especially in the presumably LS state. The position of pre-edge peaks for **FeTrz-1** seems more aligned and with a smaller spread along the temperature-dependence, which may result from the more gradual character of the spin transition for **FeTrz-4**.

Based on the temperature-dependent XANES results, the difference spectra were calculated and presented in Figure 5.2.11. This figure presents the spectral differences observed for samples **FeTrz-1** and **FeTrz-4** as a function of temperature, with reference data recorded at 320 K – the lowest temperature measurement obtained for **FeTrz-4** – serving as the standard baseline. These absorption variations, which are directly linked to the spin-crossover (SCO) process, were systematically analysed to determine the fraction of the high-spin (γ_{HS}) phase as a function of temperature. The results of this analysis, depicted in Figure 5.2.12, reveal a well-defined thermal transition, where the LS phase, initially predominant around room temperature, gradually diminishes and becomes a minority phase in the high-temperature region. The transformation is characterized by a distinct hysteretic behaviour observed between the heating and cooling scans, indicative of the cooperative nature of the SCO transition. This hysteresis effect suggests that the thermal switching between spin states is not a simple reversible process but rather involves energetic barriers influenced by structural and intermolecular interactions within the sample. The shape of $\gamma_{HS}(T)$ dependences is in good agreement with the shape of $\chi T(T)$ plots, where much broader hysteresis is observed for complex **FeTrz-4**. The differences of $\gamma_{HS}(T)$ calculated for **FeTrz-4** based on two temperature runs confirm that during the second heating/cooling cycle, the temperature range was not sufficient to achieve full spin crossover process, so the γ_{HS} fraction did not reach saturation, which brings about the narrowing of thermal hysteresis.

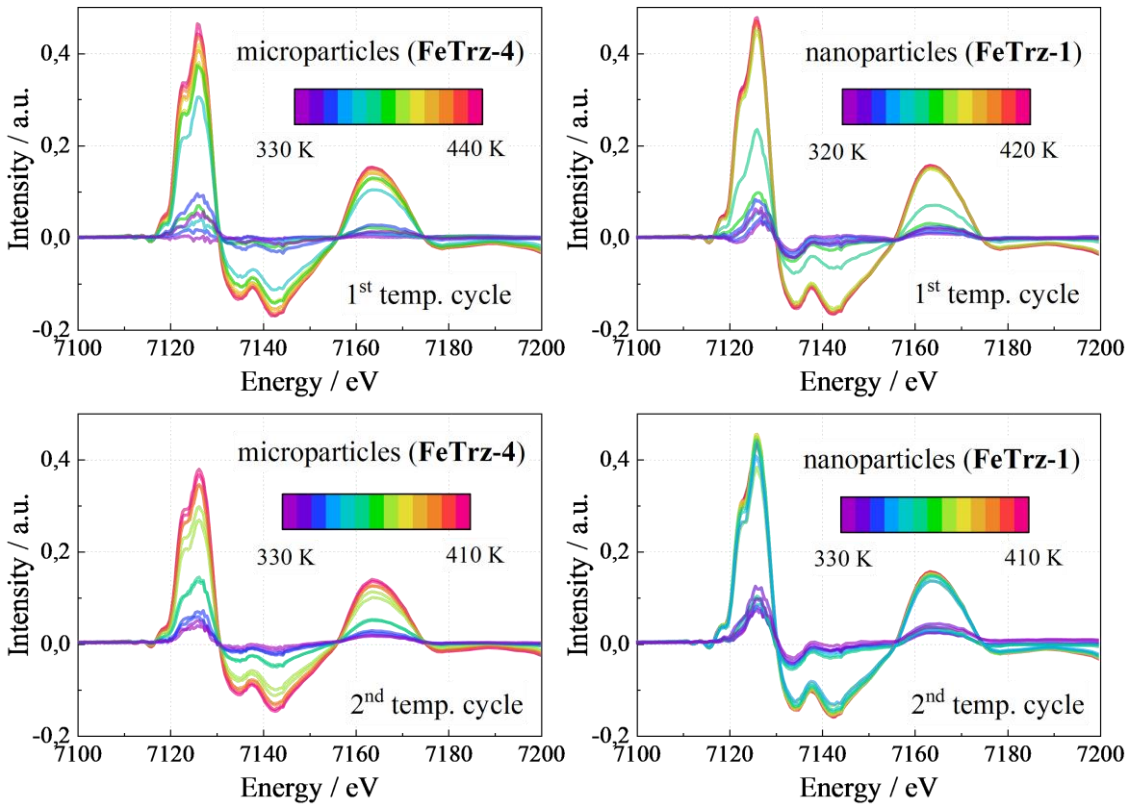

Figure 5.2.11 Difference spectra from temperature-dependent XAS measurements recorded for **FeTrz-4** (left column) and **FeTrz-1** (right column) in two consecutive heating-cooling cycles. The difference was calculated by subtracting normalised spectra recorded for microparticles at 320 K in the 1st temp. cycle.

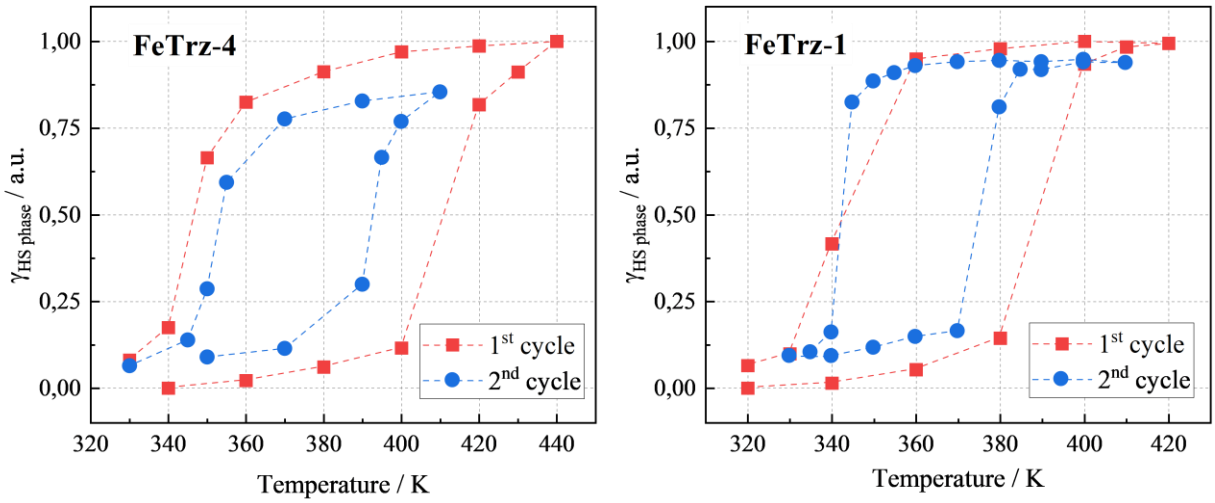

Figure 5.2.12 Calculated fraction of the high spin (HS) phase γ_{HS} from the difference spectra for Fe K-edge in the 7110-7175 eV range for the two following heating-cooling cycles. HS fraction γ_{HS} has been calculated from dividing the integrated area at a certain temperature T by the integrated area of the highest value (measurement at the highest temperature for 1st temperature cycle – 440 K for **FeTrz-4** and 420 K for **FeTrz-1**).

The determination of the HS fraction for nanoparticles and microparticles as a function of temperature was used for detailed structure determination on the basis of the EXAFS signal extracted from the oscillations after the main Fe K-edge jump. The k^2-weighted EXAFS oscillation function was obtained after following several normalization steps: pre-edge baseline

subtraction, post-edge background estimation using a quadratic polynomial function, and establishing E_0 at the position of 0.5 of the normalized absorption coefficient. Additionally, the data were corrected for artifacts observed around ~250 eV near the absorption edge step, which were caused by non-uniform dispersion of the studied material within the prepared pellets. In Figure 5.2.13, the Fourier transforms of $k^2\chi(k)$ following temperatures used during the 1st heating-cooling cycles for both **FeTrz-1** and **FeTrz-4** are depicted. In the analysis of EXAFS signal, the following Δk_{FT} ranges have been utilized: Δk_{FT} = 2.7-9.7 Å^{-1} for LS dominant spectra and Δk_{FT} = 2.6-8.9 Å^{-1}, tailored based on data quality.

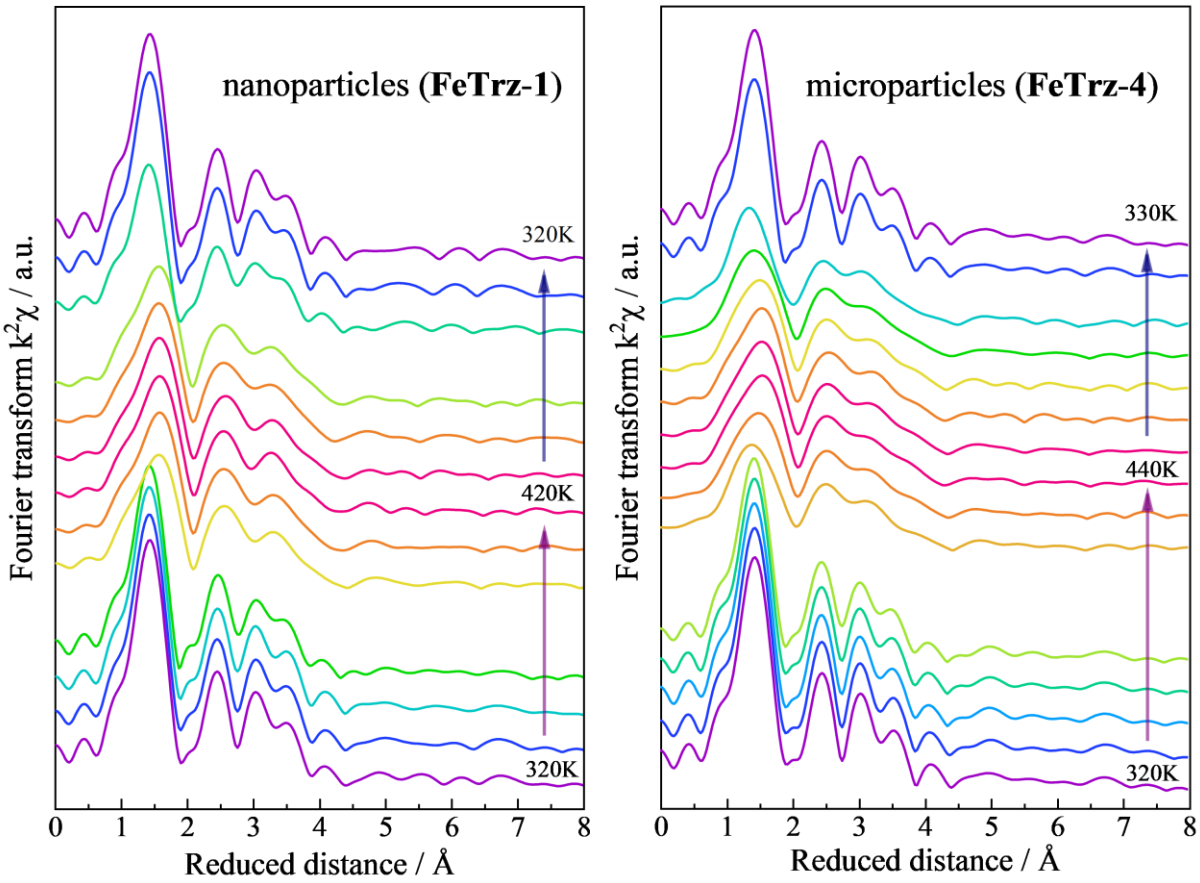

Figure 5.2.13 Temperature-dependent Fourier transform of k^2-weighted function $\chi(k)$ extracted for the 1st heating–cooling cycle for nanoparticles (left) and microparticles (right).

According to previous structural studies on the Fe-triazole family of coordination compounds, the one-dimensional chain of Fe(II) ions bridged by three triazole ligands, as presented in Figure 5.2.14, together with scattering paths taken into consideration in ab initio calculations[187]. The first nearest neighbours of Fe are six nitrogen atoms of triazole ligands, for which the dominant peaks at 1.6-2 Å in Figure 5.2.13 can be ascribed. Both for **FeTrz-1** and **FeTrz-4,** there is a noticeable shift of these peaks with a simultaneous reduction in the Fourier magnitude for the highest temperatures related to spin switching. In the 2-4 Å range, several scattering contributions can be expected from the next coordination shells, such as Fe–C/N or Fe–Fe, together with some multi-scattering paths, where atoms from the 1st and 2nd coordination sphere are involved.

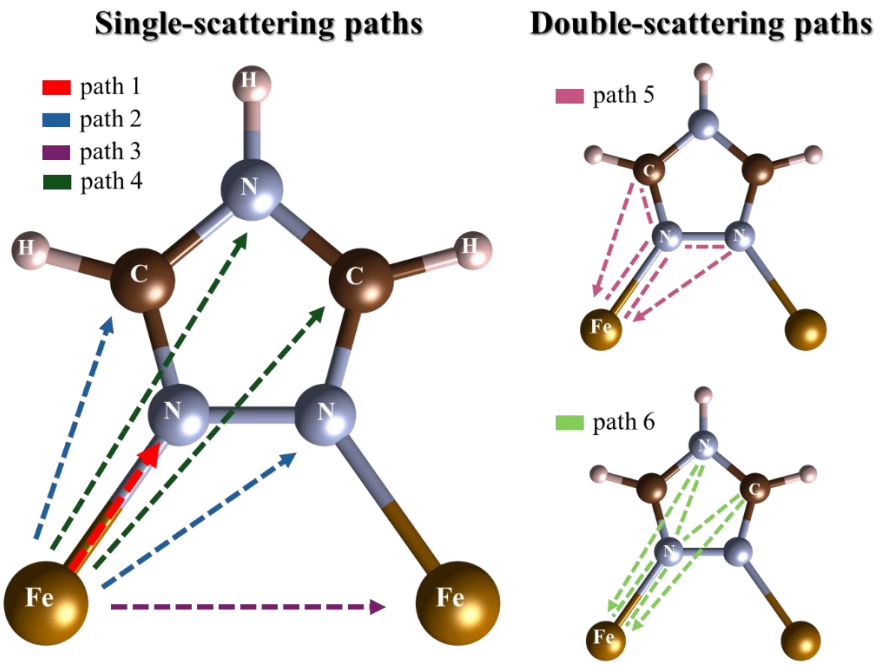

Figure 5.2.14 Generated fragment of the molecular chain of FeTrz with marked single and double scattering paths taken into account during EXAFS signal fitting.

EXAFS functions were simulated by ab initio calculation in the program FEFF6 with Fe as an X-ray absorbing atom. For obtaining three-dimensional coordinates and estimating possible scattering paths, the HS and LS crystallographic structures of $[Fe(Htrz)_2(trz)](BF_4)$ obtained and refined by Grosjean et al.[180] were employed. In the chosen model for HS state, the starting averaged distance between Fe and the nearest neighbour atoms (Fe-N) is equal to 2.041 Å, for the C/N atoms in the second shell is in the range 2.940-3.249 Å, and for the Fe-Fe distance is 3.891 Å. In case of the LS state, in model two, sites for nearest neighbouring nitrogen atoms have been distinguished at the distance of 1.827 Å and 1.918 Å for equatorially and axially positioned N atoms, respectively. The distance to carbon and nitrogen atoms in the 2nd coordination shell lies in the range of 2.921-3.077 Å, while to the next Fe atom is equal to 3.671 Å.

During fitting of EXAFS signal to reduce the number of independent variables the reduction factor S_0^2 and the edge energy shift ΔE_0 were fixed at the values obtained from the 1st shell fitting: $S_0^2 = 0.75$ and $\Delta E_0 = 3$ eV (LS) and 5.6 eV (HS), whereas coordination number was assumed from the structural model, e.g. for 1st shell N it was fixed at 6. Both for HS and LS structures, paths 1-6 (presented in Figure 5.2.14) were incorporated to fit each with a pair of separate parameters: the interatomic distance R and the Debye–Waller factor C_2. For three single-scattering paths (1-3) both parameters were fitted, while for the single-scattering path 4 and two double-scattering paths (5-6) the Debye–Waller factor was fixed to values: 0.006 (LS) / 0.001 (HS) – for path 4; 0.005 (LS) / 0.003 (HS) – for path 5; 0.001 (LS) / 0.003 (HS) – for path 6. The EXAFS fitting analysis was performed for the ΔR ranges of 1.1-4.3 Å for both LS and HS states. The comparison of experimental data with results obtained from fitting in the form of k^2-weighted Fourier transform has been depicted in Figure 5.2.15 (grey line – experimental data, red line – fit), for both **FeTrz-1** and **FeTrz-4** from the 1st heating–cooling cycle,

at the chosen temperatures. Parameters obtained from fitting at the corresponding temperature are shown in Table 5.2.3 for paths 1-3, together with the discrepancy factor of the fit.

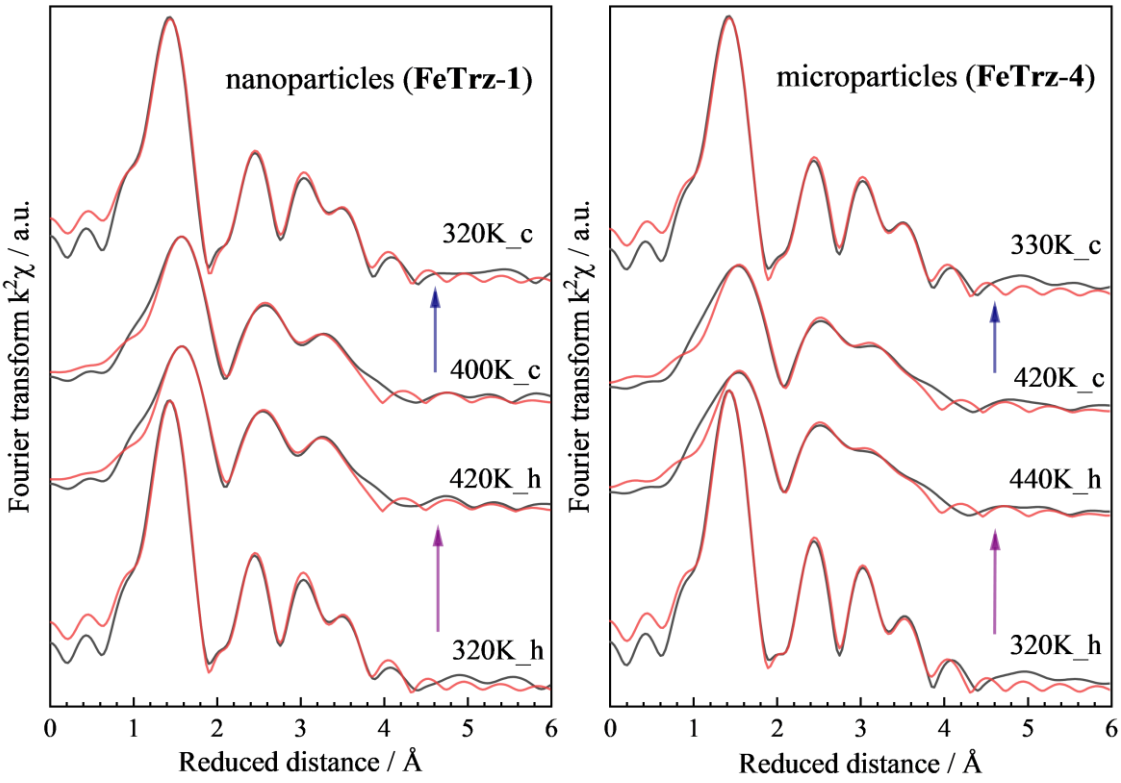

Figure 5.2.15 Fitted signal for nanoparticles (left) and microparticles (right) in k^2-weighted Fourier transform at chosen temperatures during the first thermal cycle (h – heating, c – cooling).

Table 5.2.3 Summarised fitted parameters (distance – ΔR and Debye-Waller factor - C_2) for paths 1-3, together with discrepancy factor of the performed fit (R-factor shown in percentage) for nanoparticles and microparticles, at chosen temperatures from heating and cooling at 1st thermal cycle.

Temp. / K	ΔR(p1) / Å	C_2(p1) /Å	ΔR(p2) / Å	C_2 (p2) /Å	ΔR(p3) / Å	C_2 (p3) /Å	R-factor / %
Nanoparticles (**FeTrz-1**)							
320K_h	0.126(6)	0.0029(9)	-0.06(2)	0.004(2)	0.05(4)	0.008(5)	1.4
420K_h	0.113(8)	0.011(1)	-0.05(2)	0.0017(16)	-0.13(4)	0.010(6)	1.0
400K_c	0.113(8)	0.011(1)	-0.04(2)	0.0015(15)	-0.13(3)	0.008(5)	1.1
320K_c	0.133(6)	0.0042(9)	-0.05(1)	0.004(2)	0.05(4)	0.009(5)	1.3
Microparticles (**FeTrz-4**)							
320K_h	0.122(5)	0.0021(8)	-0.06(1)	0.0020(18)	0.04(3)	0.006(3)	1.0
440K_h	0.104(9)	0.012(1)	-0.06(2)	0.0023(20)	-0.14(3)	0.006(4)	1.6
420K_c	0.104(9)	0.012(1)	-0.06(2)	0.0022(20)	-0.13(3)	0.006(5)	1.7
330K_c	0.126(6)	0.0032(9)	-0.06(1)	0.003(2)	0.040(36)	0.007(4)	1.3

The average distances from the X-ray absorber to the nearest neighbours – N in 1st coordination sphere, N/C in 2nd shell, and the next Fe atoms have been summarised in Table 5.2.4 for **FeTrz−1** and **FeTrz−4** at both spin states. In general, parameters obtained for microparticles

show lower average values in comparison to nanoparticles. However, the trend of longer distances from the central Fe to atoms in the 1st and 2nd coordination sphere for HS structure is observed in both **FeTrz-1** and **FeTrz-4**. In comparison to the utilized structural model, the obtained averaged distances, especially to the nearest N atoms, are characterized by higher values, which may be in part due to the partial Fe(III) content in the compound. However, in literature an example of EXAFS fitting performed on Fe-triazole nanoparticles with mean diameter size > 20 nm could be found, for which the coordination distance from absorbing Fe atom to the nearest N atoms is equal to 1.96(1) Å for LS and 2.14(1)-2.19(4) Å for HS[178], which is close to the values obtained during the fitting carried out for **FeTrz-1** and **FeTrz-4**.

Table 5.2.4 Comparison of selected distances from central Fe atom for structures in HS and LS state derived from EXAFS fitting of experimental data for nanoparticles (**FeTrz-1**) and microparticles (**FeTrz-4**).

Selected distances from central Fe	**FeTrz-1** @HS / Å	**FeTrz-1** @LS / Å	**FeTrz-4** @HS / Å	**FeTrz-4** @LS / Å
Fe-N (1st shell)	2.150(8)	1.960(7) 2.051(7)	2.13(1)	1.953(7) 2.044(6)
Fe-C/N (2nd shell)	2.89(2) – 3.20(2)	2.87(2) – 3.05(2)	2.88(2) – 3.17(2)	2.86(1) – 3.05(1)
Fe-Fe	3.75(3)	3.72(4)	3.74(4)	3.71(3)

The plotted change of interatomic distances in the 1st coordination shell as a function of temperature is presented in Figure 5.2.16, together with the dependence of Debye-Waller factor on temperature of measurement for nanoparticles (**FeTrz-1**) and microparticles (**FeTrz-4**). The values of interatomic Fe-N distance in the 1st and 2nd heating–cooling cycles for **FeTrz-1** overlap once fully transitioned to LS or HS states. In the case of **FeTrz-4**, discrepancies in the distance for the 2nd cycle at high temperature phase most probably derive from not obtaining complete transition into the HS state. The temperature dependence of the Debye–Waller factor, which reflects the degree of local structural disorder, was analysed for both nanoparticles and microparticles in the low-spin (LS) state. At lower temperatures, the Debye–Waller factor exhibits lower values (~0.004 Å), which increase as the temperature rises, corresponding to the transition of both structures to the high-spin (HS) state, where the factor reaches values around ~0.012 Å. For both parameters, thermal hysteresis can be found, following the course of the HS fraction from the XANES difference spectra. At the phase-transition temperatures, an abrupt change in interatomic distance is observed, especially to N atoms at equatorial positions, coupled with an observable increase of the Debye-Waller parameter at the temperatures near the SCO transition, due to the disorder derived from the coexistence of both states. Divergent behaviour observed in Debye–Waller factor originates from the abrupt change of interatomic distance at the spin state switching from LS to HS and vice versa, which is characterized as a first–order phase transition[187,188].

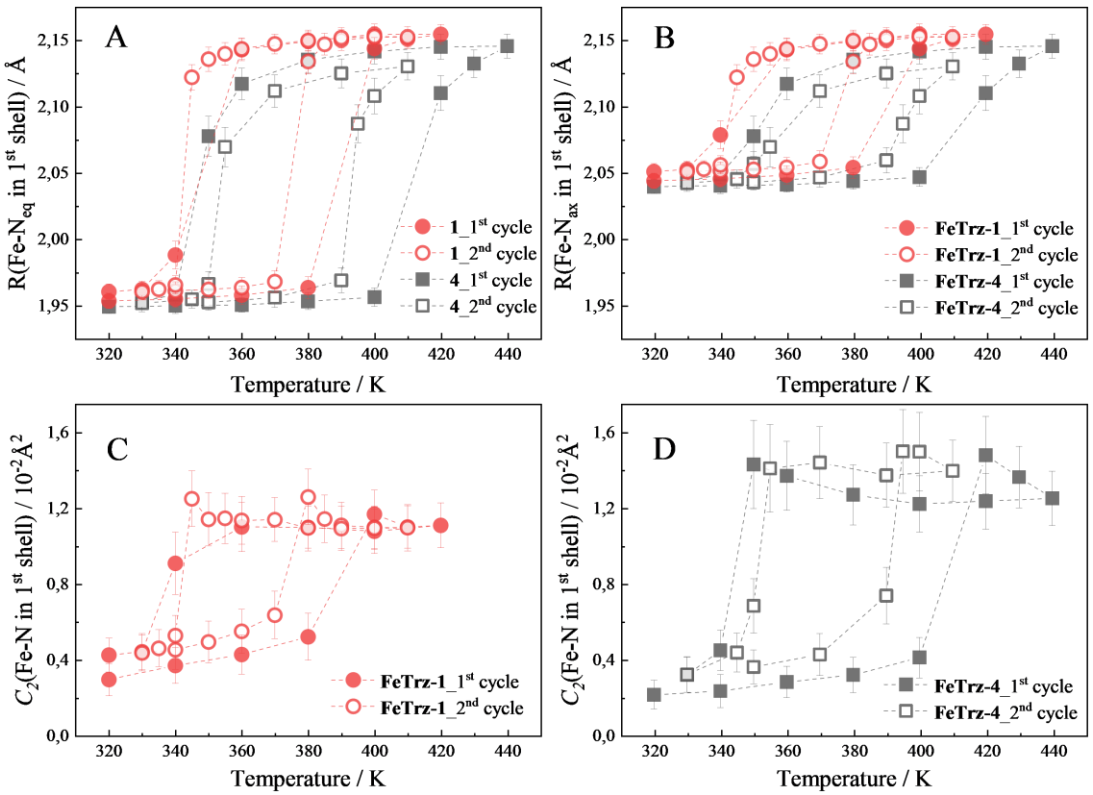

Figure 5.2.16 (A, B) The comparison of the temperature influence on the fitted bond length with error bars for the Fe-N bonds in the 1st coordination sphere (N at equatorial and axial positions) between microparticles (grey) and nanoparticles (red). (C, D) The comparison of the temperature influence on the fitted Debye-Waller factors for the nearest neighbours distances Fe-N for nanoparticles (left) and microparticles (right) obtained for the 1st and 2nd heating-cooling cycles.

In fitting the EXAFS signal, a scattering path from an X-ray absorbing Fe atom to the nearest Fe atom was taken into account (path 3). The temperature-dependence of interatomic distance between metal centres for nanoparticles (**FeTrz-1**) and microparticles (**FeTrz-4**) is presented in Figure 5.2.17, combined with *R*-factor describing the discrepancy of fits in the function of temperature. For extracted Fe-Fe distance in the function of measurement temperatures, the appearance of a hysteresis loop is visible in the case of both types of studied material, with noticeable difference in transition temperatures between nanoparticles characterized by lower $T_{1/2}$ and microparticles. However, in both cases, the difference in Fe-Fe distance between LS and HS states is much smaller compared to the literature value[187] and the starting model (0.23 Å)[180]. The temperature-dependence of the *R*-factor, showing how well the model has been fitted in the analysis for both structures, takes on lower values on the fits, where the experimental data relate to structures after complete transition (> 2%), whereas at the temperatures near SCO transitions they increase up to ~4%. Interestingly, at temperatures in which the LS state occurs for microparticles (**FeTrz-4**), the fitted model is characterized by lower *R*-factor values. In contrast, for the highest temperatures, the HS-dominant state fitted model of nanoparticles (**FeTrz-1**) is described by lower *R*-factor values.

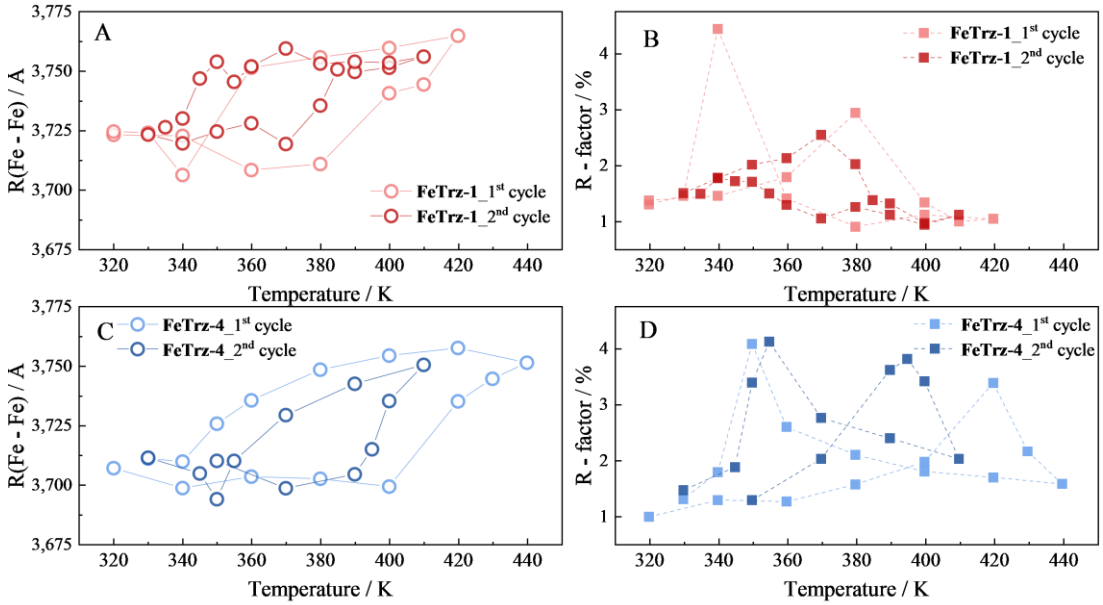

Figure 5.2.17 The comparison of the temperature influence on the fitted distances between two Fe centres, for nanoparticles (A) and microparticles (C). Comparison of the *R*-factors (shown in %) in the function of temperature for the performed fits of the EXAFS signal for nanoparticles (B) and microparticles (D) in the 1st and 2nd heating-cooling cycles.

A comparative analysis of X-ray absorption spectroscopy (XAS), Mössbauer spectroscopy, and magnetic susceptibility data reveals discrepancies in the transition temperature ($T_{1/2}$) values obtained from each technique. These variations in the measured transition temperatures arise from differences in the sensitivity of each method to the electronic and magnetic properties of the Fe(II) spin-crossover (SCO) system. Such mismatches have been previously reported for other Fe(II) SCO molecular systems and are a well-documented phenomenon in the study of spin transitions. One possible explanation for this discrepancy is the influence of core exciton formation, which can introduce perturbations in the bistability of the SCO system over a broad temperature range. These excitonic effects may affect the energetic landscape of the spin transition, leading to deviations in the transition temperature depending on the technique used for measurement. Additionally, surface effects have been identified as a contributing factor, particularly in XAS measurements. Ultimately, these differences highlight the complexity of characterizing SCO transitions and emphasize the need for a multi-technique approach to fully capture the nuanced electronic and magnetic behaviour of Fe(II) SCO materials. Understanding the interplay between surface effects, excitonic influences, and bulk properties is crucial for accurately interpreting experimental data and optimizing the performance of SCO-based materials in practical applications.

5.3 Composite materials based on **FeTrz** NPs

In the subsequent study, the materials introduced earlier in the chapter were further investigated concerning their incorporation into an organic polymer matrix, specifically in the form of electrospun fibres. To assess the impact of the matrix structure on the properties of the **FeTrz** nanoparticles, the selected materials were embedded in polyvinylpyrrolidone (**PVP**). These composites were prepared both as electrospun fibres and drop-cast films for comparative analysis. The results presented in the following subsection are part of research which is currently under review for publication[189].

Preparation of composite materials with incorporated **FeTrz** NPs

The choice of the organic polymer matrix for the **FeTrz** system is the same as for PBAs presented in the previous chapter. And so for the preparation of polymer-based solutions for electrospinning and drop-casting, **PVP** with a molecular weight equal to M_w = 360 kDa was chosen with methanol as the solvent. The protocol for the referenced **PVP** fibres has been described in Chapter 4.

In the preparation of polymer solutions, **FeTrz** nanoparticles coated with SiO_2 were used as fillers. The average lengths of the nanoparticles were 37.6 ± 7.3 nm (**FeTrz-1**), 44.0 ± 12.1 nm (**FeTrz-2**), and 119.6 ± 16.9 nm (**FeTrz-3**). To ensure a homogeneous suspension of the **PVP** matrix and **FeTrz** nanoparticles, the required amounts of FeTrz NPs, as listed in Table 5.3.1, were re-dispersed in 4 ml of methanol using an ultrasonic homogenizer and magnetic stirring for 24 hours. Subsequently, **PVP** 360 powder (~0.45 g) was added to the suspension to achieve a 12% weight concentration of **PVP** in methanol. The resulting solution was mixed on a gyromixer for an additional 24 hours to ensure complete dissolution of the polymer. Notably, the intensity of the violet hue in the polymer suspensions, shown in Table 5.3.1, increased with the initial concentration of **FeTrz** NPs.

Table 5.3.1 Experimental details for the preparation of PVP polymer solutions with incorporated **FeTrz** NPs.

Polymer suspensions	**FeTrz-1/PVP**		**FeTrz-2/PVP**			**FeTrz-3/PVP**	
SCO NP concentration	3.5%	10%	3.5%	10%	20%	3.5%	10%
Amount of SCO NP / mg	16.3	47.51	14.47	48.31	111.0	15.97	48.31
PVP 360 / g	0.459	0.455	0.454	0.454	0.455	0.455	0.459
Methanol / ml	4	4	4	4	4	4	4

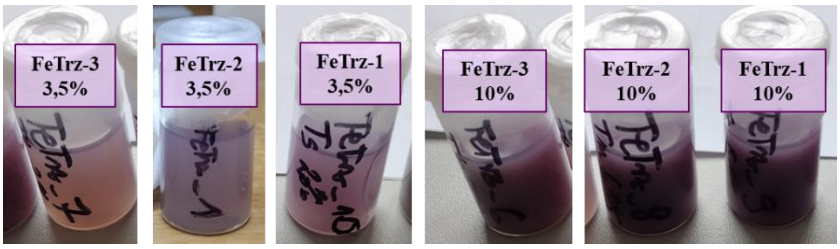

Figure 5.3.1 Photographs of electrospinning polymer suspensions of **FeTrz-1**, **-2,** and **-3**.

The materials were electrospun at room temperature, with an applied voltage of 13 kV, a relative humidity range of 35–50%, and a constant flow rate of 1.5 mL/h, maintained by a syringe pump. The fibrous mats were deposited onto the metallic plate collector randomly, at a distance of 10.5 cm from the tip of the needle to the counter electrode. The series of samples was prepared with an initial concentration of the filler in the solvent-free material equal to 3.5% and 10% by weight for **FeTrz-1, FeTrz-2,** and **FeTrz-3,** with additional samples of **FeTrz-2** containing 20% of the NPs. Most of the composite mats produced through electrospinning exhibited a predominantly white appearance, regardless of the size or concentration of the nanoparticles incorporated. However, a notable difference was observed in the sample with the highest nanoparticle concentration (20%), as the electrospun mat developed a distinct violet hue (Figure 5.3.2). This colour change is attributed to the significant presence of spin crossover (SCO) nanoparticles within the fibre matrix, indicating successful integration and uniform dispersion at higher loading levels.

Figure 5.3.2 The photography of electrospun composite of the **FeTrz-2/PVP-20%** fibres.

Additionally, samples prepared in the form of drop-casted foils have been fabricated with the use of the same polymeric suspensions of **FeTrz** in the polymer solution of PVP/MeOH (Table 5.3.1). A few drops of homogeneously dispersed suspensions have been placed onto the cleaned glass substrate, used without any additional preparation, and put aside for complete solvent evaporation. After the foils dried, they were scraped and used without any additional preparation. Due to the form of the polymer matrix, the foils have been discontinued. However, they maintained the intensive violet colour, similar to the used suspensions, presented in Figure 5.3.1.

5.3.1 Morphology and structural analysis of the electrospun composites

The fabricated electrospun fibres were characterized using SEM imaging. The analysis revealed that all mats with varying concentrations of **FeTrz** NPs are composed of fibres with an average

diameter of 670 ± 450 nm, as presented in Figure 5.3.3. A more detailed inspection of the materials indicated two distinct morphological regions along the length of the fibre. The first region observed in the produced fibres is characterised by a smooth surface, with no visible disturbances. On the other hand, there are areas of highly deformed regions, with the appearance of bubble-like structures along the fibres and with surfaces of higher roughness.

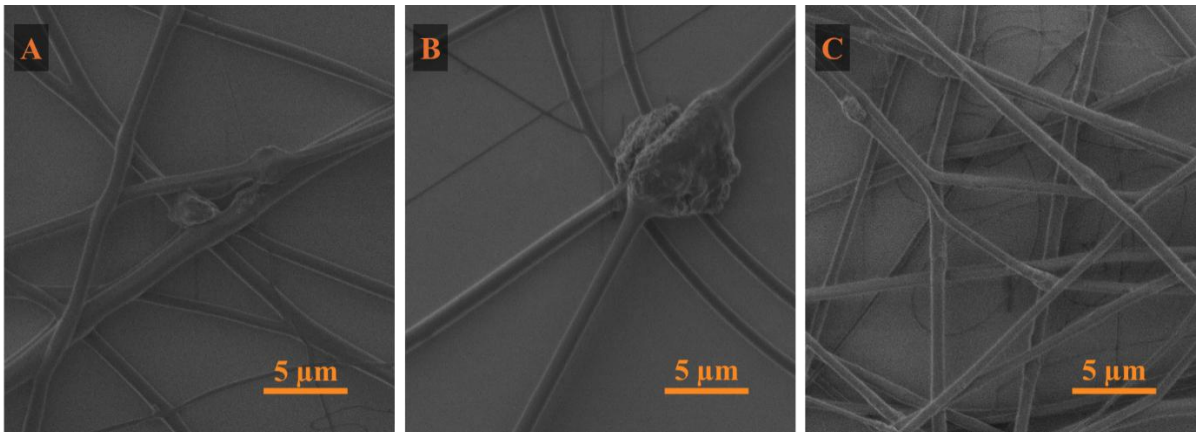

Figure 5.3.3 SEM images of the **FeTrz-2/PVP-10%/20%** fibres.

Upon closer inspection of the smooth region under transmission electron microscope (TEM), **FeTrz** nanoparticles could be found, placed within the **PVP** matrix (Figure 5.3.4). Within the smooth areas of fibres, there were domains of slightly larger fibre diameter. TEM observations revealed that they originated from the accumulation of nanoparticles inside the space of the fibre, while increasing its diameter (see Figure 5.3.4ABF). Interestingly, TEM also confirmed the presence of NPs dispersed along the smooth regions of the fibres, which were not initially visible in SEM images, indicating that the NPs could be embedded without significantly altering the polymer's external morphology. Furthermore, the rod-like topology of NPs does not play a significant role in the alignment, as the diameter of the fibres is significantly larger than the fillers' length, with non-uniform placement of nanoparticles within the matrix.

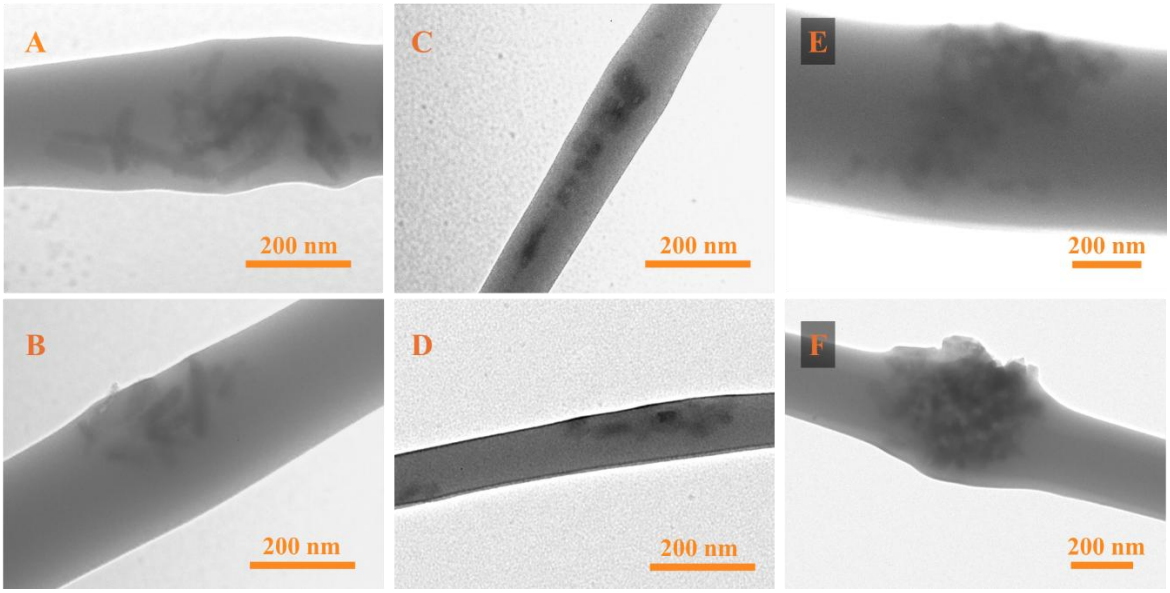

Figure 5.3.4 TEM images of electrospun composites: **FeTrz-1/PVP-10%** (a), **FeTrz-2/PVP-10%** (b, c), and **FeTrz-3/PVP-10%** (d, e, f).

For the composite materials with a higher concentration of the NPs, notable deformations began to emerge in the fibres, characterized by the formation of bubble-like structures outside the main fibre structure. These bubbles can be associated with the aggregation of SCO filler and are accompanied by disruptions or even breakages in the fibre surface (Figure 5.3.4a). The energy dispersive spectroscopy (EDS) has been used to map the bubbled regions, to confirm the observations made during SEM imaging. Due to the characteristics of the measurements and type of studied materials for **FeTrz** NPs embedded in the organic matrix, only the Fe atoms could be mapped, as an indication of the filler. For the matrix, carbon was chosen, as it is a main building element. Additionally, Si was mapped, which is associated with the used substrate upon which the fibres were electrospun and not the SiO_2 shell, which coats the individual **FeTrz** nanoparticles. It is worth mentioning that the X-ray characteristic radiation originating from the substrate was much more intense compared to the other two elements, due to the significantly thicker and more dense material, unlike individual composite fibres.

The mapped bubbled forms along fibres with 10% NPs are presented in Figure 5.3.5. As it was mentioned above, the mapping of Si corresponds to the substrate, which, in particular, can be seen as a dark fragment in the place of the bubble on the Si map. On the other hand, the carbon signal follows the shape of the fibres and the bubbles on the fibres. And finally, the content of Fe significantly increases on the bubbles, whereas the signal from the rest of the mapped area is most probably due to the noise. Thus, the association of bubbles along the fibres with aggregated **FeTrz** NPs**,** regardless of the size of the nanoparticles, with EDS mapping confirmed the observation. It is worth mentioning that the overlapping carbon and iron maps at the bubble may suggest that NPS in the thickenings along the fibres are most probably still covered with the matrix polymer.

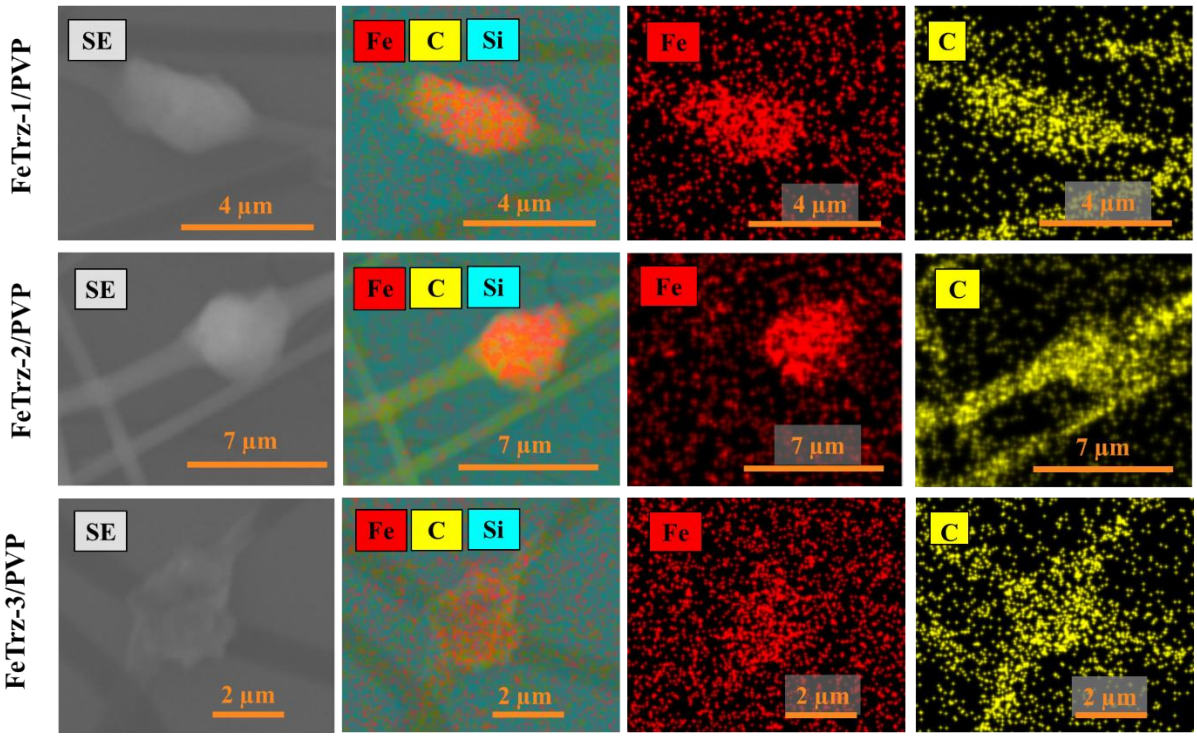

Figure 5.3.5 SEM image of **FeTrz-NP/PVP-10%** composite fibres and the corresponding EDS mapping of C, Fe, and Si.

5.3.2 Calorimetric measurements of **FeTrz** NPs and their electrospun fibres

Differential Scanning Calorimetry (DSC) was employed to investigate the presence of spin-crossover (SCO) features in the fibres by identifying phase transitions directly associated with the SCO phenomenon. To estimate any potential thermal signals originating from the PVP matrix, which could overlap with the SCO transitions, DSC measurements were first performed on pure PVP fibres as a control (see Figure 5.3.6A). Before the measurement, fibres have been cut into smaller fragments to fit into the measuring vessel, and they have not been subjected to any additional processing, e.g. heated to remove residual solvent from freshly manufactured material.

The measurement of the pure **PVP** matrix was essential for identifying thermal transitions specific to the matrix and their characteristics. This step was crucial to isolate the spin-crossover phenomenon of the embedded nanoparticles from the intrinsic properties of the polymer matrix. The results confirmed the initial assumptions, as the **PVP** matrix showed no thermal transitions within the temperature range relevant to the SCO effect (300–400 K). This ensured that any subsequent thermal features observed in the composites could be exclusively attributed to the SCO nanoparticles embedded in the fibres. The feature observed in the polymer matrix, characterized by a strong and broad peak in the heating (endothermic) curve between 300 K and 380 K, is most likely associated with solvent residues or moisture adsorbed on the fibres, as PVP is a polymer with hygroscopic properties[190]. While heating above 400 K, around 455 K, a small peak appears, associated with the glass transition of the polymer. The temperature of

455.65 K corresponds to the tabular value for this transition of poly(vinylpyrrolidone) with molecular weight equal to 360 kDa[191].

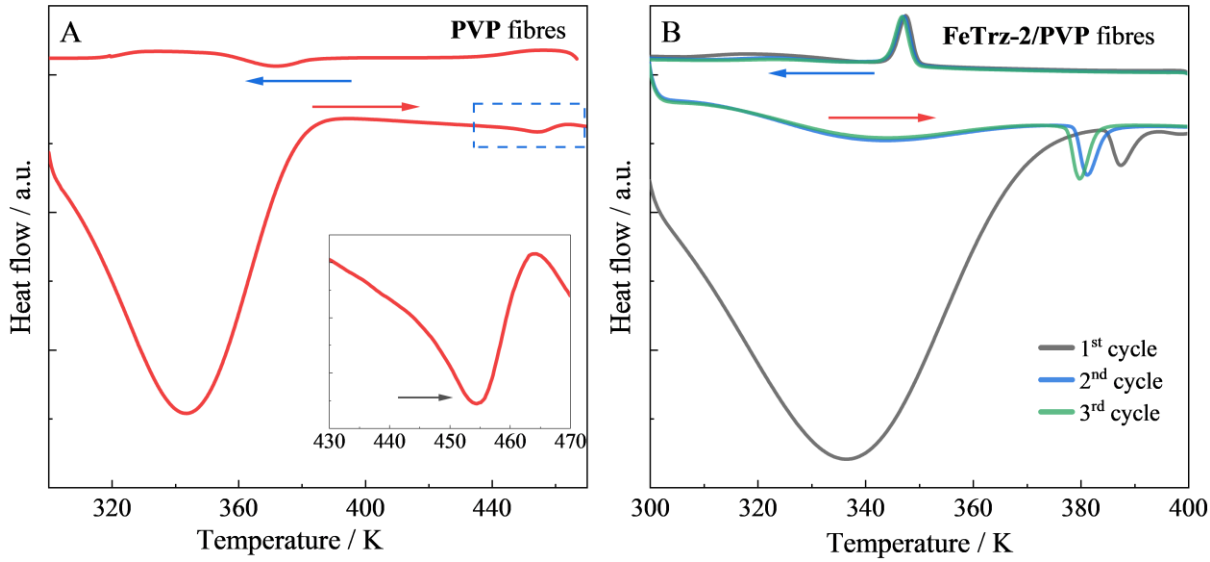

Figure 5.3.6 A) DSC curves in heating (lower curve) and cooling (upper curve) for pure PVP fibres. Insert presents the enlarged transition at ~455 K related to the glass transition of the polymer. B) DSC curves in heating (lower curves) and cooling (upper curves) for **FeTrz-2-10%** composite fibres. 1st scan marked in grey, 2nd in blue and 3rd in green.

As an example of the full DSC measurement with three consecutive scans performed on composite **FeTrz-2-10%** is presented in Figure 5.3.6B. The 1st DSC run differs in the course, especially on the heating curve. The characteristic broad peak in the range below 380 K associated with the residual moisture in the **PVP** fibres disappears in the following scans, with an additional shift of the first endothermic peak of embedded NPs toward higher temperature. The next two DSC runs show better reproducibility, especially with the location of the sharp peak in the heating curves. In the comparison of DSC signals of composites with the behaviour of pure NPs, only the third measurement scans were taken into account.

DSC measurements conducted on composite materials containing SCO nanoparticles in comparison to powdered NPs are presented in Figure 5.3.7. As it was partially described at the beginning of this chapter, upon heating, NPs exhibit a sharp endothermic transition originating from the low to high-spin state. For the pure nanoparticle powdered samples, the temperature transition was recorded from 375 K for **FeTrz-1** to 382 K for **FeTrz-3**. Conversely, while cooling, the scans for NPs recorded the exothermic transition from the high-spin (HS) to the low-spin (LS) states. The cooling peaks appeared at 345 K, 348 K, and 351 K, for the samples **FeTrz-1**, **FeTrz-2**, and **FeTrz-3**, respectively.

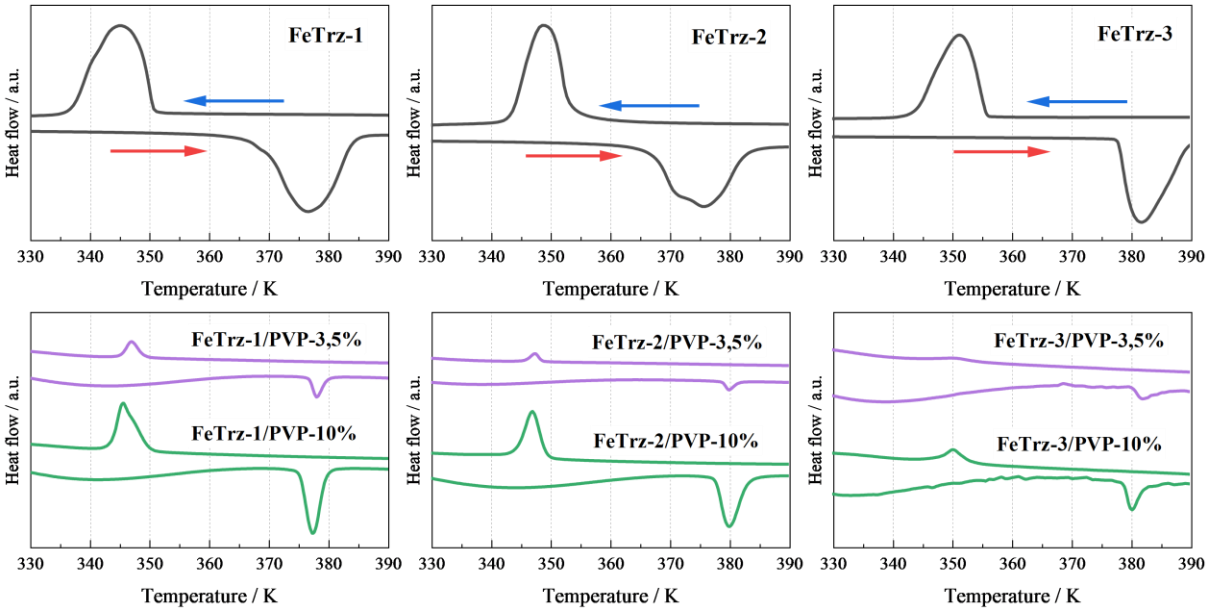

Figure 5.3.7 Comparison of DSC curves measured with a warming/cooling rate of 10 K·min^{-1} for **FeTrz-1**, **FeTrz-2**, and **FeTrz-3** NPs and **FeTrz-1/PVP-3.5%**, **FeTrz-1/PVP-10%, FeTrz-2/PVP-3.5%**, **FeTrz-2/PVP-10%, FeTrz-3/PVP-3.5%** and **FeTrz-3/PVP-10%** electrospun composites.

Notably, in all composite materials, the DSC curves revealed the same characteristic sharp peaks during both cooling and heating cycles, reflecting the SCO behaviour of the embedded nanoparticles. The temperatures related to the endothermic and exothermic peaks for composites and NPs have been summarized in Table 5.3.2. The observed shift of temperatures suggests that the interaction between the **PVP** matrix and the nanoparticles affects the thermal behaviour of the SCO transitions, potentially due to confinement effects or interfacial interactions between the polymer and the embedded nanoparticles.

Table 5.3.2. The comparison of the position of the endo- and exothermic peaks for powdered **FeTrz** NPs and their electrospun composites.

Sample	T_{endo}(↑) / K	T_{exo} (↓) / K
FeTrz-1	375	345
FeTrz-1@PVP-10%	377	345
FeTrz-1@PVP-3,5%	378	347
FeTrz-2	376	348
FeTrz-2@PVP-10%	380	347
FeTrz-2@PVP-3,5%	380	347
FeTrz-3	382	351
FeTrz-3@PVP-10%	380	350
FeTrz-3@PVP-3,5%	382	350

To further assess the stability of the SCO behaviour in electrospun fibres, DSC measurements were performed over six heating-cooling cycles for **FeTrz-1/PVP-10%** and **FeTrz-2/PVP-10%**, with the results shown in Figure 5.3.8. The temperature range of the measurement did not exceed 420 K, therefore, the glass temperature of the polymer matrix was not being achieved. Following Figure 5.3.7 cycles no. 4-6 overlap with the 3rd heating-cooling cycles for both samples. Starting from the 1st cooling cycles, the exothermic peaks do not shift with the following scans. In contrast, there are minor discrepancies in the endothermic peak, as with each scan the temperature is lowered; however, compared to the 1st heating scan, above the 3rd scan, they are not as significant.

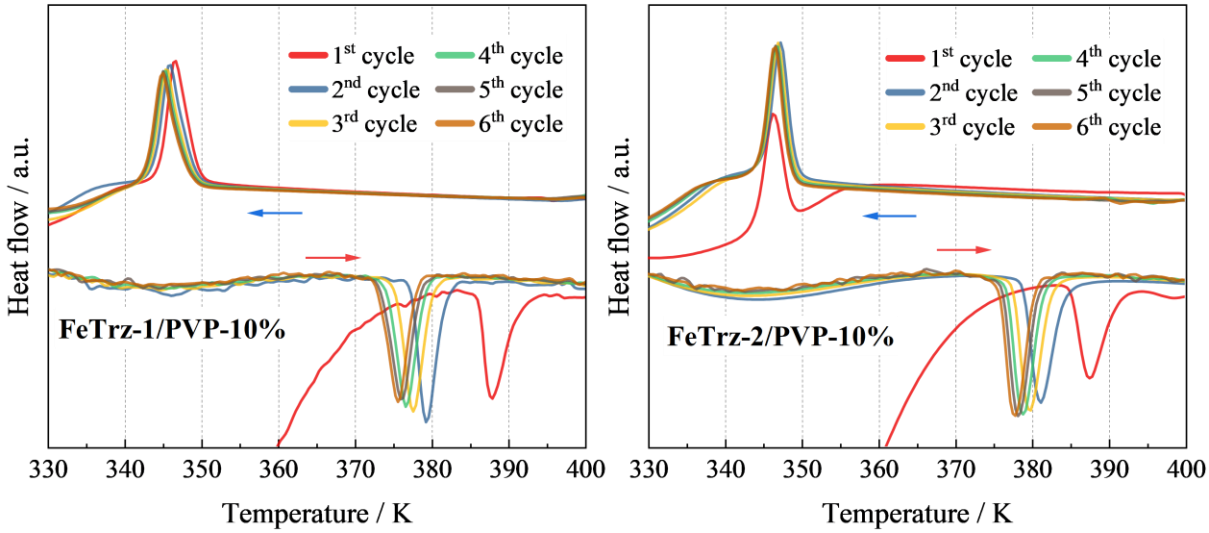

Figure 5.3.8 DSC curves measured for **FeTrz-1/PVP-10%** (A) and **FeTrz-2/PVP-10%** (B) after 6 measurement cycles performed in the temperature range 300-400 K to confirm the repeatability of SCO behaviour in fibres.

5.3.3 Magnetic properties of **FeTrz** NPs in the electrospun-based and drop-casted composite materials

To further investigate the spin-crossover properties of the fillers in the composite, magnetic susceptibility was measured as a function of temperature in the range of 300-400 K, under an applied field of 1 kOe. Within those temperatures, pre-synthesized NPs have been shown to undergo a complete spin crossover transition characterized by high cooperativity. The electrospun fibres have been used for the magnetic measurements immediately after manufacturing, without any additional treatment. During sample preparation, composite materials have been folded into small cubes and placed into the gelatine capsules in order to give a sufficiently good magnetic signal, due to the high dilution of SCO material in the matrix.

Following a methodology of pristine SCO NPs, to obtain consistent magnetic data, multiple temperature cycles were measured (from 3 to 5), with varying sweeping rates of 1 or 2 K/min. Similarly to DSC curves, in the first characterization of the composites' properties, the initial thermal cycles exhibited a slightly different course, which was attributed to remanent solvent loss and adsorbed moisture on the electrospun fibres. From the third measurement cycle, the magnetic data for the composites stabilized, signalling the achievement of a stable phase.

Consequently, the data from the third cycle (recorded at 1 K/min) was used for all subsequent discussions of the examined samples.

Uncorrected data of magnetic susceptibility in the function of temperature showed behaviour associated with the residual paramagnetic impurities derived from the matrix (similar to **RbMnFe/PVP** composite materials in Chapter 4). To extract the magnetic signal of embedded NPs, the obtained data have been corrected experimentally using the Curie-Weiss law, according to the equation (6). The comparison of thermal hysteresis recorded for NPs and their **PVP**-based composites with 10% and 3.5% content of **FeTrz** NPs has been presented in Figure 5.3.9.

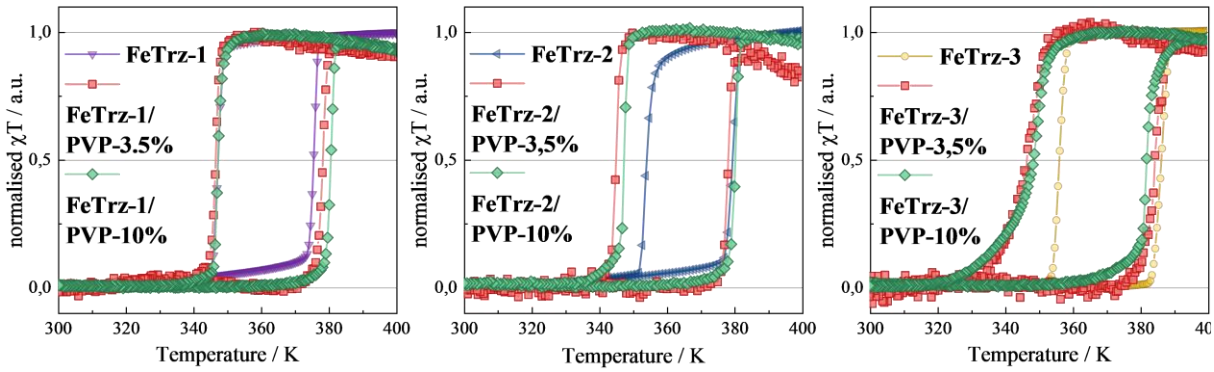

Figure 5.3.9 Thermal variation of normalised χT for **FeTrz** NPs and their electrospun composites with NPs nominal concentration of 3.5% and 10%.

While comparing the SCO characteristics of composites to the behaviour of respective NPs, the expansion of the thermal hysteresis is quite evident; however, no apparent trend is noticeable. For **FeTrz-1** based fibres, $T_{1/2}(\uparrow)$ shifts toward higher values (from 376 K to 381 K), resulting in a ~34 K wide hysteresis, compared to ~28 K for the pure nanoparticles. In the case of **FeTrz-2**-based composites, both $T_{1/2}(\uparrow)$ and $T_{1/2}(\downarrow)$ go in opposite directions, leading to the more evident widening of thermal hysteresis from ~26 K for the NPs alone to ~34 K after embedding into electrospun fibres. Finally, for the composites based on the largest NPs (**FeTrz−3**), the shift of $T_{1/2}(\downarrow)$ toward lower temperatures is more noticeable, followed by the expansion of the hysteresis from ~30 K (NPs) up to ~37 K for the electrospun fibres.

In addition to the alterations in temperature ranges at which the transition between pure NPs and their composites occurs, it is crucial to highlight the markedly abrupt nature of the SCO transitions observed in fibre-based composites. These observations align with literature examples, where pre-synthesized spin-crossover micro/nanoparticles have been integrated into different polymer matrices. Examples include their incorporation in epoxy-based photoresist SU- 8[99] or micrometre-thick films in piezoelectric polymers[96], also listed in Table 5.3.3. Notably, key features such as the widening of thermal hysteresis during magnetic measurements and the retention of a high degree of cooperativity are observed.

Table 5.3.3 The summary of the magnetic properties of prepared electrospun samples and drop-casted foils with comparison to literature examples.

Sample	Type of material	$T_{1/2}$ (↑) / K	$T_{1/2}$ (↓) / K	ΔT / K
FeTrz-1	powder	376	347	28
FeTrz-1/PVP-3.5%	Electrospun fibres	378	347	31
FeTrz-1/PVP-10%	Electrospun fibres	381	347	34
	Drop-casted foil	375	340	35
FeTrz-2	powder	380	354	26
FeTrz-2/PVP-3.5%	Electrospun fibres	378	345	33
FeTrz-2/PVP-10%	Electrospun fibres	381	347	34
	Drop-casted foil	381	340	41
FeTrz-2/PVP-20%	Electrospun fibres	377	347	30
	Drop-casted foil	384	338	46
FeTrz-3	powder	386	356	30
FeTrz-3/PVP-3.5%	Electrospun fibres	385	348	37
FeTrz-3/PVP-10%	Electrospun fibres	382	349	33
	Drop-casted foil	387	340	47
$[Fe(Htrz)_2(trz)](BF_4)$ with average particle size ~85 nm	powder	~380	~350	30
In SU-8[a] resin	Spray-coated layer	386	327	59
$[Fe\{(Htrz)_2(trz)\}_{0.9}(NH_2\text{-}trz)_{0.3}](BF_4)_{1.1}$ with average particle size ~20 nm	powder	335	327	8
in piezoelectric polymer (P(VDF-TrFE)[b]	Drop-casted film	340	327	13
$[Fe(atrz)_3]Cl_2$	powder	350	342	8
$[Fe(atrz)_3]Cl_2$ in PMMA[c][89]	Electrospun fibres	353	345	8
$[Fe(atrz)_3](2ns^d)_2$	powder	317	293	24
$[Fe(atrz)_3](2ns)_2$ in PMMA[89]	Electrospun fibres	315	296	19

[a] epoxy-based photoresist; [b] poly(vinylidene fluoride-co-trifluoro-ethylene); [c] poly(methyl methacrylate); [d] 2-Naphthalenesulfonate

According to the literature search for the examples of embedded SCO-based components into the fibres, the magnetic properties have been investigated twice[87,89], for which the SCO properties have been summarized in the above Table 5.3.3. In these investigations, composites were produced by dispersing or dissolving SCO compounds within organic polymer matrices. The first study examined fibres composed of a blend of atactic polystyrene (aPS) and [Fe(4-octadecyl-1,2,4-triazole)$_3$(ClO_4)$_2$], demonstrating that the spin-transition temperature of the

composite was comparable to that of the pure complex[87]. However, the transition in the composite was more gradual, and unlike the pure SCO material, the composite showed no hysteresis in the spin transition.

Another study was devoted to investigate the magnetic behaviour of a composite containing iron(II) triazole complexes embedded in a poly(methyl methacrylate) (PMMA) nanofibres matrix[89]. The results showed that the composite retained SCO characteristics with only minor changes in hysteresis relative to the pure SCO complex, indicating that the electrospinning process had minimal impact on the material's magnetic properties. A separate study involving pre-synthesized SCO nanoparticles focused on the incorporation of $[Fe(NH_2\text{-}trz)_3]_2$ nanoparticles within a polylactic acid (PLA) matrix, with spin transitions analysed using Mössbauer spectroscopy. The findings revealed that the composites exhibited a mixture of high-spin (HS) and low-spin (LS) states at room temperature, with additional Fe(III)-HS centres detected at both low (77 K) and high (293 K) temperatures, likely as a result of the electrospinning process. Additionally, the incorporation of the bulk $[Fe(Htrz)_2(trz)]BF_4$ material into electrospun polymer matrix was investigated, where the Fe(II)-HS population at 273 K was observed in the PLA-embedded material. This observation contrasts with the behaviour of the bulk material, which at RT exhibits a low spin state. These results suggest that the electrospinning process may influence the behaviour of SCO fillers, as evidenced by the mixed state observed at low-spin temperatures, as supported by Mössbauer data[192].

As it was shown in Figure 5.3.9, after embedding pre-synthesized **FeTrz** NPs into PVP electrospun fibres, the SCO effect is characterized by high cooperativity. To compare how the technique of the composite preparation and so the effect of the matrix may influence the SCO behaviour of the filler, composite films were prepared by drop-casting the electrospinning solution onto a substrate. The comparison of the magnetic susceptibility as a function of temperature for both electrospun fibres and films has been presented in Figure 5.3.10, with the magnetic characteristic also included in Table 5.3.3. The spin transition characteristic changes significantly when employing a drop-casting method in chosen SCO NPs coated with a thin silica coating and placed in the PVP film. The temperatures of the transition are shifted toward lower temperatures, mainly $T_{1/2}(\downarrow)$. Additionally, the SCO transition becomes more gradual, with a noticeable decrease in abruptness. These results demonstrate that a change from the composite preparation protocol from electrospun fibres to drop-casted films may induce some additional effects, most probably involving the silica (TEOS) shell of NPs and the polymer matrix (PVP).

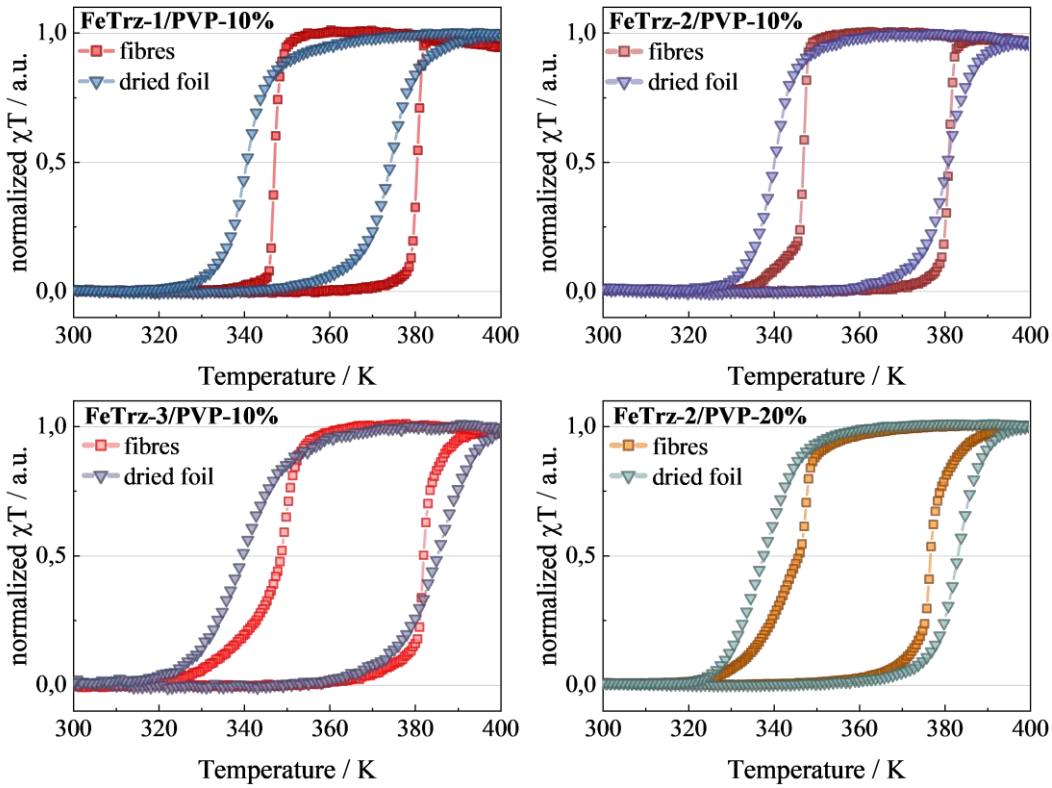

Figure 5.3.10 The $\chi \cdot T$ vs. T plots for electrospun fibres and films obtained from the same solutions: **1-10%** (A), **2-10%** (B), and **3-10%** (C).

According to the literature on the comparison of electrospun blend of TEOS/PVP and its corresponding drop-casted films[193], there can be found significant structural differences. The authors of the mentioned research analysed ATR-FTIR spectra and found that the divergent behaviour of the same solutions comes from the effectiveness of solvent evaporation during composite preparation. As it was described in the introductory Chapter 3 about electrospinning methodology, in this process, the solvent evaporation starts from the very beginning of fibre formation, whereas for drop-casted foils, the solidification of the composites may take up to a few days, depending greatly on the amount left for evaporation. In the mentioned study, TEOS/PVP blends in the form of electrospun fibres exhibited stronger bonding interactions and more organized silica networks. On the other hand, drop-casted films retained more moisture and showed incomplete silica networks.

The presented magnetic results of electrospun fibres in comparison to dried foils have demonstrated that fibres replicate and even enhance the SCO effect of the fillers, while the films show the opposite. The differences in the preparation of electrospun composites and drop-cast films, primarily due to variations in solvent evaporation efficiency, may influence the spin-crossover behaviour of the embedded **FeTrz** nanoparticles. These observations highlight the importance of carefully selecting the preparation method, as it can significantly affect the material's properties, depending on the components used.

To elaborate on the SCO properties of NPs in the electrospun fibres, the magnetic properties of composites based on **FeTrz-2** and powdered NPs have been monitored by applying different temperature sweep rates, while recording magnetic moment as a function of temperature (see

Figure 5.3.11). In the field, it has been established that in SCO materials with faster scan and heating/cooling rates, the transition temperatures change, and there is evident widening of thermal hysteresis[194]. In the case of the presented results, the evolution of the width of magnetic hysteresis was investigated with scan rates in the range of 0.5-6 K/min.

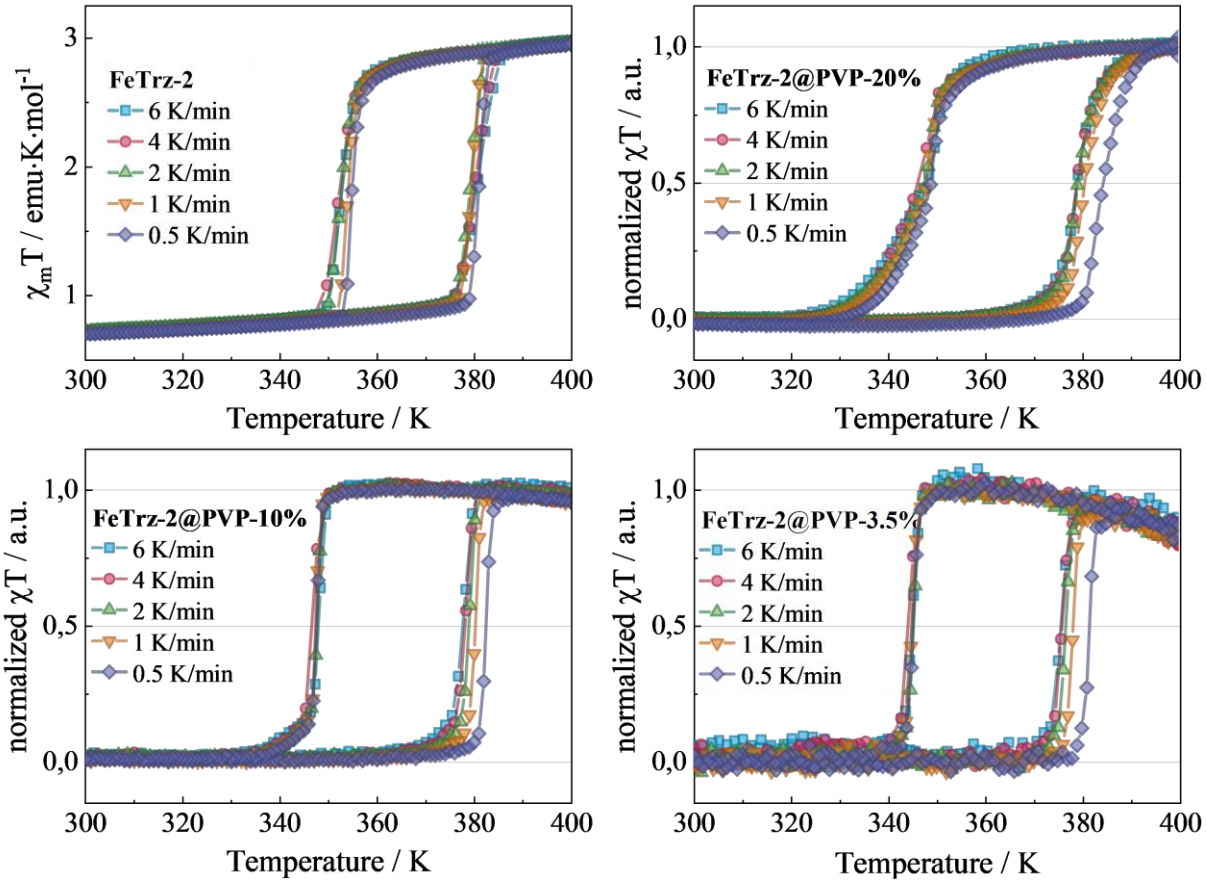

Figure 5.3.11 Normalised temperature dependence of $\chi \cdot T$ vs. T at scan rates ranging from 0.5 K·min^{-1} to 6 K·min^{-1} measured for powder **FeTrz-2** (top left), and it electrospun fibres with 3 concentrations: **20%** (top right), **10%** (down left), and **3.5%** (down right).

Firstly, for the reference powder sample, **FeTrz-2** NPs have been monitored, and only minimal changes were observed in the χT vs. T curves with varying temperature sweep rates, especially in cooling, when with an increase of the sweeping rate, the branch of the hysteresis shifted slightly to lower temperatures. Also worth noting is the minimal shift of the heating curve to the higher temperatures for the lowest sweeping rate (0.5 K/min).

A more significant impact of the temperature sweep rate on the SCO behaviour was observed in the electrospun fibres with three different concentrations of NPs (namely 20%, 10%, and 3.5%), summarized in Table 5.3.4. As the sweep rate decreased, the thermal hysteresis loops in the composites broadened, suggesting a stronger dependence on the scanning speed. This effect was particularly noticeable in the heating cycle, where the scan rate had a pronounced influence on the transition behaviour. This pronounced dependence suggests that the polymer matrix plays a critical role in modulating the kinetics of the SCO process, likely affecting how the nanoparticles respond to thermal stimuli and altering the transition dynamics compared to the

pure NPs. This influence of the polymer matrix on the thermal response highlights the importance of the composite structure in tuning the SCO behaviour.

Table 5.3.4 The summary of the magnetic properties of **FeTrz-2** NPs and their electrospun samples with different NPs content (**20%**, **10%** and **3.5%**) derived from temperature dependence of $\chi_m T$ vs T at scan rates ranging from 0.5 K min^{-1} to 6 K min^{-1}.

Sample	Scan rate / K·min^{-1}	$T_{1/2}$ (↑) / K	$T_{1/2}$ (↓) / K	ΔT / K
FeTrz-2	0.5	381.2	355.0	26.2
	1	379.7	354.1	25.6
	2	379.5	352.7	26.8
	4	380.5	352.5	28.0
	6	380.8	352.8	28.0
FeTrz-2/PVP-20%	0.5	384.7	348.6	36.1
	1	381.0	347.0	34.0
	2	379.5	346.0	33.5
	4	379.3	345.9	33.4
	6	379.3	346.1	33.2
FeTrz-2/PVP-10%	0.5	382.7	347.5	35.2
	1	380.5	347.4	32.9
	2	379.1	347.7	31.4
	4	378.5	346.5	32.0
	6	377.9	347.9	30.0
FeTrz-2/PVP-3.5%	0.5	381.5	345.3	36.2
	1	378.2	345.0	33.2
	2	376.7	345.3	31.4
	4	375.8	344.3	31.5
	6	375.8	345.0	30.8

At last, the properties of electrospun-based SCO composites were monitored over time in terms of stability. The results from magnetic measurements obtained from the freshly electrospun fibres were compared with data acquired after approximately four months (Figure 5.3.12A), with almost no or small changes in the spin-crossover response. Whereas, the degrading effect over time has been spotted for the suspensions used in the electrospinning process, resulting in a gradual loss of violet hue (Figure 5.3.12B).

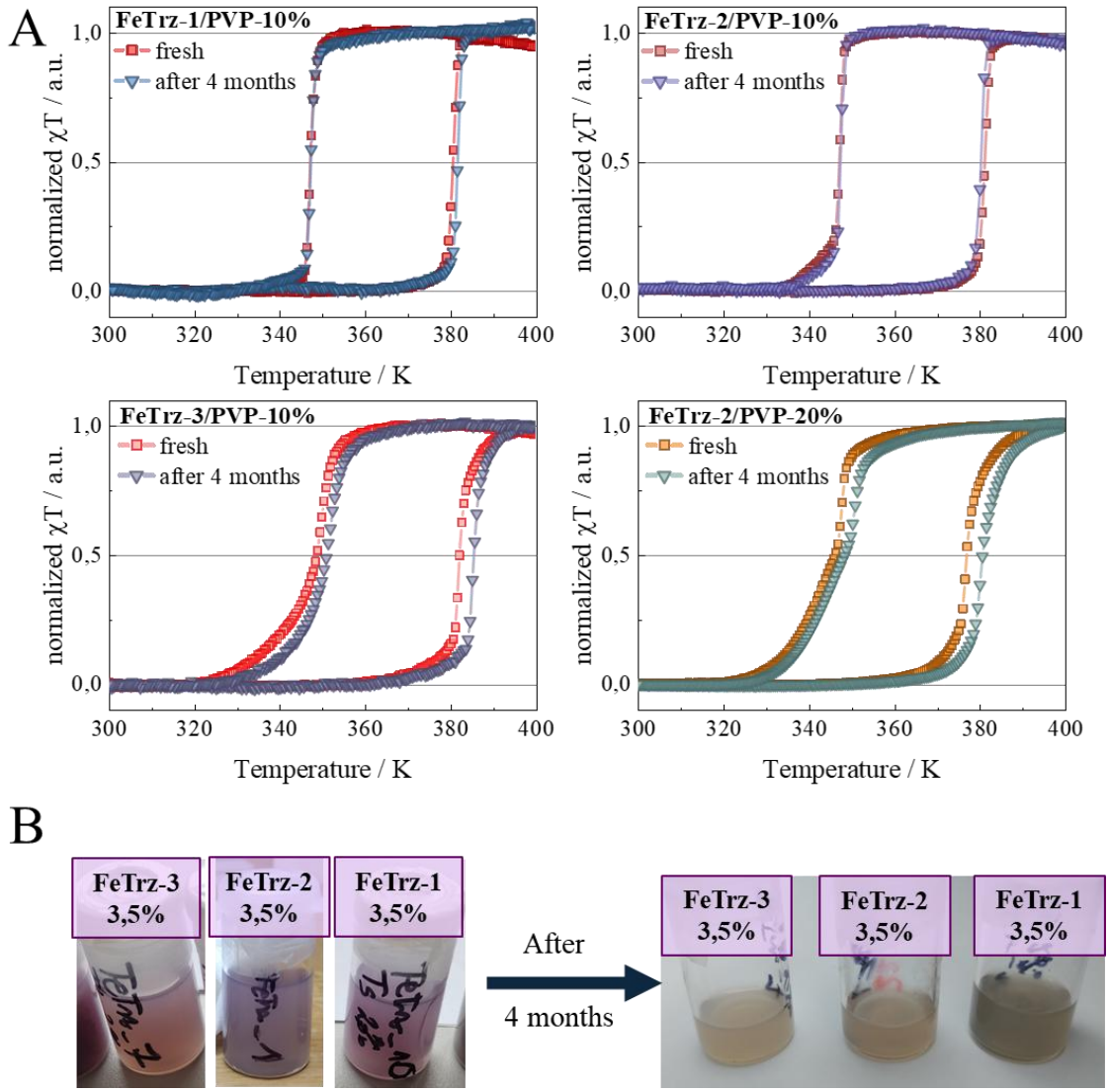

Figure 5.3.12 A) Comparison of the normalised $\chi \cdot T$ vs. T plots for electrospun fibres: **FeTrz-1/PVP-10%** (top left), **FeTrz-2/PVP-10%** (top right), **FeTrz-3/PVP-10%** (bottom left), and **FeTrz-2/PVP-20%** (bottom right) measured as freshly prepared electrospun samples and measured again after 4 months. B) Photographs of the electrospinning suspensions freshly prepared and after 4 months for the lowest **FeTrz** concentration.

5.4 Summary of the chapter

This chapter explores the characterization of Fe(II) spin-crossover (SCO) nanoparticles (NPs) and their incorporation into electrospun polymer-based composite fibres for advanced functional materials. The initial section focuses on the electronic and magnetic properties of **FeTrz** SCO NPs, probed through X-ray absorption spectroscopy, Mössbauer spectroscopy, and magnetic susceptibility measurements. Comparative analysis revealed variations in the spin transition temperature ($T_{1/2}$) across these techniques, driven by their differing sensitivities to the NPs' electronic and magnetic states. Factors such as core exciton formation and surface effects, particularly evident in XAS, contribute to these discrepancies, emphasizing the complexity of SCO transitions. These findings highlight the importance of a multi-technique approach to capture the interplay between surface, excitonic, and bulk properties, which is essential for optimizing SCO materials for practical applications.

The subsequent section details the preparation of composite materials by dispersing synthesized **FeTrz** NPs into an organic solvent compatible with a selected PVP polymer, followed by an electrospinning process to produce composite fibre mats. Variations in NP size and concentration led to distinct fibre morphologies, as observed via SEM, with NPs clustering in specific regions. DSC and magnetic measurements confirmed robust spin transitions in all samples, with NP size influencing transition temperatures and hysteresis widths. The SCO-based fibres exhibited stable magnetic properties over time, and compared to drop-casted films, they demonstrated superior spin-crossover behaviour, likely due to enhanced polymer-NP interactions and efficient solvent evaporation during electrospinning. Electron microscopy and magnetic analyses further validated the uniform integration of NPs within the fibre matrix, while the absence of significant degradation ensured the retention of SCO functionality.

The final section evaluates the potential of these electrospun SCO-based fibres for smart fabric applications. The fibres displayed improved mechanical properties, such as flexibility and robustness, compared to standalone NPs, which are often brittle. The electrospinning process ensured solvent-free composites with homogeneous NP distribution, minimizing degradation from prolonged solvent exposure. Comparative studies with drop-casted films highlighted the significant matrix effect in the electrospun fibres, where polymer interactions and silica coatings on the nanoparticles enhanced the SCO performance. This work presents a scalable and efficient method for fabricating multifunctional, switchable fibres, demonstrating their potential for applications in smart textiles and responsive materials, with dynamic and stable responses to temperature-induced spin transitions.

6. Composites based on the CT molecular chain

The following chapter will focus on the coordination chain based on the Fe and Ni metal centres $\{NH_4[Ni(cyclam)][Fe(CN)_6]\cdot 5\,H_2O\}_n$ (cyclam=1,4,8,11-tetraazacyclotetradecane), which at certain external conditions undergoes the charge transfer (CT) process, involving the metal centres, often called metal-to-metal charge transfer[66]. The chapter contains results from the synthesis and miniaturization, followed by studies of the electronic structure by X-ray absorption spectroscopy. The latter part of the chapter includes information on the preparation of composite materials based on the NiFe-chain particles in the organic polymer matrix in the form of electrospun fibre mats and drop-casted foils. Their properties, such as morphology, bistable properties, and reaction to external stimuli, are discussed. The results in the following subsections are part of a research study for which the manuscript has been submitted and is currently under review[195].

6.1 Multifunctional coordination chain based on Ni and Fe

The CN-bridged coordination chain $\{NH_4[Ni(cyclam)][Fe(CN)_6]\cdot 5H_2O\}_n$ (**NiFe-chain**) is a unique multistable system, which exhibits reversible thermal MMCT phase transition with bistability in the room temperature region. This recently designed compound serves as an analogue to the previously synthesized and extensively characterized polymer $\{(H_3O)[Ni(cyclam)][Fe(CN)_6]\cdot 5H_2O\}_n$[196], which is recognized for its ability to change the oxidation states of nickel and iron ions in response to dehydration and rehydration processes. The structure of $\{NH_4[Ni(cyclam)][Fe(CN)_6]\cdot 5H_2O\}_n$ chain magnet is shown in Figure 6.1.1.

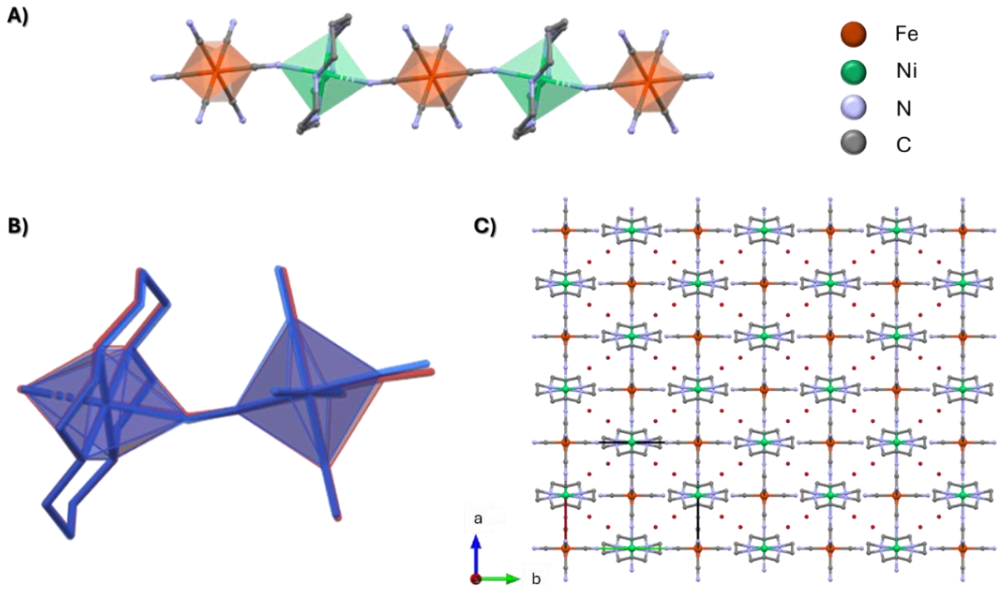

Figure 6.1.1 Structure visualisations of **NiFe-chain**. A) View of the molecular chain segment. (B) Superimposed LT (blue) and HT (red) structures within one Ni–Fe assembly centre and the neighbouring cyclam and cyano-ligands. (C) View along the *c*-axis of **NiFe-chains** packing along the *a*-axis, with intercalated NH_4^+ and H_2O molecules.

The selected coordination chain exhibits a remarkable ability to exist in three distinct forms at room temperature, with its state being switchable under external stimuli such as temperature, humidity, and pressure. These external factors induce changes in its magnetic properties (e.g., magnetic susceptibility) and optical properties (e.g., colour). At room temperature, the chain undergoes reversible transitions between two stable phases: a high-temperature (HT) Ni(II)-Fe(III) phase, characterized by a red coloration, and a low-temperature (LT) Ni(III)-Fe(II) phase, exhibiting a dark blue colour. The electron-transfer-driven phase transition is accompanied by thermal hysteresis within the room-temperature range, which can shift to higher temperatures under the influence of pressure. Notably, this enables the transition from the HT to the LT phase without the need for cooling. Moreover, dehydration of the chain results in its transformation into an anhydrous form, $\{(NH_4)[Ni(II)(cyclam)][Fe(III)(CN)_6]\}_n$ (deh), which is yellow. In this dehydrated state, electron transfer from Fe(III) to Ni(II) is inhibited; however, the process can be reversed through rehydration. Consequently, this complex demonstrates the capacity to exist at room temperature in three stable forms, each characterized by distinct magnetic and optical properties. The transitions between these forms are governed by electron transfer processes controlled by external stimuli (Figure 6.1.2).

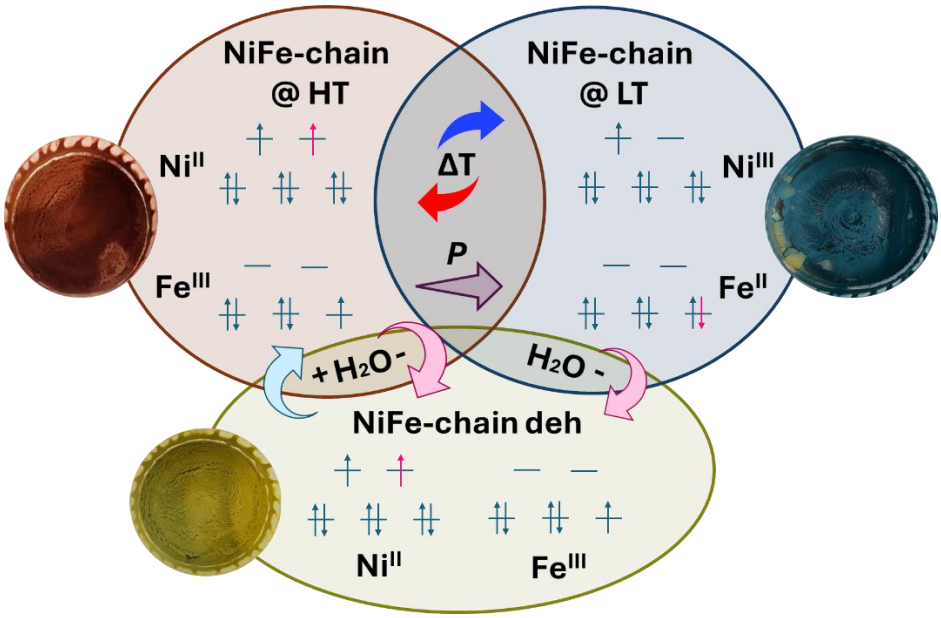

Figure 6.1.2 Schematic representation of stimuli-responsive changes in the electronic structure of **NiFe-chain**, between three stable phases: high-temperature (HT) phase, low-temperature (LT) phase, dehydrated phase.

6.1.1 Miniaturisation process of multifunctional coordination **NiFe-chain**

The preparation of bimetallic 1D chain-like structure $\{NH_4[Ni(cyclam)][Fe(CN)_6]\cdot 5\,H_2O\}_n$ crystals (**NiFe-crystals**) was performed according to the literature protocol[66]. The reaction undergoes in the aqueous solution of ammonium chloride (2M) into which $[Ni(cyclam)]^{2+}$ cation and $[Fe(CN)_6]^{3-}$ anion are introduced by dissolving pre-synthesised $[Ni(cyclam)](NO_3)_2$ and commercially available $K_3[Fe(CN)_6]$. The initial concentrations of the cationic and anionic parts are equal to 5 mM, each. After dissolution of the substrates, they are combined into one bottle, which results in immediate precipitation of the brown powder of a 2D honeycomb-like structure $\{[Ni(cyclam)]_3[Fe(CN)_6]_2\cdot z\,H_2O\}_n$ (**NiFe-layer**)[197]. For the process of recrystallization to take place and for better crystal growth, the bottle with precipitate in the NH_4Cl solution must be put aside in the water bath at a temperature of 40 °C for 2-4 weeks. The resulting dark-brown crystals of needle-like topology (typical dimensions: 3 mm length and 0.5 mm width) were taken out from the mother solution and quickly washed with warm distilled water at 40 °C to discard residual NH_4Cl on the surface.

To obtain sub-micro and nanoparticles of the **NiFe-chain** at the preliminary phase, two approaches were taken into account[198]. A top-down strategy, which involved direct miniaturization of the freshly synthesised crystals[199]. The second one, a bottom-up technique, required modifications at the stage of the synthesis, during formation of the coordination structure[200]. However, the fragility of the system to the changes of aqueous conditions, such as the addition of organic polymer during synthesis, resulted in the formation of the initial **NiFe-layer**. Due to the necessity of the presence of ammonium cation NH_4^+ and the prolonged time of the recrystallization phase, the modifications of the synthetic protocol to obtain nanoscale crystals of **NiFe-chain** have proved to be unsuccessful. And so, to obtain sub-micro and nanoscale

particles of the bistable **NiFe-chain,** the top-down approach has been utilized as the most effective method.

In the first step of the post-synthetic modifications, freshly synthesised as HT phase dark brown **NiFe-crystals** have been placed in the agate mortar and manually crashed to the point where, apart from the change to the powdered form, their colour transformed to blue, indicating change to the LT phase in response to the applied pressure. The prepared powder was transferred into the 20 ml vial and covered with chloroform or dimethylformamide (DMF) (~20 ml). The resulting suspensions of the **NiFe-chain** particles turned immediately dark green, indicating a dehydration of the **NiFe-chain** particles. As prepared suspensions were subjected to the sonification procedure, using an ultrasonication homogenizer probe operating at 30% power amplitude without pulsation for 45 minutes. To minimize solvent evaporation caused by overheating during the reduction process, the procedure was divided into three stages. Each was composed of 15 minutes of sonification followed by the time for cooling of the solvent. After the sonification stage, the suspensions were placed in a Petri dish and left aside for the complete evaporation of the solvent, with DMF being less prone to evaporate. The resulting light green powder of minimised **NiFe-chain** particles formed in chloroform (named **NiFe-microcrystals**) was scraped from the bottom of the vessel. In the case of particles prepared with DMF (named **NiFe-microcrystals/DMF**), a partial transition to brown powder was observed.

6.1.2 Morphology and magnetic properties after miniaturisation

In the first approach, the effectiveness of the top-down miniaturization technique was analysed with SEM microscopy. The samples for imaging were prepared by placing a drop of the suspension onto the cleaned silicon wafer and were used after the evaporation of the solvent. The freshly synthesised **NiFe-chain** crystals show a characteristic needle-like topology, shown in Figure 6.1.3. The proposed method to obtain sub-micro to nanoscale particles (**NiFe-microcrystals**) resulted in irregularly shaped grains, with evident loss of needle-like topology. The analysis of the particles' dimensions showed a fairly large size distribution, with an average size equal to 0.136 (± 0.100) μm for particles sonicated in $CHCl_3$ and 0.141 (± 0.093) μm in the case of DMF-sonicated crystals. Additionally, for the latter, hexagonally shaped particles were noticed, suggesting a partial recrystallization of the **NiFe-layer**, most probably due to the prolonged evaporation of solvent. For this reason, further study on **NiFe-microcrystals** was conducted only on powder after sonification in chloroform.

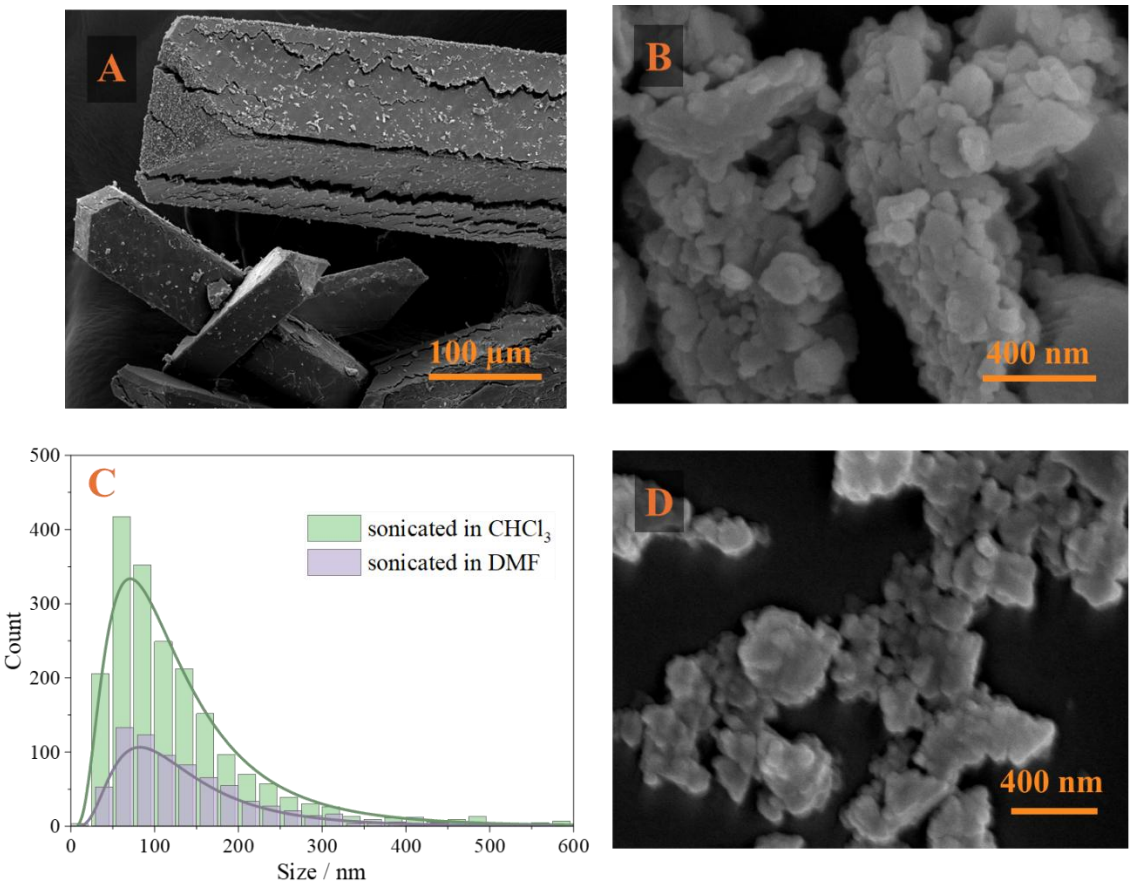

Figure 6.1.3 SEM image of NiFe-chain crystals before miniaturisation (A) and after sonication in CHCl3 (B) and DMF (D), with the histogram of their particle size distribution of NiFe-microcrystals (C).

As it was proven several times in literature, the size reduction of the coordination molecular magnetic materials may lead to changes in magnetic behaviour. These observations were mostly based on PBA structures[176], where superparamagnetic states were observed, or SCO systems[201], for which extensive research for the synthesis of nanoparticles was conducted through the years. For the latter, the changes of properties due to the diminished size were connected with surface effects, for which at the nanoscale their influence is much greater due to the increased surface-to-volume ratio.

To demonstrate that the charge transfer effect is preserved in the **NiFe-chain** after size reduction via sonication, magnetic measurements were conducted. For this purpose, both the crystalline form of the **NiFe-chain** (referred to as **NiFe-crystals**) and the sonicated powder form (**NiFe-microcrystals**), obtained through treatment in chloroform, were studied using magnetometry. Samples were placed in double-layer polyethylene (PE) bags, moistened with a few drops of 2 M aqueous NH_4Cl solution, and then sealed. The addition of ammonium chloride ensured that the magnetic measurements were conducted on hydrated phases, which are required for observing temperature-dependent electron transfer. Figure 6.1.4 shows the temperature dependence of magnetic susceptibility for the **NiFe-chain** before and after the miniaturization process, confirming the retention of the charge transfer effect post-sonication. At first glance, the profile for the miniaturized **NiFe-chain** shows hysteretic behaviour, which confirms that the optically observed change of colour derives from the thermally induced electron

transfer bistability. The visible difference in the profiles indicates that diminishing the size of particles makes the transition to the low-temperature (LT) phase more gradual, over a larger temperature range (ΔT = 19 K). This way, the full transition of the oxidation pair from Ni(II)–Fe(III) at high temperatures to Ni(III)-Fe(II) at low temperatures is reached at 265 K, making it 15 K lower than for the freshly synthesised crystals. On the other hand, the reverse transition, so change from LT to HT phase for **NiFe-microcrystals,** occurs at the same temperature range as for **NiFe-crystals**, without much change of the sharpness of the transition.

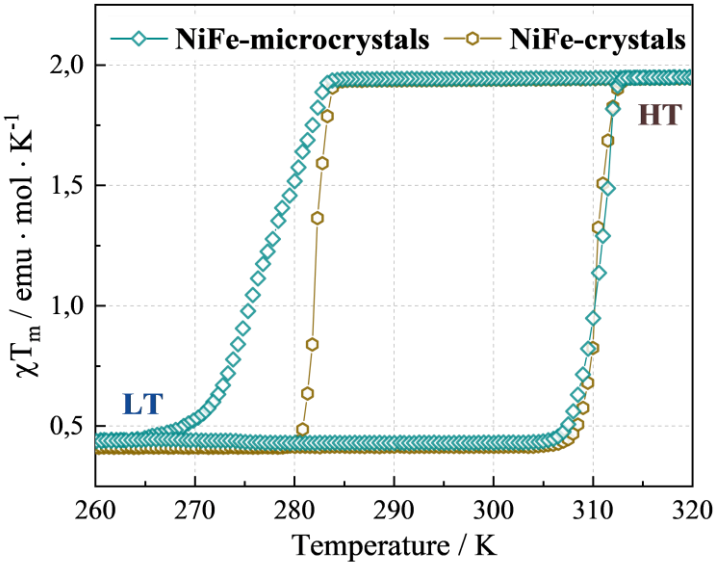

Figure 6.1.4 Thermal variation of χT for **NiFe-crystal** and **NiFe-microcrystal** samples.

6.1.3 XAS measurements on crystals and microcrystals

To directly probe the electronic structures of the metal ions in the **NiFe-chain** before and after miniaturization, XAS measurements at the Fe and Ni K-edges were performed as a function of temperature. The samples of **NiFe-chain** during measurement were sealed in a Polyethylene (PE) foil bag under a protective layer of 2M NH_4Cl solution. The Fe K-edge and Ni K-edge spectra of **NiFe-crystals** and **NiFe-microcrystals** recorded at 330 K and 250 K / 260 K are compared to the Fe and Ni K-edge of references: $K_4[Fe(CN)_6]/K_3[Fe(CN)_6]$ and $[Ni(cyclam)]^{2+}/[Ni(cyclam)]^{3+}$ nitrate salts (Figure 6.1.5). With the change of temperature, the antagonistic behaviour of Fe and Ni K-edges is observed, which confirms the complementary roles played by the two metal ions during the charge transfer process. The spectra recorded at 330 K correspond to the high-temperature (HT) phase: Ni(II)-Fe(III), while spectra measured at 250 K / 260 K correspond to the low-temperature (LT) phase: Ni(III)-Fe(II). This is fully consistent with the results obtained for the reference samples.

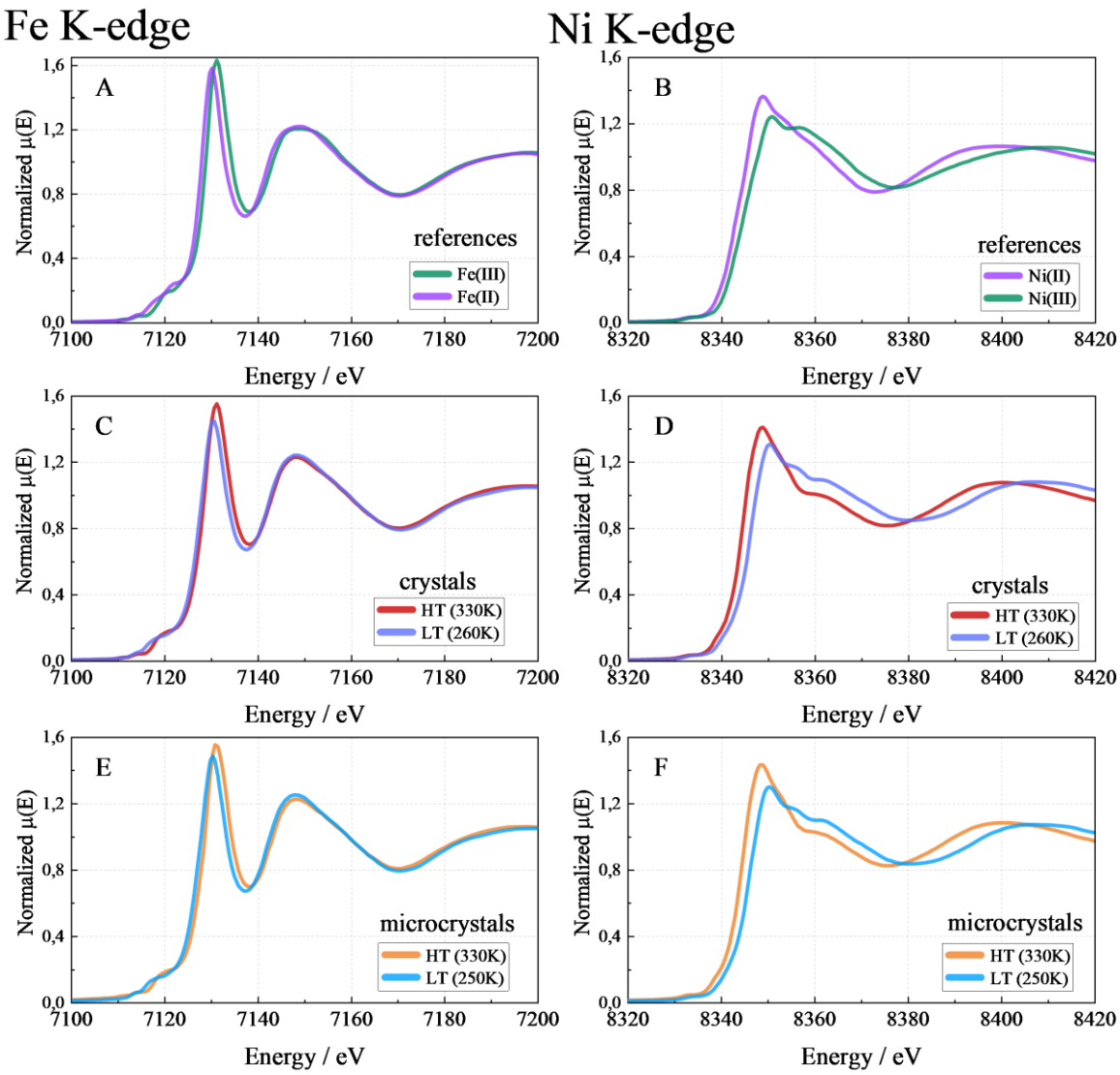

Figure 6.1.5 Normalized absorption coefficient at Fe (A, C, E) and Ni (B, D, F) K-edge for recorded references ($K_4[Fe(CN)_6]/K_3[Fe(CN)_6]$ and $[Ni(cyclam)]^{2+}/[Ni(cyclam)]^{3+}$ salts) and **NiFe-chain** in the form of crystals and microcrystals, for the last two recorded at temperature-dependent measurements at the border temperatures (330K for high temperature and 250 K or 260 K for low temperature), showcasing the antagonist change of XANES characteristics between Fe and Ni K-edges, due to the charge transfer effect.

While the overall modification of the Fe K-edge is relatively minor, due to the low spin state of Fe atoms in both HT and LT phases, significantly larger variations are observed at the Ni K−edge. These changes are attributed to the shortening of Ni–N bonds at low temperatures and a notable alteration in the Ni coordination sphere[202,203]. The primary characteristics of the K-edge spectra arise from the electric dipole-allowed 1s → 4p transitions, which dominate the spectral profile. However, in addition to these main features, small peaks or shoulders appear at lower energies, corresponding to the less intense 1s → 3d electric quadrupole transitions. Although these transitions are generally weaker, they provide valuable insights into the local electronic structure of the metal centre. In particular, the pre-edge region is widely utilized in the literature as a diagnostic tool for determining both the oxidation and spin states of transition metal ions, such as Fe or Ni. By analysing the intensity, energy position, and shape of these

pre-edge features, it is possible to gain crucial information about the electronic configuration and coordination environment of the metal centres.

Since the samples of interest contain Ni and Fe in both phases, which are 6-coordinated, the pre-edge features associated with octahedral coordination show the lowest intensity[184]. This is because, in centrosymmetric environments, these features correspond to electric dipole forbidden transitions. Nevertheless, very weak pre-edge peaks are still experimentally detected, with electric quadrupole coupling being the most likely mechanism behind the observed intensity. The analysis of the extracted pre-edge region (Figure 6.1.6) clearly shows temperature-dependent changes in the oxidation states of the Fe and Ni metal ions. Specifically, as the temperature decreases from 330 K to 260 K, Fe ions are reduced from Fe(III) to Fe(II), while Ni ions are oxidized from Ni(II) to Ni(III). Notably, at 250 K, the XAS features characteristic of Ni(II) and Fe(III) are completely absent. The observed shifts in the pre-edge positions, particularly for Ni, align with the trend observed for electric dipole-allowed 1s → 4p transitions, where higher oxidation states cause the peak position to shift to higher energies by approximately 1 eV (see Tables 6.1.1 and 6.1.2).

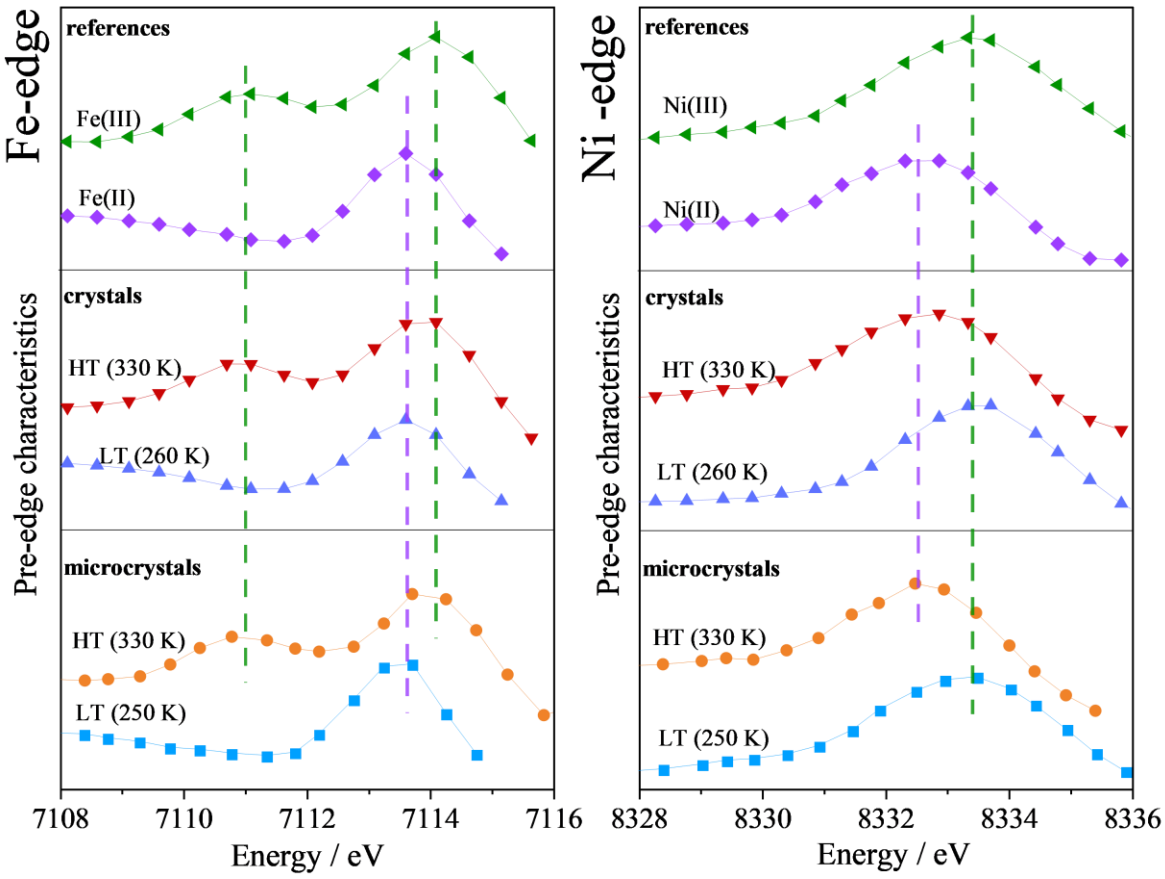

Figure 6.1.6 Pre-edge region of normalized absorption coefficient at Fe and Ni K-edge for references, **NiFe-crystals** and **NiFe-microcrystals** from temperature-dependent measurements (at the border temperatures).

The energy position and splitting of pre-edge features were found to vary systematically with oxidation and spin state, along with the geometry, which in the interested samples remained octahedral for both Ni and Fe in both phases. As it is observed for the reference samples only

for Fe(III), more than one feature appears in the pre-edge region. Being in a low-spin state and octahedral coordination, the ground state of the Fe(III) complex has a $(t_{2g})^1(e_g)^4$ hole configuration with two one-electron allowed excited configurations of $(t_{2g})^0(e_g)^4$ and $(t_{2g})^1(e_g)^3$. It results in the appearance of two pre-edge features of different intensity at ~7111 and ~7114 eV. Whereas, for Fe(II) complex in a low-spin octahedral coordination the ground state has $(t_{2g})^0(e_g)^4$ hole configuration and so $(t_{2g})^0(e_g)^3$ is the only allowed excited hole configuration, giving rise to a single quadrupole allowed transition into excited state, and the appearance of a single pre-edge feature at ~7113.5 eV. A change from two to one feature, when going from Fe(III) to Fe(II) also takes place for crystals and microcrystals upon heating (to Fe(III) at 330 K) and cooling (to Fe(II) at 250 K / 260 K), what has been presented in details in Table 6.1.1. In the case of Ni reference samples, there is no change in the number of pre-edge features, as Ni(II) in an octahedral environment d^8 electronic configuration allows only one possible configuration for the excited state, resulting in a single peak in this region. The same is true for Ni(III) complex, provided that it remains 6-coordinated in a low-spin state, with a ground state $(t_{2g})^0(e_g)^3$ hole configuration, and giving rise to an excited state of $(t_{2g})^0(e_g)^2$ and appearance of a single peak. However, the position of this single pre-edge peak shifts from ~8332.5 eV to ~8333.5 eV upon oxidation from Ni(II) to Ni(III). Similarly to Fe, the data originating from **NiFe-chain** in the form of crystals and microcrystals at marginal temperatures exhibit comparable characteristics (Table 6.1.2). These observations suggest that the electron transfer is highly efficient and proceeds to full completion under applied conditions for both **NiFe-crystals** and **NiFe-microcrystals**, leading to a quantitative conversion of Fe(III) to Fe(II) and Ni(II) to Ni(III).

Table 6.1.1 The analysis of pre-edge peak positions for Fe K-edge for reference salts, **NiFe-crystals**, and **NiFe-microcrystals** at maximal and minimal measured temperatures.

Compound	$K_3[Fe(CN)_6]$	$K_4[Fe(CN)_6]$	**NiFe-chain crystals**		**NiFe-chain microcrystals**	
Temperature	RT	RT	330 K	260 K	330 K	250 K
Metal oxidation	Fe(III)	Fe(II)	Fe(III)	Fe(II)	Fe(III)	Fe(II)
Pre-edge peak(s) energy	7111.20(8) 7114.11(3)	7113.59(2)	7111.05(7) 7113.90(3)	7113.57(3)	7111.07(9) 7114.03(4)	7113.40(3)

Table 6.1.2 The analysis of pre-edge peak positions for Ni K-edge for reference salts, **NiFe-crystals**, and **NiFe-microcrystals** at maximal and minimal measured temperatures.

Compound	[Ni(cyclam)] $(NO_3)_2$	[Ni(cyclam)] $(NO_3)_3$	**NiFe-chain crystals**		**NiFe-chain microcrystals**	
Temperature	RT	RT	330 K	260 K	330 K	250 K
Metal oxidation	Ni(II)	Ni(III)	Ni(II)	Ni(III)	Ni(II)	Ni(III)
Pre-edge peak energy	8332.58(4)	8333.51(4)	8332.74(4)	8333.57(1)	8332.75(7)	8333.42(5)

To gain deeper insight into the dynamics of the MMCT process, XAS spectra were measured in the broad temperature range (260-330 K) during heating and cooling. Figure 6.1.7 presents the spectral differences observed for **NiFe-crystals** and **NiFe-microcrystals** as a function of temperature, with reference data for **NiFe-crystals** recorded at 330 K, representing the highest temperature measurement, used as the standard. These absorption variations, directly associated with the charge transfer process, were subsequently utilized to calculate the fraction of the high-temperature (HT) phase (χ_{HT} phase)[188], by extracting the integrated area under the curves for certain temperatures (A_T) and normalized with the upper and lower limit, for LT (A_{LT}) and HT (A_{HT}) phase respectively, according to following equation:

$$x_{\mathrm{HS\ phase}} = \frac{(A_T - A_{\mathrm{LT}})}{(A_{\mathrm{HT}} - A_{\mathrm{LT}})}$$

The results are displayed in Figure 6.1.8, illustrating a clear transition from a predominant HT phase at elevated temperatures to a minority phase in the low-temperature region. This transformation exhibits a pronounced hysteretic behaviour between the heating and cooling scans. Moreover, a visible shift towards lower temperature is observed for the **NiFe-microcrystals** sample in comparison to **NiFe-crystals**. This observation is more distinct in comparison to the magnetic behaviour of the microcrystalline sample, especially in the heating curve. The discrepancies may derive from the difference in temperature stabilization, as for XAS, temperature was stabilised each time (during full scan measurements for two edges, ~1 h), whereas for magnetic measurement, it was performed in sweeping mode. Nevertheless, these results show that size reduction results in a lower temperature for the onset of the charge transfer process, thereby promoting the transition from the HT to the LT phase at reduced temperatures.

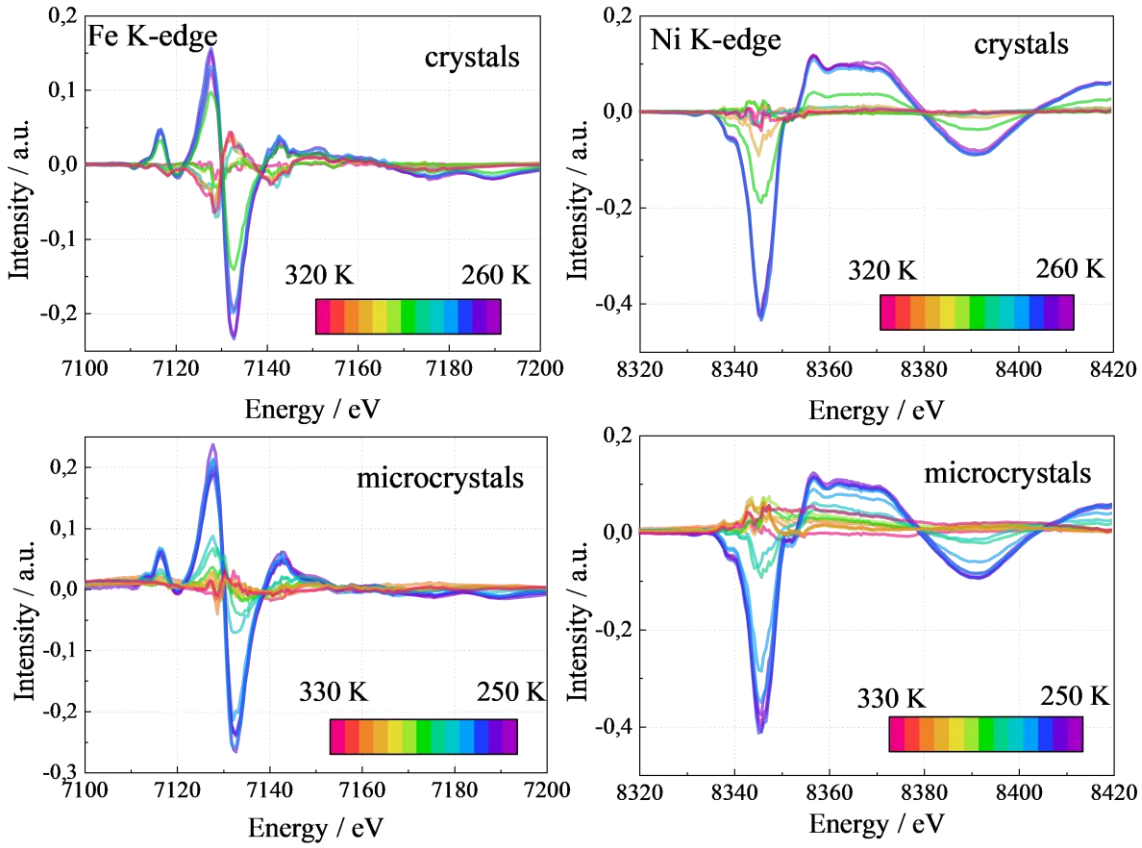

Figure 6.1.7 Temperature-dependent difference spectra for Fe (left panel) and Ni (right panel) edge, for **NiFe-crystals** (upper panel) and **NiFe-microcrystals** (lower panel). Difference spectra have been obtained by subtracting the data recorded on the Fe and Ni edges at 330 K, as the highest temperature measurement for **NiFe-crystals.**

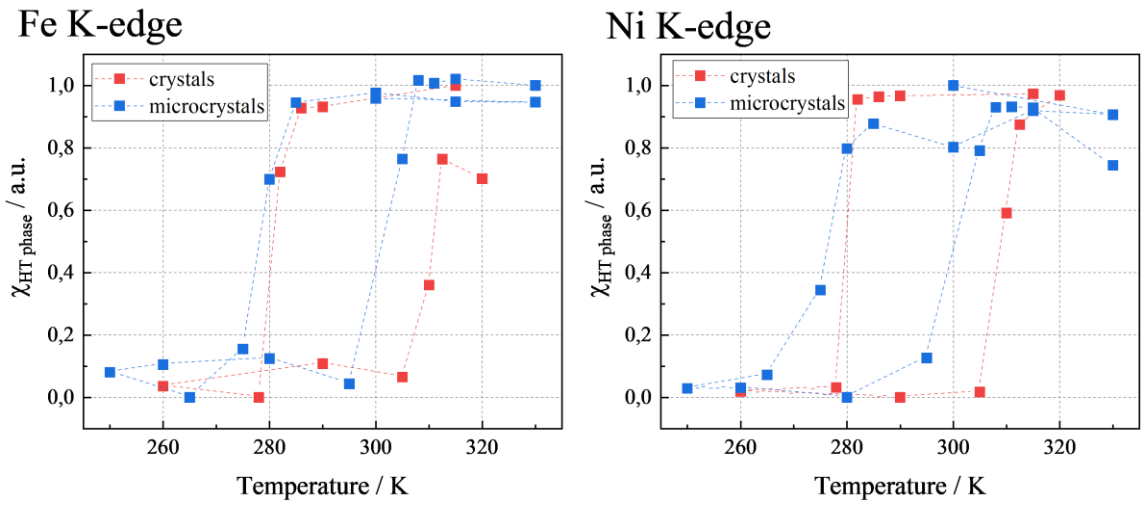

Figure 6.1.8 Calculated fraction of the high-temperature (HT) phase $\chi_{HT\ phase}$ from the difference spectra in the following ranges: for Fe K-edge in the 7110-7165 eV range and Ni K-edge in the 8330-8404 eV range.

6.2 Electrospun-based composites with **NiFe-micro-crystals**

In the subsequent study, the miniaturisation methodology of **NiFe-chain** was further developed by incorporation of as-prepared **NiFe-microcrystals** into an organic polymer matrix, specifically in the form of electrospun fibres. Due to the fragility of the **NiFe-chain** under aqueous/alcoholic conditions, certain modifications in the choice of polymer, solvents, and the polymer suspension preparation were undertaken, compared to previous chapters. The following subsection describes the analysis of polymer matrix influence on the possibilities to obtain switchable electrospun fibres containing **NiFe-chain** particles.

6.2.1 Preparation of electrospun fibre mats

During the preparation of electrospun mats with embedded **NiFe-chain** particles**,** two kinds of organic polymers were chosen: 1) hydrophobic and semi-crystalline poly(ε-lactone) (**PCL**) with M_w = 80 000; 2) amphiphilic and amorphous poly(2-vinylpyridine-co-styrene) (**P2VP-PS**) with M_w = 220 000. In the composite preparation for effective fibre production, two types of solvents were taken into account: 1) a mixture of chloroform–methanol with a volume ratio of $CHCl_3$: MeOH equal to 3:1, for both **PCL** and **P2VP-PS**; 2) pure dimethylformamide DMF for **P2VP-PS** fibre production.

Electrospun fibres of pure polymers

Before introducing **NiFe-chain** particles into the solutions containing organic polymers such as **PCL** or **P2VP-PS**, it was necessary to establish an optimized electrospinning process. Due to the relatively high popularity of **PCL** polymer in producing electrospun fibres, the most suitable concentration of the polymer in the solvent mixture, such as chloroform-methanol (3:1), was known without prior optimization (10% wt.)[204]. The copolymer **P2VP-PS**, being relatively less explored for electrospun fibre production, required an initial optimization process. For the commonly used chloroform–methanol solvent mixture, an optimal polymer concentration of 12 wt% was selected based on established laboratory protocols[145]. However, when the solvent was changed to dimethylformamide (DMF), further optimization was necessary. Due to DMF's significantly lower volatility compared to the chloroform–methanol system, a higher polymer concentration, up to 22 wt%, was required to achieve successful fibre formation[205,206]. SEM images showcasing the morphology of the pure electrospun fibres of **PCL** (from $CHCl_3$ with MeOH), **P2VP-PS** ($CHCl_3$+MeOH), and **P2VP-PS** (DMF) are shown in Figure 6.2.1. It is worth noticing the difference between the polymers, as without any other additions, **PCL** fibres are more prone to form a lumpy texture, whereas fibres of **P2VP-PS** form a more porous structure along the fibres. It is even more evident for the DMF sample, as during the electrospinning process, this solvent evaporates more slowly than a mixture of chloroform and methanol, which was shown to have a great effect on the porosity of the electrospun fibres. The difference between the pure polymer fibres is also evident in the analysis of the average diameter presented in the form of a histogram. For the same reason as it was for increasing porosity, the DMF-based fibres are characterised by the lowest value of the average diameter, 0.539 (± 0.157) μm,

with the smallest size dispersion among the others. On the contrary, the preparation of the **P2VP-PS** fibres from the $CHCl_3$ and MeOH mixture provided fibres with the highest value of the average diameter and increased size distribution – 1.350 (± 0.451) µm. Changing to the **PCL** polymer provides fibres with a decreased average diameter of 0.787 (± 0.274) µm.

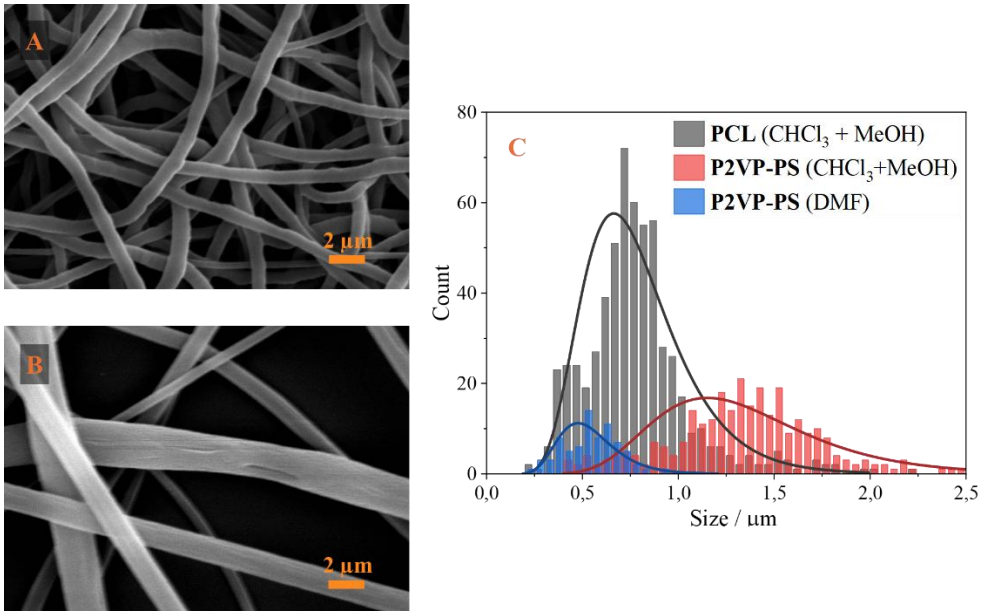

Figure 6.2.1 SEM images of **PCL** (A) and **P2VP-PS** (B) electrospun from $CHCl_3$ and MeOH mixture, with the comparison of the size distribution of the average diameter of produced electrospun fibres of pure polymers used to prepare composite materials with **NiFe-chain** (C).

Preparation of electrospinning solutions containing **NiFe-microcrystals**

It is important to emphasize the sensitivity of the **NiFe-chain** system to certain solvents, particularly water and low-carbon alcohols such as methanol and ethanol. Exposure of **NiFe-chain** crystals to these solvents induces a structural transformation from the original one-dimensional (1D) chain configuration to a two-dimensional (2D) honeycomb-like **NiFe-layer**, typically observed as a brown powder. This recrystallization is driven by the removal of ammonium cations from the coordination framework, an essential component for maintaining the charge transfer properties of the system. The explanation of the importance of NH_4^+ is based on the formation of hydrogen bonds, which favour the electron transfer between metal centres. For this reason, following the correct step order in composite preparation is crucial for successfully producing bistable composites based on the **NiFe-chain.** Additionally, during optimization of composite production, it was noticed that the **NiFe-chain** will remain stable under certain solvents, such as DMF. However, due to prolonged evaporation, the recrystallization process starts to take place for the suspension of **NiFe-microcrystals** in DMF without any other additions. And so, for this solvent, electrospun composites containing **NiFe-chain** were prepared in a slightly different manner.

Chloroform-methanol (3:1) mixture

For the preparation of electrospinning solutions using a $CHCl_3$ – MeOH mixture, miniaturized **NiFe-chain** powder was incorporated as a component in both **PCL** and **P2VP-PS** polymer

matrices. To achieve a homogeneous dispersion of **NiFe-chain** particles in the organic polymer solution, the powder was first redispersed in an appropriate amount of chloroform and briefly sonicated using an ultrahomogenizer probe for approximately 45 minutes. Next, methanol was added to the vial. The dark green colour of the suspension was a good indicator that, at that time, no recrystallization was taking place due to the presence of MeOH molecules. Then, an appropriate organic polymer was quickly added to the suspension. The amounts of the organic polymer were calculated based on the weight of the suspensions to provide a mass concentration of PCL in the polymer suspension equal to 10% wt. (**NiFe- fibres 1**) or the percentage of suspension equivalent to 12% wt. for P2VP-PS polymer (**NiFe-fibres 2**). Immediately after adding the organic matrix to the vessels, the mixtures were placed onto the gyromixer to provide a constant mixing during a slow dissolution of organic polymers into the suspensions. Additionally, it also allowed the suspended particles of **NiFe-chain** to constantly mix in the whole volume of the polymer solution and decrease the probability of forming clusters, which then would settle on the bottom of the vial. Detailed amounts of each component are presented in Table 6.2.1.

DMF-based solution

The preparation of polymer solutions in DMF containing **NiFe-chain** and **P2VP-PS** polymer required a different approach for the preparation of initial **NiFe-microcrystals**. However, as it was shown, the change of the solvent to DMF did not have any greater influence on the size of the particles. As there was no evaporation stage, for the **NiFe-chain** to remain in its form, the suspension was sonicated with an ultrahomogenizer probe in 5 intervals with a short 2-min sonication time, to minimize the effect of overheating. Then, appropriate amounts of **P2VP-PS** were added into the vial to give a mass concentration of the polymer to the whole content of the vessel equal to 22% wt. (for details, see Table 6.2.1). The bottle was placed onto the gyromixer to the point of complete dissolution of the **P2VP-PS** polymer.

Table 6.2.1 Detailed amounts of the used materials to produce electrospinning solutions containing **NiFe-chain** with calculated **NiFe-chain** mass concentration in final electrospun fibres.

Sample	Amount of **NiFe-microcrystals** / mg	$CHCl_3$: MeOH / ml: ml	DMF / ml	PCL / g	P2VP-PS / g	% wt. **NiFe-chain** in electrospun fibres
NiFe-fibres 1 (PCL)	180	6: 2	-	1.096	-	14.1
NiFe-fibres 2 (P2VP-PS)	160	6: 2	-	-	1.200	11.8
NiFe-fibres 3 (P2VP-PS)	180	-	4	-	1.117	13.9

Electrospinning process of composites based on **NiFe-chain**

In the protocol for obtaining electrospun mats, the prepared polymer suspensions were introduced into the plastic syringe, attached to the electrospinning setup described in Chapter 3.

After cleaning the metal plate as counter electrode, high voltage was applied of either 11 kV for **PCL** and **P2VP-PS** solutions based on the $CHCl_3$ – MeOH mixture (**NiFe-fibres 1** and **NiFe-fibres 2**). For the DMF-based solutions with **P2VP-PS** polymer, the applied voltage was equal to 13 kV (sample **NiFe-fibres 3**). During the electrospinning process, the temperature oscillated around 20-210 °C, and the relative humidity in the electrospinning chamber was kept in the range from 36% to 47%. The syringe filled with a composite polymer solution was connected to the pump, which kept a constant flow rate at 1.5 ml/h. In the cases of clogging of the needle, the flow rate was momentarily increased to 4 ml/h. The fibrous mats were collected randomly on a metallic plate, placed at a distance of 10.5 cm from the tip of the needle. From all the polymeric suspensions containing **NiFe-chain** with an initial dark green colour of the solutions, the resulting mats had a distinctive light yellow colour.

6.2.2 Morphology of the electrospun composites with NiFe-chain

Composite materials of **NiFe-chain** obtained in the form of electrospun fibres were first observed under an optical microscope for mats in both polymers (PCL and P2VP-PS). The images (Figure 6.2.2) present continuous materials without any disruptions, with visible changes in their colours depending on the external conditions. And so, a freshly obtained fibre mat is characterized by a light yellow colour. After placing them in high humidity, a change to light brown is noticed, and later, by setting them aside in the fridge at 40 °C, it turns to light blue. Additionally, noticeable differences between polymers can be pointed out, such as the formation of a paper-like layer by electrospun **PCL** matrix and a cloud-like material with the use of **P2VP-PS** in the formation of composites. In both cases, the presence of small dots of **NiFe-chain** clusters can be observed within the materials with the magnification available by the optical microscope. The colour changes derived from the functionality of the coordination system are easily distinguishable but of much lower intensity than the pure powdered form.

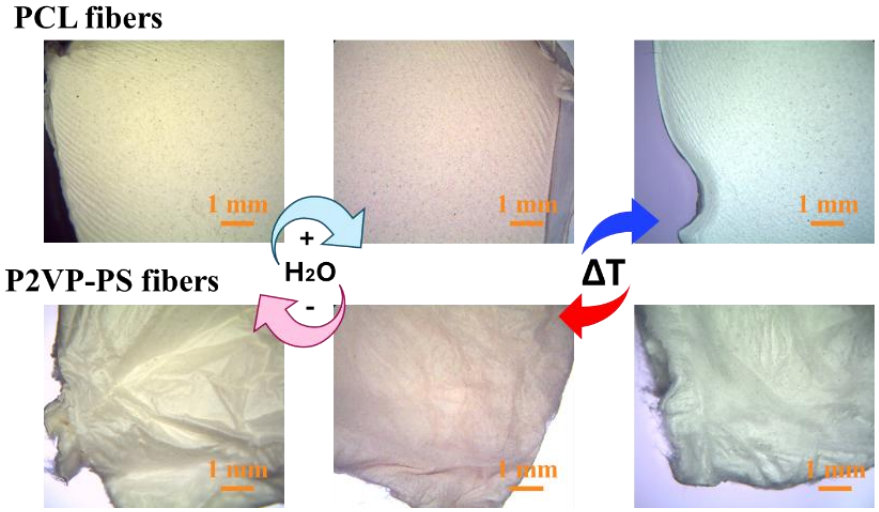

Figure 6.2.2 Optical microscope images of **NiFe-fibres 1** (PCL) (upper row) and **NiFe-fibres 2** (P2VP-PS) (lower row) in three different forms, as dehydrated (yellow), in HT form (light brown), and LT form (light blue).

To take a closer look at electrospun fibres with **NiFe-chain**, a series of SEM images were made for all three types of the composites (**NiFe-fibres 1, NiFe-fibres 2,** and **NiFe-fibres 3**), which are presented in Figure 6.2.3. For SEM imaging, the fibres were directly collected on the cleaned silicon wafer in small portions and sputtered with Au, for better imaging, as fibres represent 3D structures. The morphology of the pure polymer fibres remains similar in the composites, with the appearance of thicker regions along the fibres.

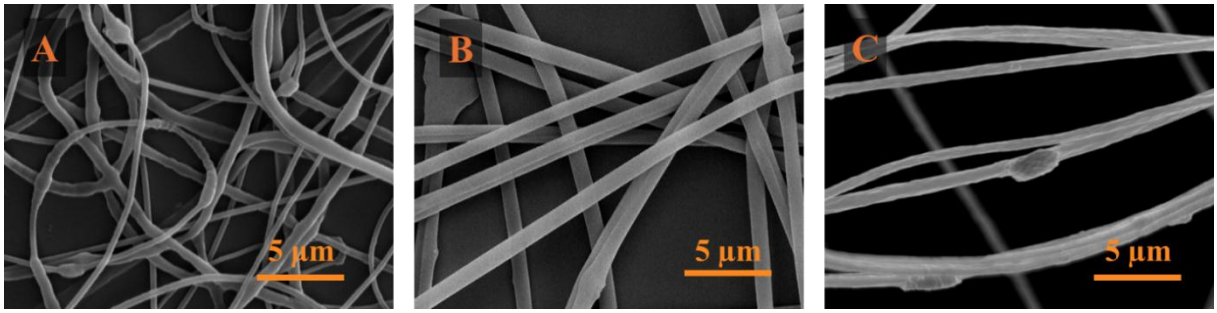

Figure 6.2.3 SEM images of **NiFe-fibres 1**/PCL (A)**, NiFe-fibres 2**/P2VP-PS (B), and **NiFe-fibres 3**/P2VP-PS (C) obtained with SE detection.

To correlate the thicker regions of the fibres with the presence of **NiFe-chain** particles, a different detection was chosen – instead of secondary electrons (SE), backscattered electrons (BSE) were measured. For this type of imaging, it was necessary to use carbon-coated fibres, as the layer of Au on the surface of the organic polymer would not give any other signal, except for gold. Images obtained with this type of detection are presented in Figure 6.2.4. To correctly interpret them, it is important to mention the relation used in electron microscopy, that chemical elements with higher atomic number appear brighter and with better contrast during imaging. With a BSE detector and carbon coating, it was possible to distinguish regions with higher electron content, such as Ni and Fe atoms, compared to the organic matrix composed of C, H, O, and N. In this approach to characterize the obtained fibres, the appearance of the thickenings in the fibres can be explained, as **NiFe-chain** grains of irregular shapes can be easily noticed along the fibres. Not only that, the filler particles can also be found along fibres, where no expansion of the matrix is evident, or the space along the fibre is only partially occupied.

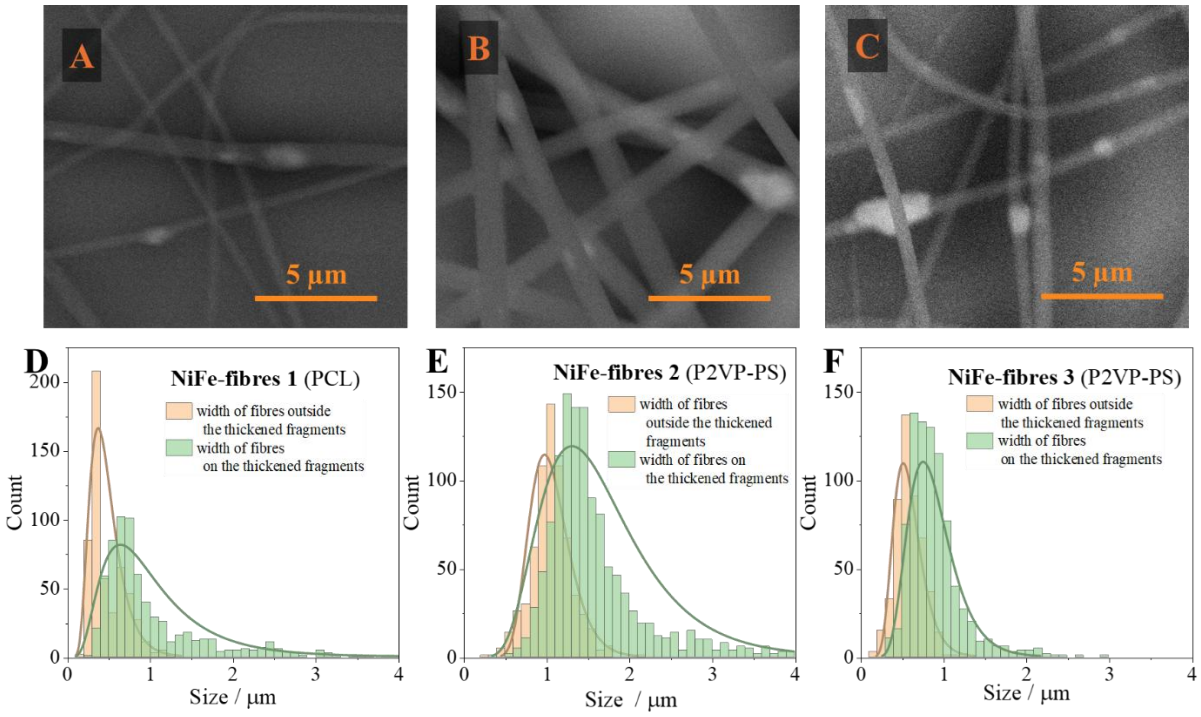

Figure 6.2.4 SEM images of **NiFe-fibres 1** (A)**, NiFe-fibres 2** (B), and **NiFe-fibres 3** (C) obtained with BSE detection and their appropriate size distribution of fibre diameters outside and at NiFe-chain grains embedded in electrospun fibres (D–F).

The knowledge of the fibres' composition was used during the analysis of the fibres' diameters, as it was divided into two regions – purely organic fibre and the diameters of the broadened fragments, with histograms presented in Figure 6.2.4. For the fibres based on **PCL,** the predominant diameter distribution falls within the range of 0.473 (± 0.198) µm in the thinner regions, described as outside the thickened part. The fragments enriched with the **NiFe-chain** increased the size of the fibres up to 1.052 (± 0.659) µm. As for the thickest strings produced with **P2VP-PS** polymer obtained from the chloroform-methanol mixture, this trend was also evident after introducing the **NiFe-chain**. For this material, the average diameter of the fibres' width ranges from 1.062 (± 0.254) µm to 1.689 (± 0.727) µm, in the regions without and with **NiFe-chain** filler, respectively. In correlation to the purely polymeric electrospun fibres of **P2VP-PS** from DMF solvent, the incorporation of the coordination particles increased the average diameters of the fibres from 0.595 (± 0.183) µm in the regions without evident presence of **NiFe-chain** particles to 0.890 (± 0.295) µm at the sites with embedded grains. The values for the average size of fibres before and after the incorporation of functional material have been summarized in Table 6.2.2, together with the size of **NiFe-microcrystals** mentioned in the previous subsection.

Table 6.2.2 Size distribution of composite fibres width (**NiFe-fibres 1/2/3**) measured in two regions: far from the **NiFe-chain** grains and in the regions rich in **NiFe-chain** particles. For comparison, the average size of **NiFe-microcrystals** after sonication in $CHCl_3$ and DMF is given, together with the average width of electrospun fibres of undoped **PCL** and **P2VP-PS** polymers.

Sample	Polymer matrix	Solvent	Mean diameter of the fibre far from the NiFe grains / µm	Mean diameter of the fibre at the NiFe grains / µm
NiFe-fibres 1	PCL	$CHCl_3$ +MeOH	0.473 (± 0.198)	1.052 (± 0.659)
NiFe-fibres 2	P2VP-PS	$CHCl_3$ +MeOH	1.062 (± 0.254)	1.689 (± 0.727)
NiFe-fibres 3	P2VP-PS	DMF	0.595 (± 0.183)	0.890 (± 0.295)
Sample		Solvent	Size of the grains deposited after miniaturization / µm	
NiFe-microcrystals		$CHCl_3$	0.136 (± 0.100)	
NiFe-microcrystals/DMF		DMF	0.141 (± 0.093)	
Sample		Solvent	Mean diameter of pure fibres / µm	
PCL fibres		$CHCl_3$ + MeOH	0.787 (± 0.274)	
P2VP-PS fibres		$CHCl_3$ + MeOH	1.350 (± 0.451)	
P2VP-PS fibres		DMF	0.539 (± 0.157)	

The validity of the observations derived from the SEM imaging with SE and BSE detection modes was also confirmed by EDS mapping. The measurements were performed on the uncoated samples, but due to the relatively small percentage of areas rich with high atomic number elements, such as Ni or Fe, in comparison to the silicon wafer and carbon-rich organic matrix, the signal-to-noise ratio is small. However, regions that were correlated with areas enriched with **NiFe-chain** particles (the thickenings along the fibres) are quite easily distinguishable, with much more intensive colours both for Ni and Fe, compared to the rest (Figure 6.2.5).

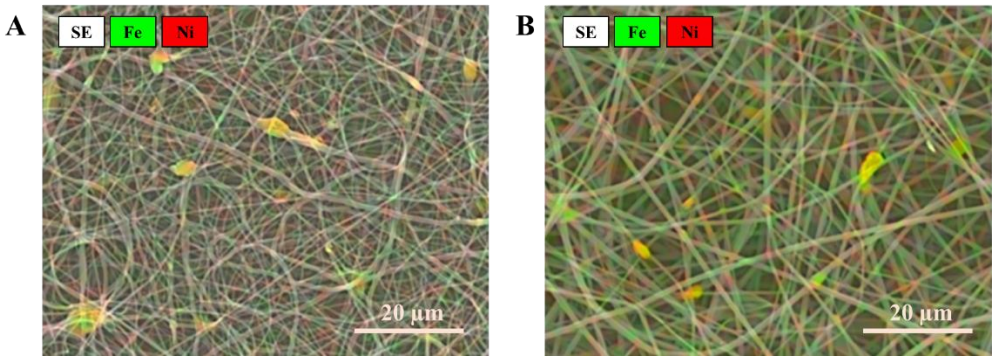

Figure 6.2.5 EDS mapping of Fe (green) and Ni(red) performed for (A) **NiFe-fibres 1** (PCL) and (B) **NiFe-fibres 2** (P2VP-PS).

In the case of grains that in Figure 6.2.4 are of much smaller size compared to organic fibre, it was necessary to perform a further in-depth analysis with the use of much more advanced equipment. For that reason, fibres of **NiFe-fibres 3** (P2VP-PS) were investigated under EDS coupled with a high-angle annular dark-field scanning transmission electron microscope (HAADF-STEM). Image obtained from EDS resulted in the more precise mapping of the elements (Ni and Fe), illustrating that during the preparation, fibres with finely tuned and partially separated **NiFe-chain** particles were produced, without much interference into the structure of the polymer string (Figure 6.2.6), what had consequences on the properties of the material.

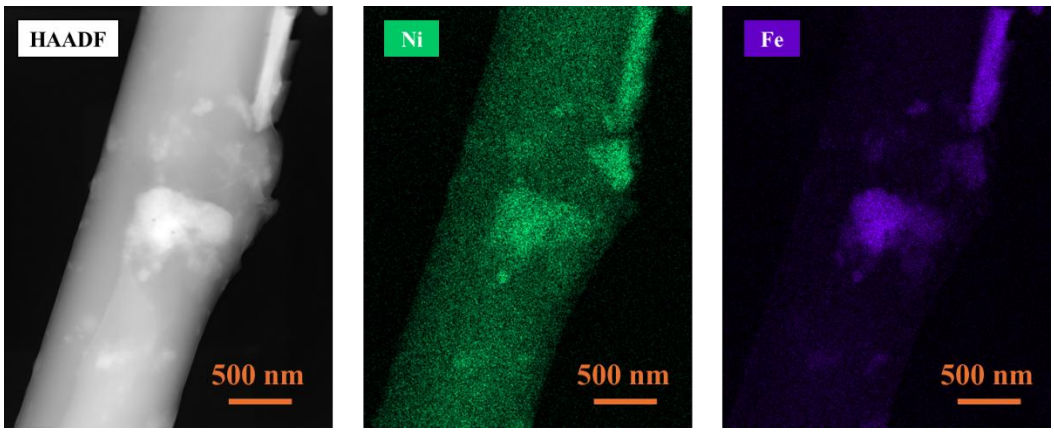

Figure 6.2.6 HAADF-STEM image (left) and corresponding elemental distribution maps of Ni (green) and Fe (violet) in **NiFe-fibres 3** (P2VP-PS) composite fibre.

The incorporation of **NiFe-chain** into the electrospun fibres was also studied with a Raman spectrometer with a 532 nm laser. In the original study reporting the synthesis of the **NiFe−chain**, IR spectroscopy was employed to investigate the vibrational states of the coordination structure. However, in the case of the composite materials, the results were inconclusive due to the dominant IR signal from the organic polymer, which overshadowed the spectral features of the NiFe coordination network. During measurements of **NiFe-chain** powder, a laser power of only 1% was required, as the sample was highly sensitive to laser-induced burning. In the resulting spectra, a characteristic double band was observed, corresponding to the stretching vibrations of the cyano-ligands, with peaks at 2126 cm^{-1} and 2146 cm^{-1} (Figure 6.2.7). For the composite material containing the organic polymer, a laser power of 10% was used without causing thermal degradation. The surrounding polymer matrix appeared to provide thermal protection, resulting in significantly improved signal quality for the **NiFe-chain**. Furthermore, the higher laser power enabled effective probing of the thicker regions of the electrospun fibres, which were enriched with the **NiFe-chain**. As for the organic polymer matrices (**PCL** and **P2VP-PS**) in the region of Raman shift between 2000 cm^{-1} and 2200 cm^{-1}, no bands appear. So then, for **NiFe-fibres 1** (PCL) and **NiFe-fibres 2** (P2VP-PS), the double bands that can be found at ~2125 cm^{-1} and ~2145 cm^{-1} can only correspond to the cyano-ligand in the coordination structure. There are no evident changes after embedding the **NiFe-chain** into the semi-crystalline and amorphous polymers. Only a slight blue shift is observed for the **P2VP−PS** based fibres to 2128 cm^{-1} and 2148 cm^{-1}. In the case of the polymer matrix, for the **PCL,** a characteristic band in the range between 1700 cm^{-1} and 1750 cm^{-1} corresponds to the stretching vibration of the carbonyl group C=O in the **PCL** chain (marked with a violet box)[207].

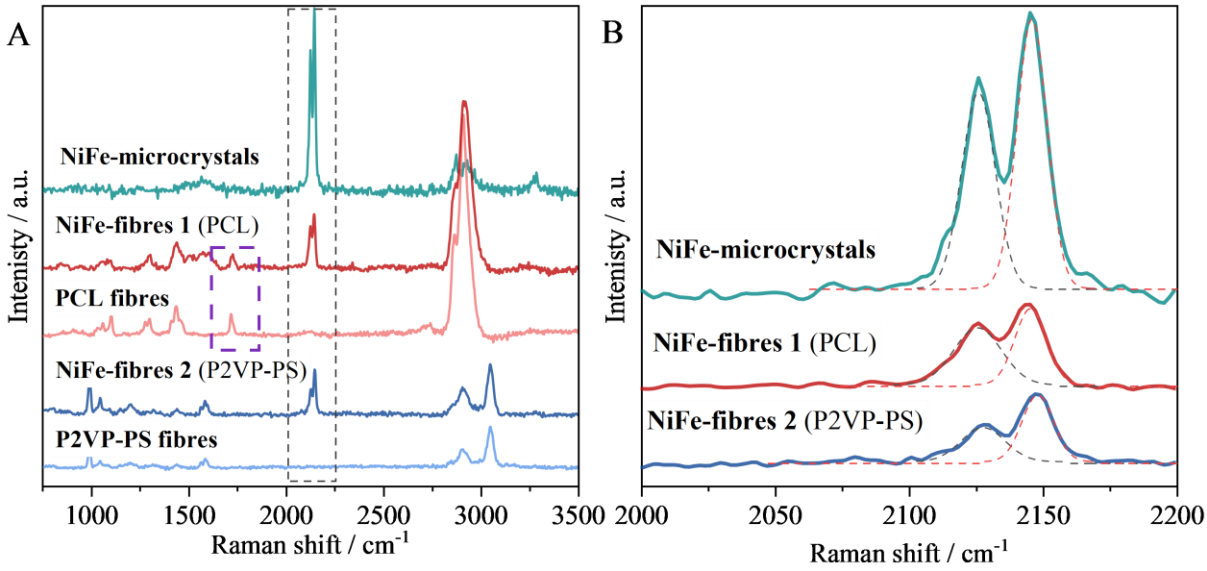

Figure 6.2.7 (A) Raman spectra for the **NiFe-chain** and its composites, **NiFe-fibres-1** and **NiFe-fibres-2**. (B) Enlarged region of Raman spectra with bands derived from vibrational stretching of the cyano-ligands.

6.2.3 Magnetic characterisation of electrospun **NiFe-chain** composites

To probe the temperature-induced charge transfer effect on the composite materials and confirm the origin of the colour change to the electron transfer (Figure 6.2.8), DC magnetization was measured with variable temperature (250-320K) and applied field of 1000 Oe. In initial tests, magnetization appeared temperature-independent, and samples retrieved from the straw holder exhibited a yellow colour, suggesting possible dehydration during measurement. To mitigate this, the composite samples were sealed in double-layer polyethylene (PE) foil bags, as was done for the **NiFe-crystals**, to prevent dehydration under the vacuum conditions of the SQUID magnetometer. To ensure stability and reproducibility in the thermal hysteresis behaviour of magnetic susceptibility, multiple temperature cycling experiments were performed. Similar to spin crossover-based systems, the magnetic susceptibility data were corrected using the Curie–Weiss law to isolate the contribution from the **NiFe-chain**. The analysis of the temperature-dependent magnetic susceptibility of the electrospun fibres filled with **NiFe-microcrystals** showed reproduced behaviour recorded for **NiFe-chain** crystals (Figure 6.1.4). All the information about the transition temperatures and width of the thermal hysteresis loops for composites and starting **NiFe-chain** material has been summarized in Table 6.2.3. In general, the composites exhibit a slight shift toward lower values of the transition temperatures both in the cooling and heating cycles. The most pronounced differences can be observed for the **P2VP-PS** fibres produced from both types of solvent, the mixture of $CHCl_3$ with MeOH and from DMF.

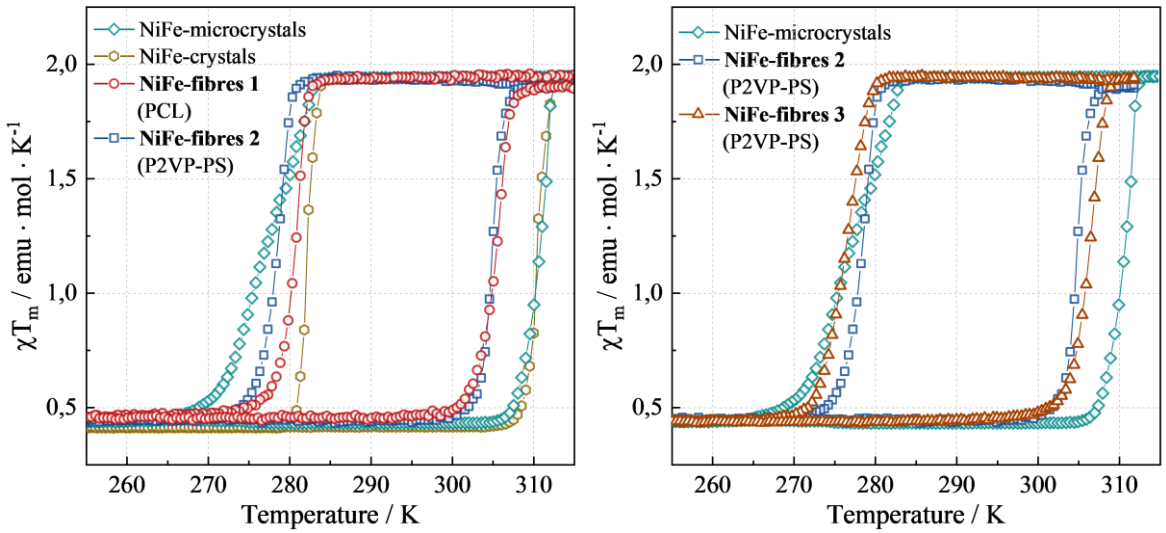

Figure 6.2.8 Variable-temperature magnetic susceptibility recorded at a sweeping rate of 1 K/min at 1kOe for the composites of **NiFe-chain** in comparison to **NiFe-chain** in the form of crystals and microcrystals. For the composite samples, the results are shown after employing a correction based on the Curie-Weiss law.

The concentration of **NiFe-chain** particles embedded within electrospun fibres of PCL and P2VP-PS has been quantified using molar magnetic susceptibility measurements as a function of temperature. Under the assumption of a complete transition from the high-temperature (HT) to low-temperature (LT) phase for the composite materials, the inter-branch distance was adjusted by multiplying the mass of the composite sample by a parameter indicative of mass concentration (Table 6.2.3; calc. wt%). A comparison of the experimentally derived values with those theoretically predicted based on the synthetic protocol reveals a consistently lower content of **NiFe-chain** particles across all three types of electrospun fibres, with the most notable reduction observed in the PCL-based fibres. The observed discrepancies are likely attributed to the specific preparation protocol and procedural steps involved during sample fabrication.

Table 6.2.3 Comparison of magnetic measurement data for **NiFe-chain** and its composites.

Sample	$T_{½}$ ↓ / K	$T_{½}$ ↑ / K	Hysteresis width / K	Synthesis wt%	Calculated wt%
NiFe-crystals	282	310	28	-	-
NiFe-microcrystals	276	310	34	-	-
NiFe-fibres 1 (PCL)	280	306	26	14.1	7.8
NiFe-fibres 2 (P2VP-PS)	278	305	27	11.8	10.7
NiFe-fibres 3 (P2VP-PS)	276	306	30	13.9	10.2

6.2.4 Hydration/dehydration effects on the **NiFe-chain** electrospun fibres

The ability to reversibly hydrate-dehydrate crystals of **NiFe-chain** facilitates changes in the material colour between brown and yellow and, more importantly, switches on and off the electron transfer. This behaviour prompted the research on composites to focus on the effect of humidity and their stability. As it was shown in the original study, sorption-desorption isotherms recorded at room temperature for **NiFe-chain** exhibit a fairly wide hysteresis in the range of 20-80% relative humidity (RH), with a sharp transition during water intake and release. The characteristic steps derived from the incorporation of five water molecules per formula unit into the structure at high humidity create a pentahydrate phase, and their release in the low relative humidity regime, forming a dehydrated phase. The process is fully reversible and can be repeated without material fatigue. However, at the first desorption step, **NiFe-chain** crystals lose crystallinity, which is associated with the decrease of the unit cell volume. With exposure of the material to humid air (above 80% RH), the water molecules are incorporated with restored crystallinity.

To extract the behaviour of the embedded **NiFe-chain** in the electrospun fibres, it was necessary to investigate the sorption properties of the matrix itself. For that purpose, undoped **PCL** and **P2VP-PS** fibres have been studied with a dynamic vapor sorption (DVS) apparatus (Figure 6.2.9). The isotherms recorded for **PCL-based** fibres showed no sign of sorption-desorption hysteresis in the range of 0-97% relative humidity. The slight increase in the mass change below 0.75% can be attributed to the adsorption of the water molecules on the surface of the electrospun mat. On the other hand, the latter reference material – **P2VP-PS** fibres, in varied relative humidity at constant temperature, reveal a different behaviour for the hydration and dehydration of water molecules. Contrary to the **NiFe-chain,** the hysteresis is gradual without an evident step, but spans over a broad range of relative humidity, 20-96% RH. Compared to **PCL** fibres, in **P2VP-PS,** the mass change due to the water intake is much higher, reaching a value of 7% at the highest humidity.

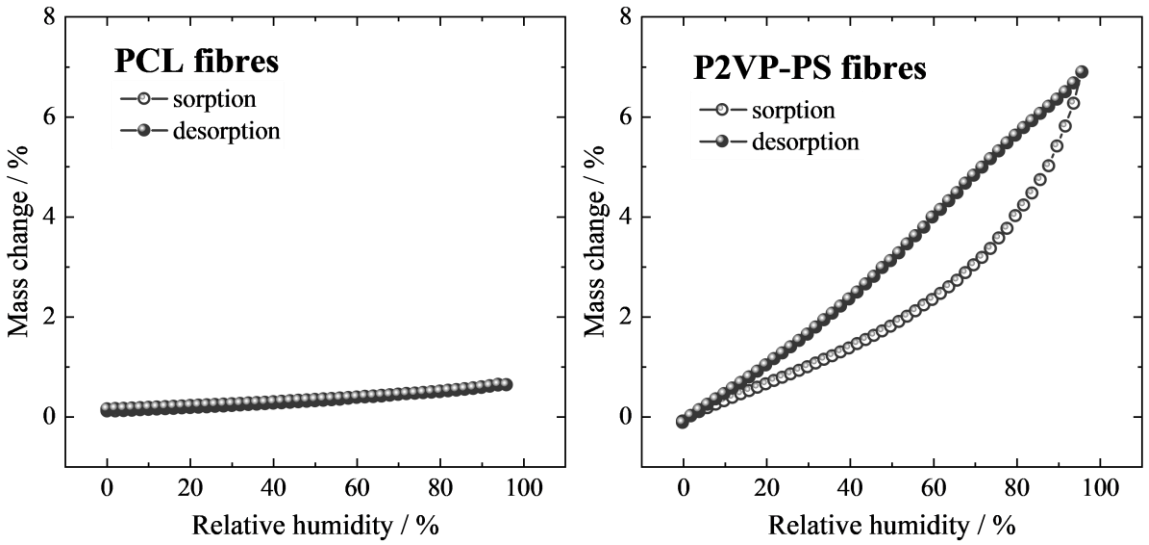

Figure 6.2.9 Sorption-desorption isotherms for **PCL** and **P2VP-PS** based electrospun fibres recorded at 298 K as a reference for the composite materials.

The sorption-desorption isotherms recorded at the temperature of 298 K for the **NiFe-microcrystals** loaded electrospun composites are presented in Figure 6.2.10. They can be easily characterized as a combination of the polymer matrices' isotherms with abrupt transitions originating from **NiFe-chain** crystals. The indicator for the presence of the latter is sharp changes in mass, especially in desorption, which occur at similar humidity parameters for all composite samples. Contrary to the behaviour of pure **NiFe-microcrystal** filler, the isotherms of the composite show a slight change between the first and the second sorption cycles in the high humidity regime. For the **PCL-based** fibres, it is much more evident that during the first sorption cycle, the sharp change in mass is shifted towards higher relative humidity (occurs at 92%). After effective dehydration and second rehydration, the abrupt step derived from the **NiFe-chain** appears at 82% RH, recreating its characteristics in the complete sorption/desorption cycle. The explanation for this difference between the first and the second hydration/dehydration cycles may lie in the fabrication methodology, in particular, the use of non-polar solvents. Additionally, the properties of the polymer matrix may also play a crucial role; as for the **P2VP-PS**-based fibres, this behaviour is less pronounced. For the samples **NiFe-fibres 2** and **3** (P2VP-PS), in the desorption sharp transition at 20% RH also appears from between the polymer matrix background behaviour. During sorption at the high humidity regimes, the difference in the first and the second run is less visible in mass change as, in general, the transitions are more gradual compared to **PCL-based** fibres.

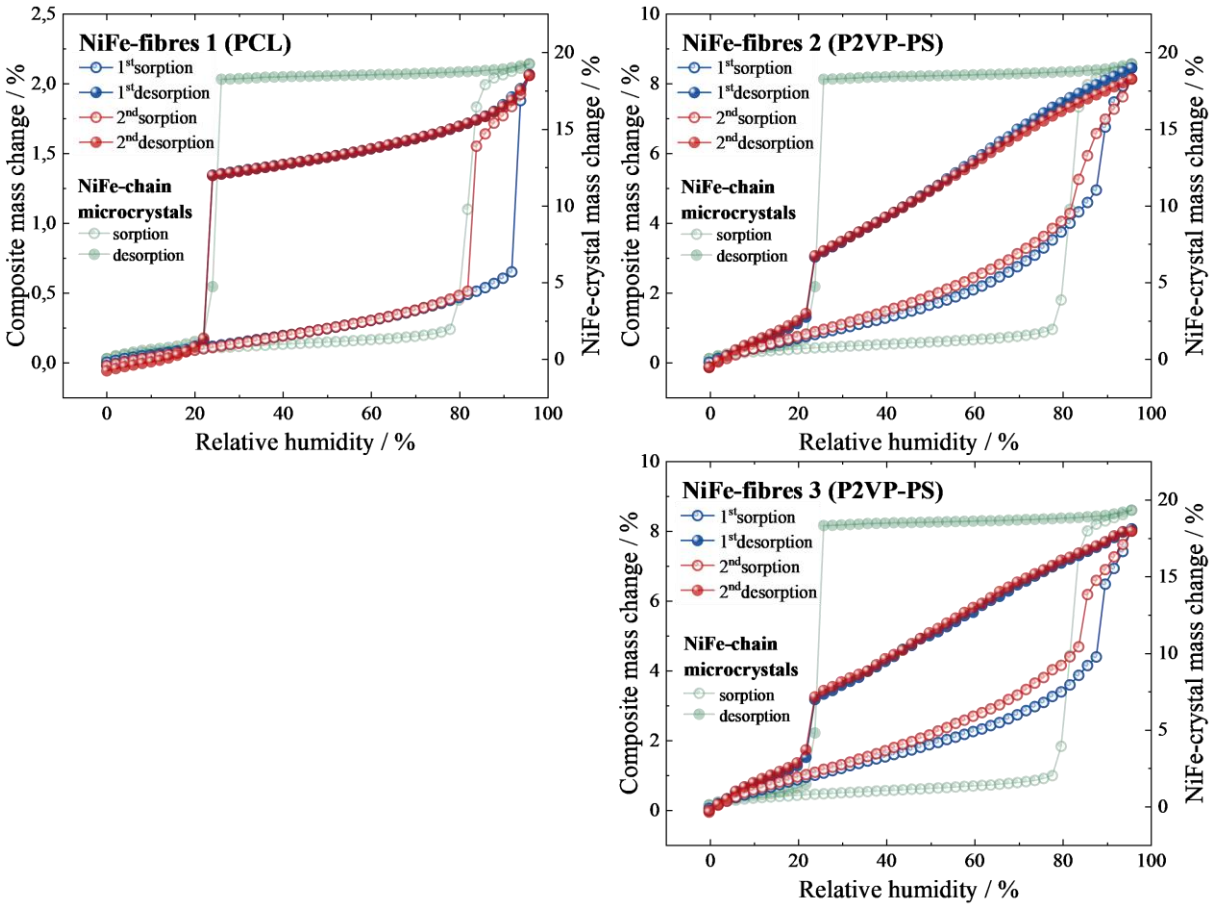

Figure 6.2.10 Sorption-desorption isotherms for **PCL** and **P2VP-PS** based electrospun fibres composites containing **NiFe-microcrystals** recorded at 298 K.

The DVS experiments are known to be very sensitive to any changes in the mass that take place due to the sorption/desorption of water molecules by the material. For that reason, the obtained data was used to calculate the content of **NiFe-chain** in the electrospun fibres in comparison to the theoretical percentage of the filler in the final material derived from the synthetic protocol. A method for the calculation was based on the difference in desorption mass change at ~20%RH, as in both polymer matrices, the **NiFe-chain** step change is very characteristic and cannot be mistaken for the behaviour ascribed to organic polymer. When considering a mass change for **NiFe-chain** crystals, the difference in the desorption is equal to 16.88%. As for the composites with the highest **NiFe-microcrystal** initial content, after subtraction, the values of the step are as follows: 1.24% (**NiFe-fibres 1**), 1.85% (**NiFe-fibres 2**), and 2.07% (**NiFe-fibres 3**). Based on these proportions, the calculated **NiFe-microcrystal** mass concentration for the mentioned composites is equivalent to 7.4, 10.9, and 12.3 %, respectively (Table 6.2.4). The comparison of the calculated concentration of the functional filler in fibres is in line with the % wt extracted from magnetic measurements; however, comparing the values to the theoretical ones, there is an interesting correlation between the polymer type and the calculated amounts. For the co-polymer **P2VP-PS** composites from the chloroform-methanol mixture **NiFe-fibres 2** and from DMF **NiFe-fibres 3**, the calculated values are consistent with the synthetic ones. On the other hand, the calculations for the **PCL** composites give amounts that are almost twice underestimated. This discrepancy may have its origin in the hydrophobic character

of the polymer matrix itself. As shown in Figure 6.2.9, electrospun mats of pure **PCL** polymer practically do not absorb any water molecules up to 96% RH. Therefore, it is plausible that the polymer matrix may partially block the access of water molecules from being incorporated into the crystal structure of the **NiFe-chain.** Also, it is probable that the sharp transitions in sorption and desorption for the **PCL-based** electrospun mats may come from the larger particles of **NiFe-microcrystals** with relatively small polymer coverage. Whereas the smaller particles that are deeply embedded into the fibres do not contribute to the effective hydration/dehydration, contrary to the **P2VP-PS**-based composites.

Table 6.2.4 The comparison of the theoretical and calculated amounts of **NiFe-chain** in the electrospun composites.

Sample	Polymer	Solvent	% wt Synthesis	% wt SQUID	% wt DVS
NiFe-fibres 1	PCL	$CHCl_3$ +MeOH	14.1	7.8	7.4
NiFe-fibres 2	P2VP-PS	$CHCl_3$ +MeOH	11.8	10.7	10.9
NiFe-fibres 3	P2VP-PS	DMF	13.9	10.2	12.3

6.2.5 Diffraction studies on the electrospun composites

To corroborate on the switching between the hydrated and dehydrated phases of **NiFe-chain** in the electrospun fibres of **PCL** and **P2VP-PS**, the structural changes of the coordination system have been studied with X-ray diffraction (PXRD) experiments. Fibres were directly collected onto the Si(100) wafer with a high degree of sample uniformity and mounted on the diffractometer for data collection without additional preparations. To study the degree of structural changes in the composite materials (**NiFe-fibres 1/2/3**), their references have been measured: polymer matrix **PCL** and **P2VP-PS** and **NiFe-microcrystals** in the dehydrated phase. For comparison, the diffractogram of the fully hydrated HT phase has been simulated from the literature data. Additionally, for a better understanding of structural changes in the composites in response to changes in external conditions, it was necessary to include the structure of a 2D honeycomb-like **NiFe-layer**.

As pointed out in the previous chapter about the sorption properties of **NiFe-chain** crystals, the structural transformation associated with the reversible hydration/dehydration process induces changes in unit cell parameters. During the transition from pentahydrate to dehydrate, the volume of a unit cell is reduced, leading to a collapse of the crystals (presented in Figure 6.2.11). In the diffraction pattern, a shift of the peaks to higher 2θ values is observed, along with slight peak broadening. However, **NiFe-chain** presents an interesting ability to reversibly lose and regain its crystallinity over several cycles, after exposing the material to dry and humid air alternately. As it was mentioned in the passage devoted to the preparation of the studied materials, direct contact of **NiFe-chain** crystals with water induces a recrystallization process by leaching ammonium cations from the 1D coordination structure into the 2D honeycomb-like

topology of the **NiFe-layer**. In the diffraction pattern, the beginning of this transformation can be observed by the appearance of diffraction peaks at 2θ below 7.5° (marked with violet dashed box), which do not appear for any of the three phases of **NiFe-chain** (neither HT, LT, nor dehydrated).

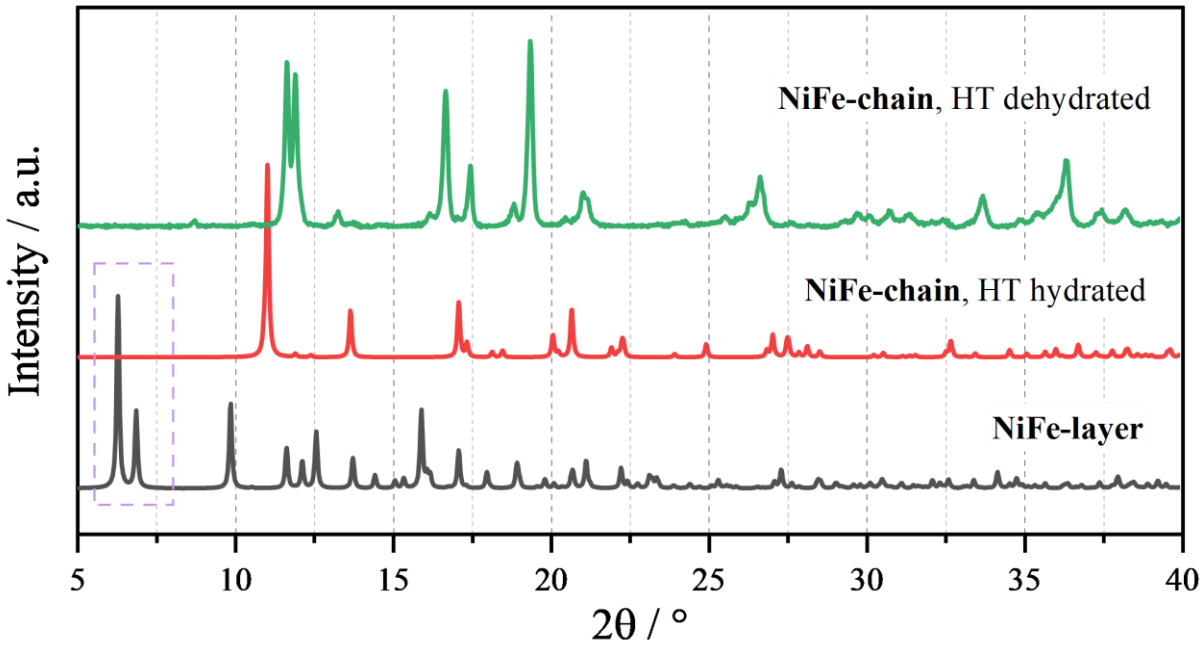

Figure 6.2.11 Diffraction patterns for **NiFe-chain** in HT dehydrated state (measured) and HT hydrated state (generated from cif)[66] in comparison to **NiFe-layer**[197].

When analysing the structural transformation of the **NiFe-chain** in the electrospun fibres, it was necessary to establish the base diffraction pattern originating from the polymer matrix. In the description of chosen polymer matrices (Chapter 3), it was mentioned that **PCL** and **P2VP-PS** polymers differ in the degree of crystallinity, as they are characterized as semi-crystalline and amorphous, respectively. And so in XRD measurements it can be easily distinguish by the appearance of sharp diffraction peaks at 21.347(1)° and 23.708(3)° for **PCL** electrospun mat, whereas for **P2VP-PS** based composites there are only very broad maxima at 11.07(3)° and 19.36(1)°, which is in agreement with literature data[208–210] (Figure 6.2.12). For that reason, the interpretation of the structural transformations of **NiFe-chain** in the electrospun fibres for the latter one may be much more straightforward; however, the lack of diffraction peaks at low angles (below 20°) for **PCL** facilitated the identification of changes in the **NiFe-chain** structure.

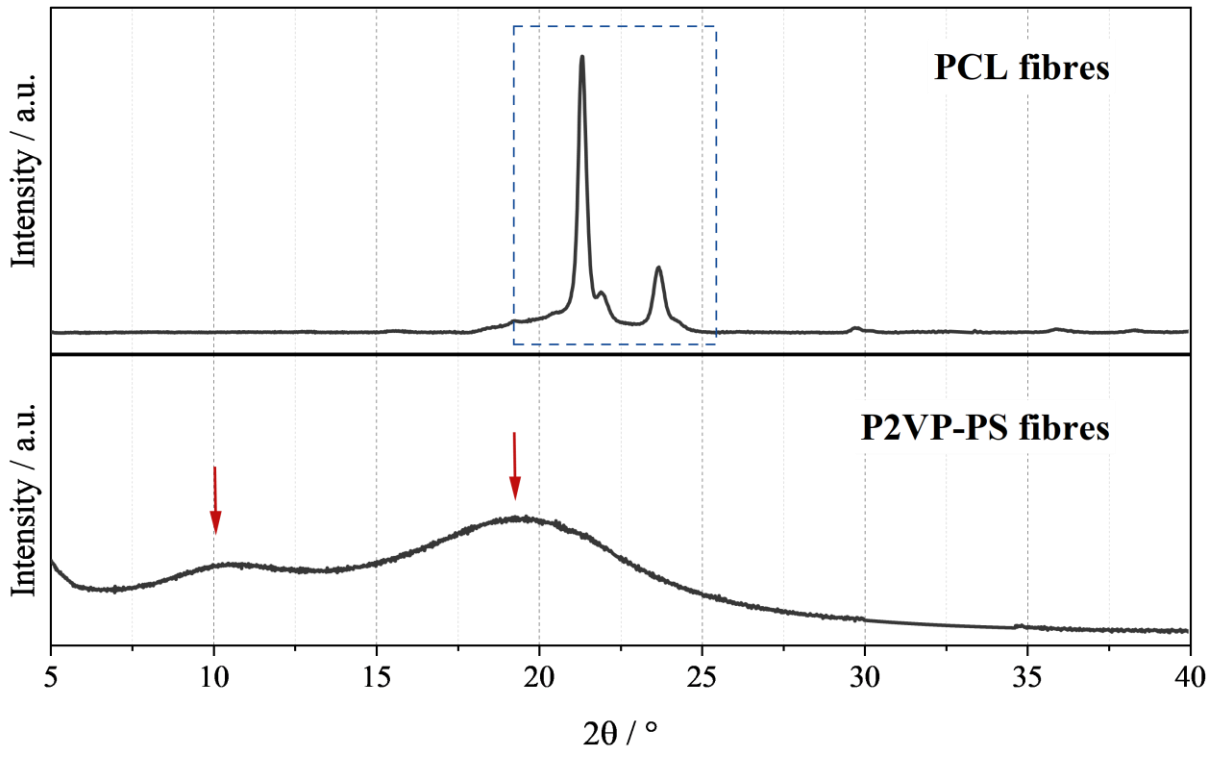

Figure 6.2.12 Diffraction patterns for undoped **PCL** (upper panel) and **P2VP-PS** (lower panel) fibres**.**

According to the preparation protocol, when depositing the fibres from either **PCL** or **P2VP−PS** polymer, the characteristic yellow colour of the materials can be observed (Figure 6.2.2), which derives from the dehydrated **NiFe-chain**. Diffraction patterns for **NiFe-fibres 1** (PCL), **NiFe-fibres 2** (P2VP-PS), and **NiFe-fibres 3** (P2VP-PS) support these observations presented in Figure 6.2.13 as a bottom green pattern for each of the samples. Interestingly, for **PCL-based** fibres at ~11.6°, a double peak can be found, contrary to **P2VP-PS**-based fibre mats. It may indicate a higher degree of crystallinity of **NiFe-microcrystals** when freshly deposited. When exposed to conditions of high water vapour content for several hours, the colour change occurs to light brown in all three examples. Diffractograms obtained after this transformation of the freshly deposited mats display an intriguing correlation between the polymer matrix and structural changes of the filler. For **P2VP-PS**-based electrospun fibres, a complete transformation to hydrated **NiFe-chain** is observed both in **NiFe-fibres 2** (electrospun from chloroform-methanol mixture) and **NiFe-fibres 3** (electrospun from DMF). On the other hand, for **NiFe-fibres 1** (PCL), the diffractogram presents itself as a mix of partially hydrated and dehydrated particles of **NiFe-microcrystals.** This observation supports the proposition from sorption studies described in previous paragraph, as only a part of encapsulated grains of **NiFe−chain** inside **PCL** based fibres undergoes the change into hydrated HT phase, giving an explanation to the discrepancies in calculated content of filler in **PCL** mats from sorption/desorption isotherms, as well as in concentration derived from magnetic measurements (Table 6.2.4).

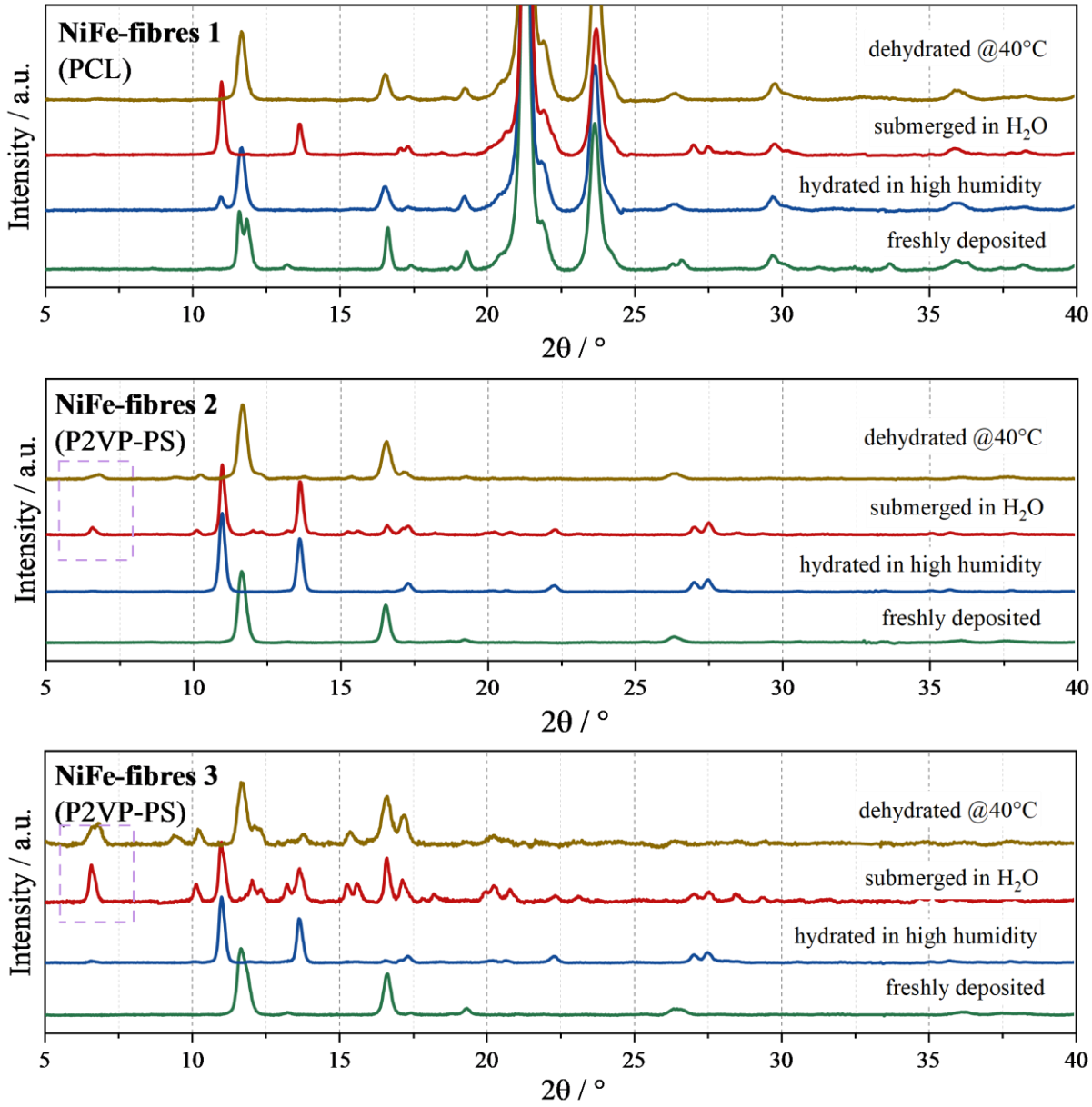

Figure 6.2.13 The comparison of the structural changes of **NiFe-chain** in the composites **NiFe-fibres 1** (PCL, upper panel), **NiFe-fibres 2** (P2VP-PS, middle panel), and **NiFe-fibres 3** (P2VP-PS, lower panel).

To observe a full transition from the dehydrated to the hydrated form of the **NiFe-chain** in all three materials, the samples have been submerged in distilled water for 1 hour. Diffractograms obtained after this procedure show the successful hydration of all **NiFe-chain** particles in **PCL** electrospun mats without any additional phase. In contrast to that, for **P2VP-PS**-based fibres after immersion in water, diffraction Bragg peaks for 2θ below 7.5° start to appear, which derive from the **NiFe-layer**. These observations point out that the **PCL** matrix acts as a barrier even for the largest **NiFe-chain** particles from water, whereas **P2VP-PS** can be penetrated by water molecules, especially for the sample electrospun from DMF, which was characterized by the smallest value of the average fibre diameter. Introducing all three samples into the oven at a temperature of 40°C for 1 h causes complete dehydration of the **NiFe-chain** in the case of **NiFe-fibres 1** (PCL) mat or only partial transformation into anhydrous **NiFe-chain** in the

P2VP-PS based fibres. In the diffraction patterns of **NiFe-fibres 2** and **NiFe-fibres 3,** the Bragg peaks ascribed to the **NiFe-layer** below 7.5 degrees do not disappear, especially for the sample electrospun from DMF. As for the **PCL-based** composite, interestingly, the peak at 11.6° after dehydration does not split into two, which may imply that after the hydration-dehydration cycle, the degree of crystallinity of embedded **NiFe-chain** grains decreases.

6.3 Drop-casted composite foil with **NiFe-chain**

The multifunctional properties of the **NiFe-chain** come not only from reversible phase transitions between high-temperature (HT) and low-temperature (LT) states with temperature change but also between hydrated and dehydrated phases under varying humidity conditions. An important feature highlighted in previous studies on a crystalline form of **NiFe-chain** is the effect of small applied pressure on the phase transition temperature, which shifts linearly from 309 K at ambient pressure to 339 K at 85 MPa. Additionally, the transition between the LT and HT phases becomes more gradual under pressure, suggesting that mechanical stress influences the memory effect within the bistability region. This property positions the **NiFe-chain** as a promising candidate for use in pressure sensing applications. Building on this, the following study investigates pressure-induced MMCT in **NiFe-chain**-based composites, specifically in drop-casted foils, where **NiFe-microcrystals** are embedded in a PCL polymer matrix. These composites feature higher filler concentrations compared to electrospun fiber-based materials, providing a platform for further exploration of their pressure-sensitive behaviour.

Preparation of composite foils

As the primary purpose of foil preparation was not only to compare their properties to electrospun fibers but to prepare materials for an experiment at the SOLARIS National Synchrotron Facility in Kraków, several parameters of the final foil had to be taken into account. Namely, it was necessary to guarantee an adequate concentration of MMCT-active additive and ensure relatively high homogeneity of the samples. In the production of the films, the fragility of **NiFe−chain** crystals has to be taken into account, as the preparation involved pouring the suspensions onto a certain surface and waiting for the complete solvent evaporation, solvents that would induce the recrystallization of **NiFe-chain** to **NiFe-layer** had to be omitted, namely methanol or DMF. For this reason, the drop-casted films were prepared from the "safe" solvents – chloroform or dichloromethane; however, only the latter was chosen due to slightly better properties of the final drop-casted films. Furthermore, the high volatility of dichloromethane served as an advantage in reducing the level of **NiFe-chain** particle aggregation and nonuniform drying out of the polymer matrix, which, to some extent, could not be avoided. Additionally, only one of the polymers was chosen for film fabrication – **PCL**. Because of its properties, it could be easily peeled off the surface without damaging the film.

The protocol to prepare the drop-casted films with **NiFe-chain** was as follows. Powdered **NiFe−1p** was covered with small amounts (5-10 ml) of CH_2Cl_2 and shortly sonicated for better dispersion. Then, **PCL** polymer was introduced to give the **NiFe-chain** concentration in the final solvent-free drop-casted film equal to 10, 20, or 30% wt. Detailed amounts of the used substrates can be found in Table 6.3.1. After full dissolution of the polymer with the use of a gyromixer, the suspensions have been poured into the Petri dish (with diameters of 5 cm), covered with crystallization vials, and left aside for complete evaporation of the solvents. Freshly produced films were characterized by partially green/dark green and blue/dark blue colours, with a difference in colour being more noticeable in films of the lowest concentration. After holding the foils above hot water, vapours changed into a uniformly brown colour was

observed, which could be reversed by placing the samples in the fridge at around 4°C, which resulted in a uniform blue/dark blue colour (Figure 6.3.1).

Table 6.3.1 Preparation details used for **PCL** drop-casted foils with **NiFe-chain** particles.

Sample	Amount of **NiFe-chain** [mg]	PCL [mg]	% wt. **NiFe-chain** in drop-casted films
NiFe-foil 1	19	174	10%
NiFe-foil 2	51	204	20%
NiFe-foil 3	78	187	30%

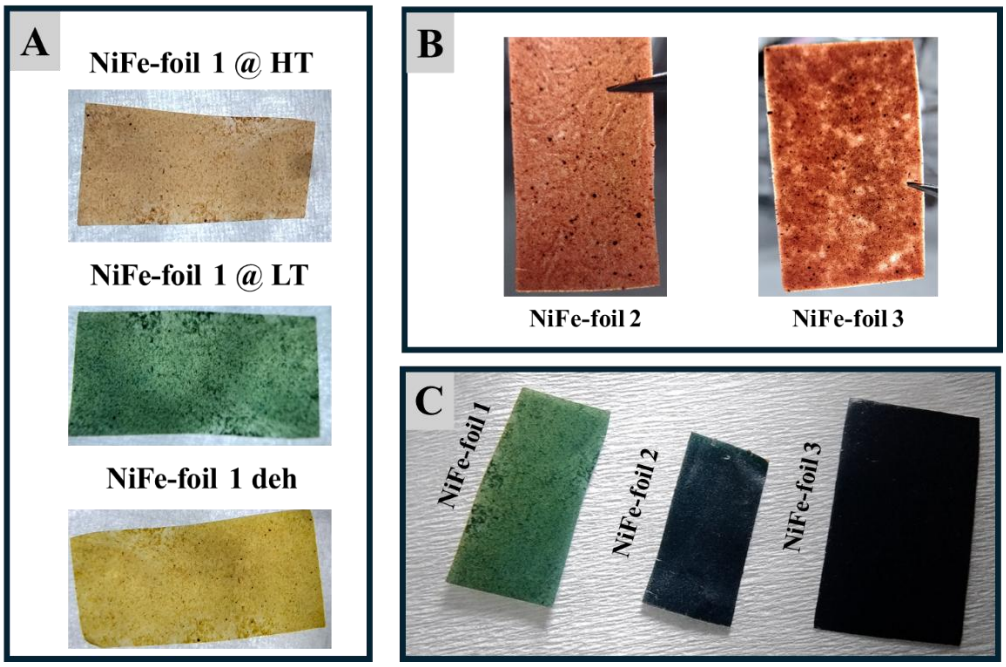

Figure 6.3.1 A) Images taken for three phases (HT, LT, and dehydrated) for the least concentrated **NiFe-foil 1**. B) Photographic representation of **NiFe-chain** in the high-temperature phase for **NiFe-foil 2** and **3**. C) The comparison of the low-temperature phase of the **NiFe-chain** in three prepared drop-casted foils in **PCL** matrix.

6.3.1 Morphology and switching properties of drop-casted foils

Drop-casted foils composed of **PCL** matrix with various % wt. of **NiFe-chain** particles were characterised by a relatively uniform thickness of ~ 0.5 mm and a smooth surface. Owing to the properties of the **PCL** polymer matrix, samples could be seamlessly cut into the necessary dimensions. As shown in Figure 6.3.1, prepared films are characterized by colours derived from **NiFe-chain** filler, the intensity increases with initial concentration, which is even more evident in comparison to much less concentrated electrospun fibers' composites. However, the appearance of larger particles or their aggregations is more pronounced, even with organoleptic

observations, especially in **NiFe-foil 3**. The closer inspection of composites with an optical microscope presented in Figure 6.3.2A showed that on a microscopic level, the surface is less uniform, visible through the difference in object focus. Nevertheless, **NiFe-chain** particles appear to be dispersed throughout the **PCL** matrix, giving a blue hue even in between particles or their aggregation placed on the surface of the foil.

The switchability of prepared **NiFe-foils** has been studied with SQUID magnetometry to provide a working temperature range. As shown in Figure 6.3.2B, **NiFe-foil 1** presents an abrupt transition with temperatures $T_{1/2}$ = 276 K and $T_{1/2}$ = 306 K in the heating and cooling stages, respectively. Comparing these values to the characteristics of **PCL-based** electrospun fibres **NiFe-fibers 1 (PCL)**, which showed transition at temperatures equal to $T_{1/2}$ = 281 K and $T_{1/2}$ = 306 K, drop-casted foil with a similar concentration as fibers does not show any relevant discrepancies, especially in the abrupt characteristics of the spin transition.

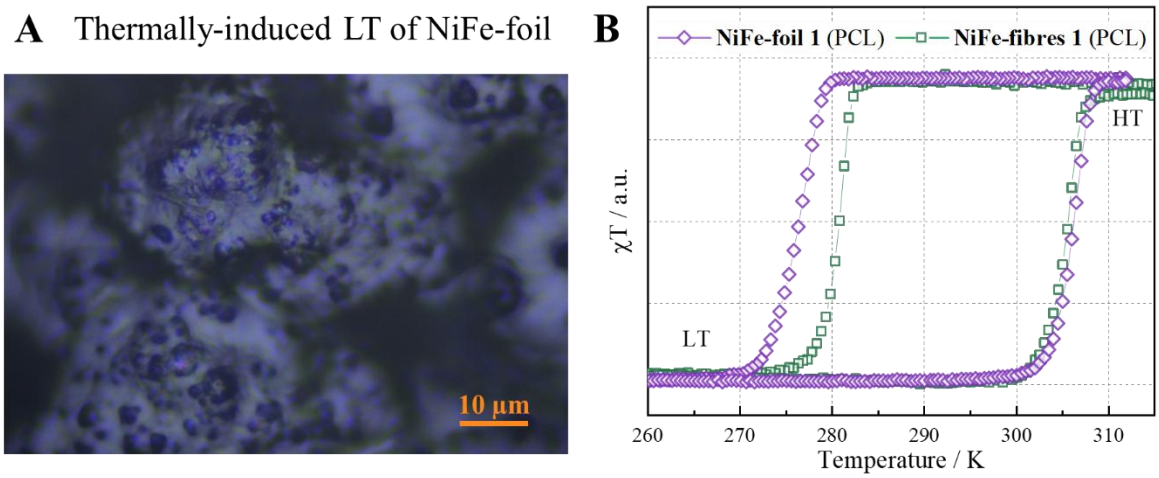

Figure 6.3.2 (A) Thermally induced LT phase in **NiFe-foil 1** obtained from optical microscope with 100x magnification. (B) Temperature dependence of the magnetic susceptibility temperature product (χT) for **NiFe-foil 1** (purple) in comparison to PCL-based electrospun fibers **NiFe-fibres 1** (green).

To ensure that pressure-induced MMCT of **NiFe-chain** was observed after incorporating particles into **PCL**-based foils, a preliminary test was performed to check whether it is possible to apply point pressure to the material in the form of writing (Figure 6.3.3). For this test, foil with the lowest **NiFe-chain** concentration appeared to give the most visible results. After covering the surface with protective film (paper-thick PE foil), the pressure was applied by hand-writing on it with a glass rod. To check the reversibility of the process, the foil with a visible dark blue inscription was placed above the hot water vapours, resulting in the disappearance of the caption and the foil turning completely brown.

Figure 6.3.3 Example of writing test on the **NiFe-foil 1.**

After a successful point pressure-induced change of the colour from brown to blue on the prepared composite foils, it was important to check the feasibility of uniformly applying pressure to the whole area of the sample for XAS measurements at the ASTRA beamline. After turning the samples into a uniformly brown colour, assigned to the HT phase, samples of appropriate dimensions were placed between plexiglass plates, and with the use of a lab-scale hydraulic press, the pressure of 3.5 tons was slowly applied. This resulted in foils turning uniformly to a dark blue colour, without any evident breakage of the **PCL** film, shown in Figure 6.3.4. To check the reversibility of this process, foils were once again shortly heated up above hot water vapours, and the pressure test was repeated with the same result. Additionally, at the IFJ institute, a custom-made stamp was minted from brass, and the IFJ institute logo was pressed onto **NiFe-foil** with the use of a laboratory hydraulic press.

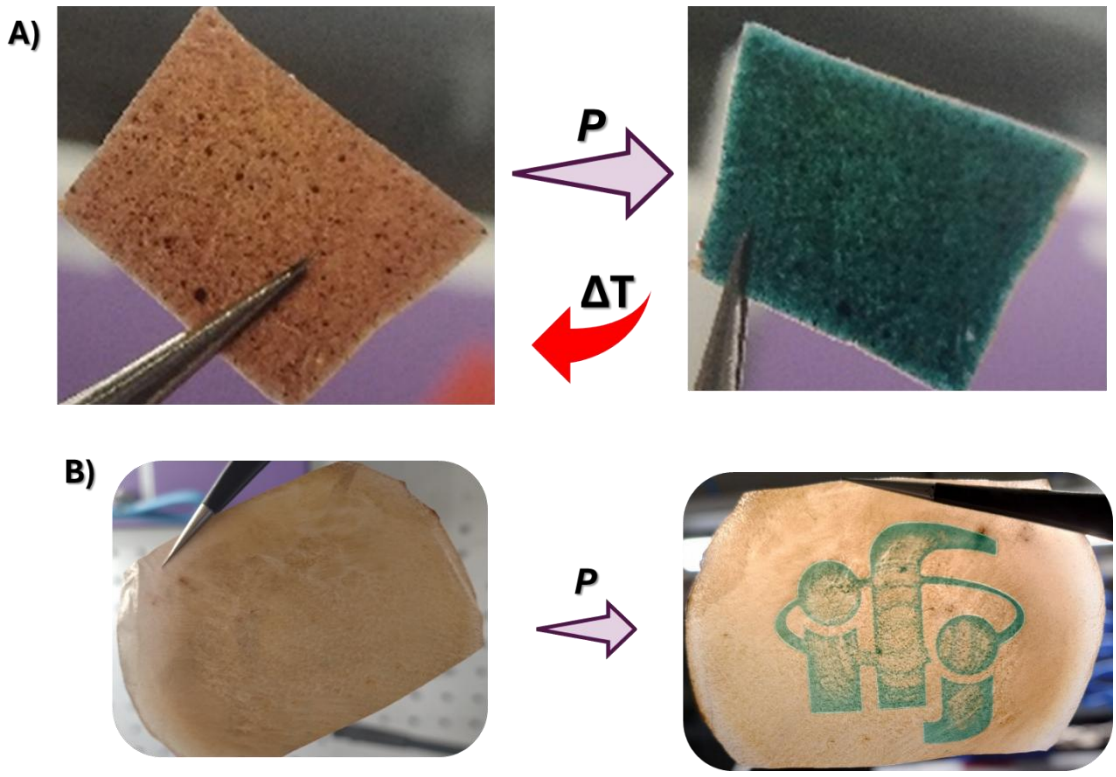

Figure 6.3.4 (A) Photographic representation of **NiFe-foil 2** before (brown) and after (dark blue) applying external pressure. (B) Example of pressed **NiFe-foil 2** with custom-made stamp with the IFJ institute logo.

6.3.2 Pressure-induced MMCT studied with XAS spectroscopy

To investigate the electronic structure of the NiFe-chain filler in composite foils under external pressure at room temperature, X-ray absorption spectroscopy (XAS) measurements at the Fe and Ni K-edges were conducted. Like the crystal and microcrystal samples, the NiFe foils were sealed in polyethylene (PE) foil bags containing residual water droplets. This precaution was taken to minimize exposure to the low-humidity environment inside the experimental hall and measuring chamber and to mitigate the risk of partial transition to the inactive, dehydrated MMCT form of NiFe-chain (see Figure 6.3.5). All three concentrations of NiFe-chain in the composite foils were tested during the experiment, with the highest concentration of 30% (**NiFe-foil 3**) yielding the best-quality data, which is presented below. A custom-designed sample holder facilitated temperature control within the range of 250 K to 320 K, utilizing liquid nitrogen for cooling and a resistive heater as a heat source. The homogeneous nature of the **NiFe foils** was maintained throughout the measurements.

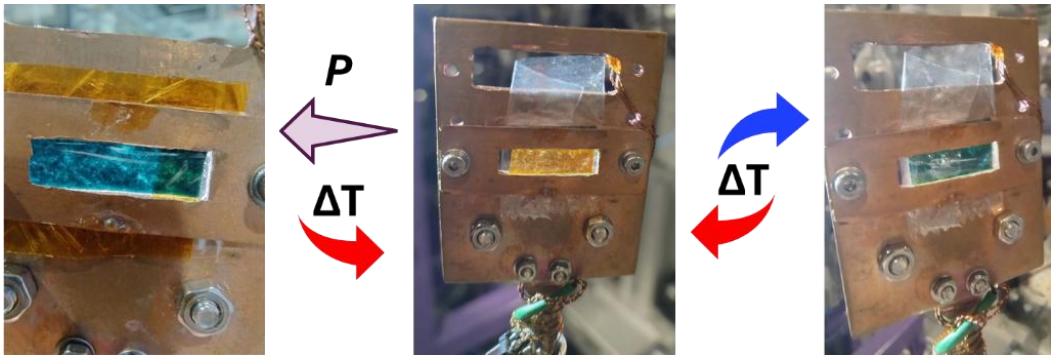

Figure 6.3.5 Photographs of the measured sample at the ASTRA beamline in SOLARIS with a custom-made sample holder with temperature stability.

The pressure-induced MMCT study conducted at the ASTRA beamline followed a systematic procedure, outlined in the subsequent steps. Initially, **NiFe-foil 3** was precisely cut to fit the dimensions of a custom-made holder and placed over hot water vapour to ensure the entire sample volume transitioned to the HT phase. The foil was then sealed in a polyethylene (PE) bag, positioned in the custom sample holder, and subjected to X-ray absorption spectroscopy (XAS) at the Fe and Ni K-edges, recorded as a single scan at room temperature. This measurement is referred to as the "sample before applying pressure @RT." Subsequently, the sample, prepared analogously, was placed between flat plates, and a pressure of 3.5 tons was applied using a laboratory-scale hydraulic press. A notable change in the sample's colour to deep blue, indicative of the LT phase, was observed (see Figure 6.3.5). The sample was again sealed in the PE bag and measured at both K-edges at room temperature, referred to as the "pressed sample @RT." To confirm the completion of the phase transition to LT, the sample was cooled in the measurement chamber using liquid nitrogen to 250 K, allowed to stabilize thermally, and then measured (referred to as "sample pressed and cooled @250 K"). Finally, the composite foil was gradually reheated to 312 K, with the holder wrapped in aluminium foil to ensure a uniform and complete colour change to brown in the measurement spot. The sample was then

measured at both K-edges without additional heating, referred to as "sample pressed and heated @312 K." The XANES spectra obtained at the Fe and Ni K-edges are presented in Figure 6.3.6.

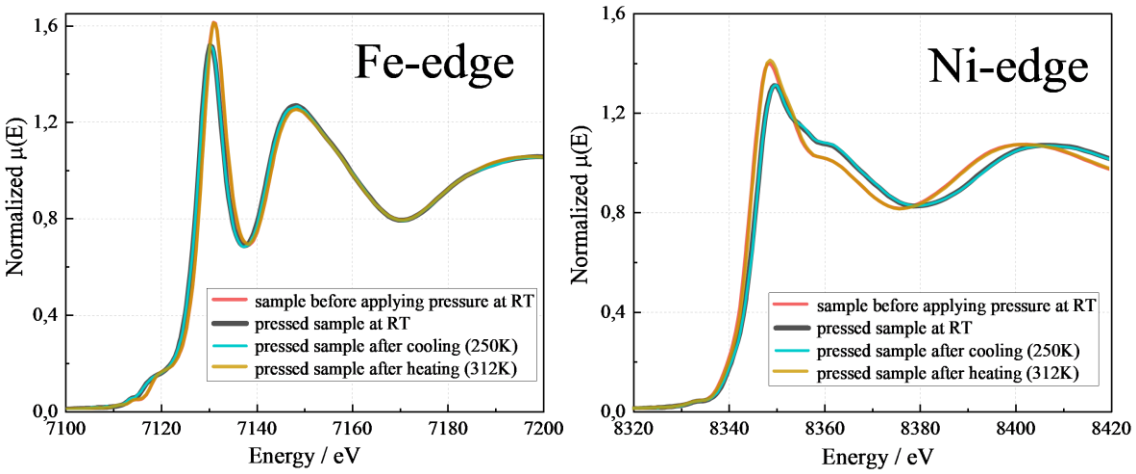

Figure 6.3.6 Normalized absorption coefficient and its derivative at Fe (A, C) and Ni (B, D) K-edge recorded for composite PCL foils containing NiFe-chain microcrystals, showcasing the antagonist change of XANES characteristics between Fe and Ni K-edges after applying 3.5 t pressure to the sample, cooling it down to 250 K and heating it up to 312 K.

After applying pressure to the sample, @RT, the antagonistic behaviour of Fe and Ni K-edges is observed. More specifically, for the former the edge is shifting toward lower energies, while for the latter it goes to higher, corresponding to complementary roles Fe and Ni metal ions play in the charge transfer process, from Ni(II)-Fe(III) pair into Ni(III)-Fe(II) pair. With additional cooling of the pressed sample, no shift is observed for both edges, contrary to the heating process, which results in a return to the initial state.

The spectra were quantitatively analysed by linear combination fitting (LCF) of reference spectra, where data of **NiFe-foil** were linearly fitted using least-squares fitting[108]. Fitting was performed within the function of the Athena software in the Demeter package, in the near-edge energy region on the normalized μ(E). The reference data, which were weighted during the procedure, were obtained for the purely crystalline samples (**NiFe-crystals**) at high (330 K) and low (260 K) temperature phases, and were used due to the similarities in the curves, particularly in the post-edge region. The results of the fitting procedure are presented in Figure 6.3.7, where experimental data have been compared to the fitted spectra. Extracted weights (***w***) of HT and LT phases, summarised in Table 6.3.2, show almost complete transition from HT to LT phase upon applying pressure at room temperature, and the reversibility of the process while heating in the case of Fe K-edge. As for the spectra recorded for Ni K-edge, LCF fitting results in partial transition into the LT phase upon applying pressure with w(HT) = 0.298 and w(LT) = 0.702. Under the influence of cooling, the spin transition does not show many signs of full transition, as weights for the HT and LT phases are equal to w(HT) = 0.264 and w(LT) = 0.736. These discrepancies in the degree of transition between Fe and Ni K-edge may be mostly related to the associated with a greater difference in the edge position between +2 and +3 oxidation states. For **NiFe-crystals,** it was shown that for Ni K-edge, the shift in edge position was ~2 eV, whereas for Fe K-edge, it was below 1 eV.

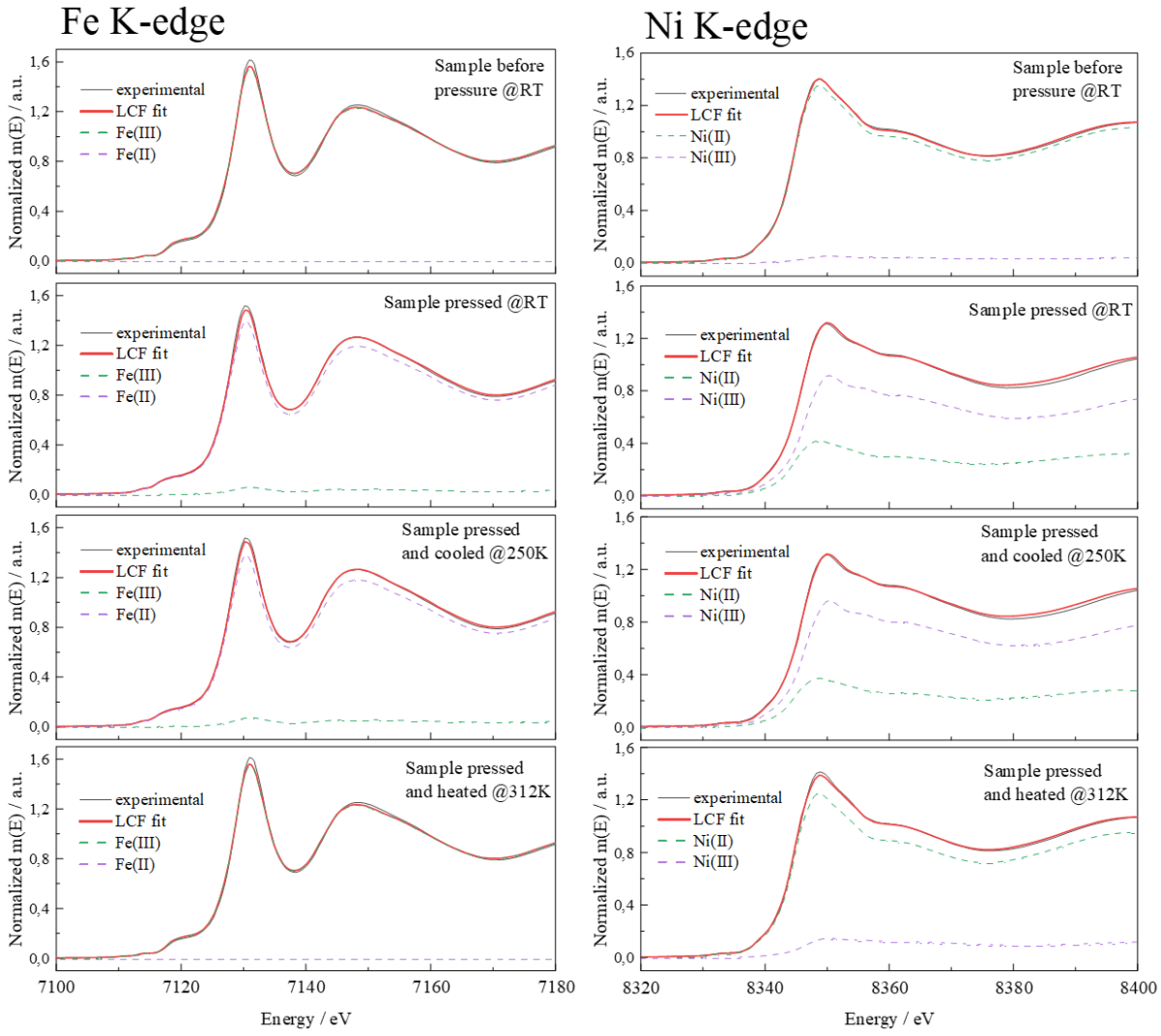

Figure 6.3.7 Normalized absorption coefficient and its derivative at Fe (A, C) and Ni (B, D) K-edge recorded for composite PCL foils containing **NiFe-chain microcrystals**, showcasing the antagonist change of XANES characteristics between Fe and Ni K-edges after applying 3.5 t pressure to the sample, cooling it down to 250 K and heating it up to 312 K.

Table 6.3.2 LCF for NiFe-foil 30% before and after pressing, with standards being boundary measurements for crystals.

Sample	Temperature / K	*w*(Fe(II))	*w*(Fe(III))	*w*(Ni(II))	*w*(Ni(III))
Sample before pressure	300 (RT)	0	1	0.960	0.040
Sample pressed @RT	300 (RT)	0.962	0.038	0.298	0.702
Sample pressed cooled	250	0.952	0.048	0.264	0.736
Sample pressed heated	312	0	1	0.887	0.113

For a more detailed analysis of the pressure-induced MMCT transition in the composite foils, the pre-edge region of the recorded spectra has been studied. In Figure 6.3.8 presented below, **NiFe-foil 3** sample changes have been compared to the pre-edge characteristics of reference samples, where oxidation and spin states are known and stable throughout measurement.

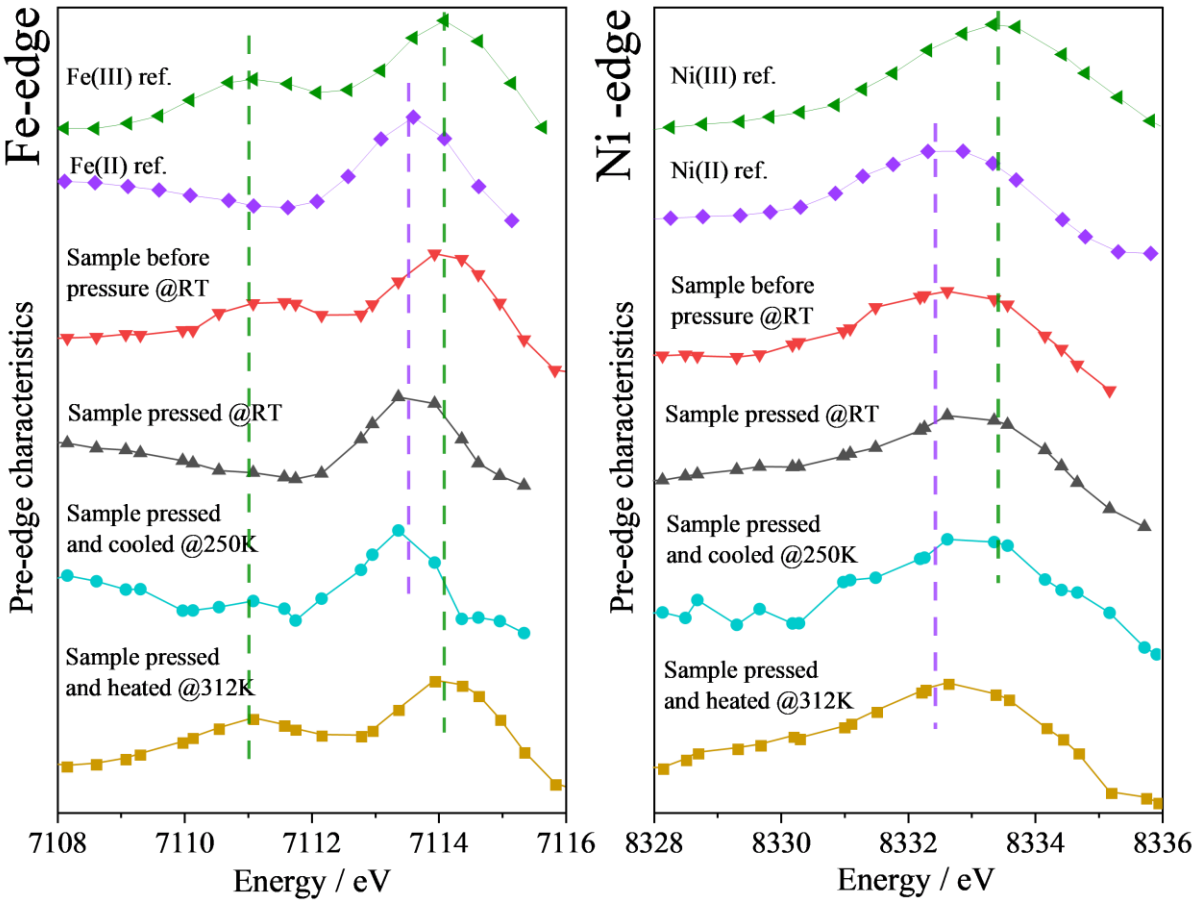

Figure 6.3.8 Comparison of pre-edge characteristics in Fe and Ni K-edge extracted from the normalized absorption coefficient for **NiFe-foil 3** before and after applying pressure, with the addition of cooling and heating pressed sample. On top experimental data for the reference samples are shown: $K_4[Fe(II)(CN)_6]$ (violet) and $K_3[Fe(III)(CN)_6]$ (green) / [Ni(II)(cyclam)] $(NO_3)_2$ (violet) and [Ni(III)(cyclam)] $(NO_3)_3$ (green) with dashed lines derived from the pre-edge maxima for those references.

Extracted pre-edge region, especially for Fe K-edge, clearly shows the change from two pre-edge peaks at 7111.5 and 7114 eV (red points), with the latter of higher intensity, to a single pre-edge peak at ~7113.5 eV (black points), before and after applying the pressure @RT to **NiFe-foil** (see Table 6.3.3 for detailed positions of pre-edge peaks). After cooling to 250 K, the pre-edge does not undergo any changes (light blue points), suggesting that @RT pressure-induced change was complete. The reversibility of the transition upon heating is also observed (dark yellow points), by shift of the peak with higher intensity to ~7114 eV and reappearance of the smaller pre-edge peak at ~7111.25 eV. Whereas, for Ni K-edge, the pre-edge transitions are less evident, with smaller changes in pre-edge peaks positions in comparison to the reference samples. However, the trend is similar, that before applying pressure, the peak is positioned at lower energies and shifts toward higher energies upon pressing the sample. No changes to peak position are recorded with further cooling, while heating once again shifts the single pre-edge peak into lower energies, related to the change of oxidation of Ni from 3+ to 2+. These observations fully correlate with the transitions recorded for **NiFe-chain** as crystals, confirming one-directional pressure-induced charge transfer from HT to LT phase, which is equivalent to temperature-induced transition.

Table 6.3.3 Pre-edge positions in Fe and Ni K-edges for **NiFe-foil 3** before and after applying pressure with comparison to the reference data.

Compound	**Sample before pressure**	**Sample pressed**	**Sample pressed and cooled**	**Sample pressed and heated**
Temperature / K	300 (RT)	300 (RT)	250	312
Metal oxidation	Ni(II)	Ni(III)	Ni(III)	Ni(II)
Pre-edge peak energy / eV	8332.73(4)	8333.06(5)	8333.01(8)	8332.70(6)
Pre-edge peak energy of reference data / eV	[Ni(II)(cyclam)] $(NO_3)_2$: 8332.58(4) [Ni(III)(cyclam)] $(NO_3)_3$: 8333.51(4)			
Metal oxidation	Fe(III)	Fe(II)	Fe(II)	Fe(III)
Pre-edge peak(s) energy / eV	7111.50(7) 7114.11(3)	7113.59(2)	7113.38(7)	7111.24(6) 7114.17(3)
Pre-edge peak energy of reference data / eV	$K_4[Fe(II)(CN)_6]$: 7113.59(2) $K_3[Fe(III)(CN)_6]$: 7111.20(8) and 7114.11(3)			

6.4 Summary of the chapter

This chapter presents an efficient and adaptable method for preparing organic polymer-based composites incorporating a miniaturized bimetallic **NiFe** coordination chain with reversible metal-to-metal charge transfer (MMCT). Although a precise synthetic protocol for uniform **NiFe-chain** nanoparticles is lacking, the size reduction process was optimized through the use of solvents ($CHCl_3$ or CH_2Cl_2) and sonication, maintaining particle functionality. Magnetic measurements showed that MMCT is reproducible in **NiFe-microcrystals** but occurs more gradually. Probing Ni and Fe metal centres with synchrotron radiation revealed that miniaturization does not affect the oxidation states of metal centres, which behave similarly under the change of temperature in **NiFe-microcrystals** as in **NiFe-chain**.

In preparing the composites, electrospinning was employed to create **PCL** and **P2VP-PS** polymer mats embedded with **NiFe-microcrystals**. Electron microscopy revealed the placement of nonuniform particles within the polymer fibres. While Raman spectroscopy showed no significant changes, magnetic measurements revealed some discrepancies, though the switchable nature of **NiFe-microcrystals** remained. Sorption-desorption studies indicated that the polymer matrices did not limit the reversible solvatomagnetic properties of the **NiFe-chain**. X-ray diffraction analysis showed that **PCL** provided the best protection against water degradation of the **NiFe-chain**, a key issue with this compound. The resulting composites exhibited improved mechanical properties, such as flexibility and malleability, compared to brittle and fragile **NiFe−crystals**. Additionally, the electrospinning technique resulted in solvent-free materials, ensuring a homogenous distribution of the functional **NiFe-chain** filler within the polymer matrix while minimizing degradation caused by prolonged solvent evaporation.

The final section of the chapter explores the preparation and characterization of drop-casted **PCL** foils embedded with **NiFe-microcrystals**, with a focus on their potential application in pressure sensor materials. The study investigates the pressure-induced MMCT transition in the composites, beginning with the ability to observe point-pressure effects, such as the alteration of properties when writing on the surface, and culminating in the complete MMCT transition from high-temperature (HT) to low-temperature (LT) phase upon the application of pressure at room temperature. This process was monitored at Fe and Ni K-edges using the SOLARIS synchrotron, providing a detailed insight into the material's behaviour under pressure. The change in oxidation state of the metal centres was confirmed through additional cooling during XAS measurements, utilizing a custom-made sample holder. Furthermore, the reversible transition back to the HT phase of the **NiFe-chain** was demonstrated by carefully heating the sample. This section highlights the promising potential of the **NiFe-foil** composites as advanced materials for pressure sensors, showcasing their dynamic response to external stimuli and their ability to undergo reversible phase transitions.

7. Summary of the thesis

This thesis presents the successful development of a new class of functional polymer-based composite materials that incorporate various inorganic and coordination compounds, focusing on their structural integrity, magnetic and electronic properties, and responsiveness to external stimuli.

The first major achievement is the integration of pre-synthesized Prussian Blue analogue (PBA) nanoparticles into electrospun polymer fibres. These composites retained the structural and magnetic properties of the PBAs, despite the high-voltage processing involved. Unlike traditional soft-matrix composites, the electrospinning method ensured the particles were embedded within the fibre core rather than on the surface, minimizing aggregation and enhancing mechanical strength. Importantly, the fibres remained elastic and structurally coherent at relatively high nanoparticle loadings, showing potential for robust, flexible magnetic materials.

The second key contribution lies in the development of Fe(II) spin-crossover (SCO) nanoparticle–polymer composites. A multi-technique characterization revealed size-dependent changes in the SCO behaviour and demonstrated the value of combining Mössbauer spectroscopy, X−ray absorption spectroscopy, and magnetometry for comprehensive analysis. Electrospun fibre mats incorporating these SCO nanoparticles exhibited thermally reversible spin transitions with improved cooperativity and long-term stability compared to drop-cast films. The resulting materials were both mechanically resilient and magnetically responsive, showing promise for smart fabric and adaptive material technologies.

The third core achievement is the creation of polymer composites incorporating a miniaturised NiFe charge-transfer coordination chain, which exhibits reversible metal-to-metal charge transfer (MMCT). Using solvent-assisted sonication, the NiFe chains were successfully reduced to microcrystals while preserving their functional properties. These were embedded in polymer matrices via electrospinning and drop-casting. The electrospun fibres showed homogeneous particle distribution and improved water resistance, especially in PCL matrices. Most significantly, drop-cast films demonstrated clear pressure-induced MMCT transitions at room temperature, fully reversible upon mild heating. Synchrotron-based measurements confirmed the oxidation state changes, validating the potential of these materials for flexible pressure sensors.

In conclusion, this work establishes scalable and adaptable fabrication techniques for hybrid polymer–inorganic materials with switchable magnetic and electronic functionalities. By combining electrospinning with careful nanoparticle engineering, the thesis opens pathways to smart, responsive materials suitable for applications in sensors, wearable electronics, and soft device.

8. Bibliography

(1) Batten, S. R.; Neville, S. M.; Turner, D. R. *Coordination Polymers: Design, Analysis and Application*; The Royal Society of Chemistry: Cambridge, 2008. https://doi.org/10.1039/9781847558862.

(2) Murphy, R. A.; Long, J. R.; David Harris, T. A Hard Permanent Magnet through Molecular Design. *Commun. Chem.* **2021**, *4* (1), 1–4. https://doi.org/10.1038/S42004-021-00509-Y.

(3) Noro, S. I.; Mizutani, J.; Hijikata, Y.; Matsuda, R.; Sato, H.; Kitagawa, S.; Sugimoto, K.; Inubushi, Y.; Kubo, K.; Nakamura, T. Porous Coordination Polymers with Ubiquitous and Biocompatible Metals and a Neutral Bridging Ligand. *Nat. Commun. 2015 61* **2015**, *6* (1), 1–9. https://doi.org/10.1038/ncomms6851.

(4) Shivanna, M.; Yang, Q. Y.; Bajpai, A.; Patyk-Kazmierczak, E.; Zaworotko, M. J. A Dynamic and Multi-Responsive Porous Flexible Metal–Organic Material. *Nat. Commun. 2018 91* **2018**, *9* (1), 1–7. https://doi.org/10.1038/s41467-018-05503-y.

(5) Mingabudinova, L. R.; Vinogradov, V. V.; Milichko, V. A.; Hey-Hawkins, E.; Vinogradov, A. V. Metal–Organic Frameworks as Competitive Materials for Non-Linear Optics. *Chem. Soc. Rev.* **2016**, *45* (19), 5408–5431. https://doi.org/10.1039/C6CS00395H.

(6) Mahfoud, T.; Molnár, G.; Bonhommeau, S.; Cobo, S.; Salmon, L.; Demont, P.; Tokoro, H.; Ohkoshi, S. I.; Boukheddaden, K.; Bousseksou, A. Electric-Field-Induced Charge-Transfer Phase Transition: A Promising Approach toward Electrically Switchable Devices. *J. Am. Chem. Soc.* **2009**, *131* (41), 15049–15054. https://doi.org/10.1021/JA9055855.

(7) Hoshino, N.; Iijima, F.; Newton, G. N.; Yoshida, N.; Shiga, T.; Nojiri, H.; Nakao, A.; Kumai, R.; Murakami, Y.; Oshio, H. Three-Way Switching in a Cyanide-Bridged [CoFe] Chain. *Nat. Chem.* **2012**, *4* (11), 921–926. https://doi.org/10.1038/NCHEM.1455.

(8) Ohkoshi, S. I.; Imoto, K.; Tsunobuchi, Y.; Takano, S.; Tokoro, H. Light-Induced Spin-Crossover Magnet. *Nat. Chem.* **2011**, *3* (7), 564–569. https://doi.org/10.1038/NCHEM.1067.

(9) Pinkowicz, D.; Rams, M.; Mišek, M.; Kamenev, K. V.; Tomkowiak, H.; Katrusiak, A.; Sieklucka, B. Enforcing Multifunctionality: A Pressure-Induced Spin-Crossover Photomagnet. *J. Am. Chem. Soc.* **2015**, *137* (27), 8795–8802. https://doi.org/10.1021/JACS.5B04303.

(10) Haldar, R.; Heinke, L.; Wöll, C. Advanced Photoresponsive Materials Using the Metal–Organic Framework Approach. *Adv. Mater.* **2020**, *32* (20), 1905227. https://doi.org/10.1002/ADMA.201905227.

(11) Maspoch, D.; Ruiz-Molina, D.; Wurst, K.; Domingo, N.; Cavallini, M.; Biscarini, F.; Tejada, J.; Rovira, C.; Veciana, J. A Nanoporous Molecular Magnet with Reversible Solvent-Induced Mechanical and Magnetic Properties. *Nat. Mater.* **2003**, *2* (3), 190–195. https://doi.org/10.1038/NMAT834.

(12) Ohkoshi, S. I.; Arai, K. I.; Sato, Y.; Hashimoto, K. Humidity-Induced Magnetization and

Magnetic Pole Inversion in a Cyano-Bridged Metal Assembly. *Nat. Mater.* **2004**, *3* (12), 857–861. https://doi.org/10.1038/NMAT1260.

(13) Ferrando-Soria, J.; Vallejo, J.; Castellano, M.; Martínez-Lillo, J.; Pardo, E.; Cano, J.; Castro, I.; Lloret, F.; Ruiz-García, R.; Julve, M. Molecular Magnetism, Quo Vadis? A Historical Perspective from a Coordination Chemist Viewpoint☆. *Coord. Chem. Rev.* **2017**, *339*, 17–103. https://doi.org/10.1016/J.CCR.2017.03.004.

(14) Miller, J. S.; Epstein, A. J.; Reiff, W. M. Molecular/Organic Ferromagnets. *Science (80-.).* **1988**, *240* (4848), 40–47. https://doi.org/10.1126/SCIENCE.240.4848.40.

(15) Ferlay, S.; Mallah, T.; Ouahès, R.; Veillet, P.; Verdaguer, M. A Room-Temperature Organometallic Magnet Based on Prussian Blue. *Nature* **1995**, *378* (6558), 701–703. https://doi.org/10.1038/378701A0.

(16) Holmes, S. M.; Girolami, G. S. Sol−Gel Synthesis of KVII[CrIII(CN)6]·2H2O: A Crystalline Molecule-Based Magnet with a Magnetic Ordering Temperature above 100 °C. *J. Am. Chem. Soc.* **1999**, *121* (23), 5593–5594. https://doi.org/10.1021/JA990946C.

(17) Sato, O.; Iyoda, T.; Fujishima, A.; Hashimoto, K. Photoinduced Magnetization of a Cobalt-Iron Cyanide. *Science (80-.).* **1996**, *272* (5262), 704–705. https://doi.org/10.1126/SCIENCE.272.5262.704.

(18) Ohkoshi, S. I.; Tokoro, H. Photomagnetism in Cyano-Bridged Bimetal Assemblies. *Acc. Chem. Res.* **2012**, *45* (10), 1749–1758. https://doi.org/10.1021/AR300068K.

(19) Pedersen, K. S.; Perlepe, P.; Aubrey, M. L.; Woodruff, D. N.; Reyes-Lillo, S. E.; Reinholdt, A.; Voigt, L.; Li, Z.; Borup, K.; Rouzières, M.; Samohvalov, D.; Wilhelm, F.; Rogalev, A.; Neaton, J. B.; Long, J. R.; Clérac, R. Formation of the Layered Conductive Magnet CrCl2(Pyrazine)2 through Redox-Active Coordination Chemistry. *Nat. Chem. 2018 1010* **2018**, *10* (10), 1056–1061. https://doi.org/10.1038/s41557-018-0107-7.

(20) Larionova, J.; Kahn, O.; Gohlen, S.; Ouahab, L.; Clérac, R. Structure, Ferromagnetic Ordering, Anisotropy, and Spin Reorientation for the Two-Dimensional Cyano-Bridged Bimetallic Compound K2Mn3(H2O)6[Mo(CN)7]2 · 6H2O. *J. Am. Chem. Soc.* **1999**, *121* (14), 3349–3356. https://doi.org/10.1021/JA9832717.

(21) Clérac, R.; Miyasaka, H.; Yamashita, M.; Coulon, C. Evidence for Single-Chain Magnet Behavior in a MnIII-NiII Chain Designed with High Spin Magnetic Units: A Route to High Temperature Metastable Magnets. *J. Am. Chem. Soc.* **2002**, *124* (43), 12837–12844. https://doi.org/10.1021/JA0203115.

(22) Gatteschi, D.; Sessoli, R. Quantum Tunneling of Magnetization and Related Phenomena in Molecular Materials. *Angew. Chemie - Int. Ed.* **2003**, *42* (3), 268–297. https://doi.org/10.1002/ANIE.200390099.

(23) Gatteschi, D.; Caneschi, A.; Pardi, L.; Sessoli, R. Large Clusters of Metal Ions: The Transition from Molecular to Bulk Magnets. *Science (80-.).* **1994**, *265* (5175), 1054–1058. https://doi.org/10.1126/SCIENCE.265.5175.1054.

(24) Sessoli, R.; Gatteschi, D.; Caneschi, A.; Novak, M. A. Magnetic Bistability in a Metal-Ion Cluster. *Nature* **1993**, *365* (6442), 141–143. https://doi.org/10.1038/365141A0.

(25) Mavragani, N.; Murugesu, M. Mn12 and the Dawn of Single-Molecule Magnets. *Nat.*

Chem. **2025**, *17* (2), 302. https://doi.org/10.1038/S41557-024-01718-3.

(26) Verdaguer, M. Molecular Electronics Emerges from Molecular Magnetism. *Science (80-.).* **1996**, *272* (5262), 698–699. https://doi.org/10.1126/SCIENCE.272.5262.698.

(27) Chiesa, A.; Privitera, A.; Macaluso, E.; Mannini, M.; Bittl, R.; Naaman, R.; Wasielewski, M. R.; Sessoli, R.; Carretta, S. Chirality-Induced Spin Selectivity: An Enabling Technology for Quantum Applications. *Adv. Mater.* **2023**, *35* (28), 2300472. https://doi.org/10.1002/ADMA.202300472.

(28) Rocha, A. R.; García-SUÁREZ, V. M.; Bailey, S. W.; Lambert, C. J.; Ferrer, J.; Sanvito, S. Towards Molecular Spintronics. *Nat. Mater.* **2005**, *4* (4), 335–339. https://doi.org/10.1038/NMAT1349.

(29) Coronado, E. Molecular Magnetism: From Chemical Design to Spin Control in Molecules, Materials and Devices. *Nat. Rev. Mater.* **2020**, *5* (2), 87–104. https://doi.org/10.1038/s41578-019-0146-8.

(30) Kahn, O.; Kröber, J.; Jay, C. Spin Transition Molecular Materials for Displays and Data Recording. *Adv. Mater.* **1992**, *4* (11), 718–728. https://doi.org/10.1002/ADMA.19920041103.

(31) Kitagawa, S.; Kitaura, R.; Noro, S. I. Functional Porous Coordination Polymers. *Angew. Chemie - Int. Ed.* **2004**, *43* (18), 2334–2375. https://doi.org/10.1002/ANIE.200300610.

(32) Stanley, P. M.; Haimerl, J.; Shustova, N. B.; Fischer, R. A.; Warnan, J. Merging Molecular Catalysts and Metal–Organic Frameworks for Photocatalytic Fuel Production. *Nat. Chem. 2022 1412* **2022**, *14* (12), 1342–1356. https://doi.org/10.1038/s41557-022-01093-x.

(33) Lin, J.; Ouyang, J.; Liu, T.; Li, F.; Sung, H. H. Y.; Williams, I.; Quan, Y. Metal-Organic Framework Boosts Heterogeneous Electron Donor–Acceptor Catalysis. *Nat. Commun. 2023 141* **2023**, *14* (1), 1–11. https://doi.org/10.1038/s41467-023-43577-5.

(34) Nowicka, B.; Reczyński, M.; Rams, M.; Nitek, W.; Kozieł, M.; Sieklucka, B. Larger Pores and Higher Tc: {[Ni(Cyclam)]3[W(CN)8]2·solv}n – a New Member of the Largest Family of Pseudo-Polymorphic Isomers among Octacyanometallate-Based Assemblies. *CrystEngComm* **2015**, *17* (18), 3526–3532. https://doi.org/10.1039/C5CE00287G.

(35) Magott, M.; Gaweł, B.; Sarewicz, M.; Reczyński, M.; Ogorzały, K.; Makowski, W.; Pinkowicz, D. Large Breathing Effect Induced by Water Sorption in a Remarkably Stable Nonporous Cyanide-Bridged Coordination Polymer. *Chem. Sci.* **2021**, *12* (26), 9176–9188. https://doi.org/10.1039/D1SC02060A.

(36) Southon, P. D.; Liu, L.; Fellows, E. A.; Price, D. J.; Halder, G. J.; Chapman, K. W.; Moubaraki, B.; Murray, K. S.; Létard, J. F.; Kepert, C. J. Dynamic Interplay between Spin-Crossover and Host-Guest Function in a Nanoporous Metal-Organic Framework Material. *J. Am. Chem. Soc.* **2009**, *131* (31), 10998–11009. https://doi.org/10.1021/JA902187D.

(37) Sato, Y.; Ohkoshi, S. I.; Arai, K. I.; Tozawa, M.; Hashimoto, K. Solvatomagnetism-Induced Faraday Effect in a Cobalt Hexacyanochromate-Based Magnet. *J. Am. Chem. Soc.* **2003**, *125* (47), 14590–14595. https://doi.org/10.1021/JA030375V.

(38) Kahn, O.; Larionova, J.; Yakhmi, J. V. Molecular Magnetic Sponges. *Chem. - A Eur. J.* **1999**, *5* (12), 3443–3449. https://doi.org/https://doi.org/10.1002/(SICI)1521-3765(19991203)5.

(39) Sato, O. Dynamic Molecular Crystals with Switchable Physical Properties. *Nat. Chem.* **2016**, *8* (7), 644–656. https://doi.org/10.1038/nchem.2547.

(40) Bhatt, P.; Kumar, A.; Yusuf, S. M. Multifunctional Properties and Potential Applications of Prussian Blue Analogue Magnets. *Chem. Mater.* **2025**. https://doi.org/10.1021/ACS.CHEMMATER.4C02904.

(41) Huang, Y.; Ren, S. Multifunctional Prussian Blue Analogue Magnets: Emerging Opportunities. *Appl. Mater. Today* **2021**, *22*, 100886. https://doi.org/10.1016/J.APMT.2020.100886.

(42) Hatlevik, Ø.; Buschmann, W. E.; Zhang, J.; Manson, J. L.; Miller, J. S. Enhancement of the Magnetic Ordering Temperature and Air Stability of a Mixed Valent Vanadium Hexacyanochromate(III) Magnet to 99 °C (372 K). *Adv. Mater.* **1999**, *11* (11), 914–918. https://doi.org/10.1002/(SICI)1521-4095(199908)11:11<914::AID-ADMA914>3.0.CO;2-T.

(43) Ohkoshi, S. ichi; Tokoro, H.; Collet, E. Thermally Induced and Photoinduced Phase Transitions in Rubidium Manganese Hexacyanoferrate Combining Charge Transfer and Structural Reorganization. *Comptes Rendus Chim.* **2019**, *22* (6–7), 498–507. https://doi.org/10.1016/J.CRCI.2019.05.002.

(44) Davidson, R. A.; Miller, J. S. Pressure Dependence of the Magnetic Ordering Temperature (Tc) for the Na2Mn[Mn(CN)6] Noncubic Prussian Blue Analogue. *Inorg. Chem.* **2021**, *60* (17), 12766–12771. https://doi.org/10.1021/ACS.INORGCHEM.1C00777.

(45) Aguilà, D.; Prado, Y.; Koumousi, E. S.; Mathonière, C.; Clérac, R. Switchable Fe/Co Prussian Blue Networks and Molecular Analogues. *Chem. Soc. Rev.* **2015**, *45* (1), 203–224. https://doi.org/10.1039/C5CS00321K.

(46) Ohkoshi, S. I.; Nakagawa, K.; Tomono, K.; Imoto, K.; Tsunobuchi, Y.; Tokoro, H. High Proton Conductivity in Prussian Blue Analogues and the Interference Effect by Magnetic Ordering. *J. Am. Chem. Soc.* **2010**, *132* (19), 6620–6621. https://doi.org/10.1021/JA100385F.

(47) Kraft, A. Some Considerations on the Structure, Composition, and Properties of Prussian Blue: A Contribution to the Current Discussion. *Ionics (Kiel).* **2021**, *27* (6), 2289–2305. https://doi.org/10.1007/S11581-021-04013-0.

(48) Coronado, E. Molecular Magnetism: From Chemical Design to Spin Control in Molecules, Materials and Devices. *Nat. Rev. Mater.* **2020**, *5* (2), 87–104. https://doi.org/10.1038/S41578-019-0146-8.

(49) Wyczesany, M.; Zakrzewski, J. J.; Sieklucka, B.; Chorazy, S. Metal-Cyanido Molecular Modulators of the Sensing Range and Performance in Lanthanide-Based Luminescent Thermometers. *J. Mater. Chem. C* **2022**, *10* (33), 12054–12069. https://doi.org/10.1039/D2TC02591D.

(50) Zakrzewski, J. J.; Liberka, M.; Wang, J.; Chorazy, S.; Ohkoshi, S. I. Optical Phenomena in Molecule-Based Magnetic Materials. *Chem. Rev.* **2024**, *124* (9), 5930–6050.

https://doi.org/10.1021/ACS.CHEMREV.3C00840.

(51) Zhang, Z.; Avdeev, M.; Chen, H.; Yin, W.; Kan, W. H.; He, G. Lithiated Prussian Blue Analogues as Positive Electrode Active Materials for Stable Non-Aqueous Lithium-Ion Batteries. *Nat. Commun. 2022 131* **2022**, *13* (1), 1–13. https://doi.org/10.1038/s41467-022-35376-1.

(52) Nie, P.; Shen, L.; Luo, H.; Ding, B.; Xu, G.; Wang, J.; Zhang, X. Prussian Blue Analogues: A New Class of Anode Materials for Lithium Ion Batteries. *J. Mater. Chem. A* **2014**, *2* (16), 5852–5857. https://doi.org/10.1039/C4TA00062E.

(53) Bavykina, A.; Kolobov, N.; Khan, I. S.; Bau, J. A.; Ramirez, A.; Gascon, J. Metal-Organic Frameworks in Heterogeneous Catalysis: Recent Progress, New Trends, and Future Perspectives. *Chem. Rev.* **2020**, *120* (16), 8468–8535. https://doi.org/10.1021/ACS.CHEMREV.9B00685.

(54) Yang, D.; Gates, B. C. Catalysis by Metal Organic Frameworks: Perspective and Suggestions for Future Research. *ACS Catal.* **2019**, *9* (3), 1779–1798. https://doi.org/10.1021/ACSCATAL.8B04515.

(55) Li, W.; Xu, P.; Wang, Z.; He, Y.; Qin, H.; Zeng, Y.; Li, Y.; Zhang, Z.; Gao, J. MOFs Meet Membrane: Application in Water Treatment and Separation. *Mater. Chem. Front.* **2023**, *7* (21), 5140–5170. https://doi.org/10.1039/D3QM00487B.

(56) Sun, L.; Li, X.; Vandenbulcke, C.; Belmouri, N. E. I.; Bouchez, G.; Robeyns, K.; Rotaru, A.; Boukheddaden, K.; Garcia, Y. Stimuli-Responsive Spin Crossover Behavior in 3D Fe(II) Porous Coordination Polymers for Guest Molecules. *Mater. Adv.* **2024**, *5* (21), 8564–8574. https://doi.org/10.1039/D4MA00527A.

(57) Liu, D.; He, C.; Poon, C.; Lin, W. Theranostic Nanoscale Coordination Polymers for Magnetic Resonance Imaging and Bisphosphonate Delivery. *J. Mater. Chem. B* **2014**, *2* (46), 8249–8255. https://doi.org/10.1039/C4TB00751D.

(58) Suárez-García, S.; Arias-Ramos, N.; Frias, C.; Candiota, A. P.; Arús, C.; Lorenzo, J.; Ruiz-Molina, D.; Novio, F. Dual T1/ T2 Nanoscale Coordination Polymers as Novel Contrast Agents for MRI: A Preclinical Study for Brain Tumor. *ACS Appl. Mater. Interfaces* **2018**, *10* (45), 38819–38832. https://doi.org/10.1021/ACSAMI.8B15594.

(59) Fitta, M.; Prima-Garcia, H.; Czaja, P.; Korzeniak, T.; Krupiński, M.; Wojtyniak, M.; Bałanda, M. Magnetic and Magneto-Optical Properties of Nickel Hexacyanoferrate/Chromate Thin Films. *RSC Adv.* **2017**, *7* (3), 1382–1386. https://doi.org/10.1039/C6RA25775E.

(60) Fitta, M.; Sas, W.; Korzeniak, T. Tunable Critical Temperature and Magnetocaloric Effect in Ternary Prussian Blue Analogue. *J. Magn. Magn. Mater.* **2018**, *465*, 640–645. https://doi.org/10.1016/j.jmmm.2018.06.053.

(61) Tokoro, H.; Ohkoshi, S. I.; Matsuda, T.; Hashimoto, K. A Large Thermal Hysteresis Loop Produced by a Charge-Transfer Phase Transition in a Rubidium Manganese Hexacyanoferrate. *Inorg. Chem.* **2004**, *43* (17), 5231–5236. https://doi.org/10.1021/IC030332F.

(62) Azzolina, G.; Tokoro, H.; Imoto, K.; Yoshikiyo, M.; Ohkoshi, S. ichi; Collet, E. Exploring Ultrafast Photoswitching Pathways in RbMnFe Prussian Blue Analogue. *Angew. Chemie Int. Ed.* **2021**, *60* (43), 23267–23273.

https://doi.org/10.1002/ANIE.202106959.

(63) Jonas, K.; Jean-Paul, A.; Renée, C.; Epiphane, C.; Olivier, K.; Haasnoot, J. G.; Françoise, G.; Charlotte, J.; Bousseksou, A.; Jorge, L.; François, V.; Anne, G. V. Spin Transitions and Thermal Hysteresis in the Molecular-Based Materials [Fe(Htrz)2(Trz)](BF4) and [Fe(Htrz)3](BF4)2·H2O (Htrz = 1,2,4-4H-Triazole; Trz = 1,2,4-Triazolato). *Chem. Mater.* **1994**, *6* (8), 1404–1412. https://doi.org/10.1021/CM00044A044.

(64) Coronado, E.; Galán-Mascarós, J. R.; Monrabal-Capilla, M.; García-Martínez, J.; Pardo-Ibáñez, P. Bistable Spin-Crossover Nanoparticles Showing Magnetic Thermal Hysteresis near Room Temperature. *Adv. Mater.* **2007**, *19* (10), 1359–1361. https://doi.org/10.1002/ADMA.200700559.

(65) Torres-Cavanillas, R.; Gavara-Edo, M.; Coronado, E. Bistable Spin-Crossover Nanoparticles for Molecular Electronics. *Adv. Mater.* **2024**, *36* (1), 2307718. https://doi.org/10.1002/ADMA.202307718.

(66) Reczyński, M.; Pinkowicz, D.; Nakabayashi, K.; Näther, C.; Stanek, J.; Kozieł, M.; Kalinowska-Tłuścik, J.; Sieklucka, B.; Ohkoshi, S. ichi; Nowicka, B. Room-Temperature Bistability in a Ni–Fe Chain: Electron Transfer Controlled by Temperature, Pressure, Light, and Humidity. *Angew. Chemie - Int. Ed.* **2021**, *60* (5), 2330–2338. https://doi.org/10.1002/anie.202012876.

(67) Kahn, O.; Martinez, C. J. Spin-Transition Polymers: From Molecular Materials toward Memory Devices. *Science (80-.).* **1998**, *279* (5347), 44–48. https://doi.org/10.1126/SCIENCE.279.5347.44.

(68) Meng, Y. S.; Liu, T. Manipulating Spin Transition To Achieve Switchable Multifunctions. *Acc. Chem. Res.* **2019**, *52* (5), 1369–1379. https://doi.org/10.1021/ACS.ACCOUNTS.9B00049.

(69) Berlin Heidelberg, S.-V.; Gütlich, P.; Goodwin, H. A. Spin Crossover—An Overall Perspective. *Top Curr Chem* **2012**, *233*, 1–47. https://doi.org/10.1007/B13527.

(70) Gütlich, P.; Gaspar, A. B.; Garcia, Y. Spin State Switching in Iron Coordination Compounds. *Beilstein J. Org. Chem. 939* **2013**, *9* (1), 342–391. https://doi.org/10.3762/BJOC.9.39.

(71) Létard, J. F. Photomagnetism of Iron(II) Spin Crossover Complexes—the T(LIESST) Approach. *J. Mater. Chem.* **2006**, *16* (26), 2550–2559. https://doi.org/10.1039/B603473J.

(72) Arcis-Castíllo, Z.; Zheng, S.; Siegler, M. A.; Roubeau, O.; Bedoui, S.; Bonnet, S. Tuning the Transition Temperature and Cooperativity of Bapbpy-Based Mononuclear Spin-Crossover Compounds: Interplay between Molecular and Crystal Engineering. *Chem. – A Eur. J.* **2011**, *17* (52), 14826–14836. https://doi.org/10.1002/CHEM.201101301.

(73) Molnár, G.; Mikolasek, M.; Ridier, K.; Fahs, A.; Nicolazzi, W.; Bousseksou, A. Molecular Spin Crossover Materials: Review of the Lattice Dynamical Properties. *Ann. Phys.* **2019**, *531* (10), 1900076. https://doi.org/10.1002/ANDP.201900076.

(74) Molnár, G.; Rat, S.; Salmon, L.; Nicolazzi, W.; Bousseksou, A. Spin Crossover Nanomaterials: From Fundamental Concepts to Devices. *Adv. Mater.* **2018**, *30* (5), 1703862. https://doi.org/10.1002/ADMA.201703862.

(75) Volatron, F.; Catala, L.; Rivière, E.; Gloter, A.; Stéphan, O.; Mallah, T. Spin-Crossover Coordination Nanoparticles. *Inorg. Chem.* **2008**, *47* (15), 6584–6586. https://doi.org/10.1021/IC800803W.

(76) Giménez-Marqués, M.; García-Sanz De Larrea, M. L.; Coronado, E. Unravelling the Chemical Design of Spin-Crossover Nanoparticles Based on Iron(II)–Triazole Coordination Polymers: Towards a Control of the Spin Transition. *J. Mater. Chem. C* **2015**, *3* (30), 7946–7953. https://doi.org/10.1039/C5TC01093D.

(77) Mathonière, C. Metal-to-Metal Electron Transfer: A Powerful Tool for the Design of Switchable Coordination Compounds. *Eur. J. Inorg. Chem.* **2018**, *2018* (3–4), 248–258. https://doi.org/10.1002/EJIC.201701194.

(78) Li, D.; Clérac, R.; Roubeau, O.; Harté, E.; Mathonière, C.; Le Bris, R.; Holmes, S. M. Magnetic and Optical Bistability Driven by Thermally and Photoinduced Intramolecular Electron Transfer in a Molecular Cobalt-Iron Prussian Blue Analogue. *J. Am. Chem. Soc.* **2008**, *130* (1), 252–258. https://doi.org/10.1021/JA0757632.

(79) Meng, Y. S.; Sato, O.; Liu, T. Manipulating Metal-to-Metal Charge Transfer for Materials with Switchable Functionality. *Angew. Chemie - Int. Ed.* **2018**, *57* (38), 12216–12226. https://doi.org/10.1002/ANIE.201804557.

(80) Podgajny, R.; Chorazy, S.; Nitek, W.; Rams, M.; Majcher, A. M.; Marszałek, B.; Zukrowski, J.; Kapusta, C.; Sieklucka, B. Co–NC–W and Fe–NC–W Electron-Transfer Channels for Thermal Bistability in Trimetallic {Fe6Co3[W(CN)8]6} Cyanido-Bridged Cluster. *Angew. Chemie Int. Ed.* **2013**, *52* (3), 896–900. https://doi.org/10.1002/ANIE.201208023.

(81) Yadav, J.; Konar, S. Spin State Modulation and Kinetic Control of Thermal Contraction in a [Fe2Co2] Discrete Prussian Blue Analogue. *Chem. Sci.* **2024**, *16* (1), 130–138. https://doi.org/10.1039/D4SC05792A.

(82) Goodwin, A. L.; Calleja, M.; Conterio, M. J.; Dove, M. T.; Evans, J. S. O.; Keen, D. A.; Peters, L.; Tucker, M. G. Colossal Positive and Negative Thermal Expansion in the Framework Material Ag3[Co(CN)6]. *Science (80-.).* **2008**, *319* (5864), 794–797. https://doi.org/10.1126/SCIENCE.1151442.

(83) Nakamura, K.; Guérin, L.; Privault, G.; Nakabayashi, K.; Hervé, M.; Collet, E.; Ohkoshi, S. I. Ultrafast Charge-Transfer-Induced Spin Transition in Cobalt-Tungstate Molecular Photomagnets. *Nat. Commun.* **2025**, *16* (1), 1–10. https://doi.org/10.1038/S41467-025-60401-4.

(84) Enriquez-Cabrera, A.; Rapakousiou, A.; Piedrahita Bello, M.; Molnár, G.; Salmon, L.; Bousseksou, A. Spin Crossover Polymer Composites, Polymers and Related Soft Materials. *Coord. Chem. Rev.* **2020**, *419*, 213396. https://doi.org/https://doi.org/10.1016/j.ccr.2020.213396.

(85) Xie, C. L.; Hendrickson, D. N. Mechanism of Spin-State Interconversion in Ferrous Spin-Crossover Complexes: Direct Evidence for Quantum Mechanical Tunneling. *J. Am. Chem. Soc.* **1987**, *109* (23), 6981–6988. https://doi.org/10.1021/JA00257A013.

(86) Basak, S.; Hui, P.; Chandrasekar, R. Flexible and Optically Transparent Polymer Embedded Nano/Micro Scale Spin Crossover Fe(II) Complex Patterns/Arrays. *Chem. Mater.* **2013**, *25* (17), 3408–3413. https://doi.org/10.1021/CM401058S.

(87) Echeverria, C.; Rubio, M.; Mitchell, G. R.; Roig, A.; Lõpez, D. Hybrid Polystyrene Based Electrospun Fibers with Spin-Crossover Properties. *J. Polym. Sci. Part B Polym. Phys.* **2015**, *53* (11), 814–821. https://doi.org/10.1002/POLB.23702.

(88) Brehme, J.; Kilic, M. S.; Pawlak, J.; Renz, F.; Sindelar, R. F. Soluble Molecular Switches in Electrospun Nanofibers. *Interactions* **2024**, *245* (1), 1–13. https://doi.org/10.1007/S10751-024-01842-Z.

(89) Kilic, M. S.; Brehme, J.; Pawlak, J.; Tran, K.; Bauer, F. W.; Shiga, T.; Suzuki, T.; Nihei, M.; Sindelar, R. F.; Renz, F. Incorporation and Deposition of Spin Crossover Materials into and onto Electrospun Nanofibers. *Polym. 2023, Vol. 15, Page 2365* **2023**, *15* (10), 2365. https://doi.org/10.3390/POLYM15102365.

(90) Tokarev, A.; Long, J.; Guari, Y.; Larionova, J.; Quignard, F.; Agulhon, P.; Robitzer, M.; Molnár, G.; Salmon, L.; Bousseksou, A. Spin Crossover Polysaccharide Nanocomposites. *New J. Chem.* **2013**, *37* (11), 3420–3432. https://doi.org/10.1039/C3NJ00534H.

(91) Voisin, H.; Aimé, C.; Vallée, A.; Coradin, T.; Roux, C. A Flexible Polymer–Nanoparticle Hybrid Material Containing Triazole-Based Fe(II) with Spin Crossover Properties for Magneto-Optical Applications. *Inorg. Chem. Front.* **2018**, *5* (9), 2140–2147. https://doi.org/10.1039/C8QI00494C.

(92) Durand, P.; Pillet, S.; Bendeif, E. E.; Carteret, C.; Bouazaoui, M.; El Hamzaoui, H.; Capoen, B.; Salmon, L.; Hébert, S.; Ghanbaja, J.; Aranda, L.; Schaniel, D. Room Temperature Bistability with Wide Thermal Hysteresis in a Spin Crossover Silica Nanocomposite. *J. Mater. Chem. C* **2013**, *1* (10), 1933–1942. https://doi.org/10.1039/C3TC00546A.

(93) Larionova, J.; Salmon, L.; Guari, Y.; Tokarev, A.; Molvinger, K.; Molnμr, G.; Bousseksou, A.; Larionova, J.; Guari, Y.; Tokarev, A.; Salmon, L.; Molnμr, G.; Bousseksou, A.; Molvinger, K. Towards the Ultimate Size Limit of the Memory Effect in Spin-Crossover Solids. *Angew. Chemie Int. Ed.* **2008**, *47* (43), 8236–8240. https://doi.org/10.1002/ANIE.200802906.

(94) Shepherd, H. J.; Gural'Skiy, I. A.; Quintero, C. M.; Tricard, S.; Salmon, L.; Molnár, G.; Bousseksou, A. Molecular Actuators Driven by Cooperative Spin-State Switching. *Nat. Commun.* **2013**, *4* (1), 1–9. https://doi.org/10.1038/NCOMMS3607.

(95) Gural'Skiy, I. A.; Quintero, C. M.; Costa, J. S.; Demont, P.; Molnár, G.; Salmon, L.; Shepherd, H. J.; Bousseksou, A. Spin Crossover Composite Materials for Electrothermomechanical Actuators. *J. Mater. Chem. C* **2014**, *2* (16), 2949–2955. https://doi.org/10.1039/C4TC00267A.

(96) Rat, S.; Piedrahita-Bello, M.; Salmon, L.; Molnár, G.; Demont, P.; Bousseksou, A. Coupling Mechanical and Electrical Properties in Spin Crossover Polymer Composites. *Adv. Mater.* **2018**, *30* (8), 1705275. https://doi.org/10.1002/ADMA.201705275.

(97) Piedrahita-Bello, M.; Martin, B.; Salmon, L.; Molnár, G.; Demont, P.; Bousseksou, A. Mechano-Electric Coupling in P(VDF–TrFE)/Spin Crossover Composites. *J. Mater. Chem. C* **2020**, *8* (18), 6042–6051. https://doi.org/10.1039/D0TC00780C.

(98) Rat, S.; Nagy, V.; Suleimanov, I.; Molnár, G.; Salmon, L.; Demont, P.; Csóka, L.; Bousseksou, A. Elastic Coupling between Spin-Crossover Particles and Cellulose Fibers.

Chem. Commun. **2016**, *52* (75), 11267–11269. https://doi.org/10.1039/C6CC06137K.

(99) Manrique-Juárez, M. D.; Mathieu, F.; Laborde, A.; Rat, S.; Shalabaeva, V.; Demont, P.; Thomas, O.; Salmon, L.; Leichle, T.; Nicu, L.; Molnár, G.; Bousseksou, A. Micromachining-Compatible, Facile Fabrication of Polymer Nanocomposite Spin Crossover Actuators. *Adv. Funct. Mater.* **2018**, *28* (29), 1801970. https://doi.org/10.1002/ADFM.201801970.

(100) Piedrahita-Bello, M.; Piedrahita-Bello, M.; Angulo-Cervera, J. E.; Angulo-Cervera, J. E.; Courson, R.; Molnár, G.; Malaquin, L.; Thibault, C.; Tondu, B.; Salmon, L.; Bousseksou, A. 4D Printing with Spin-Crossover Polymer Composites. *J. Mater. Chem. C* **2020**, *8* (18), 6001–6005. https://doi.org/10.1039/D0TC01532F.

(101) Kulkarni, O.; Enriquez-Cabrera, A.; Yang, X.; Foncy, J.; Nicu, L.; Molnár, G.; Salmon, L. Stereolithography 3D Printing of Stimuli-Responsive Spin Crossover@Polymer Nanocomposites with Optimized Actuating Properties. *Nanomaterials* **2024**, *14* (15), 1243. https://doi.org/10.3390/NANO14151243/S1.

(102) Bushuev, M. B.; Pishchur, D. P.; Korolkov, I. V.; Vinogradova, K. A. Prototypical Iron(II) Complex with 4-Amino-1,2,4-Triazole Reinvestigated: An Unexpected Impact of Water on Spin Transition. *Phys. Chem. Chem. Phys.* **2017**, *19* (5), 4056–4068. https://doi.org/10.1039/C6CP06854E.

(103) Tran, K.; Sander, P.; Seydi Kilic, M.; Brehme, J.; Sindelar, R.; Renz, F. Facile Approach for the Fabrication of Vapor Sensitive Spin Transition Composite Nanofibers. *Eur. J. Inorg. Chem.* **2024**, *27* (33), e202400363. https://doi.org/10.1002/EJIC.202400363.

(104) Sun, L.; Rotaru, A.; Robeyns, K.; Garcia, Y. A Colorimetric Sensor for the Highly Selective, Ultra-Sensitive, and Rapid Detection of Volatile Organic Compounds and Hazardous Gases. *Ind. Eng. Chem. Res.* **2021**, *60* (24), 8788–8798. https://doi.org/10.1021/ACS.IECR.1C01389.

(105) Schneider, C. A.; Rasband, W. S.; Eliceiri, K. W. NIH Image to ImageJ: 25 Years of Image Analysis. *Nat. Methods* **2012**, *9* (7), 671–675. https://doi.org/10.1038/NMETH.2089.

(106) Qureshi, N. Mag2Pol: A Program for the Analysis of Spherical Neutron Polarimetry, Flipping Ratio and Integrated Intensity Data. *urn:issn:1600-5767* **2019**, *52* (1), 175–185. https://doi.org/10.1107/S1600576718016084.

(107) Buchner, M.; Höfler, K.; Henne, B.; Ney, V.; Ney, A. Tutorial: Basic Principles, Limits of Detection, and Pitfalls of Highly Sensitive SQUID Magnetometry for Nanomagnetism and Spintronics. *J. Appl. Phys.* **2018**, *124* (16), 161101. https://doi.org/10.1063/1.5045299/1030088.

(108) Ravel, B.; Newville, M. ATHENA, ARTEMIS, HEPHAESTUS: Data Analysis for X-Ray Absorption Spectroscopy Using IFEFFIT. *urn:issn:0909-0495* **2005**, *12* (4), 537–541. https://doi.org/10.1107/S0909049505012719.

(109) Newville, M. Larch: An Analysis Package for XAFS and Related Spectroscopies. *J. Phys. Conf. Ser.* **2013**, *430* (1), 012007. https://doi.org/10.1088/1742-6596/430/1/012007.

(110) Bianchi, C. L.; Djellabi, R.; Ponti, A.; Patience, G. S.; Falletta, E. Experimental Methods in Chemical Engineering: Mössbauer Spectroscopy. *Can. J. Chem. Eng.* **2021**, *99* (10),

2105–2114. https://doi.org/10.1002/CJCE.24216.

(111) Ghosal, K.; Chandra, A.; Praveen, G.; Snigdha, S.; Roy, S.; Agatemor, C.; Thomas, S.; Provaznik, I. Electrospinning over Solvent Casting: Tuning of Mechanical Properties of Membranes. *Sci. Rep.* **2018**, *8* (1), 1–9. https://doi.org/10.1038/S41598-018-23378-3.

(112) Ji, D.; Lin, Y.; Guo, X.; Ramasubramanian, B.; Wang, R.; Radacsi, N.; Jose, R.; Qin, X.; Ramakrishna, S. Electrospinning of Nanofibres. *Nat. Rev. Methods Prim. 2024 41* **2024**, *4* (1), 1–21. https://doi.org/10.1038/s43586-023-00278-z.

(113) Greiner, A.; Wendorff, J. H. Electrospinning: A Fascinating Method for the Preparation of Ultrathin Fibers. *Angew. Chemie Int. Ed.* **2007**, *46* (30), 5670–5703. https://doi.org/10.1002/ANIE.200604646.

(114) Han, W. H.; Wang, M. Q.; Yuan, J. X.; Hao, C. C.; Li, C. J.; Long, Y. Z.; Ramakrishna, S. Electrospun Aligned Nanofibers: A Review. *Arab. J. Chem.* **2022**, *15* (11), 104193. https://doi.org/10.1016/J.ARABJC.2022.104193.

(115) Garg, K.; Bowlin, G. L. Electrospinning Jets and Nanofibrous Structures. *Biomicrofluidics* **2011**, *5* (1). https://doi.org/10.1063/1.3567097/385871.

(116) Reneker, D. H.; Yarin, A. L. Electrospinning Jets and Polymer Nanofibers. *Polymer (Guildf).* **2008**, *49* (10), 2387–2425. https://doi.org/10.1016/J.POLYMER.2008.02.002.

(117) Kailasa, S.; Sai Bhargava Reddy, M.; Raj Maurya, M.; Geeta Rani, B.; Venkateswara Rao, K.; Kumar Sadasivuni, K.; Kailasa, S.; B Reddy, M. S.; Rani, B. G.; Rao, K. V; Maurya, M. R.; Sadasivuni, K. K. Electrospun Nanofibers: Materials, Synthesis Parameters, and Their Role in Sensing Applications. *Macromol. Mater. Eng.* **2021**, *306* (11), 2100410. https://doi.org/10.1002/MAME.202100410.

(118) Mailley, D.; Hébraud, A.; Schlatter, G. A Review on the Impact of Humidity during Electrospinning: From the Nanofiber Structure Engineering to the Applications. *Macromol. Mater. Eng.* **2021**, *306* (7), 2100115. https://doi.org/10.1002/MAME.202100115.

(119) Prajapati, B. G.; Patel, P.; Patel, D. Mouth Dissolving Film as a Potential Dosage Form for Paediatric Usage. *J. Pharm. Biol. Sci.* **2024**, *11* (2), 133–141. https://doi.org/10.18231/J.JPBS.2023.021.

(120) Safo, I. A.; Werheid, M.; Dosche, C.; Oezaslan, M. The Role of Polyvinylpyrrolidone (PVP) as a Capping and Structure-Directing Agent in the Formation of Pt Nanocubes. *Nanoscale Adv.* **2019**, *1* (8), 3095–3106. https://doi.org/10.1039/C9NA00186G.

(121) Koczkur, K. M.; Mourdikoudis, S.; Polavarapu, L.; Skrabalak, S. E. Polyvinylpyrrolidone (PVP) in Nanoparticle Synthesis. *Dalt. Trans.* **2015**, *44* (41), 17883–17905. https://doi.org/10.1039/C5DT02964C.

(122) Liu, H. L.; Ko, S. P.; Wu, J. H.; Jung, M. H.; Min, J. H.; Lee, J. H.; An, B. H.; Kim, Y. K. One-Pot Polyol Synthesis of Monosize PVP-Coated Sub-5 Nm Fe3O4 Nanoparticles for Biomedical Applications. *J. Magn. Magn. Mater.* **2007**, *310* (2), e815–e817. https://doi.org/10.1016/J.JMMM.2006.10.776.

(123) Uemura, T.; Kitagawa, S. Prussian Blue Nanoparticles Protected by Poly(Vinylpyrrolidone). *J. Am. Chem. Soc.* **2003**, *125* (26), 7814–7815. https://doi.org/10.1021/JA0356582.

(124) Zhang, Q.; Zhu, G.; Shen, X.; Tong, L.; Ye, Z.; Chen, K. Coordination Polymer Micro/Nano-Crystals: Controlled Synthesis and Formation Mechanism in the Case of Mn2Mo(CN)8·xH2O. *CrystEngComm* **2013**, *15* (15), 2909–2915. https://doi.org/10.1039/C3CE26917E.

(125) Chen, S.-M.; Li, S.-H.; Thiagarajan, S.; Pajerowski, D. M.; Frye, F. A.; Talham, D. R.; Meisel, M. W. Size Dependence of the Photoinduced Magnetism and Long-Range Ordering in Prussian Blue Analogue Nanoparticles of Rubidium Cobalt Hexacyanoferrate. *New J. Phys.* **2007**, *9* (7), 222. https://doi.org/10.1088/1367-2630/9/7/222.

(126) Sun, B.; Duan, B.; Yuan, X. Preparation of Core/Shell PVP/PLA Ultrafine Fibers by Coaxial Electrospinning. *J. Appl. Polym. Sci.* **2006**, *102* (1), 39–45. https://doi.org/10.1002/APP.24297.

(127) Utkarsh; Hegab, H.; Tariq, M.; Syed, N. A.; Rizvi, G.; Pop-Iliev, R. Towards Analysis and Optimization of Electrospun PVP (Polyvinylpyrrolidone) Nanofibers. *Adv. Polym. Technol.* **2020**, *2020* (1), 4090747. https://doi.org/10.1155/2020/4090747.

(128) Liu, W.; Zhong, T.; Liu, T.; Zhang, J.; Liu, H. Preparation and Characterization of Electrospun Conductive Janus Nanofibers with Polyaniline. *ACS Appl. Polym. Mater.* **2020**, *2* (7), 2819–2829. https://doi.org/10.1021/ACSAPM.0C00364.

(129) Choi, J.; Lee, J.; Choi, J.; Jung, D.; Shim, S. E. Electrospun PEDOT:PSS/PVP Nanofibers as the Chemiresistor in Chemical Vapour Sensing. *Synth. Met.* **2010**, *160* (13–14), 1415–1421. https://doi.org/10.1016/J.SYNTHMET.2010.04.021.

(130) Ntrivala, M. A.; Pitsavas, A. C.; Lazaridou, K.; Baziakou, Z.; Karavasili, D.; Papadimitriou, M.; Ntagkopoulou, C.; Balla, E.; Bikiaris, D. N. Polycaprolactone (PCL): The Biodegradable Polyester Shaping the Future of Materials – a Review on Synthesis, Properties, Biodegradation, Applications and Future Perspectives. *Eur. Polym. J.* **2025**, *234*, 114033. https://doi.org/10.1016/J.EURPOLYMJ.2025.114033.

(131) Sruthi, R.; Balagangadharan, K.; Selvamurugan, N. Polycaprolactone/Polyvinylpyrrolidone Coaxial Electrospun Fibers Containing Veratric Acid-Loaded Chitosan Nanoparticles for Bone Regeneration. *Colloids Surfaces B Biointerfaces* **2020**, *193*, 111110. https://doi.org/10.1016/J.COLSURFB.2020.111110.

(132) Cipitria, A.; Skelton, A.; Dargaville, T. R.; Dalton, P. D.; Hutmacher, D. W. Design, Fabrication and Characterization of PCL Electrospun Scaffolds—a Review. *J. Mater. Chem.* **2011**, *21* (26), 9419–9453. https://doi.org/10.1039/C0JM04502K.

(133) Matumba, K. I.; Mokhena, T. C.; Ojijo, V.; Sadiku, E. R.; Ray, S. S. Morphological Characteristics, Properties, and Applications of Polylactide/Poly(ε-Caprolactone) Blends and Their Composites—A Review. *Macromol. Mater. Eng.* **2024**, *309* (8), 2400056. https://doi.org/10.1002/MAME.202400056.

(134) Radisavljevic, A.; Stojanovic, D. B.; Perisic, S.; Djokic, V.; Radojevic, V.; Rajilic-Stojanovic, M.; Uskokovic, P. S. Cefazolin-Loaded Polycaprolactone Fibers Produced via Different Electrospinning Methods: Characterization, Drug Release and Antibacterial Effect. *Eur. J. Pharm. Sci.* **2018**, *124*, 26–36. https://doi.org/10.1016/J.EJPS.2018.08.023.

(135) Orlov, M.; Tokarev, I.; Scholl, A.; Doran, A.; Minko, S. PH-Responsive Thin Film

Membranes from Poly(2-Vinylpyridine): Water Vapor-Induced Formation of a Microporous Structure. *Macromolecules* **2007**, *40* (6), 2086–2091. https://doi.org/10.1021/MA062821F.

(136) Fujii, S.; Kameyama, S.; Armes, S. P.; Dupin, D.; Suzaki, M.; Nakamura, Y. PH-Responsive Liquid Marbles Stabilized with Poly(2-Vinylpyridine) Particles. *Soft Matter* **2010**, *6* (3), 635–640. https://doi.org/10.1039/B914997J.

(137) Kennemur, J. G. Poly(Vinylpyridine) Segments in Block Copolymers: Synthesis, Self-Assembly, and Versatility. *Macromolecules* **2019**, *52* (4), 1354–1370. https://doi.org/10.1021/ACS.MACROMOL.8B01661.

(138) Wang, Z.; Ma, C.; Huang, X.; Lu, G.; Winnik, M. A.; Feng, C. Self-Seeding of Oligo(p-Phenylenevinylene)- b-Poly(2-Vinylpyridine) Micelles: Effect of Metal Ions. *Macromolecules* **2021**, *54* (14), 6705–6717. https://doi.org/10.1021/ACS.MACROMOL.1C00965.

(139) Zhao, J.; Chen, X. C.; Green, P. F. Nanoparticle Encapsulation in Thin Film Micellar Structures: A Physical Method for Functional Materials Design. *Soft Matter* **2013**, *9* (26), 6128–6134. https://doi.org/10.1039/C3SM50175B.

(140) Mössmer, S.; Spatz, J. P.; Möller, M.; Aberle, T.; Schmidt, J.; Burchard, W. Solution Behavior of Poly(Styrene)-&Zoc&-Poly(2-Vinylpyridine) Micelles Containing Gold Nanoparticles. *Macromolecules* **2000**, *33* (13), 4791–4798. https://doi.org/10.1021/MA992006I.

(141) Voylov, D. N.; Holt, A. P.; Doughty, B.; Bocharova, V.; Meyer, H. M.; Cheng, S.; Martin, H.; Dadmun, M.; Kisliuk, A.; Sokolov, A. P. Unraveling the Molecular Weight Dependence of Interfacial Interactions in Poly(2-Vinylpyridine)/Silica Nanocomposites. *ACS Macro Lett.* **2017**, *6* (2), 68–72. https://doi.org/10.1021/ACSMACROLETT.6B00915.

(142) Göbel, C.; Palamarciuc, T.; Lochenie, C.; Weber, B. Synthesis of Microcrystals of the [Fe(L)(Bipy)] Spin Crossover Coordination Polymer in a Poly-4-Vinylpyridine Matrix. *Chem. – An Asian J.* **2014**, *9* (8), 2232–2238. https://doi.org/10.1002/ASIA.201402144.

(143) Göbel, C.; Hils, C.; Drechsler, M.; Baabe, D.; Greiner, A.; Schmalz, H.; Weber, B. Confined Crystallization of Spin-Crossover Nanoparticles in Block-Copolymer Micelles. *Angew. Chemie - Int. Ed.* **2020**, *59* (14), 5765–5770. https://doi.org/10.1002/ANIE.201914343.

(144) Göbel, C.; Marquardt, K.; Baabe, D.; Drechsler, M.; Loch, P.; Breu, J.; Greiner, A.; Schmalz, H.; Weber, B. Realizing Shape and Size Control for the Synthesis of Coordination Polymer Nanoparticles Templated by Diblock Copolymer Micelles. *Nanoscale* **2022**, *14* (8), 3131–3147. https://doi.org/10.1039/D1NR07743K.

(145) Adamczyk, O.; Deptuch, A.; Tarnawski, T. R.; Zieliński, P. M.; Drzewicz, A.; Juszyńska-Gałązka, E. Electrospun Fiber Mats with Metronidazole: Design, Evaluation, and Release Kinetics. *J. Phys. Chem. B* **2025**, *129*, 4546. https://doi.org/10.1021/ACS.JPCB.5C00873.

(146) Loiola, L. M. D.; Cortez Tornello, P. R.; Abraham, G. A.; Felisberti, M. I. Amphiphilic Electrospun Scaffolds of PLLA–PEO–PPO Block Copolymers: Preparation, Characterization and Drug-Release Behaviour. *RSC Adv.* **2016**, *7* (1), 161–172.

https://doi.org/10.1039/C6RA25023H.

(147) Shi, X.; Xu, Z.; Huang, C.; Wang, Y.; Cui, Z. Selective Swelling of Electrospun Block Copolymers: From Perforated Nanofibers to High Flux and Responsive Ultrafiltration Membranes. *Macromolecules* **2018**, *51* (6), 2283–2292. https://doi.org/10.1021/ACS.MACROMOL.8B00220.

(148) Sas, W.; Czaja, P.; Fitta, M. A Novel Approach for Extracting Magnetic Properties of Double-Shell Nanotubes of Prussian Blue and Its Cr Analog with the Use of a Mathematical Hysteresis Decomposition. *J. Magn. Magn. Mater.* **2023**, *577*, 170805. https://doi.org/10.1016/J.JMMM.2023.170805.

(149) Pacanowska, A.; Muniraju, N. K. C.; Sas, W.; Perzanowski, M.; Mitura-Nowak, M.; Fitta, M. Prussian Blue Analogues Cubes in the Organic Polymer Electrospun Fibres. *Acta Phys. Pol. A ISSN 1898-794X* **2024**, *145* (2), 133–133. https://doi.org/10.12693/APHYSPOLA.145.133.

(150) Catala, L.; Mallah, T. Nanoparticles of Prussian Blue Analogs and Related Coordination Polymers: From Information Storage to Biomedical Applications. *Coord. Chem. Rev.* **2017**, *346*, 32–61. https://doi.org/10.1016/j.ccr.2017.04.005.

(151) Keßler, S.; González-Rubio, G.; Reinalter, E. R.; Kovermann, M.; Cölfen, H.; Gonzá Lez-Rubio, G.; Reinalter, R.; Kovermann, M.; Cö, H. Synthesis of Nickel Hexacyanoferrate Nanocubes with Tuneable Dimensions via Temperature- Controlled Ni2+-Citrate Complexation. *Chem. Commun.* **2020**, *56* (92), 14439–14442. https://doi.org/10.1039/d0cc04628k.

(152) Baranowska-Korczyc, A.; Warowicka, A.; Jasiurkowska-Delaporte, M.; Grześkowiak, B.; Jarek, M.; Maciejewska, B. M.; Jurga-Stopa, J.; Jurga, S. Antimicrobial Electrospun Poly(ε-Caprolactone) Scaffolds for Gingival Fibroblast Growth. *RSC Adv.* **2016**, *6* (24), 19647–19656. https://doi.org/10.1039/C6RA02486F.

(153) Sawczak, M.; Jendrzejewski, R.; Maskowicz, D.; Garcia, Y.; Dîrtu, M.; Kumar, V.; Śliwiński, G. Host-Guest Exchange Contribution to Transition Temperature Downshift in Nanocrystalline Fe(Pyrazine)[Pt(CN)4] Thin Films Prepared by Matrix-Assisted Pulsed Laser Evaporation. *J. Appl. Phys.* **2021**, *129* (15). https://doi.org/10.1063/5.0047749/1080223.

(154) Maskowicz, D.; Sawczak, M.; Jendrzejewski, R.; Gazda, M.; Tokoro, H.; Ohkoshi, S. ichi; Garcia, Y.; Śliwiński, G. Functional Phase Bistability in a Nanocrystalline RbMn[Fe(CN)6] Thin Film Fabricated by Matrix-Assisted Laser Evaporation. *Scr. Mater.* **2020**, *183*, 50–54. https://doi.org/10.1016/J.SCRIPTAMAT.2020.03.019.

(155) Vaidya, S.; Veselska, O.; Zhadan, A.; Daniel, M.; Ledoux, G.; Fateeva, A.; Tsuruoka, T.; Demessence, A. Flexible and Luminescent Fibers of a 1D Au(I)–Thiophenolate Coordination Polymer and Formation of Gold Nanoparticle-Based Composite Materials for SERS. *J. Mater. Chem. C* **2020**, *8* (24), 8018–8027. https://doi.org/10.1039/D0TC01706J.

(156) Kettle, S. F. A.; Diana, E.; Marchese, E. M. C.; Boccaleri, E.; Stanghellini, P. L. The Vibrational Spectra of the Cyanide Ligand Revisited: The ν(CN) Infrared and Raman Spectroscopy of Prussian Blue and Its Analogues. *J. Raman Spectrosc.* **2011**, *42* (11), 2006–2014. https://doi.org/10.1002/JRS.2944.

(157) Yuri Borodko, †; Susan E. Habas, ‡; Matthias Koebel, †; Peidong Yang, †; Heinz Frei, § and; Gabor A. Somorjai*, †. Probing the Interaction of Poly(Vinylpyrrolidone) with Platinum Nanocrystals by UV−Raman and FTIR. *J. Phys. Chem. B* **2006**, *110* (46), 23052–23059. https://doi.org/10.1021/JP063338+.

(158) Taylor, L. S.; Langkilde, F. W.; Zografi, G. Fourier Transform Raman Spectroscopic Study of the Interaction of Water Vapor with Amorphous Polymers. *J. Pharm. Sci.* **2001**, *90* (7), 888–901. https://doi.org/10.1002/JPS.1041.

(159) Adak, S.; Daemen, L. L.; Hartl, M.; Pandey, A. K.; Nakotte, H. Thermal Expansion in Prussian Blue Analogs M3[Cr(CN)6]2.NH2O (M = Mn, Fe, Co, Ni). *Solid State Sci.* **2024**, *157*, 107712. https://doi.org/10.1016/J.SOLIDSTATESCIENCES.2024.107712.

(160) Zaumseil, P. High-Resolution Characterization of the Forbidden Si 200 and Si 222 Reflections. *J. Appl. Crystallogr.* **2015**, *48* (2), 528–532. https://doi.org/10.1107/S1600576715004732.

(161) Razzak, M. T.; Zainuddin; Erizal; Dewi, S. P.; Lely, H.; Taty, E.; Sukirno. The Characterization of Dressing Component Materials and Radiation Formation of PVA–PVP Hydrogel. *Radiat. Phys. Chem.* **1999**, *55* (2), 153–165. https://doi.org/10.1016/S0969-806X(98)00320-X.

(162) Ahmed, M. A.; Khafagy, R. M.; Bishay, S. T.; Saleh, N. M. Effective Dye Removal and Water Purification Using the Electric and Magnetic Zn0.5Co0.5Al0.5Fe1.46La0.04O4/Polymer Core–Shell Nanocomposites. *J. Alloys Compd.* **2013**, *578*, 121–131. https://doi.org/10.1016/J.JALLCOM.2013.04.182.

(163) Ohkoshi, S. I.; Tokoro, H.; Hashimoto, K. Temperature- and Photo-Induced Phase Transition in Rubidium Manganese Hexacyanoferrate. *Coord. Chem. Rev.* **2005**, *249* (17–18), 1830–1840. https://doi.org/10.1016/J.CCR.2004.11.015.

(164) Thiet Vu, T.; Daro, N.; Marchivie, M.; Mornet, S.; Freysz, E.; Chastanet, G. Rational Direct Synthesis of RbMnFe Nanoparticles (RbMnFe = RbxMn[Fe(CN)6](2+ x)/3· NH2O Prussian Blue Analogue). *Inorg. Chem.* **2022**, *61* (6), 2945–2953. https://doi.org/10.1021/ACS.INORGCHEM.1C03826.

(165) Pacanowska, A.; Sas, W.; Gondek, Ł.; Maximienko, A.; Gazdowicz, G.; Fitta, M.; Muniraju, N. K. C. Electrospun Composites Integrating RbxMn[Fe(CN)6](2+x)/3 NH2Omicrocrystals and Organic Polymer. *under Revis.* **2025**.

(166) Phu, P. K.; Thuan, N. M.; van Minh, N. Synthesis, Characterisation and Structural Studies of Rb[Fe(CN)6]. *J. Exp. Nanosci.* **2012**, *7* (3), 336–343. https://doi.org/10.1080/17458080.2010.533294.

(167) Vertelman, E. J. M.; Lummen, T. T. A.; Meetsma, A.; Bouwkamp, M. W.; Molnar, G.; Van Loosdrecht, P. H. M.; Van Koningsbruggen, P. J. Light- And Temperature-Induced Electron Transfer in Single Crystals of RbMn[Fe(CN)6]·H2O. *Chem. Mater.* **2008**, *20* (4), 1236–1238. https://doi.org/10.1021/CM7032965.

(168) Fukaya, R.; Nakajima, M.; Tokoro, H.; Ohkoshi, S.; Suemoto, T. Photoinduced Charge-Transfer Process in Rubidium Manganese Hexacyanoferrate Probed by Raman Spectroscopy. *J. Chem. Phys.* **2009**, *131* (15), 51. https://doi.org/10.1063/1.3245863/317207.

(169) Fukaya, R.; Asahara, A.; Ishige, S.; Nakajima, M.; Tokoro, H.; Ohkoshi, S. I.; Suemoto,

T. Probing of Local Structures of Thermal and Photoinduced Phases in Rubidium Manganese Hexacyanoferrate by Resonant Raman Spectroscopy. *J. Chem. Phys.* **2013**, *139* (8), 84303. https://doi.org/10.1063/1.4818809/74181.

(170) Tokoro, H.; Ohkoshi, S. Photo-Induced Phase Transition in RbMnFe Prussian Blue Analog-Based Magnet. *Springer Ser. Opt. Sci.* **2010**, *155*, 1–35. https://doi.org/10.1007/978-3-642-03951-5_1.

(171) Nieto-Castro, D.; Graf, A. W.; Gispert-Guirado, F.; Galán-Mascarós, J. R. Magnetic and Electrical Bistability in Hybrid Composites of Conducting Organic Polymers with [Fe(NH2-Trz)3]n[SO4]N. *J. Mater. Chem. C* **2023**, *11* (33), 11325–11332. https://doi.org/10.1039/D3TC00595J.

(172) Torres-Cavanillas, R.; Lima-Moya, L.; Tichelaar, F. D.; Zandbergen, H. W.; Giménez-Marqués, M.; Coronado, E. Downsizing of Robust Fe-Triazole@SiO2 Spin-Crossover Nanoparticles with Ultrathin Shells. *Dalt. Trans.* **2019**, *48* (41), 15465–15469. https://doi.org/10.1039/C9DT02086A.

(173) Herrera, J. M.; Titos-Padilla, S.; Pope, S. J. A.; Berlanga, I.; Zamora, F.; Delgado, J. J.; Kamenev, K. V.; Wang, X.; Prescimone, A.; Brechin, E. K.; Colacio, E. Studies on Bifunctional Fe(II)-Triazole Spin Crossover Nanoparticles: Time-Dependent Luminescence, Surface Grafting and the Effect of a Silica Shell and Hydrostatic Pressure on the Magnetic Properties. *J. Mater. Chem. C* **2015**, *3* (30), 7819–7829. https://doi.org/10.1039/C5TC00685F.

(174) Regueiro, A.; Martí-Carrascosa, M.; Torres-Cavanillas, R.; Coronado, E. Unlocking Room-Temperature Bistable Spin Transition at the Nanoscale: The Synthesis of Core@shell [Fe(NH2trz)3(NO3)2]@SiO2 Nanoparticles. *Dalt. Trans.* **2024**, *53* (20), 8764–8771. https://doi.org/10.1039/D4DT00911H.

(175) Sindoro, M.; Yanai, N.; Jee, A. Y.; Granick, S. Colloidal-Sized Metal-Organic Frameworks: Synthesis and Applications. *Acc. Chem. Res.* **2014**, *47* (2), 459–469. https://doi.org/10.1021/AR400151N.

(176) Catala, L.; Mallah, T. Nanoparticles of Prussian Blue Analogs and Related Coordination Polymers: From Information Storage to Biomedical Applications. *Coord. Chem. Rev.* **2017**, *346*, 32–61. https://doi.org/10.1016/J.CCR.2017.04.005.

(177) Weber, B. Synthesis of Coordination Polymer Nanoparticles Using Self-Assembled Block Copolymers as Template. *Chem. - A Eur. J.* **2017**, *23* (72), 18093–18100. https://doi.org/10.1002/chem.201703280.

(178) Galán-Mascarós, J. R.; Coronado, E.; Forment-Aliaga, A.; Monrabal-Capilla, M.; Pinilla-Cienfuegos, E.; Ceolin, M. Tuning Size and Thermal Hysteresis in Bistable Spin Crossover Nanoparticles. *Inorg. Chem.* **2010**, *49* (12), 5706–5714. https://doi.org/10.1021/IC100751A.

(179) Tissot, A.; Bardeau, J. F.; Rivière, E.; Brisset, F.; Boillot, M. L. Thermo- and Photoswitchable Spin-Crossover Nanoparticles of an Iron(II) Complex Trapped in Transparent Silica Thin Films. *Dalt. Trans.* **2010**, *39* (33), 7806–7812. https://doi.org/10.1039/C0DT00321B.

(180) Grosjean, A.; Négrier, P.; Bordet, P.; Etrillard, C.; Mondieig, D.; Pechev, S.; Lebraud, E.; Létard, J. F.; Guionneau, P. Crystal Structures and Spin Crossover in the Polymeric

Material [Fe(Htrz)2(Trz)](BF4) Including Coherent-Domain Size Reduction Effects. *Eur. J. Inorg. Chem.* **2013**, *2013* (5–6), 796–802. https://doi.org/10.1002/EJIC.201201121.

(181) Siddiqui, S. A.; Domanov, O.; Schafler, E.; Vejpravova, J.; Shiozawa, H. Synthesis and Size-Dependent Spin Crossover of Coordination Polymer [Fe(Htrz)2(Trz)](BF4). *J. Mater. Chem. C* **2021**, *9* (3), 1077–1084. https://doi.org/10.1039/D0TC03878D.

(182) Dîrtu, M. M.; Schmit, F.; Naik, A. D.; Rusu, I.; Rotaru, A.; Rackwitz, S.; Wolny, J. A.; Schünemann, V.; Spinu, L.; Garcia, Y. Two-Step Spin Transition in a 1D FeII 1,2,4-Triazole Chain Compound. *Chem. - A Eur. J.* **2015**, *21* (15), 5843–5855. https://doi.org/10.1002/CHEM.201406231.

(183) Van Koningsbruggen, P. J.; Garcia, Y.; Codjovi, E.; Lapouyade, R.; Kahn, O.; Fournès, L.; Rabardel, L. Non-Classical FeII Spin-Crossover Behaviour in Polymeric Iron(II) Compounds of Formula [Fe(NH2trz)3]X2xH2O (NH2trz=4-Amino-1,2,4-Triazole; X=derivatives of Naphthalene Sulfonate). *J. Mater. Chem.* **1997**, *7* (10), 2069–2075. https://doi.org/10.1039/A702690K.

(184) Yamamoto, T. Assignment of Pre-Edge Peaks in K-Edge x-Ray Absorption Spectra of 3d Transition Metal Compounds: Electric Dipole or Quadrupole? *X-Ray Spectrom.* **2008**, *37* (6), 572–584. https://doi.org/10.1002/XRS.1103;JOURNAL:JOURNAL:10974539.

(185) Westre, T. E.; Kennepohl, P.; DeWitt, J. G.; Hedman, B.; Hodgson, K. O.; Solomon, E. I. A Multiplet Analysis of Fe K-Edge 1s → 3d Pre-Edge Features of Iron Complexes. *J. Am. Chem. Soc.* **1997**, *119* (27), 6297–6314. https://doi.org/10.1021/JA964352A.

(186) Usmani, S.; Mikolasek, M.; Gillet, A.; Sanchez Costa, J.; Rigoulet, M.; Chaudret, B.; Bousseksou, A.; Lassalle-Kaiser, B.; Demont, P.; Molnár, G.; Salmon, L.; Carrey, J.; Tricard, S. Spin Crossover in Fe(Triazole)–Pt Nanoparticle Self-Assembly Structured at the Sub-5 Nm Scale. *Nanoscale* **2020**, *12* (15), 8180–8187. https://doi.org/10.1039/D0NR02154G.

(187) Yokoyama, T.; Murakami, Y.; Kiguchi, M.; Komatsu, T.; Kojima, N. Spin-Crossover Phase Transition of a Chain Fe(II) Complex Studied by x-Ray-Absorption Fine-Structure Spectroscopy. *Phys. Rev. B* **1998**, *58* (21), 14238. https://doi.org/10.1103/PhysRevB.58.14238.

(188) Boča, R.; Vrbová, M.; Werner, R.; Haase, W. Spin Crossover in Iron(II) Tris(2-(2-Pyridyl)Benzimidazole) Complex Monitored by the Variable Temperature EXAFS. *Chem. Phys. Lett.* **2000**, *328* (1–2), 188–196. https://doi.org/10.1016/S0009-2614(00)00902-7.

(189) Pacanowska, A.; Regueiro, A.; Clemente-León, M.; Coronado, E.; Forment-Aliaga, A.; Fitta, M. Stimuli-Responsive Electrospun Fibers Based on Spin Crossover Nanoparticles and Organic Polymers. *under Revis.* **2025**.

(190) Elishav, O.; Beilin, V.; Rozent, O.; Shter, G. E.; Grader, G. S. Thermal Shrinkage of Electrospun PVP Nanofibers. *J. Polym. Sci. Part B Polym. Phys.* **2018**, *56* (3), 248–254. https://doi.org/10.1002/POLB.24538.

(191) Ko, J. H. Poly(N-Vinyl Pyrrolidone). *Polym. Data Handb.* **2009**, 1181–1183. https://doi.org/10.1093/OSO/9780195181012.003.0206.

(192) Dreyer, B.; Natke, D.; Klimke, S.; Baskas, S.; Sindelar, R.; Klingelhöfer, G.; Renz, F.

Implementation of Spin Crossover Compounds into Electrospun Nanofibers. *Hyperfine Interact.* **2018**, *239* (1), 1–8. https://doi.org/10.1007/S10751-017-1483-X.

(193) Bramanti, E.; Bonaccorsi, L.; Campanella, B.; Ferrari, C.; Malara, A.; Freni, A. Structural Characterization of Electrospun Tetraethylortosilicate (TEOS)/Polyvinylpyrrolidone (PVP) Microfibres. *Mater. Chem. Phys.* **2022**, *287*, 126248. https://doi.org/10.1016/J.MATCHEMPHYS.2022.126248.

(194) Brooker, S. Spin Crossover with Thermal Hysteresis: Practicalities and Lessons Learnt. *Chem. Soc. Rev.* **2015**, *44* (10), 2880–2892. https://doi.org/10.1039/C4CS00376D.

(195) Pacanowska, A.; Wota, G.; Jasiurkowska-Delaporte, M.; Muniraju, N. K. C.; Komędera, K.; Tabiś, W.; Maximienko, A.; Gazdowicz, G.; Czaja, P.; Perzanowski, M.; Mitura-Nowak, M.; Nowicka, B.; Fitta, M. Bistable Molecular Chain Magnet in Electrospun Polymer Fibers. *under Revis.* **2025**.

(196) Nowicka, B.; Reczyński, M.; Rams, M.; Nitek, W.; Żukrowski, J.; Kapusta, C.; Sieklucka, B. Hydration-Switchable Charge Transfer in the First Bimetallic Assembly Based on the [Ni(Cyclam)]3+ – Magnetic CN-Bridged Chain {(H3O)[NiIII(Cyclam)][FeII(CN)6]·5H2O}n. *Chem. Commun.* **2015**, *51* (57), 11485–11488. https://doi.org/10.1039/C5CC02805A.

(197) Nowicka, B.; Reczyński, M.; Balanda, M.; Fitta, M.; Gawel, B.; Sieklucka, B. The Rule Rather than the Exception: Structural Flexibility of [Ni(Cyclam)]2+-Based Cyano-Bridged Magnetic Networks. *Cryst. Growth Des.* **2016**, *16* (8), 4736–4743. https://doi.org/10.1021/ACS.CGD.6B00800.

(198) Usman, K. A. S.; Maina, J. W.; Seyedin, S.; Conato, M. T.; Payawan, L. M.; Dumée, L. F.; Razal, J. M. Downsizing Metal–Organic Frameworks by Bottom-up and Top-down Methods. *NPG Asia Mater.* **2020**, *12* (1), 1–18. https://doi.org/10.1038/S41427-020-00240-5.

(199) Li, P. Z.; Maeda, Y.; Xu, Q. Top-down Fabrication of Crystalline Metal–Organic Framework Nanosheets. *Chem. Commun.* **2011**, *47* (29), 8436–8438. https://doi.org/10.1039/C1CC12510A.

(200) Uemura, T.; Kitagawa, S. Nanocrystals of Coordination Polymers. *Chem. Lett.* **2005**, *34* (2), 132–137. https://doi.org/10.1246/cl.2005.132.

(201) Tangoulis, V.; Polyzou, C. D.; Gkolfi, P.; Lalioti, N.; Malina, O.; Polaskova, M. 2-D Spin Crossover Materials at the Nanometric Scale: The Effects of the Size-Reduction on the Magnetic Properties. *Dalt. Trans.* **2021**, *50* (9), 3109–3115. https://doi.org/10.1039/D1DT00250C.

(202) Mathonière, C.; Mitcov, D.; Koumousi, E.; Amorin-Rosario, D.; Dechambenoit, P.; Fatima Jafri, S.; Sainctavit, P.; Cartier dit Moulin, C.; Toupet, L.; Trzop, E.; Collet, E.; Arrio, M. A.; Rogalev, A.; Wilhelm, F.; Clérac, R. Metal-to-Metal Electron Transfer in a Cyanido-Bridged {Fe2Co2} Square Complex Followed by X-Ray Diffraction and Absorption Techniques. *Chem. Commun.* **2022**, *58* (86), 12098–12101. https://doi.org/10.1039/D2CC04246K.

(203) Hallmeier, K. H.; Sauter, S.; Szargan, R. XANES and EXAFS Investigations of Bonding and Structure of Ni and Co Derivatives from Prussian Blue Coordination Compounds. *Inorg. Chem. Commun.* **2001**, *4* (3), 153–156. https://doi.org/10.1016/S1387-

7003(01)00151-4.

(204) Jasiurkowska-Delaporte, M.; Juszyńska-Gałązka, E.; Sas, W.; Zieliński, P. M.; Baranowska-Korczyc, A. Soft versus Hard Confinement Effects on the Phase Transitions, and Intra- and Inter- Molecular Dynamics of 6BT Liquid Crystal Constrained in Electrospun Polymer Fibers and in Nanopores. *J. Mol. Liq.* **2021**, *331*, 115817. https://doi.org/10.1016/J.MOLLIQ.2021.115817.

(205) Uyar, T.; Besenbacher, F. Electrospinning of Uniform Polystyrene Fibers: The Effect of Solvent Conductivity. *Polymer (Guildf).* **2008**, *49* (24), 5336–5343. https://doi.org/10.1016/J.POLYMER.2008.09.025.

(206) Melo, G. H. F.; Sundararaj, U. Influence of Mixed Solvent in the Morphology and Hydrophobicity of Electrospun Polystyrene Porous Fibers. *Macromol. Rapid Commun.* **2024**, *45* (21), 2400403. https://doi.org/10.1002/MARC.202400403.

(207) Kotula, A. P.; Snyder, C. R.; Migler, K. B. Determining Conformational Order and Crystallinity in Polycaprolactone via Raman Spectroscopy. *Polymer (Guildf).* **2017**, *117*, 1–10. https://doi.org/10.1016/J.POLYMER.2017.04.006.

(208) Salehi, S.; Bahners, T.; Gutmann, J. S.; Gao, S. L.; Mäder, E.; Fuchsluger, T. A. Characterization of Structural, Mechanical and Nano-Mechanical Properties of Electrospun PGS/PCL Fibers. *RSC Adv.* **2014**, *4* (33), 16951–16957. https://doi.org/10.1039/C4RA01237B.

(209) Kavesh, S.; Schultz, J. M. Meaning and Measurement of Crystallinity in Polymers: A Review. *Polym. Eng. Sci.* **1969**, *9* (5), 331–338. https://doi.org/10.1002/PEN.760090504.

(210) Wang, X.; Zhao, H.; Turng, L. S.; Li, Q. Crystalline Morphology of Electrospun Poly(ε-Caprolactone) (PCL) Nanofibers. *Ind. Eng. Chem. Res.* **2013**, *52* (13), 4939–4949. https://doi.org/10.1021/IE302185E.

List of publications

- A. Pacanowska, N.K. Chogondahalli Muniraju, W. Sas, M. Perzanowski, M. Mitura-Nowak, M. Fitta, ***Prussian Blue Analogues Cubes in the Organic Polymer Electrospun Fibres***, Acta Physica Polonica A, 145, 133-138 (2024), doi: 10.12693/APhysPolA.145.133
- W. Sas, A. Pacanowska, M. Fitta, ***Magnetic Properties of the Thin Films of Prussian Blue Analogues Obtained by Ion ExchangeSynthesis***, Acta Physica Polonica A, 145, 109-113 (2024), doi: 10.12693/APhysPolA.145.109
- M. Mihalik Jr. A. Pacanowska, M. Orendáč, K. Csach, M. Fitta, M. Mihalik, ***Vacancy-driven magnetism of $GdMnO_{3+\delta}$ multiferroic compound***, Journal of Magnetism and Magnetic Materials, 587, 171221 (2023), doi: 10.1016/j.jmmm.2023.171221
- A. Pacanowska, M. Fitta, M. Kozieł, B. Nowicka, ***Thin Films of Solvatomagnetic CN-Bridged Coordination Polymers: From Micro to Nanoscale***, Advanced Materials Interfaces, 10, 2201834 (2023), doi: 10.1002/admi.202201834
- P. Konieczny, W.Sas, D. Czernia, A. Pacanowska, M. Fitta, R. Pełka, ***Magnetic cooling: a molecular perspective***, Dalton Transactions, 51, 12762-12780 (2022), doi: 10.1039/d2dt01565j
- A. Pacanowska, A. Regueiro, M. Clemente-León, E. Coronado, A. Forment-Aliaga, M. Fitta, ***Stimuli-responsive electrospun fibers based on spin crossover nanoparticles and organic polymers***, under revision (2025)
- A. Pacanowska. W. Sas, Ł. Gondek, A. Maximienko, G. Gazdowicz, M. Fitta, N. K. Chogondahalli Muniraju, ***Electrospun composites integrating $Rb_xMn[Fe(CN)_6]_{(2+3)/3}\cdot nH_2O$ microcrystals and organic polymer***, under revision (2025)
- A. Pacanowska, G. Wota, M. Jasiurkowska-Delaporte, N. K. Chogondahalli Muniraju, K. Komędera, W. Tabiś, A. Maximienko, G. Gazdowicz, P. Czaja, M. Perzanowski, M. Mitura-Nowak, B. Nowicka, M. Fitta, ***Bistable Molecular Chain Magnet in Electrospun Polymer Fibers***, under revision (2025)
- A. Pacanowska, A. Regueiro, P. Czaja, A. Deptuch, M. Fitta, P. Konieczny, ***Exploring the Impact of Magnetic Field and Nanoparticle Size on the Magnetic Properties of Fe(II)-triazole Spin-Crossover Nanoparticles***, under revision (2025)

Conferences and lectures

1. Zakopane School of Physics, Breaking Frontiers: Submicron Structures in Physics and Biology, Zakopane, Poland, May 2025 - oral communication; ***Pressure-induced metal-to-metal electron transfer in molecular chain composite material probed by X-ray absorption spectroscopy***
2. Multiscale Phenomena in Molecular Matter, Multis 2024, Kraków, Poland, September 2024 - poster presentation: ***Metal-to-metal electron transfer in a bistable molecular chain magnet probed by X-ray absorption spectroscopy***
3. 9th European Conference on Molecular Magnetism Young ECMM2024 (pre-conference), Kraków, Poland, July 2024 - oral communication: ***The role of organic polymer in the preparation of composites based on switchable coordination structures***
4. 10th International Conference on Superconductivity and Magnetism- ICSM2025, Fethiye-Oludeniz, Turkey, May 2024 - oral communication: ***Transforming brittle stimuli-responsive crystalline structures into temperature and pressure-sensing composites***
5. International SYLINDA Symposium, SOLARIS Kraków, Poland, March 2024 - poster presentation: ***Electronic State Determination of Spin-Crossover Nanoparticles Based on Iron(II) - Triazole Coordination Polymers***
6. Invited seminar at the Institute of Experimental Physics, Slovak Academy of Science, Košice, Slovakia, 2023 - entitled: ***From thin film deposition to nanocomposite preparation of functional coordination polymers***
7. SCIRES 2023 - Solid State Science and Research, Zagreb, Croatia, June 2023 - oral communication: ***From thin film deposition to composite materials of switchable coordination compound***
8. Zakopane School of Physics, Breaking Frontiers: Submicron Structures in Physics and Biology, Zakopane, Poland, May 2023 - oral communication: ***Introduction of spin crossover compounds into electrospun fibres***
9. 6th European Symposium on Electrohydrodynamic Atomization and Electrospinning ESEE2023, Kraków, Poland, May 2023 - poster presentation: ***The use of the electrospinning technique in the preparation of composites of bistable coordination compounds***
10. 5th International Conference on Functional Molecular Materials FUNMAT2023, Kraków, Poland, March 2023 - poster presentation: ***Electrospun polymeric composites containing spin crossover nanoparticles***
11. 4th IEEE International Conference on Advances in Magnetics IEEE AIM 2023, Moena, Italy, January 2023 - oral communication: ***Bistable molecular systems in electrospun polymer fibers***
12. Invited seminar at the Institute of Experimental Physics, Slovak Academy of Science, Košice, Slovakia, 2022 - entitled***: Bistable composite systems based on polymers and chain-like molecular magnet***

13. Multiscale Phenomena in Molecular Matter, Multis 2022, Kraków, Poland - online, 2022 - poster presentation: ***Switchable composite materials based on polymers and chain-like molecular magnet***
14. YOUNG MULTIS 2021 - Multiscale Phenomena in Condensed Mater, Kraków, Poland - online, 2021 - poster presentation: ***Towards thin films of multi-responsive molecular switches***
15. 17th International Conference on Molecule-based Magnets (ICMM2021), Manchester, UK - online, 2021 - poster presentation: ***Surface Deposition of CN-bridged Magnetic Sponges***
16. 1st Asian Conference on Molecular Magnetism (ACMM2021), Fukuoka, Japan - online, 2021 - poster presentation: ***Construction of thin film systems using solvatomagnetic coordination polymers***

Other significant achivements and activities

- Awarded for the best poster presentation at the conference Multiscale Phenomena in Molecular Matter, Multis 2024 organised in IFJ PAN, Kraków, Poland, with the poster entitled: ***Metal-to-metal electron transfer in a bistable molecular chain magnet probed by X-ray absorption spectroscopy***
- Awarded for the best poster presentation at the 1st Asian Conference on Molecular Magnetism (ACMM2021), Fukuoka, Japan, organised online, with the poster entitled: ***Construction of thin film systems using solvatomagnetic coordination polymers***
- President, Secretary and Member of the PhD Student Council of the Institute of Nuclear Physics Polish Academy of Sciences, March 2021 – July 2025
- Memeber of the Scientific Council at the Intitute of Nuclear Physics Polish Academy of Sciences, January 2022 – December 2023
- Member of organising committes for the international conferences: Zakopane School of Physics 2025, Multis2024, Zakopane School of Physics 2023, YOUNG Multis 2023, Mutlis2022 and YOUNG Multis2021